

Synthesis And Physical Properties Of Manganite Nanowires

Thesis submitted for the degree of
Doctor of Philosophy (Science)

In

Physics (Experimental)

By

Subarna Datta

Department of Physics
University of Calcutta
July 2017

To my Family

Acknowledgements

Though only my name appears on the cover of this dissertation, a team of talented people has contributed to run this project together. I would like to thank all who have made this dissertation possible and who has been helpful and inspiring during my Ph.D. work.

First, I would like to express my special appreciation and thanks to my supervisor **Dr. Barnali Ghosh Saha** for her worthwhile guidance, support, inspiration and stood by me throughout the entire process of completing my PhD at *S N Bose National Centre for Basic Sciences, Kolkata, India*. I have been wonderfully fortunate to have such an advisor who gave me the freedom to explore on my own and at the same time the guidance to recover when my steps hesitated. Her patience and support helped me to overcome many crisis situations and finish this dissertation.

I express my sincere respect and gratitude to **Prof. A. K. Raychaudhuri** for his guidance, wisdom and continuous enthusiasm which helped me to complete this dissertation. He always inspired and encouraged us to become a knowledgeable person rather than an informative one.

I wish to express my sincere thank to Prof. Ranjan Chaudhuri, Prof, P. K. Mukhopadhyay and others for representing physics in an easy way during my course work. I would like to thank Dr. S. M. Yusuf, Dr. V. Siruguri, Dr. S. D. Kaushik and Dr. Amit Kumar in Bhabha Atomic Research Centre for their active collaborations which helped me a lot in my research. I am grateful to Dr. V. Srihari for helping in XRD measurement at PF, KEK, Japan. I wish to thank Dr. H. Srikanth, Dr. S. Chandra, Dr. A. Biswas and Dr. N. Ghosh for helping me to learn different magnetic measurements.

I appreciate the financial support from the Department of Science and Technology. DST, Govt. of India and S. N. Bose National centre for Basic Sciences, Kolkata.

I acknowledge the help of all the technical cell members Shakti da, Surajit da, Urmi, Dipankar da, Amit da and special thanks to Joy and Samik da for their unconditional support and help whenever I needed in our centre. Single nanowire device fabrication would not be possible without the help of Joy and Samik da helped me in doing rigorous TEM and EELS measurement of single nanowires. I would like to thank all the people of administrative, engineering, computer, library, electrical, instrumentation, workshop, canteen, cleaner, security guards and other supporting staff of SBNBCBS for their timely help and also for their the day-to-day activities in the centre.

I feel pleasant being a member of the New Nano Lab for the friendly and healthy academic environment. I would like to thank Kaustuv da who suggested me to improve my work. Thanks to Sudeshna di for introducing me with electrical transport measurement of single

nanowire. I am gratefully acknowledging Ankita di for her constant help in my academic as well as personal matters. She has educated me the theoretical simulations which are very new and interesting things to me. She never said ‘no’ whenever I asked for help from her and she always tries to give her best. I would like to thank all my lab members, seniors, Jasashree di, Rabaya di, Manotosh da, Putul di, Rajesh da, Bipul da, Pabitra da, Rishi da and juniors Ravindra, Shaili, Bhivuti, Chandan, Avisek, Subhamita for their support and help whenever I required. We made a great memorable tour in Vizag with Chandan and Avisek. I have spent a pleasant time with all of them in the lab.

I wish to express my sincere gratitude to all my respected teachers. Without their support, inspiration and guidance it was not possible for me to achieve my success.

Most importantly, none of this would have been possible without the love and patience of my family. 26 alphabets are not enough to thank my parents, my didi who have been a great source of support and encouragement throughout my life. With all my heart, I am grateful to my father in law, mother in law for their constant love, precious support and confidence in me. I would like express my sincere thanks to my cousin Rima, Surajit Da, Sudipto da, my nephew Swapnil for their love and support. Words are not sufficient to express my deepest gratitude to my husband Soumya, for being most caring, supportive and understating. He always stood beside me at all the ups and downs I faced during my Ph.D. days. He is my best friend and I am blessed that I found him. Without his encouragement it would never been possible for me to write this dissertation.

Finally, I thank to Almighty God for making my journey so beautiful.....

Subarna Datta
S. N. Bose National Centre for Basic Sciences
Kolkata, India
July, 2017

List of Publications

1. **Subarna Datta**, A. Ghatak and B. Ghosh, *Manganite ($La_{1-x}A_xMnO_3$; $A = Sr, Ca$) nanowires with adaptable stoichiometry grown by hydrothermal method: understanding of growth mechanism using spatially resolved techniques*, **J. Mater. Sci.**, **51**, 9679–9695 (2016).*
2. **Subarna Datta**, S. Samanta, B. Ghosh and A. K. Raychaudhuri, *Low-frequency resistance fluctuations in a single nanowire (diameter ~ 45 nm) of a complex oxide and its relation to magnetic transitions and phase separation*, **Appl. Phys. Lett.** **105**, 073117 (2014).*
3. **Subarna Datta**, S. Chandra, S. Samanta, K. Das, H. Srikanth and Barnali Ghosh, *Growth and physical property study of single nanowire (diameter ~ 45 nm) of half doped manganite*, **Journal of Nanomaterials**, vol. 2013, Article ID 162315, 6 pages, 2013. doi:10.1155/2013/162315.*
4. N. Ghosh, **Subarna Datta** and B. Ghosh, *Size dependence in magnetic memory, relaxation and interaction of $La_{0.67}Sr_{0.33}MnO_3$* , **Journal of Magnetism and Magnetic Materials** **382**, 277–282 (2015).*
5. S. Chandra, A. Biswas, **Subarna Datta**, B. Ghosh, A. K. Raychaudhuri and H. Srikanth, *Inverse magnetocaloric and exchange bias effects in single crystalline $La_{0.5}Sr_{0.5}MnO_3$ nanowires*, **Nanotechnology**, **24**, 505712 (9pp) (2013).*
6. **Subarna Datta** and B. Ghosh, *Critical behaviour near the ferromagnetic – paramagnetic phase transition in $La_{0.7}Sr_{0.3}MnO_{3+d}$ nanowires synthesized by hydrothermal method*, **AIP Conference Proceedings** **1665**, 050045 (2015).*
7. S. Chandra, A. Biswas, **Subarna Datta**, B. Ghosh, A. K. Raychaudhuri, M. H. Phan and H. Srikanth, *Multiple magnetic transitions and magnetocaloric effect in hydrothermally synthesized single crystalline $La_{0.5}Sr_{0.5}MnO_3$ nanowires*, **Mater. Res. Soc. Symp. Proc. Vol. 1454** © 2012 Materials Research Society.*
8. A. Biswas, S. Chandra, T. Samanta, B. Ghosh, **Subarna Datta**, M. H. Phan and A. K. Raychaudhuri, I. Das and H. Srikanth, *Universality in the entropy change for the inverse magnetocaloric effect*, **Phys. Rev. B** **87**, 134420 (2013).
9. S. Chandra, A. Biswas, **Subarna Datta**, B. Ghosh, V. Siruguri, A. K. Raychaudhuri, M. H. Phan and H. Srikanth, *Evidence of a canted magnetic state in self-doped*

LaMnO_{3+delta} (delta = 0.04): a magnetocaloric study, **J. Phys.: Condens. Matter.** **24**, 366004 (2012).

10. **Subarna Datta**, S. D. Kaushik, V. Siruguri, Amit Kumar, S M Yusuf and B. Ghosh, *Size induced magnetic phases in half doped manganite nanowires of La_{0.5}Sr_{0.5}MnO₃: A neutron diffraction study*, **under review**.*
11. **Subarna Datta**, A. Ghatak and B. Ghosh, *High resolution TEM imaging and simulation in complex perovskite oxide nanowires: An insight into the atomic column structure and defects in nanowires*, **submitted**.*

Present thesis is based on publications marked with *

List of Abbreviations

1D: One dimensional	$-\Delta S_M$: Magnetic entropy
NW: Nanowire	γ_H : Hooge parameter
CMR: Colossal magnetoresistance	V: Applied Bias
MR: Magnetoresistance	T_C : Curie temperature
MIT: Metal insulator transition	T_N : Neel temperature
DE: Double exchange	ρ : Resistivity
SE: Super exchange	R_C : Contact resistance
EB: Exchange bias	I : Current
CO: Charge order	H_K : Anisotropy field
JT: Jahn-Teller	H_C : Coercive field
t_G : Goldschmidt tolerance factor	χ : AC susceptibility
AFM: Antiferromagnetic/Antiferromagnetism	λ : wavelength
FM: Ferromagnetic/Ferromagnetism	V: Volt
PM: Paramagnetic/Paramagnetism	K: Kelvin
DOS: Density of states	Ω : Ohm
EBL: Electron Beam Lithography	A: Ampere
FEB: Focused Electron Beam	nm: nanometer
FIB: Focused Ion Beam	R : sample Resistance
NPGS: Nano Pattern Generating System	f : Frequency
FEG: Field Emission Gun	T : Temperature
XRD: X-Ray Diffraction	M : Magnetic Moment
ND: Neutron Diffraction	H : Magnetic field
VSM: Vibrating Sample Magnetometer	σ : Conductivity
TEM: Transmission Electron Microscope	ρ_C : Contact Resistivity
EELS: Electron Energy Loss Spectroscopy	n: Carrier density
ZLP: Zero Loss Peak	ψ : Wave function
EFTEM: Energy Filtered TEM	t : time
JEMS: Java Electron Microscopy Simulation	j : Current density
SAED: Selected Area Electron Diffraction	R_p : Profile R-factor
IMCE: Inverse Magnetocaloric effect	R_{WP} : Weighted Profile R-factor
PMMA: Poly(methyl methacrylate)	R_{exp} : Expected R-factor
SEM: Scanning Electron Microscope	$S_v(f)$: Power spectral density
h : Plank's Constant	ZFC: Zero Field Cooled
k_B : Boltzmann Constant	FC: Field Cooled
VRH: Variable Range Hopping	TS: Transverse Susceptibility
SG: Spin glass	PDF: Probability Density Function
d : Nanowire diameter	

Contents

Table of Contents	viii
List of Figures	xi
List of Tables	xxii

1. Introduction	1
1.1 Introduction to manganite system.....	2
1.2 Crystal structure of manganite.....	3
1.3 Cationic disorder.....	4
1.4 Electronic structure of manganite	5
1.5 Magnetic interactions in manganite	6
1.6 Magnetization due to divalent atom doping	10
1.7 Magnetoresistance (MR) in manganite	11
1.8 Phenomena of phase coexistence in manganite.....	13
1.9 Parameters controlling the physical properties	15
1.10 Motivation of the present work	19
1.11 Structure of the thesis.....	21
Bibliography	23
2. Synthesis and Characterization	27
2.1 Introduction	28
2.2 Synthesis of $\text{La}_{1-x}\text{A}_x\text{MnO}_3$ (A = Sr, Ca; $x = 0.3$ and 0.5) nanostructures	29
2.2.1 Nanostructures growth by Hydrothermal Method	30
2.2.1.1 Influence of growth parameters in hydrothermal process	32
2.2.1.2 Growth mechanism of the nanostructures	37
2.3 Bulk growth by the sol gel method.....	39
2.4 Brief description to characterization techniques	40
2.4.1 Structural Characterization	41
2.4.1.1 X-Ray Diffraction (XRD)	41
2.4.1.2 Laboratory based X – ray sources	41
2.4.1.3 Synchrotron sources for X – ray diffraction	42
2.4.1.4 The Rietveld refinement technique	43
2.4.1.5 Neutron diffraction	46
2.4.1.6 Scanning Electron Microscope (SEM)	49
2.4.1.7 Energy dispersive X-ray Analysis (EDAX).....	51
2.4.1.8 Transmission Electron Microscope (TEM)	52
2.5 Conclusion.....	55
Bibliography	56

3. Structural analysis of single nanowire using advanced characterization tools	59
3.1 Introduction	60
3.2 Electron energy loss spectroscopy (EELS)	61
3.2.1 EELS study to estimate the valency of Mn	64
3.3 Energy Filtered TEM to check the homogeneity	66
3.4 Structural simulation of single nanowire (NW) of manganite using Java Electron Microscopy Simulation (JEMS) software.....	68
3.4.1 Basics of JEMS software.....	68
3.4.2 Importance of image simulation using JEMS software	71
3.4.3 Input parameters of JEMS software.....	72
3.4.4 Structural simulation of the nanowires	73
3.4.5 Atomic column structures of the nanowires	80
3.5 Conclusion	81
Bibliography	83
 4. Device fabrication and measurement techniques	 85
4.1 Introduction	86
4.2 Lithography processes	86
4.2.1 Photo lithography	87
4.2.1.1 The steps for photolithography process and transferring it to a Substrate.....	87
4.2.2 Electron beam lithography (EBL).....	89
4.2.2.1 The steps for generating EBL and transferring it to a substrate.....	89
4.2.3 Focused ion beam lithography	91
4.3 Device Fabrication.....	93
4.4 Experimental Techniques.....	94
4.4.1 Electrical and magneto transport measurement	94
4.4.2 Noise spectroscopy measurement	96
4.4.2.1 The noise setup and data acquisition	97
4.4.3 Magnetization measurements	99
Bibliography	101
 5. Magnetic measurement of $\text{La}_{1-x}\text{A}_x\text{MnO}_3$ (A = Ca, Sr; $x = 0.3, 0.5$) nanowires	 102
5.1 Introduction and Motivation.....	103
5.2 Experimental results and discussions	105
5.2.1 $\text{La}_{0.7}\text{Ca}_{0.3}\text{MnO}_3$ (LCMO-0.3) and $\text{La}_{0.5}\text{Ca}_{0.5}\text{MnO}_3$ (LCMO-0.5) NWs....	105
5.2.2 $\text{La}_{0.7}\text{Sr}_{0.3}\text{MnO}_3$ (LSMO-0.3) nanowires.....	111
5.2.3 $\text{La}_{0.5}\text{Sr}_{0.5}\text{MnO}_3$ (LSMO-0.5) nanowires.....	113
5.3 Conclusion.....	122
Bibliography	124

6. Crystal structure analysis using synchrotron XRD measurement and magnetic structure refinement using neutron diffraction method	128
6.1 Introduction and motivation	129
6.2 Experimental details	131
6.3 Results and discussions	131
6.3.1 $\text{La}_{0.7}\text{Ca}_{0.3}\text{MnO}_3$ (LCMO-0.3) and $\text{La}_{0.5}\text{Ca}_{0.5}\text{MnO}_3$ (LCMO-0.5) NWs...	131
6.3.2 $\text{La}_{0.7}\text{Sr}_{0.3}\text{MnO}_3$ (LSMO-0.3) nanowires	136
6.3.3 $\text{La}_{0.5}\text{Sr}_{0.5}\text{MnO}_3$ (LSMO-0.5) nanowires	138
6.4 Neutron diffraction experiment of LSMO-0.5 bulk and nanowires	139
6.5 Conclusion.....	149
Bibliography	151
7. Resistivity and $1/f$ noise measurement of single nanowire	155
7.1 Introduction and Motivation.....	156
7.2 Brief introduction of noise	158
7.2.1 Types of noise and shape of the spectra	159
7.2.2 Using of noise spectroscopy to probe the phase separation issue in manganite.....	161
7.3 Single nanowire device fabrication	162
7.4 Electrical transport measurements.....	162
7.5 Experimental Results and Discussions	163
7.5.1 $\text{La}_{0.7}\text{Ca}_{0.3}\text{MnO}_3$ (LCMO-0.3) nanowires	163
7.5.2 $\text{La}_{0.5}\text{Ca}_{0.5}\text{MnO}_3$ (LCMO-0.5) nanowires	165
7.5.3 $\text{La}_{0.5}\text{Sr}_{0.5}\text{MnO}_3$ (LSMO-0.5) nanowires	167
7.5.3.1 Noise measurement of LSMO-0.5 single nanowire	170
7.6 Conclusion.....	178
Bibliography	180
8. Summary and concluding remarks	183
8.1 Conclusions	184
8.2 Scope for future work	187
A. Size dependence in magnetic memory, relaxation and interaction of $\text{La}_{0.7}\text{Sr}_{0.3}\text{MnO}_3$ system	189
A.1 Introduction	190
A.2 Experimental details.....	190
A.3. Experimental results.....	191
A.4 Discussion	194
A.5 Summary	196
Bibliography	197

List of Figures

1.1	Schematic crystal structure of manganite system (AMnO_3).....	4
1.2	Schematic diagram of (a) the crystal field splitting (Δ_{cf}) of Mn d levels into e_g and t_{2g} levels. Further splitting of e_g levels occurs due to JT splitting (δ_{JT}) and (b) JT distortion of the MnO_6 octahedra. Image adapted from [21]	6
1.3	Schematic diagram of the double exchange mechanism. Image adapted from [25]	7
1.4	Schematic representations for double exchange mechanism. Image adapted from [27]	8
1.5	Schematic diagrams showing the spins and orbitals arrangement in super exchange. The orbitals involved are Mn e_g and O $2p$ and the dashed arrows represent the virtual transfer of the electron between these orbitals. This means that the electron is located on the oxygen ion for the majority of the time, however can be found in the manganese orbital indicated by the arrow. The three panels result in an (a) AFM, (b) AFM and (c) FM arrangement of the core manganese spins respectively. Image adapted from [30]	10
1.6	(a) MR as a function of temperature for bulk and nanoparticles of $\text{La}_{0.5}\text{Ca}_{0.5}\text{MnO}_3$ (LCMO-0.5) sample at 10 Tesla magnetic field. Adapted from [12].(b) Temperature variation of MR of $\text{La}_{0.67}\text{Ca}_{0.33}\text{MnO}_3$ nanostructured thin film and epitaxial thin film, single crystal and artificial grain boundary junction (GBJ). The MR is negative but has been plotted as its absolute value. Image adapted from [41].....	12
1.6.1	Transport properties of ultrathin $\text{La}_{0.7}\text{Ca}_{0.3}\text{MnO}_3$ (LCMO) film before and after application of nanodots. (a) Resistivity behaviour for 20 nm ultrathin film of LCMO shows insulating behaviour and no clear metal-insulator transition (MIT). (b) Resistivity data of the same film after applying Fe nanodots to surface shows a recovery to bulk-like behaviour with a MIT temperature of 255 K at 0 Tesla (note the change in scale). (c) Ferromagnetic Fe nanodots drive a huge change in the film resistivity	

	compared to the diamagnetic Cu nanodots. (Insets) Atomic force microscope images of typical nanodot coverage for Cu and Fe systems on LCMO films. (d) Magnetoresistive behaviour shows a much higher magnetic response in the spin coupled system. Images adapted from [53].	14
1.7	(a) The resistivity data of parent compound $\text{LaMnO}_{3+\delta}$ at different δ values in zero magnetic field and 12 Tesla field showing insulating behaviour throughout the temperature range (4 – 300 K). Image adapted from [72] (b) Resistivity vs. temperature of $\text{La}_{0.75}\text{Sr}_{0.25}\text{MnO}_3$ and $\text{La}_{0.7}\text{Ca}_{0.3}\text{MnO}_3$. Image adapted from [42] (c) Temperature dependence of the resistivity of $\text{La}_{0.7}\text{Ca}_{0.3}\text{MnO}_3/\text{STO}$ (200 nm), $\text{La}_{0.7}\text{Ca}_{0.3}\text{MnO}_3/\text{STO}$ (50 nm) and $\text{La}_{0.7}\text{Ca}_{0.3}\text{MnO}_3/\text{NGO}$ (50 nm). Image adapted from [40]. (d) Resistance of single crystal $\text{La}_{0.79}\text{Ca}_{0.21}\text{MnO}_3$ as function of temperature taken at different pressures in the piston-cylinder type cell. Inset shows the magnetization vs temperature curve of $\text{La}_{0.79}\text{Ca}_{0.21}\text{MnO}_3$ at a pressure of 1.3 GPa. Image adapted from [54]. (e) Magnetization vs temperature for the nanoparticle sample (upper panel) and bulk sample (lower panel) of $\text{La}_{0.5}\text{Ca}_{0.5}\text{MnO}_3$ under a magnetizing field of 0.01 Tesla and 5 Tesla. Image adapted from [12] (f) Resistivity vs temperature for $\text{La}_{0.5}\text{Ca}_{0.5}\text{MnO}_3$ (15 nm) and bulk $\text{La}_{0.5}\text{Ca}_{0.5}\text{MnO}_3$. Inset shows the resistivity of the nanoparticle sample on an extensive scale. Image adapted from [12]	17
1.8	(a) Neutron diffraction data for bulk $\text{LaMnO}_{3+\delta}$ ($\delta \sim 0.03$) crystal having orthorhombic structure in the range 25–120 K. The onset of AFM order below 120 K is seen, the AFM peak (010) is indicated by an arrow. (b) The neutron diffraction data for $\text{LaMnO}_{3+\delta}$ ($\delta \sim 0.03$) nanocrystals having Rhombohedral structure in the range 25–475 K. The onset of FM order is seen, the FM peak is indicated by an arrow. Image adapted from [11]	18
1.9	Schematic and SEM images from bulk (3D) to quantum dot (0D)	19
2.1	Flow chart of Hydrothermal Synthesis	31
2.2	Pictorial view of the growth process	31
2.3	SEM images of complex oxide nanostructures by hydrothermal method; nanoparticles of (a) LCMO-0.5, (c) LSMO-0.5 samples and nanowires (b) LCMO-0.5 (d) LSMO-0.5 samples, respectively. The hydrothermally grown nanowires (LCMO-0.5 and LSMO-0.5 samples) are 1–10 micron in length and average diameter is around 20–70 nm. The average diameter of nanoparticles is ~100 nm	35

2.4	XRD of LSMO-0.5 nanoparticles grown at different times (a) 0.5 hr (b) 15 hrs (c) 30 hrs. “*” symbol indicates LSMO-0.5 sample peak and “#” denotes unreacted peaks. At the lower time (0.5 hr) the proper phase is not formed. The corresponding SEM images are depicted in the right hand side.....	36
2.5	Phase diagram of hydrothermal synthesis of nanocrystals of perovskite oxide manganites $\text{La}_{1-x}\text{A}_x\text{MnO}_3$ ($\text{A} = \text{Ca}, \text{Sr}; x = 0.3 \text{ and } 0.5$) as a function of amount of mineralizer (KOH). The nanowires formed incorporation of lower amount of KOH (3.0–4.5 gm) and the nanocrystallites, at the higher amount of KOH (5.5–7.0 gm). The $\text{La}_{1-x}\text{Sr}_x\text{MnO}_3$ samples are formed at 230–300 °C, whereas $\text{La}_{1-x}\text{Ca}_x\text{MnO}_3$ samples are grown at 260–300 °C shown in the red-colored shaded region. The probability of formation of mixed shape/size of nanowire (NW) and faceted nanoparticle (NP) is high in the region where the amount of KOH varies in the range (4.5–5.5 gm)	36
2.6	Schematic of growth steps of nanowires and corresponding SEM images with growth time (0.5–30 hrs) of LSMO-0.5 and LCMO-0.5 samples.....	39
2.7	TEM images of LSMO-0.5 nanocrystallites formed after fast nucleation. Yellow dotted line indicates the boundary of nanocrystallites. (b) enlarged view of (a); the orientation of all the nanocrystallites is same i.e., (112) direction and lattice spacing ($\sim 0.269 \text{ nm}$) between two interplanar is almost equal	39
2.8	SEM micrograph of LSMO-0.5 bulk sample.....	40
2.9	Schematic representation of (a) Bragg’s law (b) XRD measurement technique	41
2.10	The Rietveld refinement of Synchrotron XRD data for (a) LCMO-0.3, (b) LCMO-0.5, (c) LSMO-0.3 and (d) LSMO-0.5 nanowires, respectively. The experimental data points are indicated by open circles, the calculated and difference patterns are shown by solid lines. The Bragg positions of the reflections are indicated by vertical lines below the pattern. For LSMO-0.5 and LSMO-0.3 samples, there are small amount of impurity of $\text{La}(\text{OH})_3$ estimated to be <5 %. $\text{La}(\text{OH})_3$ (impurity) is fitted with the $p63/m$ phase; $a = b = 6.5368 \text{ \AA}$ and $c = 3.8550 \text{ \AA}$ at 300 K for LSMO-0.5 and LSMO-0.3 samples	45
2.11	Schematic representation of (a) Constant wavelength and (b) Time of flight neutron diffractometer	47

2.12	Structure factor vs. $\sin\theta/\lambda$ of neutron and X – ray.....	48
2.13	Neutron diffraction pattern (along with the fits) for $\text{La}_{0.5}\text{Sr}_{0.5}\text{MnO}_3$ nanowires taken at $T = 300$ K. The difference pattern and the position of the structural and magnetic Bragg peaks are also shown. The R – factors obtained were $R_p = 2.80\%$, $R_{wp} = 3.86\%$, $R_{exp} = 1.98\%$	49
2.14	Schematic representation of the interaction of incident electron beam with sample.	50
2.15	FESEM image of ensemble of nanowires (NWs) (a) LSMO-0.5 (inset showing histogram of average diameter ~ 38 nm) (b) LCMO-0.5 (inset showing histogram of average diameter ~ 44 nm) (c) LSMO-0.3 (inset showing histogram of average diameter ~ 40 nm) (d) LCMO-0.3 (inset showing histogram of average diameter ~ 42 nm)	51
2.16	EDAX data of $\text{La}_{0.5}\text{Sr}_{0.5}\text{MnO}_3$ nanowires.....	52
2.17	(a) Single nanowire $\text{La}_{0.5}\text{Sr}_{0.5}\text{MnO}_3$ sample of diameter around ~ 45 nm, (b) the selected area diffraction pattern taken with a Transmission Electron Microscope and (c) HRTEM image shows the single crystalline nature of $\text{La}_{0.5}\text{Sr}_{0.5}\text{MnO}_3$ nanowires	54
2.18	Camera lengths (L) in the presence of imaging lenses	55
3.1	Schematic representation of EELS and EFTEM imaging. Image adapted from [7].	61
3.2	EELS spectrum of $\text{La}_{0.5}\text{Sr}_{0.5}\text{MnO}_3$ nanowire in the zero loss peak (ZLP) and low loss region	62
3.3	EELS core loss spectrum of $\text{La}_{0.5}\text{Sr}_{0.5}\text{MnO}_3$ nanowires which shows the K (inner shell excitations from 1s), L (inner shell excitations from 2p) and M (inner shell excitations from 3d) of O, Mn and La respectively	63
3.4	The EELS spectra of (a) $\text{La}_{0.5}\text{Sr}_{0.5}\text{MnO}_3$, (b) $\text{La}_{0.7}\text{Sr}_{0.3}\text{MnO}_3$, (c) $\text{La}_{0.5}\text{Ca}_{0.5}\text{MnO}_3$ and (d) $\text{La}_{0.7}\text{Ca}_{0.3}\text{MnO}_3$ nanowires, respectively, showing manganese L_3 and L_2 lines	65
3.5	The EELS spectra of (a) MnO , (b) Mn_2O_3 and (c) MnO_2 respectively, showing manganese L_3 , L_2 lines. (d) Intensity ratio of L_3 and L_2 lines of different Mn oxide compounds as a function of their known valence. Mn valence of grown nanowires can be estimated from the curve	65
3.6	Energy Filtered Transmission Electron Microscope (EFTEM) image of each constituent element: M map of La, L map of Sr and Mn and K map of O in $\text{La}_{0.5}\text{Sr}_{0.5}\text{MnO}_3$ nanowire. The red, green, blue and yellow colours	

	represent the distribution of elements O, Mn, La and Sr respectively in the nanowire.....	67
3.7	Energy Filtered Transmission Electron Microscope (EFTEM) image of each constituent element: M map of La, L map of Ca and Mn and K map of O in $\text{La}_{0.5}\text{Ca}_{0.5}\text{MnO}_3$ nanowire. The red, green, blue and yellow colours represent the distribution of elements O, Mn, La and Ca respectively in the nanowire.....	67
3.8	The multislice approximation converts a specimen (left) into many thin slices (right). The electron wave is incident on the top of the specimen and transmitted through the specimen and exits on the bottom. Each slice of the specimen is thin enough to be approximated as a phase shift of the electron wave which is propagated between slices as a free space wave	69
3.9	The multislice method successively transmits the electron wave through each slice and then propagates it to the next slice. The incident wave is a plane wave for conventional TEM	70
3.10	(a) Experimental selected area electron diffraction (SAED) pattern of single nanowire (NW) of LCMO-0.5 (b) Simulated diffraction pattern (red spots) showing the growth direction along $[121]$ of LCMO-0.5 NW (c) SAED pattern (taken from red dotted portion) of LCMO-0.3 single nanowire (inset) showing orthorhombic symmetry with a overlapping of two zone axis $[010]_0$ and $[101]_0$. (d) and (e) Theoretical simulation of $[010]_0$ and $[101]_0$ SAED patterns by JEMS software.....	74
3.11	(a) Experimental selected area electron diffraction (SAED) pattern of single nanowire (NW) of LSMO-0.5 (b) Simulated diffraction pattern (red spots) showing the growth direction along $[112]$ of LSMO-0.5 NW, (c) Experimental SAED pattern of single NW of LSMO-0.3 (d) Simulated diffraction pattern (red spots) showing the growth direction along $[110]$ of LSMO-0.3 NW	76
3.12	(a) HREM image showing single nanowire (NW) of LCMO-0.3 (b) HREM micrograph showing fringes and structural defects on single NW (c) Fourier filtered image of the (b) showing a structural modulation. (d) FFT from (b) with the two projected unit cells (white dotted markings)	77
3.13	(a) and (c) Generated HREM maps along the zone axis $[010]_0$ and $[101]_0$; respectively, showing the atomic coordinations. (b) and (d) showing	

	distortions in the MnO_6 octahedra confirming the presence of twins of LCMO-0.3 nanowires	78
3.14	Showing the generated HREM maps of LSMO-0.5 with atomic resolution and the phase object function generated at different negative defocus value	78
3.15	(a) and (b) Generated HREM maps of LSMO-0.5 showing the atomic positions in the (-1,-1,1) and (-1,1,0) directions in both i.e, single NW and Bulk. The comparison is made keeping the microscopic parameters similar, only varying the crystallographic parameters. Schematic of the simulated structures show distortion in the co-ordination of La/Sr and also shrinkage in volume in the unit cell due to size reduction.....	79
3.16	(a,c) Showing atomic column structure and arrangements of the layered atoms in LCMO-0.5 and LCMO-0.3 (b,d) Showing atomic column structure and arrangements of the layered atoms in LSMO-0.5 and LSMO-0.3. The colour code of each element is shown at the side of the picture. To understand the termination site (A-O or B-O) La/Ca or La/Sr is marked A and Mn is marked B	81
4.1	Schematic flow chart of photo lithography process	88
4.2	(a) Schematic diagram of electron beam column. (b) The photograph of Electron beam lithography system	90
4.3	Schematic flow chart of EBL process	91
4.4	Schematic of (a) typical dual-beam column configuration, (b) Gallium ion source, (c) SEM images of single NW device connected with FEB (near the NW) and FIB (far from the NW) deposited Pt	93
4.5	Schematic representation of device fabrication by top-down approach with SEM image of four probe configuration.....	94
4.6	(a) Schematic representation of cryogen free VTI measurement system. (b) Image of the entire set up. Courtesy: Ref. [7]	95
4.7	Schematic diagram of the cryostat used for noise measurement setup	97
4.8	Schematic diagram of four-probe noise measurement technique. The ac voltage bias is fed to the sample from LIA and a standard resistor is connected in series with the sample. The voltage drop across the voltage probes on the sample is fed to the low-noise preamplifier input. The amplified signal goes to the input channels of the LIA. The data is collected via ADC card by the computer	99
4.9	Schematic illustration of VSM instrument	100

5.1	(a) Plot of temperature variation of magnetization at 100 Oe of LCMO-0.3 nanowires. The inset in the Fig. 5.1 (a) shows plots of dM/dT vs. T . We take the inflection points in the $M - T$ curves to be an estimate of the Curie temperature (T_C). (b) Plot of field variation magnetization of LCMO-0.3 nanowires at 80 K and 300 K.....	106
5.2	(a) Plot of temperature variation of magnetization at 100 Oe of LCMO-0.5 nanowires. The inset in the Fig. 5.2 (a) shows plots of dM/dT vs. T . (b) Plot of field variation magnetization of LCMO-0.5 nanowires at 80 K and 300 K	106
5.3	(a) Magnetization isotherms around Curie temperature (T_C) (b) Arrott plots (M^2 vs. H/M) for LCMO-0.3 nanowires	108
5.4	(a) Magnetization isotherms around Curie temperature (T_C) (b) Arrott plots (M^2 vs. H/M) for LCMO-0.5 nanowires	109
5.5	(a) Plot of temperature variation of magnetization at 100 Oe of LSMO-0.3 nanowires. The inset in the Fig. 5.5 (a) shows plots of dM/dT vs. T . (b) Plot of field variation magnetization of LSMO-0.5 nanowires at 80 K and 300 K	112
5.6	(a) Magnetization isotherms around Curie temperature (T_C) (b) Arrott plots (M^2 vs. H/M) for LSMO-0.3 nanowires	112
5.7	Temperature variation of magnetization data measured under applied fields of (a) 100 Oe and 2.5 kOe for LSMO-0.5 nanowires (b) 200 Oe for LSMO-0.5 bulk sample. In bulk there is one FM-PM transition where as in nanowire form it exhibits multiple phase transitions	114
5.8	(a) Real and (b) imaginary parts of linear ac susceptibility versus temperature plot for different frequencies. The inset of (a) shows a magnified view of $\chi'(T)$ for more frequencies [24]	116
5.9	(a) Temperature dependence of magnetic entropy change; The inset of (a) shows the $M(H)$ curves for all temperatures. (b) M^2 vs. H/M (Arrott plot) curves for different temperatures. The insets of (b) show the Arrott plots in different temperature ranges [24]	118
5.10	(a) Representative bipolar transverse susceptibility (TS) curve at 60 K, The inset of (a) shows a magnified view to illustrate the peaks at the anisotropy fields. (b) temperature dependence of effective anisotropy fields [24]	121

5.11	(a) $M(H)$ hysteresis loops at 5 K under FC (2 Tesla) and ZFC conditions; the inset of (a) shows a magnified view at low fields. (b) Temperature dependence of exchange bias field [24].....	122
6.1	Synchrotron XRD patterns for (a) LCMO-0.3 (b) LCMO-0.5 nanowires (NWs) taken at different temperatures	132
6.2	The fitting of XRD patterns with residue obtained from the Rietveld refinement of LCMO-0.3 nanowires at (a) 20 K, (b) 300 K and of LCMO-0.5 NW at (c) 20 K and (d) 300 K respectively. Experimentally observed (red circles), Rietveld calculated (black curves) and their difference (continuous bottom line of blue colour) profiles are obtained after Rietveld analysis of the XRD data using orthorhombic space group $Pnma$. The vertical tick marks (green colour) between the observed and difference plot show the Bragg peak positions.....	133
6.3	Synchrotron XRD patterns for LSMO-0.3 nanowires (NWs) taken at different temperatures.....	136
6.4	The fitting of XRD patterns with residue obtained from the Rietveld refinement of LSMO-0.3 nanowires at (a) 25 K, (b) 300 K respectively. Experimentally observed (red circles), Rietveld calculated (black curves) and their difference (continuous bottom line of blue colour) profiles are obtained after Rietveld analysis of the XRD data using rhombohedral space group $R-3c$. The vertical tick marks (green colour) between the observed and difference plot show the Bragg peak positions.....	137
6.5	Synchrotron XRD data for LSMO-0.5 NWs in the range 14 – 300 K. At 300 K, the crystal structure is tetragonal (space group $I4/mcm$) and when the temperature is lowered below 200 K, orthorhombic phase (space group $Fmmm$) comes into play along with tetragonal phase. The inset of this Fig. shows the enlarged view of 100% peak intensity with hkl (112) at 16.7°	138
6.6	The typical profile fits of neutron diffraction patterns with residuals obtained from the Rietveld refinement of LSMO-0.5 bulk at (a) 6 K, (b) 300 K and of LSMO-0.5 NW at (c) 3 K and (d) 300 K respectively. The red circles show the experimental data, the black curve denotes the calculated pattern and the blue curve is the difference pattern. The Bragg positions of the reflections are indicated by vertical lines (green colour) below the pattern	140

6.7	Volume fraction of the <i>Fmmm</i> (red curve) and <i>I4/mcm</i> (black curve) phases of LSMO-0.5 NWs.....	143
6.8	The temperature dependence of lattice constants obtained from the Rietveld refinement of (a) LSMO-0.5 bulk and (b) LSMO-0.5 NW. The error bars are smaller than the symbol.....	143
6.9	The crystallographic structure of (a) tetragonal (<i>I4/mcm</i>) at 300 K and (b) orthorhombic (<i>Fmmm</i>) phases at 200 K (reproduced from Rietveld analysis) plotted in vesta software.....	144
6.10	The spontaneous magnetic moment for the (a) LSMO-0.5 bulk and (b) LSMO-0.5 NW obtained from the neutron diffraction data. In bulk sample there is only FM phase whereas in NW form below 200 K there is a mixture of FM and AFM phases	146
6.11	(a) Magnetic FM spin alignment of LSMO-0.5 bulk at 300 K along <i>c</i> direction. and throughout the measured temperature range (6-300 K) it shows same spin alignment. (b) Magnetic FM spin alignment of LSMO-0.5 NW at 300 K along <i>b</i> direction. (c) FM spin is canted at 3 K in LSMO-0.5 NW because of FM and AFM phase coexistence. (d) AFM spin alignment at 3 K of LSMO-0.5 NW at 3 K along <i>b</i> direction.....	147
7.1	Power spectral densities of resistance fluctuations in a good Ag film [23]. The filled circles are the $1/f$ current noise coming from the sample while the solid line is the thermal background noise	160
7.2	(a) SEM image of the four wire connected single NW ($d \sim 50$ nm) of LCMO-0.3. (b) The temperature variation of resistivity data of LCMO-0.3 NW ($d \sim 50$ nm) taken at $0.1 \mu\text{A}$	163
7.3	(a) The metal-insulator transition in $\text{La}_{0.7}\text{Ca}_{0.3}\text{MnO}_3$ at $T_P \sim 250$ K. The sample is insulating above T_P and metallic below T_P [29]. The temperature dependent resistivity data for LCMO-0.33 film is grown on SrTiO_3 with thickness ~ 500 nm. The resistivity shows high temperature polaronic insulating to low temperature metallic phase transition at $T_P \sim 270$ K [25].....	164
7.4	(a) SEM image of the four wire connected single NW ($d \sim 35$ nm) of LCMO-0.5. (b) Temperature variation of resistivity of single NW of $\text{La}_{0.5}\text{Ca}_{0.5}\text{MnO}_3$ (LCMO-0.5) ($d \sim 35$ nm) measured in the temperature range from 30 K to 300 K. Inset curve ($\ln \sigma$ versus $T^{-1/4}$) shows that conductivity data fitted with variable range hopping model for the whole	

	temperature ranges and (c) quantitative comparison of resistivity of LCMO-0.5 NWs and bulk [4]	166
7.5	Temperature dependent MR data of LCMO-0.5 single NW ($d \sim 35$ nm) at 14 Tesla.....	167
7.6	(a) Temperature variation of resistivity of single NW of LSMO-0.5 measured in the temperature range from 5 K to 310 K. Inset curve shows SEM image of the single LSMO-0.5 NW with four electrical contact pads used for resistivity measurement. Inset curve of Fig. 7.6 (a) ($\ln \sigma$ versus $T^{-1/4}$) shows that conductivity data fitted with variable range hopping model for the whole temperature ranges. (b) quantitative comparison of resistivity of LSMO-0.5 NWs and bulk [37]	168
7.7	(a) Temperature dependent MR data of LSMO-0.5 single NW ($d \sim 45$ nm) at 14 Tesla. (b) $I - V$ characteristics at different temperatures in four probe of the single LSMO-0.5 NW ($d \sim 45$ nm) device. Inset of Fig. 7.7 (b) shows the calculated contact resistance (R_C) by taking difference in the slope of $I - V$ curves between two-probe and four-probe measurements	169
7.8	(a) Schematic representations of $1/f$ noise measurement set-up. (b) Normalized variance of resistance fluctuations ($\langle \Delta R^2 \rangle / R^2$) as a function of temperature (T) for field (H) = 0 and 0.04 Tesla and the inset shows the magnetic part of $\langle \Delta R^2 \rangle / R^2$ as a function of T	172
7.9	Recorded time-series of the fluctuation in resistance (R) at different temperatures. The discrete jump in resistance at 300 K in the “**” time range enlarged in the right side figure	173
7.10	The calculated PSD at the few representative temperatures at field (H) = 0. The solid lines show the fitted curves as $S_V(f)/V^2 = A/f^\alpha + B/f^\beta$ and the inset shows temperature dependence of coefficients A and B in zero field and in an applied field.....	174
7.11	The temperature variation of frequency exponent α . Inset shows the temperature dependence of β	175
7.12	Variation of probability distribution function (PDF) of resistance jumps in single NW at different temperatures, which shows how the statistics becomes non-Gaussian with temperatures	176
7.13	Variation of $\frac{\gamma_H}{n}$ with temperature	177

A.1	Results of SEM study of (a) bulk LSMO-0.3 showing particles with the size range of 60–170 nm. (b) LSMO-0.3 nanowires having average diameter of 40 nm.....	191
A.2	Results of ZFC magnetization measurements with stops of 2 hrs at 90 K at applied field $H = 40$ Oe and the uninterrupted reference ZFC magnetization for studying memory effect of LSMO-0.3 nanowires. Inset shows the results of same measurements for LSMO-0.3 bulk.....	192
A.3	Results of relaxation experiment for LSMO-0.3 (a) NWs (b) bulk where normalized magnetization is plotted with respect to time at 95 K. Symbols are experimental points and solid line is the result of fitting with two relaxation times	193
A.4	(a) The plot of normalized m_{IRM} and m_{DCD} of LSMO-0.3 nanowires as a function of applied field H_{app} (The sign of H_{app} has been ignored). M vs. H data taken at 120 K. (b) Variation of δm with H_{app} for LSMO-0.3 nanowires	194
A.5	(a) The plot of normalized m_{IRM} and m_{DCD} of LSMO-0.3 bulk as a function of applied field H_{app} (The sign of H_{app} has been ignored). M vs. H data taken at 120 K. (b) Variation of δm with H_{app} for LSMO-0.3 bulk samples	194

List of Tables

2.1	Summary of growth parameters of nanostructures of manganite of different surface morphologies by hydrothermal synthesis method: NWs and nanoparticles	32
2.2	Lattice parameters, cell volumes, atomic positions and reliability factors from the Rietveld refinements of $\text{La}_{1-x}\text{A}_x\text{MnO}_3$; (where $\text{A} = \text{Ca}, \text{Sr}; x = 0.3$ and 0.5) at 300 K	46
3.1	Mn valence of $\text{La}_{1-x}\text{A}_x\text{MnO}_3$; ($\text{A} = \text{Sr}, \text{Ca}, x = 0.3$ and 0.5) nanowires estimated from calibration curve and compared with the calculated data	66
3.2	Parameters for HREM image simulation	73
5.1	Critical exponents of LCMO-0.3 and LCMO-0.5 nanowires obtained experimentally and compared with theoretical mean field ($\beta = 0.5, \gamma = 1$ and $\delta = 3$) values	108
6.1	Lattice parameters, selected inter-atomic distances and bond angles and reliability factors of LCMO-0.3 and LCMO-0.5 nanowires (NWs) at 300 K and 20 K determined from Rietveld refinement of XRD data using FULLPROF software and compared with the reported bulk data [50, 51]	135
6.2	Orthorhombic strains of bulk and NWs of LCMO-0.3 and LCMO-0.5 at 300 K	135
6.3	Lattice parameters and reliability factors of LSMO-0.3 nanowires (NWs) at 300 K and 25 K determined from Rietveld refinement of XRD data using FULLPROF software and compared with the reported bulk data [55]	137
6.4	Structural parameters, selected inter-atomic distances and bond angles of $\text{La}_{0.5}\text{Sr}_{0.5}\text{MnO}_3$ bulk sample at 300 K and 6 K determined from Rietveld refinement of neutron powder diffraction data using FULLPROF software	141
6.5	Structural parameters, selected inter-atomic distances and bond angles of $\text{La}_{0.5}\text{Sr}_{0.5}\text{MnO}_3$ nanowires at different temperatures determined from Rietveld refinement of neutron powder diffraction data using FULLPROF software	142
7.1	A comparative study: the characteristics of Random Telegraphic noise and typical $1/f$ noise [25]	161
7.2	Comparison of the value of K_{sample} of different materials	178
A.1	The fitting parameters and standard deviations for fitting of normalized magnetization data according to Eq. (A.3) for LSMO-0.3 nanowires and bulk samples	193

Chapter 1

Introduction

This thesis deals with one dimensional (1D) nanostructures of perovskite oxide manganite ($\text{La}_{1-x}\text{A}_x\text{MnO}_3$; $\text{A} = \text{Ca}, \text{Sr}$; $x = 0.3$ and 0.5) systems. 1D nanostructure has fascinated considerable recent attention due to their special properties, which make them important in basic scientific research and also in potential technological applications [1]. Current research in science and technology of nanowires (NWs) is being focussed mainly towards the synthesis and characterization of 1D nanoscale materials for new types of electronic, optical and magnetic devices and understanding of their physical behaviour.

During past two decades much effort has been made to synthesize and characterize 1D nanostructure of manganites in the form of NW, tube, rods etc. The issues related to control of size, shape, structure, composition, homogeneity and growth kinetics of the perovskite oxide manganite NWs are still remained unexplored. In addition to these issues, how the size reduction to one dimension affects (with large aspect ratio structure) the crystallographic, magnetic, transport and other physical properties of NWs of manganite compared to bulk has been less investigated. In this thesis, we mainly focus on these issues and the underlying physics behind this. A brief review will be given on some novel and interesting electronic, structural and magnetic properties associated with manganite system. An outline of the thesis will be presented to highlight the main studies made in this thesis.

1.1 Introduction to manganite system

One of the most interesting fields, that has received considerable attention from the scientific and engineering communities, is the one dimensional (1D) nanostructures, including nanowires (NWs), nanorods, nanotubes, nanofibers and nanobelts, due to their potential technological applications in mesoscopic physics and nanoscale devices and also in the area of basic research [1, 2]. Research in 1D nanostructure in science and technology can provide unique advantages in investigating the size and dimensionality dependence of the materials' physical properties, such as structural, electronic, magnetic, optoelectronic properties etc. and in fabricating nanoscale devices [3-7]. They are also expected to take part in significant roles in nanoscale electronic, optoelectronic, electrochemical and electromechanical devices [8–10]. Among the 1D nanostructure, 1D perovskite manganite nanostructures have been received much attention due to their unusual electron transport and magnetic properties, which are essential for the applications in microelectronic, magnetic and spintronic devices. At the nanoscale, 1D manganite nanostructures display novel physical properties that are different from their bulk counterparts. As compared to the zero dimensional manganite nanostructures (nanoparticles) [11-12] and two-dimensional nanostructures (films) [13], the research of 1D nanostructure has been less investigated because of the problems in fabrication and synthesis of these nanostructures with well-controlled dimensions, uniform sizes, phase purity and homogenous chemical compositions. The issues related to control of size, shape, structure, composition, homogeneity and growth kinetics of the perovskite oxide manganite 1D nanostructures are still remained unexplored. In addition to the size and shape tailoring issues, how the size reduction to one dimension affects the crystallographic, magnetic, transport and other physical properties of NWs of manganite system compared to bulk has been less investigated [14] and is an interesting unresolved problem.

This thesis concentrates on an important area of NWs of manganites system which are strongly correlated system with $AMnO_3$ type structure where A stands for rare-earth such as La and Mn is the transition metal ion which exhibit colossal magneto-resistance, charge ordering, giant magneto-caloric effect [15-17], metal insulator transition, phase separation etc. It shows wide range of physical properties with a correlation of electronic, structural and magnetic properties etc. Recently, the research progress on the electronic phase separation in low-dimensional manganite nanostructures (e.g., nanoparticles, NWs/nanotubes and nanostructured films and/or patterns) is reported [2]. The reduced dimensionality opens a

pathway to the new functionalities in manganite nanostructures and offers a way to gain new insight into the nature of phase separation. In this thesis, we mainly focus on the rational synthesis, growth mechanism and detailed characterization of ensemble of NWs as well as single NW of manganite ($\text{La}_{1-x}\text{A}_x\text{MnO}_3$; $\text{A} = \text{Ca}, \text{Sr}$; $x = 0.3$ and 0.5). The crystallographic structural and fundamental physical properties including magnetic and transport properties of manganite NWs are also discussed and highlighted. A brief discussion of basic crystal structure of manganites, some novel and interesting electronic, structural and magnetic properties associated with manganite system will be provided in the following sections.

1.2 Crystal structure of manganite

As mentioned earlier, manganite has AMnO_3 structure where MnO_6 octahedra ("Mn" is at the centre of the octahedra) is situated at the corner position of the cube with "A" at the centre positions of the cube as shown in Fig.1.1. As the MnO_6 octahedra can be tilted or distorted depending on Mn–O bond angles and bond lengths, the octahedra can play a vital role in the AMnO_3 structure. Although the ideal manganite structure is cubic, partial substitution of the trivalent A ion by divalent B ion ($\text{A}_{1-x}\text{B}_x\text{MnO}_3$) almost always leads to a distortion of the structure from its ideal cubic one. This distortion occurs because of the change in the average ionic size. The degree of distortion in the unit cell is quantified by the “Goldsmith tolerance factor (t_G)” which is defined in terms of the ionic radii [17,18] can be written as

$$t_G = \frac{r_A + r_O}{\sqrt{2}(r_{Mn} + r_O)}, \text{ where } r_A, r_{Mn} \text{ and } r_O \text{ are ionic radii of the A, Mn and oxygen ions}$$

respectively. The tolerance factor (t_G) can be used to differentiate the effects of different chemical compositions, having atoms of different size with different doping levels, on the unit cell structure. For an ideal cubic unit cell, $t_G = 1$ and the Mn – O – Mn angle is 180° . A small amount of deviation (depending on the ionic radii of compositional atoms) from this value leads to a significant amount of stress which leads to the displacement of atoms from their ideal positions to minimize the free energy and a distorted perovskite structure is formed. Rotations and deformations of the octahedra are the reason of lowering of the space group and $t_G < 1$. Thus, for $1 > t_G > 0.96$, the structure is rhombohedral and for $t_G < 0.96$, the structure becomes orthorhombic. For a doped manganite system, since there are two possible ions at the A site, the tolerance factor is defined as a density – weighted average of the

individual tolerance factors. The average size of the A-site cations plays an important role in determining the physical properties of manganites.

Due to the reduction of radius of the A site, MnO_6 octahedra rotate and tilt, resulting in a decrease of the Mn–O–Mn bond angle (θ) from 180° . The hopping amplitude for carriers to move from one Mn site to the next also decreases as θ is reduced from 180° (for a 90° bond, the hopping involving a p orbital at the oxygen is zero). Consequently, as the tolerance factor decreases, the tendencies to charge localization increase due to a reduction in the carrier mobility. The relevance of the crystal structure arises from the fact that in the manganites the three degrees of freedom (charge, spin and lattice) are attached to each other. Thus, a change in the structure (lattice) is reflected in a change in the magnetic state (spin degree of freedom) or electronic state (charge degree of freedom) of the system.

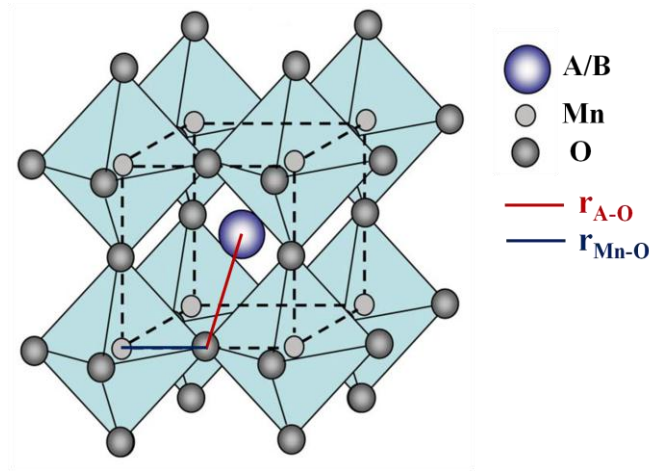


Figure 1.1 Schematic crystal structure of manganite system (AMnO_3).

1.3 Cationic disorder

The cationic radius $\langle r_A \rangle$ plays an important role to determine the physical properties of the manganites. When two or more different cations are situated on the rare earth element (A) lattice site at random, disorder is introduced in the crystal structure. The cationic disorder (σ^2) which is quantified by the variance of the A site cation radius distribution and the average A site radius $\langle r_A \rangle$ are expressed as:

$$\sigma^2 = \langle r_A^2 \rangle - \langle r_A \rangle^2 \quad (1.1)$$

where $\langle r_A \rangle$ is the average ionic radii of the A site [19]. As an example, in $\text{La}_{1-x}\text{Sr}_x\text{MnO}_3$ system, the doping level x of divalent cation Sr controls the valence of Mn ions and the average radius of the cations (both divalent Sr and trivalent La) can be expressed as:

$$\langle r_A \rangle = (1-x)r_{\text{La}}^{3+} + xr_{\text{Sr}}^{2+} \quad (1.2)$$

The variation in radius causes the distortion in lattice. The transfer integral of an e_g electron between two neighbouring Mn sites is mediated by the O 2p orbitals and hence the hybridization between Mn 3d orbitals and O 2p orbitals is sensitive to the lattice distortion and tilting of the MnO_6 octahedra. The distortion increases with the decrease of $\langle r_A \rangle$ which causes the narrowing of e_g band. This will localize the itinerant electron and the manganite system will become more insulating.

1.4 Electronic structure of manganite

The physical properties of the doped manganite system strongly depend on the electronic structure of the transition metal ion. Considered in isolation, the transition metal ion Mn has an active d shell with five degenerate levels. In the case of manganites, each Mn ion in the perovskite structure is bounded by oxygen octahedra. These degenerate levels get affected by the crystal field of the surrounding oxygen ions. In a cubic environment, since the three axes (x, y, z) are equivalent, the d_{xy} , d_{yz} and d_{zx} orbitals are affected and form a triplet (t_{2g}). The other two orbitals ($3z^2 - r^2$ and $x^2 - y^2$) form a doublet (e_g). The e_g level has a higher energy than the t_{2g} level since the orbitals of the doublet point along the directions where the negative oxygen ions are located, thereby increasing the energy due to Coulombic repulsion [20, 21]. The splitting of the degenerate d levels is shown in Fig. 1.2(a). This crystal field splitting (Δ_{cf}) between the t_{2g} and e_g states is about 1–2 eV. The Mn ion in manganites can be in its 2+, 3+ and 4+ ionization states corresponding to 5, 4 and 3 electrons in the 3d level respectively. The electrons in the t_{2g} levels form a localized core spin. Any remaining electrons occupy the e_g levels and may be localized or delocalized. Delocalization of the Mn e_g electrons occurs via the dominant oxygen O 2p levels. If there is single electron occupancy (for Mn^{3+}) at e_g level, the electron suffers a Jahn Teller (JT) distortion which causes a deformation of the oxygen octahedra surrounding Mn^{3+} . This distortion lifts the degeneracy of the e_g levels, which in turn results in the lowering of energy of the electron (shown in Fig. 1.2(a)).

Elongation of the octahedron along the axis through the apical oxygen's favours occupation of the $3z^2 - r^2$ orbitals, while compression along the said axis favours occupation

of the $x^2 - y^2$ orbitals, of the Mn. The JT effect therefore mediates a coupling between the electrons and lattice (phonon) [22] in manganites. Typical range of JT splitting energy is $\delta_{JT} \approx 0.25\text{--}1.5$ eV. In the insulating state, the e_g electron carries the distortion as it hops from site to site creating a JT polaron. When electron vacancies or holes are produced (due to the presence of Mn^{4+}) in the e_g orbital states by divalent atom substitution, the e_g electrons can be itinerant due to the lowering of JT effect. Thus it can play the role of conduction electron. This hole-doping (x) process thus corresponds to the creation of mobile Mn^{4+} species on the Mn sites and increases the conductivity of the system.

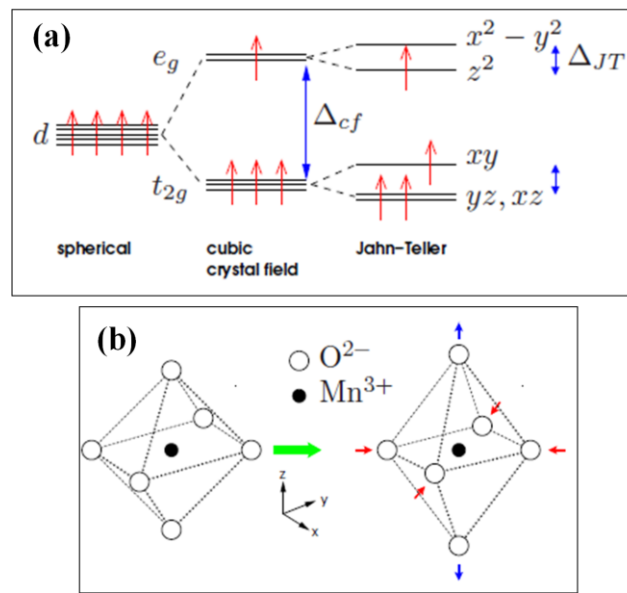


Figure 1.2 Schematic diagram of (a) the crystal field splitting (Δ_{cf}) of Mn d levels into e_g and t_{2g} levels. Further splitting of e_g levels occurs due to JT splitting (δ_{JT}) and (b) JT distortion of the MnO_6 octahedra. Image adapted from [21].

1.5 Magnetic interactions in manganite

The magnetic properties of manganite system are largely dominated by the transfer of electrons between Mn and O orbitals. Actually, there is an exchange interaction between the Mn ions spins. These interactions are comparatively large between the two Mn spins separated by an O atom and are controlled by the overlap between the Mn d -orbitals and the O p -orbitals. Depending on the types of the orbitals involved, the interaction is antiferromagnetic (AFM) or ferromagnetic (FM).

Zener [23] and Anderson [24] have shown that Mn-O-Mn bonding arrangement determines the magnetic coupling in manganites. They concluded that if neighbouring Mn ions direct their empty orbitals towards O^{2-} then Mn-Mn separation is small and coupling between Mn ions is AFM. But if one of the neighbouring Mn ion points its occupied orbital towards O then the two Mn ions will be ferromagnetically coupled. Usually there are two different types of interactions possible for magnetic coupling in these manganites that is, double exchange (DE) and super exchange (SE).

Double exchange (DE) mechanism:

In 1951, Zener offered an explanation to understand the strong correlation between ferromagnetism and metallic conductivity in doped manganites [23-24]. He introduced the concept of the ferromagnetic DE for manganites, assuming two simultaneous electron transfers: one electron from Mn^{3+} to a neighbouring O $2p$ orbital and a second electron transfer from this $2p$ orbital to an adjacent Mn^{4+} ion. After going through this process, the final and initial states are degenerate. Hence, these two states coexist and the two Mn core moments couple ferromagnetically. The schematic diagram of the DE mechanism is shown in Fig. 1.3.

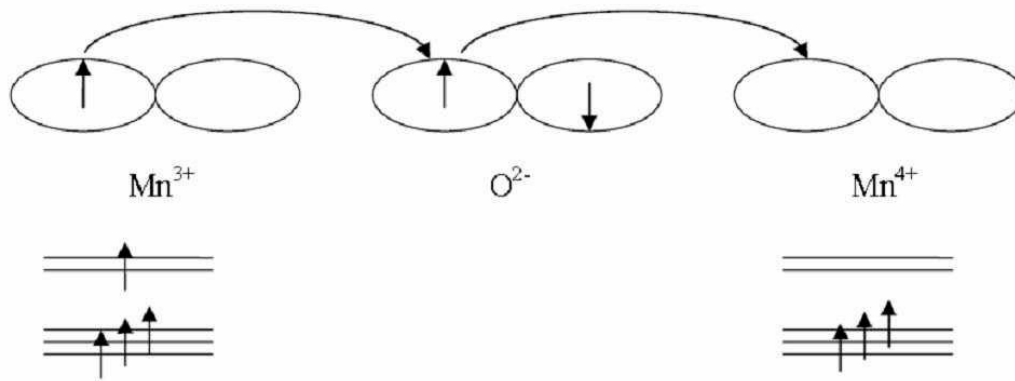


Figure 1.3 Schematic diagram of the double exchange mechanism. Image adapted from [25].

According to Zener, DE is a magnetic interaction mediated by itinerant spin polarized d electrons which are coupled according to Hund's rule to localize magnetic moments [26]. The hopping amplitude of electrons in the Mn-O-Mn bond can be expressed as: $t = t_0 \cos(\theta/2)$, where t_0 is the transfer integral and θ is the relative angle between the adjacent Mn t_{2g} core

spins as shown in Fig. 1.4. It is clear that “ t ” achieves its maximum possible value t_0 for $\theta = 0$, i.e. under the Zener DE mechanism, a FM state is also a metallic state. Typical value of t is 0.2–0.5 eV. Since the electron transfer depends on the angle between neighbouring magnetic moments, DE mechanism qualitatively explains the relationship between ferromagnetism and metallicity in mixed valence ($\text{La}_{1-x}\text{A}_x\text{MnO}_3$, A = Sr, Ca) manganites. However it cannot explain the observed metal insulator transition and colossal magnetoresistance (CMR) effect in hole doped manganites.

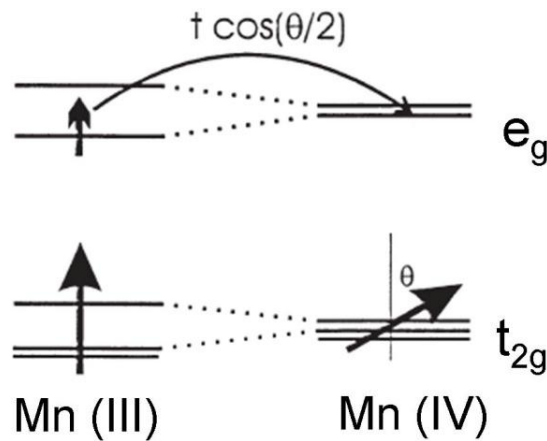


Figure 1.4 Schematic representations for double exchange mechanism. Image adapted from [27].

To explain the CMR effect and metal-insulator transition in manganites, Ramakrishnan *et al.* [28] further proposed that the two fold degenerate e_g ($d_{x^2-y^2}$ and $d_{3z^2-r^2}$) orbitals of Mn are dynamically reorganized into a set of states “l” (which are localized with large local lattice distortion and have exponentially small intersite overlap) and “b” which form a broad band by the strong JT coupling between the e_g orbitals and lattice modes of vibration of the oxygen octahedra surrounding the Mn ions. These “l” and “b” states can co-exist microscopically and can be subjective by doping (x), temperature and local Coulomb repulsion (U). This model considers all the strong interactions occur in manganites [29]. Ramakrishnan *et al.* has proposed [29] a unique model that considers the coexistence of JT distorted, localized “l” states and undistorted, broad band “b” states. This theory suggested that external stimuli change the physical properties of manganites because the “l” states, being localized and lattice distorted, are strongly influenced by local perturbations, which affects subtle relative stability of the “l” and “b” states. The existence of this localized polaronic “l” states in the presence of large “ U ” and Hund’s exchange coupling (J_H) give rise to a doping dependent ferromagnetic nearest neighbour exchange coupling J_F between the t_{2g} core spins [29]. This

arises due to effective fast hopping processes of the “I” electrons to neighbouring empty sites and back. Ramakrishnan *et. al.* suggested that this virtual, correlated DE mechanism between the localized electrons is the leading source of ferromagnetism and the FM transition temperature (T_C) in the hole doped manganites [29].

Super exchange (SE) mechanism:

This is a well known interaction in most of the oxides mainly in insulating magnetic oxides where the magnetic interaction between adjacent ions is mediated by the intermediate nonmagnetic ion with a closed shell. The intermediate ion is O^{2-} in super exchange. If two orbitals on adjacent ions point towards each other, with one orbital fully occupied and the other orbital having a vacancy, then the electron will spend part of its time in the empty orbital on the other ion. In the case of the manganites, the orbitals involved are the vacant Mn e_g orbital and the occupied O $2p$ orbital and so it is the O $2p$ electron that is ‘shared’ between the two ions. This *virtual transfer* of the electron is known as super exchange mechanism which leads to either FM or an AFM alignment of the spins, depending on the occupancy of Mn orbitals as shown in Fig. 1.5. There is strong Hund coupling between the core Mn t_{2g} spins and any e_g electron. There are two cases to consider, that is when the Mn e_g orbital has one permanent electron (Mn^{3+}) and occasionally the virtual electron, or only the virtual electron (Mn^{4+}). For Mn^{4+} , the t_{2g} and permanent e_g electron will be spin-aligned (Hund’s rules). So the spin of the transferred electron has to have the opposite sign, as required by the Pauli Exclusion Principle. Conversely, for Mn^{3+} , the electrons in the Mn t_{2g} orbitals align with the virtual electron from the oxygen ion. By applying these two rules and noting that the two electrons from the O $2p$ orbital have opposite spins, we find that two adjacent empty Mn orbitals or two half-full orbitals will lead to antiferromagnetic order, whereas an empty Mn orbital pointing towards a half-full one will lead to a ferromagnetic alignment of the core Mn spins. However, unlike DE, SE always results in an insulating state.

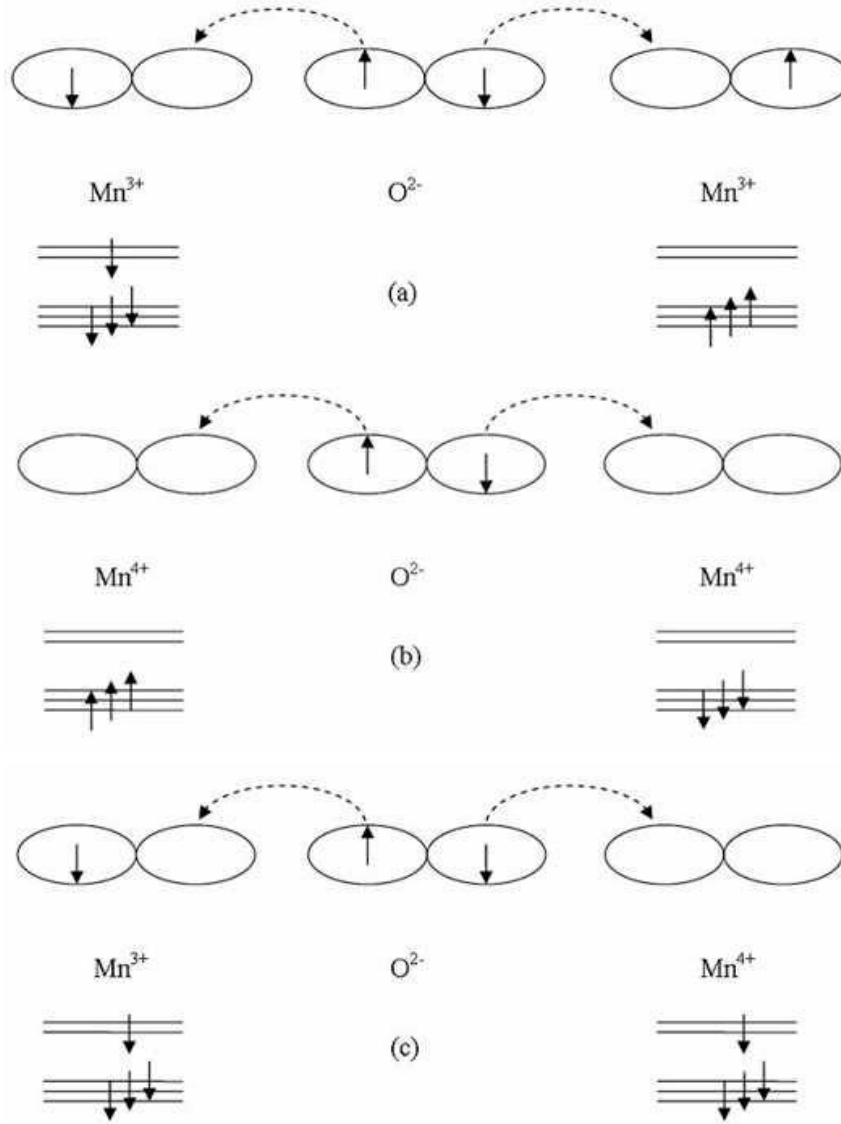


Figure 1.5 Schematic diagrams showing the spins and orbitals arrangement in super exchange. The orbitals involved are Mn e_g and O $2p$ and the dashed arrows represent the virtual transfer of the electron between these orbitals. This means that the electron is located on the oxygen ion for the majority of the time, however can be found in the manganese orbital indicated by the arrow. The three panels result in an (a) AFM, (b) AFM and (c) FM arrangement of the core manganese spins respectively. Image adapted from [30].

1.6 Magnetization due to divalent atom doping

In the previous section, we discuss that electron transfer depends on the angle between the neighbouring magnetic moments. Divalent atom doping (x) determines the concentration of Mn⁴⁺ present in a doped La_{1-x}A_xMnO₃ (A= Sr, Ca, Ba etc.) system. For $x = 0$, the material is

antiferromagnetic. However, as x increases, the DE becomes the dominant interaction and thus the FM moment increases. The maximum value of moment is observed around $x = 0.3$ where the FM moment approaches the theoretical spin-only value for a FM mixture of Mn^{3+} and Mn^{4+} (calculated as $(1-x) \mu_B + 3x \mu_B$, where μ_B is the Bohr magneton). When x is increased further FM moment starts to decrease. This is due to the direct overlap between t_{2g} orbitals, which leads to anti parallel exchange coupling because only the spin down states is empty [31-32]. For $0.33 \leq x \leq 0.5$ there exists the competition between FM ($\text{Mn}^{3+} - \text{Mn}^{4+}$) double exchange coupling and the AFM ($\text{Mn}^{4+} - \text{Mn}^{4+}$) coupling. For $x = 0.5$, AFM state becomes dominant due to super exchange, charge and orbital ordering becomes important for conduction process.

1.7 Magnetoresistance (MR) in manganite

The manganites acquire much interest due to observation of large magnetoresistance (MR) effect in these compounds. MR is defined as the change (increase or decrease) in resistance due to the externally applied magnetic field. MR is expressed as,

$\pm \text{MR}\% = (\rho(H) - \rho(0))/\rho(0)$, where $\rho(H)$, $\rho(0)$ are the resistivities of the sample with and without field, while \pm indicates the positive and negative MR. Manganites can show both positive and negative MR depending on the elements present in the sample as well as disorder in oxygen stoichiometry. MR investigation as well as a phenomenological analysis was reported for $\text{La}_{1-x}\text{Pb}_x\text{MnO}_3$ crystals in 1969 [33]. Composition dependence giant magnetoresistance was observed in bulk $\text{La}_{1-x}\text{A}_x\text{MnO}_3$ ($\text{A} = \text{Sr}, \text{Ca}$) samples [34-38]. CMR effect was discovered in thin film of $\text{La}_{0.67}\text{Ca}_{0.33}\text{MnO}_3$ having thousand fold changes in resistance at 77 K with 6 Tesla magnetic fields in mid 1990's [39]. Large MR was noticed strain-relaxed film of $\text{La}_{0.67}\text{Ca}_{0.33}\text{MnO}_3$ grown epitaxial on SrTiO_3 substrates and single crystal samples [40-43].

The MR data of bulk and nanoparticles of $\text{La}_{0.5}\text{Ca}_{0.5}\text{MnO}_3$ (LCMO-0.5) sample are plotted as a function of temperature (T) in Fig.1.6 (a). In both samples the MR is negative although the value, as well as the temperature dependence, is qualitatively different. The insulating state of the charge ordered bulk sample is completely suppressed on application of 10 Tesla magnetic fields. This is due to magnetic field induced destabilization of the charge ordered state that has been seen in many charge ordered systems. The MR at the lower most temperature is nearly 100% for the bulk sample for $T < 100$ K. In contrast, in the nanoparticle sample, the

MR values increase slowly as it is cooled and reaches the limiting value of $\sim 70\%$. The behaviour of the MR in the nano-crystal is similar to that seen in nano-structured films of ferromagnetic manganites [13, 41], which arises predominantly due to the grain boundary contributions. In Fig. 1.6 (b), we plotted the comparison of MR data of a single crystal of $\text{La}_{0.67}\text{Ca}_{0.33}\text{MnO}_3$ and an artificial grain boundary junction (GBJ 200), made on a SrTiO_3 bi-crystal substrate and have an epitaxial film of thickness 200 nm. The temperature dependence of MR clearly shows that the peak in MR observed in the epitaxial film is very similar to that of a single crystal, while the MR of the nanostructured film is similar to that of GBJ 200. The MR in the epitaxial films originates from the bulk of the platelets as in a single crystal. In the nanostructured films it is expected to originate from the grain boundaries, as in the artificial grain boundary junction. In this thesis, we will look into the issues how the MR of the single crystalline NWs is modified due to size reduction.

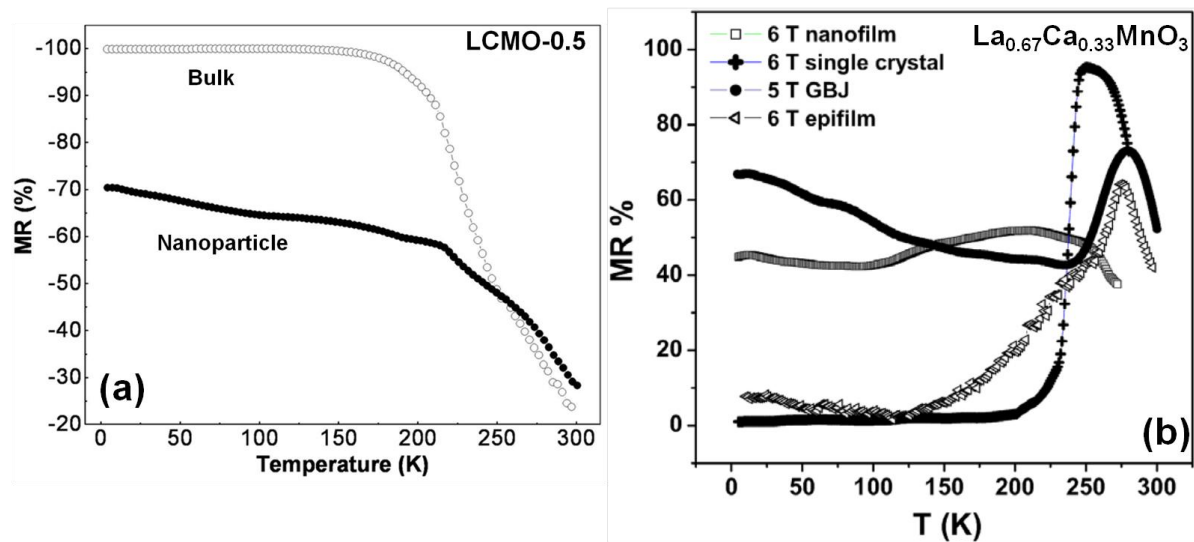


Figure 1.6 (a) MR as a function of temperature for bulk and nanoparticles of $\text{La}_{0.5}\text{Ca}_{0.5}\text{MnO}_3$ (LCMO-0.5) sample at 10 Tesla magnetic field. Adapted from [12]. (b) Temperature variation of MR of $\text{La}_{0.67}\text{Ca}_{0.33}\text{MnO}_3$ nanostructured thin film and epitaxial thin film, single crystal and artificial grain boundary junction (GBJ). The MR is negative but has been plotted as its absolute value. Image adapted from [41].

The underlying origin of CMR is closely related to the nature of CMR manganites which are strongly correlated electron systems with interplay among the lattice, spin, charge and orbital degrees of freedom, such as DE interaction, JT effect, electronic phase separation and charge ordering. The CMR effect is connected to the field-sensitive complex electron–electron and electron–lattice effects in manganites, which will result in remarkable conductivity variation

in magnetic fields. In addition, another field-dependent factor is the insulating/metallic phase separation for the observed CMR effects. Both experimental and theoretical studies have revealed that typical length scale for phase-separation in manganites is from several nanometres to sub micrometer scale, depending on the sample and the dopant level [44-48]. A phenomenological model was proposed to describe the relationship between the phase separation and CMR in manganites [49, 50]. There are several reports on the study on magnetoresistance of manganite of bulk, film and nanoparticles [12, 34-43] but no reports exists in 1D manganite NWs. In this thesis we want to explore the MR behaviour of manganite NWs and compare with its bulk counterpart.

1.8 Phenomena of phase coexistence in manganite

Manganites having very interesting phase diagram, is rich with various kind of resistive, magnetic and structural phases. The electronic energy in manganites depends on the (i) kinetic energy of e_g electrons, (ii) Hund's on site magnetic coupling between e_g and t_{2g} electron spins, (iii) coupling between e_g electrons and distortion of MnO_6 octahedra (JT Effect), (iv) crystal field splitting in the octahedral coordination, (v) Heisenberg's magnetic coupling between nearest neighbour localized electron spins and (vi) the Coulomb interaction between e_g electrons. The competition between these effects results in different electronic and magnetic ground states in manganite. Phase separation or phase coexistence in manganites can have two different origins: (i) Electronic phase separation, where competing states have different hole densities and $1/r^2$ Coulomb effects lead to nanocluster coexistence, (ii) Disorder – driven phase separation near first order transitions [51] leading to large coexisting clusters. The first phase coexistence has been observed in the system of $\text{Nd}_{0.25}\text{La}_{0.25}\text{Ca}_{0.5}\text{MnO}_3$ [52]. For an example, magnetic Fe nanodots are grown on the surface of a 20-nm-thick $\text{La}_{0.7}\text{Ca}_{0.3}\text{MnO}_3$ (LCMO) / LaAlO_3 (001) film, which could turn the film from an insulator to a metal with a high metal insulator transition (MIT) temperature, as shown in Fig. 1.7 [53]. The underlying mechanism is understood to be the local magnetic exchange field between Fe and Mn spins that aligns the local Mn spins leading to the formation of a local metallic state.

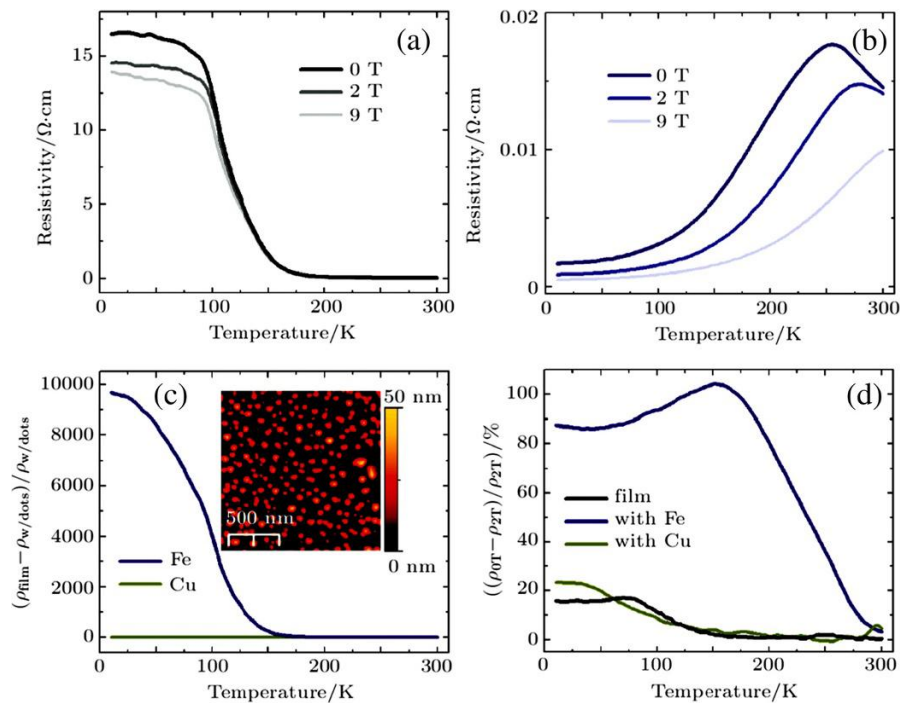


Figure 1.7 Transport properties of ultrathin $\text{La}_{0.7}\text{Ca}_{0.3}\text{MnO}_3$ (LCMO) film before and after application of nanodots. (a) Resistivity behaviour for 20 nm ultrathin film of LCMO shows insulating behaviour and no clear metal-insulator transition (MIT). (b) Resistivity data of the same film after applying Fe nanodots to surface shows a recovery to bulk-like behaviour with a MIT temperature of 255 K at 0 Tesla (note the change in scale). (c) Ferromagnetic Fe nanodots drive a huge change in the film resistivity compared to the diamagnetic Cu nanodots. (Insets) Atomic force microscope images of typical nanodot coverage for Cu and Fe systems on LCMO films. (d) Magnetoresistive behaviour shows a much higher magnetic response in the spin coupled system. Images adapted from [53].

External perturbations like pressure [54], electric field, magnetic field, strain [40-41] and even size reduction also play an important role to control these phases [12]. The physics of manganites is dominated by states that are microscopically and intrinsically inhomogeneous because of the several physical interactions such as spin, charge, lattice and/or orbital being simultaneously active. Dagotto *et al.* [55] argued from the results of theoretical calculations that the phase coexistence occurs on a wide range of length scales from nanometres to microns throughout the doping range. An appreciation of these tendencies towards phase separation is fundamental to the understanding of the properties of manganites. The type of phase separation occurs in manganites is not the result of chemical phase separation or structural inhomogeneities but it is intrinsic and caused by the similar free energies of the competing ground states. Two types of phase separation are suggested. The first is driven by disorder induced by the random substitution of ions of different sizes on the “A” site of the crystal and leads to phase separation on a scale that can be as large as microns. It has been

shown that the properties of manganites depend greatly on both the average size of the “A” site cations and also the standard deviation of the sizes of the substituted atoms [56]. The other type of phase separation suggested by Dagotto *et al.* [55] is electronic phase separation (EPS) where nanometre sized patches with different electron densities coexist although the composition of the crystal is constant. Dagotto and his colleagues have developed one-orbital FM Kondo model and two-orbital model with JT phonons to investigate the EPS phenomenon in 1D manganite system [57-60]. The manganites are intrinsically inhomogeneous at length scales of nanometres due to the strong electronic correlations. As the spatial dimension and geometry sizes of the low-dimensional manganite nanostructures are reduced to the characteristic EPS length scale, quite dramatic changes in their transport properties such as ultra sharp jumps of magnetoresistance, re-entrant MIT, negative differential resistances and intrinsic tunnelling magnetoresistance could appear, which are supposed to be caused by the EPS in manganite nanostructures [61-68]. Consequently, reduced dimensionality opens a door to the new functionalities in manganite oxides and offers a way to gain new insight into the nature of EPS. [69] Recently, theoretical calculations using the FM Kondo Hamiltonian have predicted that the intrinsic EPS persists in 1D manganite nanostructures [70]. Previously many reports are available on the phase separation of manganite nanoparticles [12, 71] and many theories are developed. However, due to the difficulty of growth of pure phase with proper stoichiometry and to maintain single-crystalline structure of manganite NWs, the EPS in manganite NWs are not completely explored. In this thesis, we are trying to explore phase separation issues in manganite NWs.

1.9 Parameters controlling the physical properties

As previously discussed that manganites have been attracting much attention because of their unusual electron-transport and magnetic properties, e.g., CMR effect [34-43, 59], a sharp MIT as a function of temperature, electric field, magnetic field, light, hydrostatic pressure, strain [40-41, 44], etc. Such MIT is also accompanied by a magnetic phase transition, paramagnetic (PM) to ferromagnetic (FM) with lowering the temperature. As a result, the phase of the material as well as the physical properties can be tuned by various external perturbations, such as control of carrier concentration (substitution) [42], crystal structure [11, 71], pressure [54], magnetic and electric fields [12], strain [41-42] and disorder, even size reduction [11].

As for example, in Fig. 1.8 (a), the resistivity data of parent compound $\text{LaMnO}_{3+\delta}$ at different δ values in zero magnetic field and 12 Tesla field showing insulating behaviour throughout the temperature range (4 – 300 K) do not exhibit a spontaneous or field-induced metal-insulator transition [72]. However, when divalent cation Sr or Ca is doped on La site, the physical property is modified. $\text{La}_{0.75}\text{Sr}_{0.25}\text{MnO}_3$ having a wide bandwidth system undergoes a PM metallic to FM metallic phase transition with $T_C \sim 342$ K (see Fig. 1.8 (b)). It remains metallic till 4.2 K with a residual resistivity, $\rho_0(\text{La}_{0.75}\text{Sr}_{0.25}\text{MnO}_3) = 41.6 \mu\Omega\text{-cm}$. Whereas, $\text{La}_{0.7}\text{Ca}_{0.3}\text{MnO}_3$, which is a medium bandwidth system, has a PM insulating-FM metallic phase transition with $T_C \sim 250$ K and also remains metallic with $\rho_0(\text{La}_{0.7}\text{Ca}_{0.3}\text{MnO}_3) = 161 \mu\Omega\text{-cm}$ (see Fig. 1.8 (b)) [42]. Fig. 1.8 (c) shows how resistivity and MIT temperature (T_P) are changed due to strain and film thickness [40]. In Fig. 1.8 (d) $\text{La}_{0.79}\text{Ca}_{0.21}\text{MnO}_3$ sample at zero pressure (P) shows a high temperature insulating phase like other manganites [54]. Even a pressure as low as 0.5 GPa can reduce the low temperature resistivity by more than two orders. At this pressure the low temperature FM insulating phase is retained albeit with lower resistivity. For $P \geq 1.3$ GPa the FM insulating phase is completely destabilized and the sample remains metallic down to 2.5 K, the lowest temperature measured. The resistivity in the metallic phase at lowest temperature is nearly eight orders of magnitude lower than that in the zero pressure FM insulating phase and this is truly a colossal pressure effect. In Fig. 1.8 (e) and (f) we have demonstrated how the magnetic and electric properties are modified under size reduction [12]. Resistivity of $\text{La}_{0.5}\text{Ca}_{0.5}\text{MnO}_3$ bulk samples are more than that of the nanoparticles due to grain boundary effect and the charge and orbital ordering are completely suppressed due to size reduction from bulk to nanoparticles.

If we concentrate on the size reduction issues in manganite nanostructured systems, we will find several reports [11-12, 71] available in manganite nanocrystals. The nano materials have at least one of its dimensions in the “nanometric” regime, hence relative surface area is increased and quantum effects come in. In the “quantum regime” or “surface dominated regime” in nano materials the physical properties need to differ from bulk.

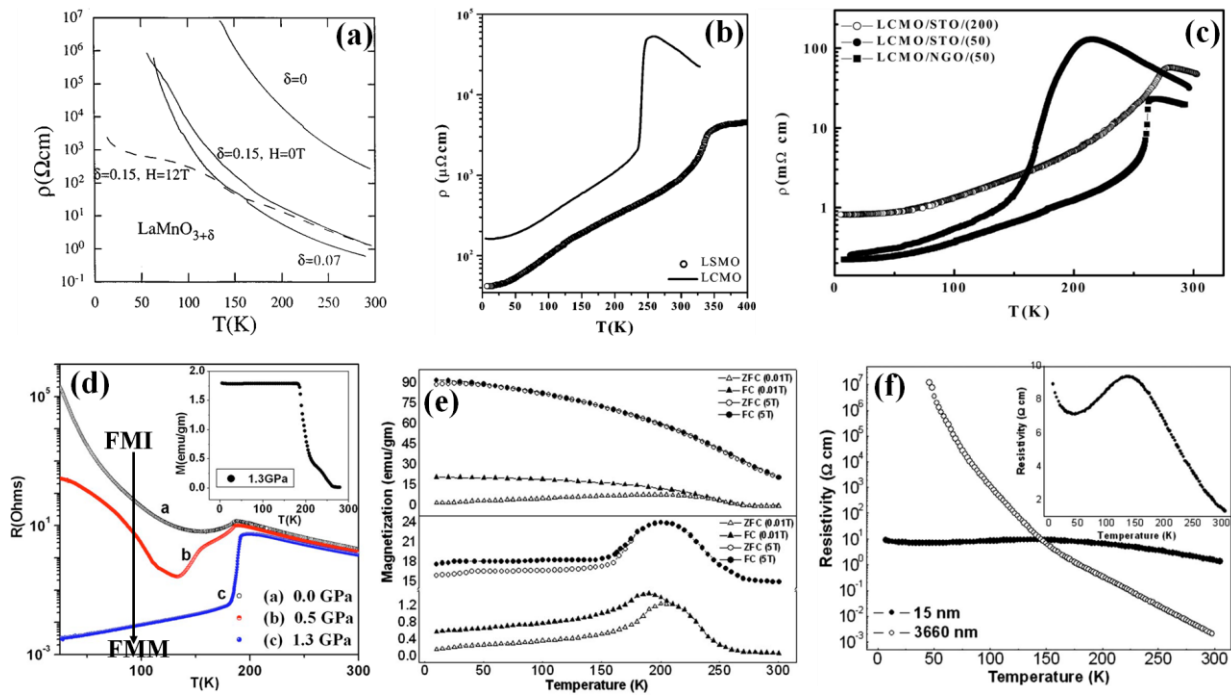


Figure 1.8 (a) the resistivity data of parent compound $\text{LaMnO}_{3+\delta}$ at different δ values in zero magnetic field and 12 Tesla field showing insulating behaviour throughout the temperature range (4 – 300 K). Image adapted from [72] (b) Resistivity vs. temperature of $\text{La}_{0.75}\text{Sr}_{0.25}\text{MnO}_3$ and $\text{La}_{0.7}\text{Ca}_{0.3}\text{MnO}_3$. Image adapted from [42] (c) Temperature dependence of the resistivity of $\text{La}_{0.7}\text{Ca}_{0.3}\text{MnO}_3/\text{STO}(200\text{nm})$, $\text{La}_{0.7}\text{Ca}_{0.3}\text{MnO}_3/\text{STO}(50\text{nm})$ and $\text{La}_{0.7}\text{Ca}_{0.3}\text{MnO}_3/\text{NGO}(50\text{nm})$. Image adapted from [40]. (d) Resistance of single crystal $\text{La}_{0.79}\text{Ca}_{0.21}\text{MnO}_3$ as function of temperature taken at different pressures in the piston-cylinder type cell. Inset shows the magnetization vs temperature curve of $\text{La}_{0.79}\text{Ca}_{0.21}\text{MnO}_3$ at a pressure of 1.3 GPa. Image adapted from [54]. (e) Magnetization vs temperature for the nanoparticle sample (upper panel) and bulk sample (lower panel) of $\text{La}_{0.5}\text{Ca}_{0.5}\text{MnO}_3$ under a magnetizing field of 0.01 Tesla and 5 Tesla. Image adapted from [12] (f) Resistivity vs temperature for $\text{La}_{0.5}\text{Ca}_{0.5}\text{MnO}_3$ (15 nm) and bulk $\text{La}_{0.5}\text{Ca}_{0.5}\text{MnO}_3$. Inset shows the resistivity of the nanoparticle sample on an extensive scale. Image adapted from [12].

As an example, the parent compound $\text{LaMnO}_{3+\delta}$ ($\delta \sim 0.03$) which is an antiferromagnetic (AFM) insulator, on size reduction to 50 nm, the structural changes occur. The crystal structure changes from orthorhombic to rhombohedral accompanied by magnetic phases change from AFM to FM as shown in Fig. 1.9 [11]. The likely origin is traced to change in magnetic exchange interactions due to change in Mn–O bond lengths which become almost identical in the MnO_6 octahedron in the rhombohedral structure in absence of JT distortion. The study provides an example of structural and magnetic phase transition driven purely by size reduction and with no change in the chemical constituents [11]. The effect of size reduction on the stability of the charge-orbital order and the AFM spin order is observed in

the bulk samples of the half-doped manganite $\text{Y}_{0.5}\text{Ca}_{0.5}\text{MnO}_3$ [71]. The size reduction from bulk to nanoparticles changes the structural parameters and suppresses the charge and orbital ordering.

In the charge ordered half-doped manganite nanoparticles, a robust charge ordering (CO) state and AFM ground state are appreciably suppressed whereas a FM ordering is exhibited [12,71,73-75]; meanwhile, there exists size-dependent exchange bias effect and glassy behaviours [76, 77]. In the nano-structured patterns of $(\text{La,Pr,Ca})\text{MnO}_3$ (LPCMO) narrow strips (spatial confined system), several new transport features are observed such as giant resistance jumps [61-64], re-entrant MIT [65], negative differential resistance and intrinsic tunnelling magnetoresistance [66, 67], which are absent in the thin films and bulks.

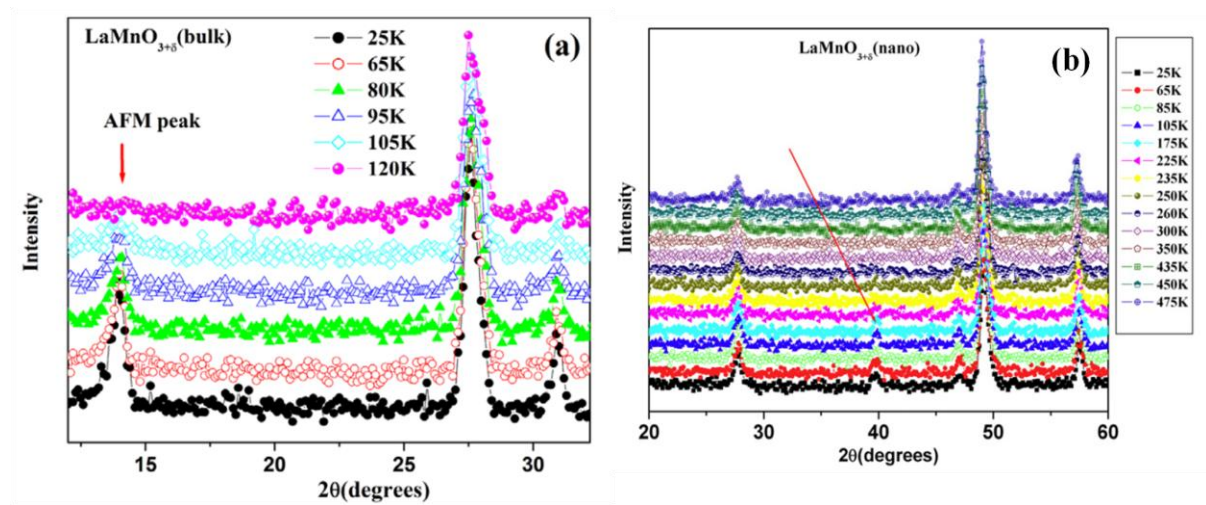


Figure 1.9 (a) Neutron diffraction data for bulk $\text{LaMnO}_{3+\delta}$ ($\delta \sim 0.03$) crystal having orthorhombic structure in the range 25–120 K. The onset of AFM order below 120 K is seen, the AFM peak (010) is indicated by an arrow. (b) The neutron diffraction data for $\text{LaMnO}_{3+\delta}$ ($\delta \sim 0.03$) nanocrystals having Rhombohedral structure in the range 25–475 K. The onset of FM order is seen, the FM peak is indicated by an arrow. Image adapted from [11].

Though several reports are available in nanoparticles, we thought if one more dimension is added in the bulk regime (where length \sim micrometer), how the crystallographic structure evolves. This may lead to significant changes in physical property which have not been explored before.

Few works have been performed which are based on the growth of one/two composition on 1D manganite NW following some methods like template based growth [78, 79], hydrothermal [80] and some initial level of characterization like magnetic transitions etc [81]. However, till date not much detailed work has been done on 1D nanostructure due to

difficulty in growth of single crystalline 1D nanostructure with proper phase and stoichiometry.

In this thesis, we will look into the details of the growth of hole doped manganite ($\text{La}_{1-x}\text{A}_x\text{MnO}_3$; A = Ca, Sr; $x = 0.3$ and 0.5) NWs, their physical properties and understanding of the basic physics behind.

1.10 Motivation of the present work

On the basis of the above discussions the main aim of this thesis is given below:

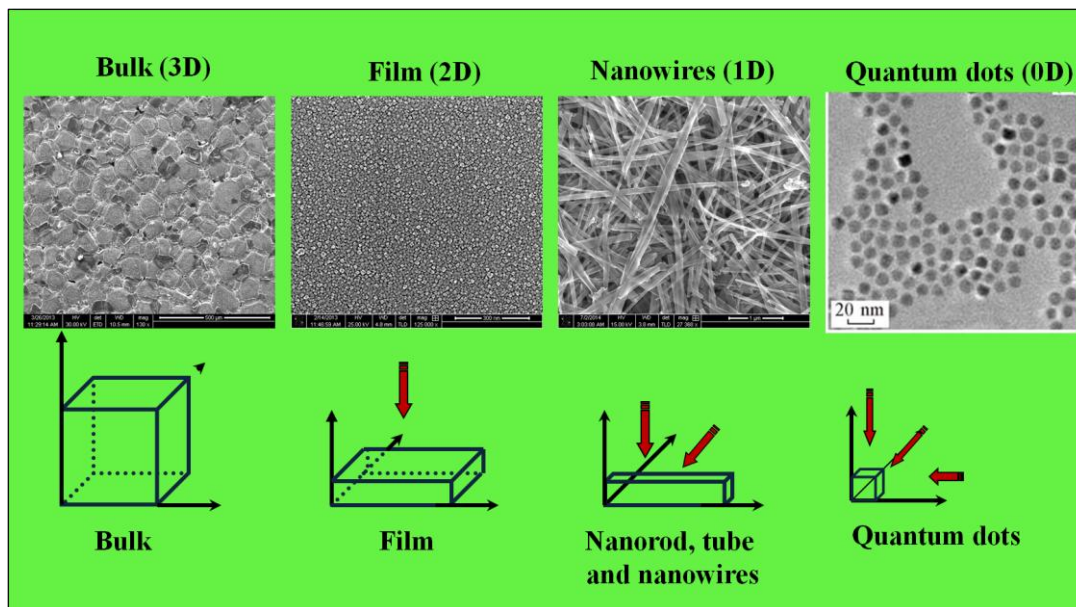


Figure 1.10 Schematic and SEM images from bulk (3D) to quantum dot (0D).

- Most of the nanomaterials, size reduction take the shape of particles (0D), wires, rods or tube (1D) in which one of its dimension in nano-metric regime (Fig. 1.10). Modification of ground state properties on size reduction to nanoparticles (0D) is well studied both from experimental and theoretical point of view. Now question arises if we add one more dimension in the bulk regime $\sim \mu\text{m}$ to it, (having a large aspect ratio of length: diameter), will it evolve a new crystallographic structure which leads to modification of other physical properties in the 1D doped manganite system?
- Among the several physical parameters like pressure, temperature, doping, strain etc. size reduction can also be an interesting parameter to engineer physical properties of

the highly single crystalline material. For detailed study on this aspect, it demands fabrication of very good quality, single crystalline (so that one can get definite results) and pure phase material with proper chemical composition, crystallographic phase with controllable shape and size morphology. The issues related to control of size, shape, structure, crystallinity, composition, homogeneity and growth kinetics of the manganite 1D nanostructures are still remained unexplored because of the difficulty in the fabrication of pure phase, homogeneous chemical composition with well controlled size, compared to other nanostructures. Few reports are available only on growth of one composition of manganite NWs [78-81]. However; no detailed study has been done. Our motivation in the present work is to provide a simple and rational synthesis route via wet chemistry to optimize 1D manganite nanostructures with controllable sizes and morphology, single crystalline structures and chemical compositions. These provide an alternative and intriguing strategy for producing manganite nanostructures in terms of material diversity, cost, throughput and the potential advantage of high-volume production. Our aim is to provide a phase diagram, which explains the possible principles of tailoring the growth of nanostructures of family of manganites with adaptable morphology and stoichiometry.

- As a result of size reduction, retention of composition, crystallinity and structural properties are important issues that are needed to be established. Often it is done on average level of ensemble of NWs. However, characterization at a single NW level using spatially tools is needed. Here we have used several spatially resolved tools based on transmission electron microscopy with the aim to investigate the chemical composition along with other structural and microscopic tools.
- Our aim of the present work is to provide how the crystallographic structure evolves on size reduction to 1D and how it affects the electrical, magnetic and other physical properties and to find out the correlation between them. No detailed study is available on this aspect till now.
- Along with the study on ensemble of NWs where size dispersion issues may arise, we want to explore single NW based transport measurement to resolve the size dispersion issues. We also performed single NW $1/f$ noise spectroscopy study with the aim to understand magnetic phase separation in manganite system. To the best of our knowledge, there is no report on single NW based transport measurement on manganites except from our group.

1.11 Structure of the thesis

This thesis is framed on the following works: (1) growth of NWs of $\text{La}_{1-x}\text{A}_x\text{MnO}_3$ ($\text{A} = \text{Ca}, \text{Sr}; x = 0.3 \text{ and } 0.5$) and their structural characterizations, (2) micro structural analysis using Transmission Electron Microscopy (TEM), (3) device fabrication (top-down approach) using lithography techniques and experimental techniques, (4) magneto transport study of ensemble of NWs, (5) crystallographic and magnetic structure study using synchrotron and neutron powder diffraction experiment of the manganite NWs, (6) temperature dependent electrical resistivity measurements of a single NW over a wide range of temperature. Few works have been reported on magnetic phase separation issue on size reduction to manganite nano particles [82]. However, no detailed investigation has been done in 1D NWs.

This thesis is divided into seven main chapters along with summary and one appendix chapter listed below:

1. In this present chapter, we presented a brief overview of the physics of manganites and the relevance of the study. This chapter includes the necessary literature of the earlier work in the field of manganite system and motivation of the present work.
2. The 2nd chapter gives a description of controlled growth of manganite NWs, growth mechanism and characterization along with experimental set-up.
3. The 3rd chapter describes advanced characterization techniques i.e. Electron Energy Loss Spectroscopy (EELS) and Energy Filtered Transmission Electron Microscopy (EFTEM) study for rigorous elemental analysis to validate the quality of the NW, single crystallinity and high resolution image simulation technique was adopted to detect lattice imperfections, like stacking disorder, twinning with atomic resolution in the complex layered compounds using multifunctional simulation software named Java electron microscopy simulation (JEMS) software. Such rigorous elemental characterization was not done before on manganite nanocrystals, especially on NWs.
4. The 4th chapter describes nano device fabrication procedure using nanolithography techniques to make single NW device and experimental techniques for electrical, $1/f$ noise spectroscopy and magnetic measurements.
5. The 5th chapter reports how the size reduction affects the magnetization behaviour in 1D case and how it differs from its bulk form. It has been found that there is an enhancement of T_C in 1D nanostructure form. Moreover it shows multiple magnetic phase transitions which are absent in their bulk phase. We tried to explain the magnetic transitions

performing magnetocaloric and transverse susceptibility measurements and found out that NWs show inverse magnetocaloric effect (IMCE). Below 200 K, the phase separation of FM and AFM phases occurs which can be explained by DE and SE mechanism respectively. The low temperature ~ 42 K transition has been explained by exchange bias effect.

6. The 6th chapter demonstrates the crystallographic and magnetic structural data of the ensemble of NWs obtained from synchrotron and neutron powder diffraction measurements respectively. In chapter 5, we have discussed about how the size reduction induces T_C enhancement, multiple phase transitions, phase separation and exchange bias (EB) effect in the NWs which are absent in its bulk form. In this chapter we would like to explore how the size reduction induced physical properties are correlated with the structural properties of the NWs. The contraction of lattice parameters due to size reduction can lead to change in magnetic properties. These structural studies show the coexistence of crystallographic (tetragonal and orthorhombic) and magnetic phases (FM and AFM respectively) below Neel temperature ($T_N < 200$ K) in $\text{La}_{0.5}\text{Sr}_{0.5}\text{MnO}_3$ NWs. In contrast, bulk $\text{La}_{0.5}\text{Sr}_{0.5}\text{MnO}_3$, showing FM tetragonal phase throughout the measured temperatures (6 - 300 K), does not show any phase separation.
7. The 7th chapter contains electrical transport measurement of single NW manganite system and compare with its bulk counterpart to understand how the electrical behaviour changes under size reduction. We have observed enough affirmation of size reduction induced modification of different physical properties, as discussed in chapter 5 and 6. The magnetic phase separation issues what we have observed in these NWs through magnetic and structural measurements may arise due to size distribution, as measurements were performed on ensemble of NWs. The phase separation observed may not be the intrinsic to single NW. Due to sensitivity and other issues, magnetic measurement of single NW is not possible, thus we have performed electrical transport experiment including $1/f$ noise spectroscopy of a single NW to explore these issues without the size dispersion problem. We demonstrated that noise spectroscopy in a single NW can cleanly detect the magnetic transitions including the phase-coexistence.

Last chapter is the summary and conclusions of this thesis. It describes main achievements of the thesis and future challenges.

This thesis ends up with appendix describing size dependence in magnetic memory, relaxation and interaction of $\text{La}_{0.7}\text{Sr}_{0.3}\text{MnO}_3$ NWs and its bulk counterpart.

Bibliography:

- [1] L. Li, L. Liang, H. Wu and X. Zhu, *Nanoscale Res. Lett.*, **11**, 121 (2016).
- [2] L. Liang, L. Li, H. Wu and X. Zhu, *Nanoscale Res. Lett.*, **9**, 325 (2014).
- [3] Z. L. Wang, *Adv. Mater.*, **12**, 1295 (2000).
- [4] X. Duan, Y. Huang, Y. Cui, J. Wang and C. M. Lieber, *Nature*, **409**, 66 (2001).
- [5] Y. Cui and C. M. Lieber, *Science*, **291**, 851 (2001).
- [6] Y. Huang, X. Duan, Y. Cui, L. J. Lauhon, K. H. Kim and C. M. Lieber, *Science*, **294**, 1313 (2001).
- [7] Y. Xia, P. Yang, Y. Sun, Y. Wu, B. Mayers, B. Gates, Y. Yin, F. Kim and H. Yan, *Adv. Mater.*, **15**, 353 (2003).
- [8] J. Hu, T. W. Odom and C. M. Lieber, *Acc. Chem. Res.*, **32**, 435 (1999).
- [9] A. J. Mieszawska, R. Jalilian, G. U. Sumanasekera, F. P. Zamborini, *Small*, **3**, 722 (2007).
- [10] B. Polyakov, B. Daly, J. Prikulis, V. Lissauskas, B. Vengalis, M. A. Morris, J. D. Holmes and D. Erts, *Adv. Mater.*, **18**, 1812 (2006).
- [11] B. Ghosh, V. Siruguri, A. K. Raychaudhuri and T. Chatterji, *J. Phys.: Condens. Matter.*, **26**, 025603 (2014).
- [12] T. Sarkar, B. Ghosh, A. K. Raychaudhuri and T. Chatterji, *Phys. Rev. B*, **77**, 235112 (2008).
- [13] B. Ghosh, S. Kar, L. K. Brar and A. K. Raychaudhuri, *J. Appl. Phys.*, **98**, 094302 (2005).
- [14] K. Bennemann, *J. Phys.: Condens. Matter*, **22**, 243201 (2010).
- [15] C. N. R. Rao and B. Raveau, *Colossal Magnetoresistance, Charge Ordering and Related Properties of Manganese Oxides*, World Scientific, 1998.
- [16] Y. Tokura, *Colossal magnetoresistive oxides*. Gordon and Breach, Amsterdam (2000).
- [17] J. M. D. Coey, M. Viret and S. von Molnar, *Adv. Phys.*, **48**, 167 (1999).
- [18] G. H. Jonker and J. H. Van Santen, *Physica*, **16**, 337 (1950).
- [19] L. M. Rodriguez-Martinez and J. P. Attfield, *Phys. Rev. B*, **63**, 024424 (2000).
- [20] T. Kubo, A. Hirai and H. Abe, *J. Phys. Soc. Japan*, **26**, 1094 (1969).
- [21] Sigrun Antje K ¨oster *Magnetic field effects on the local tunnelling conductivity of $La_{0.75}Ca_{0.25}MnO_3/MgO$ thin films* (2007).
- [22] A. J. Millis, *Nature*, **392**, 147 (1998).
- [23] C. Zener, *Phys. Rev.*, **82**, 403 (1951).
- [24] P. W. Anderson and H. Hasegawa, *Phys. Rev.*, **100**, 675 (1955).

- [25] S. Samanta, *Study of Low Frequency Conduction Fluctuations in Perovskite Manganites*, thesis submitted to Jadavpur University (2009).
- [26] E. Dagotto, *Nanoscale Phase Separation and Colossal Magnetoresistance: The Physics of Manganites and Related Compounds*, 1 ed. (Springer–Verlag, Berlin, (2002))
- [27] N. D. Mathur and P. B. Littlewood, *Solid State Commun.*, **119**, 271 (2001).
- [28] T. V. Ramakrishnan, H. R. Krishnamurthy, S. R. Hassan and G. Venketeswara Pai, *Proc. Indian Acad. Sci. (Chem. Sci.)*, **115**, 767 (2003).
- [29] T. V. Ramakrishnan and H. R. Krishnamurthy, *Pramana*, **64**, 1063 (2005).
- [30] S. S. P. Parkin, Z. G. Li and D. J. Smith, *Appl. Phys. Lett.*, **58**, 2710 (1991).
- [31] J. B. Goodenough. *Phys. Rev.*, **100**, 564 (1955);
- [32] J. B. Goodenough. *Magnetism and Chemical Bonds*. Interscience Publishing, New York, 1963.
- [33] C. W. Searle and S. T. Wang, *Can. J. Phys.*, **47**, 2023 (1969).
- [34] R. Mahendiran, R. Mahesh, A. K. Raychaudhuri and C. N. R. Rao, *Solid State Communications*, **94**, 515-518 (1995).
- [35] R. Mahesh, R. Mahendiran, A. K. Raychaudhuri and C. N. R. Rao, *J. Solid State Chem.*, **114**, 297-299 (1995).
- [36] R. Mahesh, R. Mahendiran, A. K. Raychaudhuri and C. N. R. Rao, *J. Solid State Chem.*, **120**, 204-207 (1995).
- [37] R. Mahesh, R. Mahendiran, A. K. Raychaudhuri and C. N. R. Rao, *Appl. Phys. Lett.*, **68**, 2291 (1996).
- [38] R. Mahendiran, S. K. Tiwary, A. K. Raychaudhuri, T. V. Ramakrishnan, R. Mahesh, N. Rangavittal and C. N. R. Rao, *Phys. Rev. B*, **53**, 3348 (1996).
- [39] S. Jin, T. H. Tiefel, M. McCormack, R. A. Fastnacht, R. Ramesh and L. H. Chen, *Science*, **264**, 413 (1994).
- [40] M. Paranjape, A. K. Raychaudhuri, N. D. Mathur and M. G. Blamire, *Phys. Rev. B*, **67**, 214415 (2003).
- [41] M. Paranjape, K. S. Shankar and A. K. Raychaudhuri, *J. Phys. D: Appl. Phys.*, **38**, 3674–3681 (2005).
- [42] J. Mitra, A. K. Raychaudhuri, Ya. M. Mukovskii and D. Shulyatev, *Phys. Rev. B*, **68**, 134428 (2003).
- [43] J. Mitra, M. Paranjape, A. K. Raychaudhuri, N. D. Mathur and M. G. Blamire *Phys. Rev. B*, **71**, 094426 (2005).

- [44] M. Uehara, S. Mori, C. H. Chen and S. W. Cheong, *Nature*, **399**, 560 (1999).
- [45] J. M. DeTeresa, M. R. Ibarra, P. A. Algarabel, C. Ritter, C. Marquina, J. Blasco, J. Garcia, A. delMoral and Z. Arnold, *Nature*, **386**, 256 (1997).
- [46] A. La. Spina, P. Paolicchi, A. Kryszczyńska and P. Pravec, *Nature*, **428**, 400 (2004).
- [47] G. C. Milward, M. J. C. Calderon and P. B. Littlewood, *Nature*, **433**, 607 (2005).
- [48] C. Sen, G. Alvarez and E. Dagotto, *Phys. Rev. Lett.*, **98**, 127202 (2007).
- [49] G. Li, H. D. Zhou, S. J. Feng, X. J. Fan, X. G. Li and Z. D. Wang, *J. Appl. Phys.*, **92**, 1406 (2002).
- [50] S. L. Yuan, Z. Y. Li, W.Y. Zhao, G. Li, Y. Jiang, X. Y. Zeng, Y. P. Yang, G. Q. Zhang, F. Tu, C. Q. Tang and S. Z. Jin, *Phys. Rev. B*, **63**, 172415 (2001).
- [51] A. Moreo, M. Mayr, A. Feiguin, S. Yonuki and E. Dagotto, *Phys. Rev. Lett.*, **84**, 5568 (2000).
- [52] A. Arulraj, A. Biswas, A. K. Raychaudhuri, C. N. R. Rao, P. M. Woodward, T. Vogt, D. E. Cox and A. K. Cheetham, *Phys. Rev. B*, **57**, R8115 (1998).
- [53] T. Z. Ward, Z. Gai, X. Y. Xu, H. W. Guo, L. F. Yin and J. Shen, *Phys. Rev. Lett.*, **106**, 157207 (2011).
- [54] S. Arumugam, B. Ghosh, A. K. Raychaudhuri, N. R. Tamil Selvan, T. Nakanishi, H. Yoshino, K. Murata and Ya. M. Mukovskii, *J. Appl. Phys.*, **106**, 023905 (2009).
- [55] E. Dagotto, H. Takashi and A. Moreo, *Phys. Rep.*, **344**, 1153 (2001).
- [56] L. M. Rodriguez Martinez and J. P. Attfield, *Phys. Rev. B*, **54**, 15622-15625 (1996).
- [57] R. H. Kodama, A. E. Berkowitz, E. J. McNiff Jr. and S. Foner, *Phys. Rev. Lett.*, **77**, 394 (1996).
- [58] E. Dagotto, S. Yonuki, A. L. Malvezzi, A. Moreo, J. Hu, S. Capponi, D. Poilblanc and N. Furukawa, *Phys. Rev. B*, **58**, 6414 (1998).
- [59] E. Dagotto, *Nanoscale Phase Separation and Colossal Magnetoresistance*. Berlin, Germany: Springer; 2003.
- [60] S. Yonuki, A. Moreo and E. Dagotto, *Phys. Rev. Lett.*, **81**, 5612 (1998).
- [61] H. Y. Zhai, J. X. Ma, D. T. Gillaspie, X. G. Zhang, T. Z. Ward, E. W. Plummer and J. Shen, *Phys. Rev. Lett.*, **97**, 167201 (2006).
- [62] Y. Yanagisawa, H. Tanaka, T. Kawai and L. Pellegrino, *Appl. Phys. Lett.*, **89**, 253121 (2006).
- [63] T. Z. Ward, X. G. Zhang, L. F. Yin, X. Q. Zhang, M. Liu, P. C. Snijders, S. Jesse, E. W. Plummer, Z. H. Cheng, E. Dagotto and J. Shen, *Phys. Rev. Lett.*, **102**, 087201 (2009).

-
- [64] T. Z. Ward, Z. Gai, H. W. Guo, L. F. Yin and J. Shen, *Phys. Rev. B*, **83**, 125125 (2011).
- [65] T. Z Ward, S. Liang, K. Fuchigami, L. F. Yin, E. Dagotto, E. W. Plummer and J. Shen, *Phys. Rev. Lett.*, **100**, 247204 (2008).
- [66] J. C Wu, H. Sun, H. X. Da and Z. Y Li, *Appl. Phys. Lett.*, **91**, 102501 (2007).
- [67] G. Singh-Bhalla, S. Selcuk, T. Dhakal, A. Biswas and A. F. Hebard, *Phys. Rev. Lett.*, **102**, 077205 (2009).
- [68] G. Singh-Bhalla, A. Biswas and A. F. Hebard, *Phys. Rev. B*, **80**, 144410 (2009).
- [69] J. Shen, T. Z. Ward and L. F. Yin, *Chin. Phys. B.*, **22**, 017501 (2013).
- [70] S. Yunoki, J. Hu, A. L. Malvezzi, A. Moreo, N. Furukawa and E. Dagotto, *Phys. Rev. Lett.*, **80**, 845 (1998).
- [71] P. Malla Chowdhury, B. Ghosh, A. K. Raychaudhuri, S. D. Kaushik and V. Siruguri, *J. Nanopart. Res.*, **15**, 1585 (2013).
- [72] C. Ritter M. R. Ibarra, J. M. De Teresa, P. A. Algarabel, C. Marquina, J. Blasco, J. Garcí'a, S. Oseroff and S.-W. Cheong, *Phys. Rev. B*, **56**, 8902 (1997).
- [73] S. S. Rao, S. Tripathi, D. Pandey and S. V. Bhat, *Phys. Rev. B*, **74**, 144416 (2006).
- [74] T. Zhang and M. Dressel, *Phys. Rev. B*, **80**, 014435 (2009).
- [75] Z. Jiráček, E. Hadová, O. Kaman, K. Knížek, M. Maryško, E. Pollert, M. Dlouhá and S. Vratislav, *Phys. Rev. B*, **81**, 024403 (2010).
- [76] V. Markovich, I. Fita, A. Wisniewski, G. Jung, D. Mogilyansky, R. Puzniak, L. Titelman and G. Gorodetsky, *Phys. Rev. B*, **81**, 134440 (2010).
- [77] X. H. Huang, J. F. Ding, G. Q. Zhang, Y. Hou, Y. P. Yao and X. G. Li, *Phys. Rev. B*, **78**, 224408 (2008).
- [78] K. S. Shankar and A. K. Raychaudhuri, *Nanotechnology*, **15**, 1312 (2004).
- [79] B. Ghosh and A. K. Raychaudhuri, *J. Nanosci. Nanotechnol.*, **9**, 5533–5536 (2009).
- [80] D. Zhu, H. Zhu and Y. H. Zhang, *J. Phys.: Condens. Matter*, **14**, L519– L524 (2002).
- [81] K. S. Shankar, S. Kar, G. N. Subbanna and A. K. Raychaudhuri, *Appl. Phys. Lett.*, **84**, 993 (2004).
- [82] T. Sarkar, A. K. Raychaudhuri, A. K. Bera and S. M. Yusuf, *New J. Phys.*, **12**, 123026 (21pp) (2010).
-

Chapter 2

Synthesis and Characterization

In this chapter, we have described the synthesis of perovskite oxide manganite of $La_{1-x}A_xMnO_3$; (where $A = Ca, Sr$; $x = 0.3$ and 0.5) nanostructures in cost-effective hydrothermal route and their characterizations. The bulk sample of manganite was prepared by the sol gel method followed by high temperature annealing process. The grown material are characterized by X-ray Diffraction (XRD), Neutron diffraction (ND) experiment, Scanning Electron Microscope (SEM), Energy dispersive X-ray analysis (EDX) and Transmission Electron Microscope (TEM) for structural characterizations. We have also demonstrated the techniques in brief followed by experimental results.

2.1 Introduction

One dimensional (1D) nanostructures, such as nanowires (NWs), nanotubes, nanorods have been studied for the past two decades due to their interesting and unique structural, electronic, optical, thermal, mechanical and magnetic properties. In early days of this research area, new synthesis process and their basic characterizations were greatly emphasized. The fabrication of high-quality single crystalline materials with well controlled diameter, length, composition and phase incorporated successfully into useful devices. These nanostructures possess distinct properties that are different from those of bulk materials due to their size reduction and large surface-to-volume ratios and thus are very promising candidates for realizing nanoscale devices. Those studies are mainly on binary oxide related compounds. However, due to difficulty in synthesizing NWs of complex oxides with proper stoichiometry and pure phase state, they are less studied. Among the complex oxides we have concentrated on the doped manganite system. Though there are several methods for fabrication of complex oxide NWs of manganite, like template-assisted growth along with chemical solution processing [1-3], laser-assisted vapour liquid-solid phase growth [4], lithography, solvothermal method [5], hydrothermal process [6] and so forth. However, reports are available only for few compositions [6-9], as growth with proper stoichiometry and composition is quite non trivial. Hence, the growth of NWs with controlled size, shape, composition and stoichiometry is very important issue to be resolved. In this thesis, we have standardized the growth technique in such a way, so that one can make any stoichiometry, composition, shape and size of the manganite NWs by following a common synthesis route. We have worked on a specific series of perovskite doped manganite NWs, i.e., mixed valence compound, where doping has been carried out in the rare-earth (La) site with some divalent ion e.g. Ca, Sr etc., with general formula $\text{La}_x\text{A}_{1-x}\text{MnO}_3$ ($\text{A} = \text{Ca}, \text{Sr}$). We have worked on the controlled growth of manganite nanostructures following a wet chemistry route, hydrothermal method [7-9] in different doping regime. We have shown how one can tailor size, shape and composition by means of a general synthesis route (hydrothermal route), controlling few growth parameters which is explained by a phase diagram.

It has been observed that control of few parameters, like time, temperature, amount of oxidizer, mineralizer and precursor materials during growth can tailor the shape, size of nanostructures (nanoparticle, NWs etc) with desired composition and stoichiometry. Appropriate amount of mineralizer (KOH) in the reaction reduces the energy of crystal

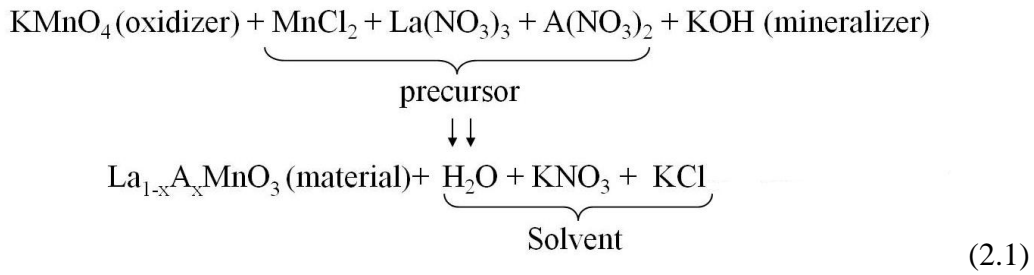
surfaces by enhancing surface adsorption and facilitates growth of 1D nanostructure along minimized surface energy direction. The most important observation is that out of various parameters during growth, the mineralizer amount controls the shape (wire, facets) and temperature maintains the composition and time controls the phase formation and also size of the crystallites. A phase diagram has been provided to understand the process of growth. We have standardized the growth technique in such a way, so that one can make any stoichiometry, composition, shape and size of the manganite NWs.

Hydrothermal method is basically a one-step synthesis process to produce different chemical compounds and materials using closed Teflon vessel named as Autoclave in a sealed thick-walled stainless steel cylinders in aqueous solutions at temperatures above 100°C and high pressures (<100 MPa) [10, 11]. The autoclave material must be inert with respect to the solvent and it must withstand high temperatures and pressure for prolonged periods of time. This method is extensively used in synthesis of nano-materials. Advantages of this method over other types of crystal growth include the ability to create crystalline phases which are unstable at the melting point. Materials which have a high vapour pressure near their melting points can also be grown by this method. It is mainly used for the growth of large good-quality single crystals while maintaining good control over their composition. The sol-gel method involves transition of monomers into a colloidal solution (sol) that acts as the precursor for an integrated network (or gel) of either discrete particles or network polymers [12].

2.2 Synthesis of $\text{La}_{1-x}\text{A}_x\text{MnO}_3$ (A = Sr, Ca; $x = 0.3$ and 0.5) nanostructures

We have grown the nano-crystals and NWs of complex oxide manganites $\text{La}_{1-x}\text{A}_x\text{MnO}_3$; (where A = Ca, Sr; $x = 0.3$ and 0.5) with adaptable stoichiometry in cost-effective hydrothermal synthesis technique in autoclave in the low-temperature range (230-300 °C) [7]. We have investigated the basic growth mechanism, the kinetic rules of size and morphology tuning and the accompanying phase transformation of this system.

The general reaction for the formation of $\text{La}_{1-x}\text{A}_x\text{MnO}_3$; (where A = Ca, Sr; $x = 0.3$ and 0.5) nanostructures is given as Eq. (2.1).



2.2.1 Nanostructures growth by Hydrothermal Method

Highly pure $\text{La}(\text{NO}_3)_3 \cdot 6\text{H}_2\text{O}$ (Aldrich, 99.9 %), $\text{Ca}(\text{NO}_3)_2 \cdot 4\text{H}_2\text{O}$ (Aldrich, 99.9 %+), KMnO_4 (s d fine, 99.5 %), $\text{MnCl}_2 \cdot 4\text{H}_2\text{O}$ (Aldrich, 99 %) and KOH (Merck, pellets, 85 %) were used for the preparation as discussed in Eq. (2.1). The initial mole ratio of the starting materials was 0.6 KMnO_4 :1.4 $\text{MnCl}_2 \cdot 4\text{H}_2\text{O}$:1.0 $\text{La}(\text{NO}_3)_3 \cdot 6\text{H}_2\text{O}$:1.0 $\text{Ca}(\text{NO}_3)_2 \cdot 4\text{H}_2\text{O}$:400 H_2O for $\text{La}_{0.5}\text{Ca}_{0.5}\text{MnO}_3$ (LCMO-0.5) NWs and 0.6 KMnO_4 :1.4 $\text{MnCl}_2 \cdot 4\text{H}_2\text{O}$:0.7 $\text{La}(\text{NO}_3)_3 \cdot 6\text{H}_2\text{O}$:0. $\text{Ca}(\text{NO}_3)_2 \cdot 4\text{H}_2\text{O}$:400 H_2O for $\text{La}_{0.7}\text{Ca}_{0.3}\text{MnO}_3$ (LCMO-0.3) NWs. The synthesis process for the hole-doped manganite NWs of $\text{La}_{0.5}\text{Sr}_{0.5}\text{MnO}_3$ (LSMO-0.5) and $\text{La}_{0.7}\text{Sr}_{0.3}\text{MnO}_3$ (LSMO-0.3) are similar to that of the growth of LCMO NWs. Here, the reaction also follows Eq. (2.1) [7-9]. In this reaction, instead of $\text{Ca}(\text{NO}_3)_2 \cdot 4\text{H}_2\text{O}$ $\text{Sr}(\text{NO}_3)_2$ (Aldrich, 99 % +) was used. Chemicals were dissolved proportionately in deionised water to form a uniform solution and the pH of the solution was adjusted to 14 by adding 3.5 gm of KOH with stirring using a magnetic stirrer. KOH and KMnO_4 were used as mineralizer and oxidizer, respectively. The solution was poured into a 50-ml Teflon vessel and then it was placed in a stainless steel cylinder. The crystallization reaction was performed in oven at 230-300 °C for 30-60 hours depending on different sample as shown in Table 2.1. Finally, the autoclave was cooled to room temperature naturally and depressurized. The obtained product of the reaction was washed with deionised water and dried overnight in air at 120 °C. The flowchart of this synthesis process is described in Fig. 2.1. The pictorial of this growth method is depicted in Fig. 2.2. The temperature and the duration of the reaction are the two vital parameters to synthesize the NWs with pure phases, otherwise, the reaction is not completed and by-product phases become dominant. These issues will be discussed later in details. Table 2.1 summarizes the growth parameters of nanostructures of manganite of two different surface morphologies i.e., NWs and nanoparticles.

Hydrothermal Synthesis of $\text{La}_{1-x}\text{A}_x\text{MnO}_3$; (where A = Ca, Sr; $x = 0.3$ and 0.5) nanostructures

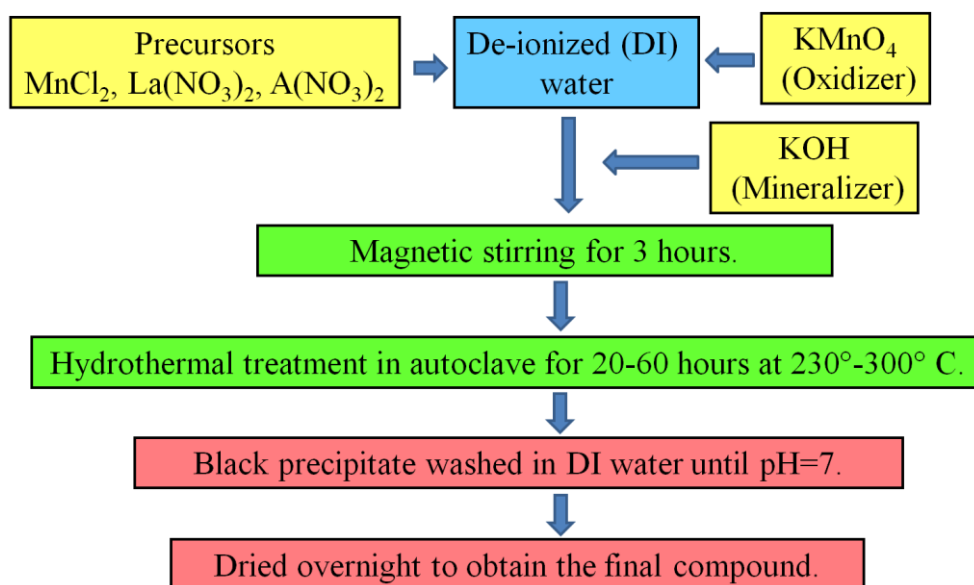


Figure 2.1 Flow chart of Hydrothermal Synthesis.

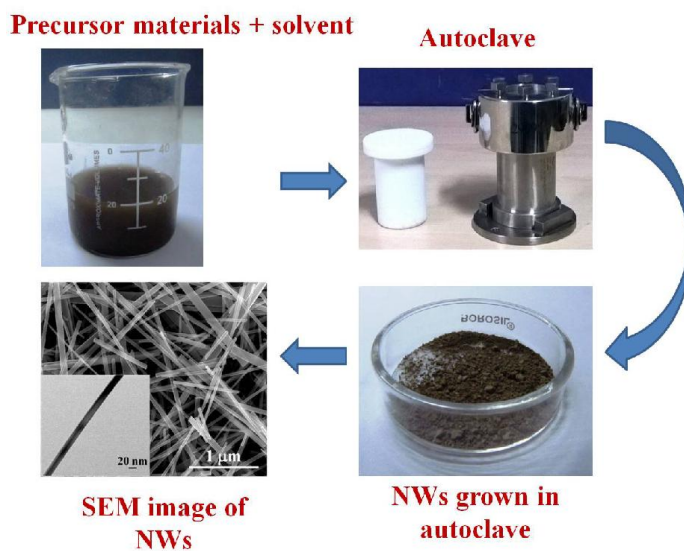


Figure 2.2 Pictorial view of the growth process.

Table 2.1 Summary of growth parameters of nanostructures of manganite of different surface morphologies by hydrothermal synthesis method: NWs and nanoparticles

Sample ID	compound	Sample Form	Time (hrs)	KOH (in gm)	Temp (°C)
LCMO-0.3	$La_{0.7}Ca_{0.3}MnO_3$	Nanowires	60	3.0-4.5	260-300
		Nano particles	20	5.5-7.0	
LCMO-0.5	$La_{0.5}Ca_{0.5}MnO_3$	Nanowires	50	3.0-4.5	260-300
		Nano particles	20	5.5-7.0	
LSMO-0.3	$La_{0.7}Sr_{0.3}MnO_3$	Nanowires	40	3.0-4.5	230-300
		Nano particles	15	5.5-7.0	
LSMO-0.5	$La_{0.5}Sr_{0.5}MnO_3$	Nanowires	30	3.0-4.5	230-300
		Nano particles	15	5.5-7.0	

2.2.1.1 Influence of growth parameters in hydrothermal process

Hydrothermal synthesis is one of the bottom-up synthesis routes to grow complex materials such as perovskite oxide compounds, especially in nano-structured form with appropriate precursors and solvents. In this growth method, various parameters like, precursors materials, solvents concentration of the medium, temperature and pressure which control the overall morphology and structure of the materials. Other than the precursor stoichiometry, reaction time, temperature and pressure, selection of appropriate mineralizer and oxidizer play an important role in the formation of end product via hydrothermal route. Detailed investigation and experimental evidences helped to understand the possible principle of growth of nanostructures of complex oxide systems with adaptable stoichiometry and shape/size. On the basis of detailed investigation done, the influence of the major parameters in the reaction has been discussed accordingly.

Effect of mineralizer (KOH, NaOH, etc.) on the growth of different nanostructures has been studied by several groups emphasizing the surfactant-free growth and shape tailoring of the metal and semiconducting nanostructures, mainly on binary oxides [13, 14-16, 17, 18-24] but not in complex oxides. Mineralizer provides an essential means to realize good control of shape/size, diameter and crystal orientation of the nanostructures (as seen in simple binary oxide cases) [13, 14-16, 24]. In our case of complex perovskite oxide system, amount of KOH was adjusted at a constant pH throughout the reaction within the autoclave. The shape

of nanostructures could be tailored by tuning the amount of KOH. Shape control in crystal growth using KOH was reported earlier in different materials [25]. It has been noticed that by maintaining the amount of the KOH (3.5 gm) in the reaction medium, wire-like (1D) structure (average size ~ 50 nm) of perovskite oxide manganite can be realised whereas, incorporation of approximate double amount of KOH (6 gm), the cube-like faceted structure with average size (~ 100 nm,) is produced (Fig. 2.3). At such higher amount of KOH, the growth speed of these facets has improved greatly, compared to that of wire-like structures. Fig. 2.3(a)–(d) shows two different shapes of the nanostructures at different amount of KOH of LCMO-0.5 and LSMO-0.5 samples. High amount of KOH helps in fast precipitation of first nuclei charging their surface (OH^- anions attachment) that ultimately, hinders nanoparticles aggregation (see Fig. 2.3(a), (c)) [13, 14, 20, 24]. Fig. 2.3(a) and (c) shows the SEM images of LCMO-0.5 and LSMO-0.5 nanoparticles, respectively. On the other hand, incorporation of moderate amount of KOH (3.5 gm) helps to enhance the aspect ratio of the nanostructures and finally forms 1D NW (size ~ 50 nm) as seen in Fig. 2.3(b) and (d) which shows the SEM images of LCMO-0.5 and LSMO-0.5 NWs, respectively. In the solution with $\text{pH} \sim 14$, solubility and coarsening rate of the surface are high, realizing a (faceted) nanoparticle-like structure (see Fig. 2.3(a), (c)) with a pure phase. Fig. 2.4(b) and (c) show the X-ray diffraction data of LSMO-0.5 nanoparticles with different reaction times. The main cause of shape tailoring issues will be discussed in the growth mechanism part. Along with the mineralizer, growth temperature is the other important parameter to complete the reaction and for pure phase formation in hydrothermal method, as appropriate temperature for a reaction has to be decided according to the solubility of the precursor material. It has been known that with increasing temperature of water, in subcritical or superheated water (with enough pressure to maintain the liquid state) increases the solubility of the material [26]. In our case, the growth of manganite NWs was realized by hydrothermal method (i.e., water as solvent) in the temperature range from 230 to 300 $^{\circ}\text{C}$, which is well below supercritical (374 $^{\circ}\text{C}$) temperature. Because of very strong hydrogen bonding, water shows many anomalous properties. In the superheated (subcritical) temperature range, the hydrogen bonds break and water becomes less polar and behaves more like an organic solvent [7] and act as a catalyst. With increasing temperature (in subcritical water), solubility of materials and gases increases by several orders of magnitude, hence the nanostructures can be realised at lower temperature (range 230-300 $^{\circ}\text{C}$) than the conventional solid state reaction. The higher soluble Sr doped nanostructures of manganite can be realised at lower temperature (< 250 $^{\circ}\text{C}$) than the lower

soluble Ca doped one ($> 250\text{ }^{\circ}\text{C}$) (Fig. 2.5). Specific heat capacity at constant pressure also increases with temperature and increased heat capacity promotes extra energy to break the bonds. Moreover, viscosity and surface tension of water drop and diffusivity increases with increasing temperature and allows molecules to move more freely which favours the growth kinetics in aqueous medium. Rabenau *et al.* also indicated that subcritical water therefore acts as a better solvent than ambient water [7].

A possible phase diagram shown in Fig. 2.5 is drawn as a function of amount of KOH vs. temperature. This explains that tuning of size, shape and composition of doped manganite ($\text{La}_{1-x}\text{A}_x\text{MnO}_3$ with $\text{A} = \text{Ca}, \text{Sr}$) is possible if one follows this phase diagram. The phase diagram can be read in the following manner. NW like structure of any composition can be realised when KOH varies in the range 3–4.5 gm and particle will be formed when KOH ranges within 5.5-7 gm. The probability of formation of mixed shape/sized NW and faceted nanoparticle is high in the region, where the amount of KOH varies in the range 4.5–5.5 gm. Considering the temperature scale in phase diagram (Fig. 2.5), Sr doped nanostructures of $\text{La}_{1-x}\text{Sr}_x\text{MnO}_3$ can be formed at $< 250\text{ }^{\circ}\text{C}$ and Ca doped one, $\text{La}_{1-x}\text{Ca}_x\text{MnO}_3$ can be grown at $> 250\text{ }^{\circ}\text{C}$ (shaded region, Fig. 2.5) of any shape/size.

The autogeneous pressure inside the autoclave defines both the kinetics of processes and the properties of resulting products. The combined effect of pressure and temperature can reduce free energies for various equilibria-stabilizing phases that might not be stable at atmospheric conditions and promote the reaction. In an autoclave the vapour coexists with liquid. Pressure for a reaction within the autoclave at a certain temperature is estimated using Clausius Clapeyron equation. Standard equation of enthalpy:

$$\ln\left(\frac{P_1}{P_2}\right) = \frac{\Delta H_{\text{vap}}}{R} \left(\frac{1}{T_2} - \frac{1}{T_1}\right) \quad (2.2)$$

$$p = A \exp\left(\frac{-\Delta H_{\text{vap}}}{RT}\right) \quad (2.3)$$

where $R = 8.3145\text{ J/mole/K}$. P_1 and P_2 are the pressures at two temperatures T_1 and T_2 respectively. The vapor pressure of water within the autoclave can be estimated as, for $T = 270^{\circ}\text{C}$, pressure $\sim 60\text{ atm}$ and for $T = 240^{\circ}\text{C}$, pressure $\sim 35\text{ atm}$.

The synthesis of the perovskite oxides with proper oxygen stoichiometry and hence the Mn valency by hydrothermal method are challenging, since control of manganese oxidation state and oxygen stoichiometry are nontrivial, as Mn in manganite is in mixed valence state. Incorporation of oxidizer (KMnO_4 in our case) in reaction mixture plays an important role in maintaining the valency of transition metal (Mn). Spooen *et al.* reported that the concentrated KOH solution involves reaction between MnO_4^- and Mn^{2+} in the presence of lanthanum and alkali-earth metal salts to give the desired (average) manganese oxidation state of 3.5 at the beginning of the reaction [27, 28-33]. The presence of the precursor phase forces the formation of the manganite with the same average oxidation state (+3.5). We could achieve the desired oxidation state of Mn and proper oxygen stoichiometry in case of perovskite manganite NWs. The Mn oxidation states have been evaluated by spatially resolved tool, TEM-based electron energy loss spectroscopy (EELS) study discussed in next chapter.

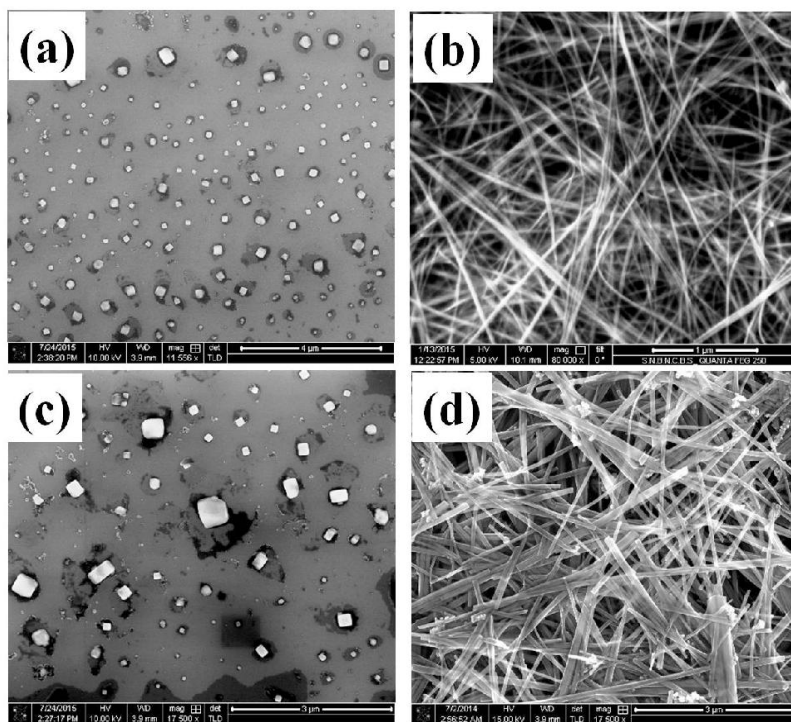


Figure 2.3 SEM images of complex oxide nanostructures by hydrothermal method; nanoparticles of (a) LCMO-0.5, (c) LSMO-0.5 samples and nanowires (b) LCMO-0.5 (d) LSMO-0.5 samples, respectively. The hydrothermally grown nanowires (LCMO-0.5 and LSMO-0.5 samples) are 1–10 micron in length and average diameter is around 20–70 nm. The average diameter of nanoparticles is ~100 nm.

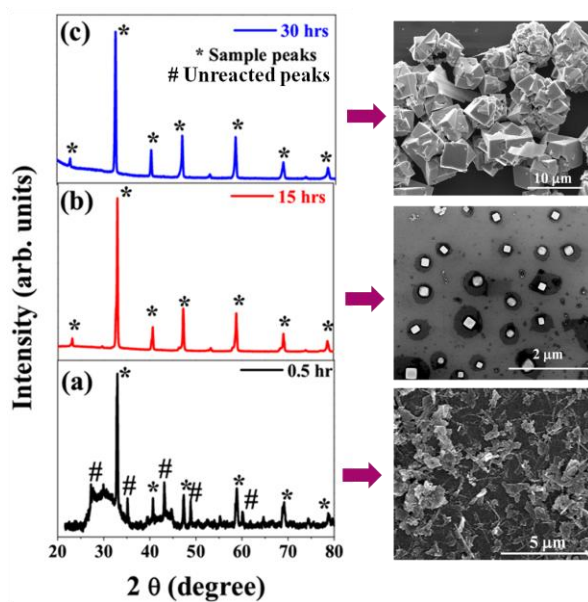


Figure 2.4 XRD of LSMO-0.5 nanoparticles grown at different times (a) 0.5 hr (b) 15 hrs (c) 30 hrs. “*” symbol indicates LSMO-0.5 sample peak and “#” denotes unreacted peaks. At the lower time (0.5 hr) the proper phase is not formed. The corresponding SEM images are depicted in the right hand side.

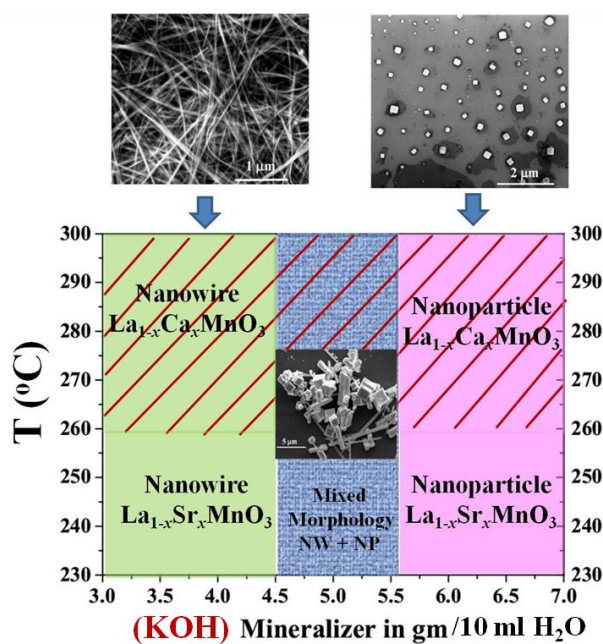


Figure 2.5 Phase diagram of hydrothermal synthesis of nanocrystals of perovskite oxide manganites $\text{La}_{1-x}\text{A}_x\text{MnO}_3$ ($\text{A} = \text{Ca}, \text{Sr}$; $x = 0.3$ and 0.5) as a function of amount of mineralizer (KOH). The nanowires formed incorporation of lower amount of KOH (3.0–4.5 gm) and the nanocrystallites, at the higher amount of KOH (5.5–7.0 gm). The $\text{La}_{1-x}\text{Sr}_x\text{MnO}_3$ samples are formed at 230–300 $^{\circ}\text{C}$, whereas $\text{La}_{1-x}\text{Ca}_x\text{MnO}_3$ samples are grown at 260–300 $^{\circ}\text{C}$ shown in the red-colored shaded region. The probability of formation of mixed shape/size of nanowire (NW) and faceted nanoparticle (NP) is high in the region where the amount of KOH varies in the range (4.5–5.5 gm).

2.2.1.2 Growth mechanism of the nanostructures

In the previous section it has been discussed in details about all the essential parameters and how they are associated with hydrothermal synthesis in realizing the desired material. When the inorganic species with proper stoichiometry are mixed with appropriate oxidizer and mineralizer in aqueous medium, at high temperature and autogeneous pressure within the autoclave, very rapid nucleation of small crystallites occurs from the supersaturated solution. Nucleation occurs due to the driving force of thermodynamics because the supersaturated solution is unstable in energy [15-17, 23-24, 34-37]. As the crystal surface with lowest surface energy grows most slowly, introduction of an appropriate amount of KOH in the reaction reduces the energy of crystal surfaces by enhancing surface adsorption and facilitates growth of 1D nanostructure of complex oxides along minimized surface energy direction, which was also observed in simple binary oxide cases [15-17, 20, 23-24].

Because of higher surface energy of the nano-crystals, it facilitates the reaction on the surface, such as the direct bonding and crystallization between particles in the presence of some ligand, surfactant, some passivation agent, capping agent by modifying the surface adsorption, surface charge and finally reduce the surface energy [15-16]. Growth, shape and size of nanostructures are dependent on adsorption of anions i.e., the mineralizer [38-39].

At the first stage of nucleation, very tiny nano-crystals (size ~20 nm) are formed rapidly. Generally in hydrothermal synthesis, the nucleation occurs (Fig. 2.6 provides images of the nano-crystals (Size ~20 nm)) in the form of small rod-like structure of very coarse surface formed after 0.5 hr of reaction. Smaller nano-crystals grow more rapidly than the larger ones, because the free energy driving force is larger for smaller crystallites than for larger ones. (See Fig. 2.6). The small nanocrystallites with common crystallographic orientations combine together to form small nanorod-like structure (size ~ few tens of nanometres) that has been confirmed by TEM image (see Fig. 2.7). The TEM image of $\text{La}_{0.5}\text{Sr}_{0.5}\text{MnO}_3$ indicates that crystallites of same orientation (112) are attached to form the NW-like structure which is further confirmed by analysis of diffraction pattern of single NW with (112) growth direction, obtained after 30 hrs of reaction (shown in Fig. 3.11 (a)-(b) in chapter 3). After 5 hrs of reaction, the sharpness of the NW surface increases and length increases to 200–300 nm (See 5 hrs growth of Fig. 2.6). In the growth via hydrothermal route of manganite, first few steps of nucleation are very rapid and surface of the NWs are not very smooth (see 5 hrs growth of Fig. 2.6). Though the NW like shape is formed after 5 hrs phase is not formed as seen in Fig. 2.6(b). The reaction is still incomplete. Finally, prolonging the heating time (for 1–2 days),

mainly leads to an elongation of the NWs to 5–10 microns with pure phase and at the end of the reaction all the NWs are generated followed by a self-sharpening process. The average lengths of NWs after completion of the reaction are 1–10 micron and diameter 20–70 nm as shown in Fig. 2.6 after 30 hrs of growth.

Generally, during synthesis of perovskite oxides in solution in the presence of some additive, growth of crystal planes may be terminated either A–O or B–O at the surface [15-16]. In a very high concentration of alkaline hydroxide (KOH) in reaction medium, the crystals are terminated with an A–O layer, leading to a positively charged surface as the bonds of A-site cations are unsaturated. Some of OH⁻ anions of KOH, in the reaction mixture may attach with the crystal surface to balance the charge and reduce the surface energy [13-14, 17, 20, 23-24]. The crystal surface with the bonded atoms is most stable. Thus, at the lower amount of KOH (3.5 gm), the OH bonds may attach with one face [(112) in case of LSMO-0.5] and reduce the overall surface energy contribution and become stable and grow along (112) direction (see Fig. 3.11 (a)-(b) in chapter 3).

On the other hand, apart from growth of NWs the growth of nanoparticle like structure can be realised with the same chemistry using higher amount of KOH in the precursor solution. When the concentration of KOH increases, the viscosity (η) of the liquid phase increases, thus the diffusion rate (D) of nanoparticles should decrease, according to the Stoke–Einstein equation, $D \propto \text{constant}/\eta$. According to the observation of several authors [20, 24], it reveals that the diffusion rate (D) of nanoparticles increases when the KOH concentration goes up. From the high resolution TEM (HRTEM) analysis (Fig. 2.7), indicates that the apparent growth inconsistency may arise due to the electric double layers surrounding the nanoparticles. As reported by other authors, it is possible that the electric double layers may arise due to strong K⁺ and OH⁻ adsorption [20, 24]. Thus, there is an electric attraction and repulsion interaction between the surface-capped nanoparticles and surrounding ions which facilitates the suspension of nanoparticles in the solution. Therefore, the higher KOH concentration leads to higher degree of the nanoparticles in the suspension. In our case, inorganic additive KOH facilitates the strong surface adsorption. In the growth of nanocrystallites, we have observed that among all the parameters mineralizer, temperature and time of growth play very important role in realising and engineering the shape and size.

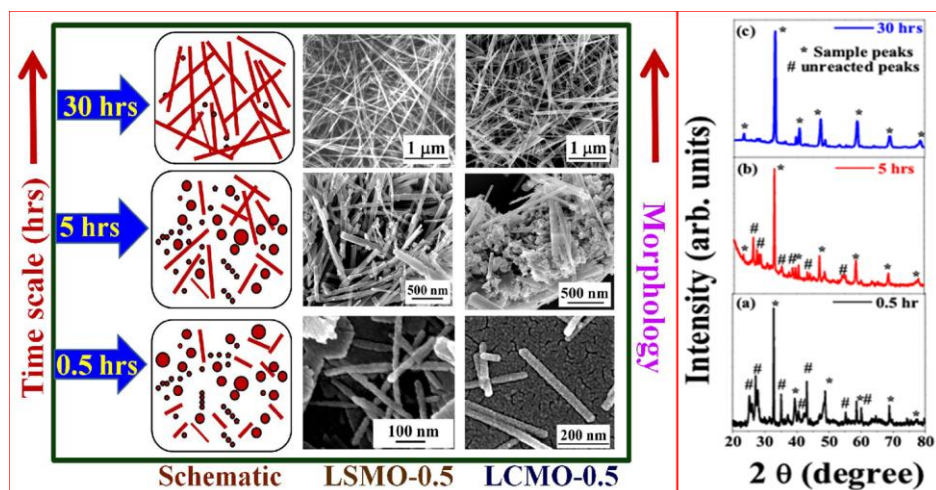


Figure 2.6 Schematic of growth steps of nanowires and corresponding SEM images with growth time (0.5–30 hrs) of LSMO-0.5 and LCMO-0.5 samples.

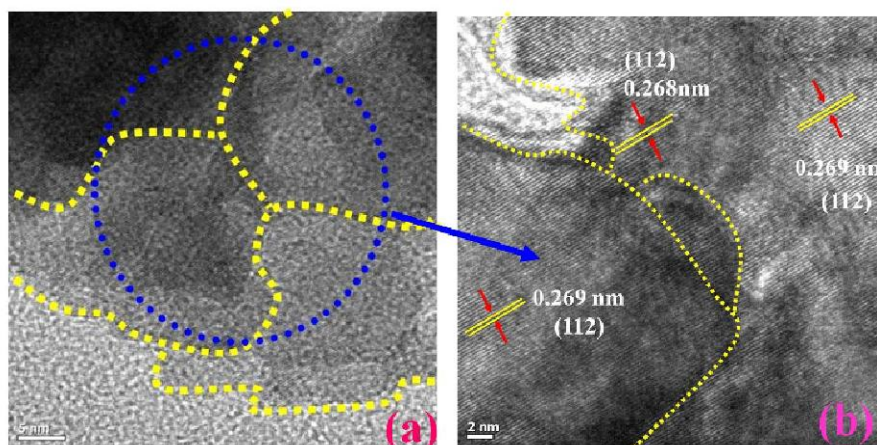


Figure 2.7 TEM images of LSMO-0.5 nanocrystallites formed after fast nucleation. Yellow dotted line indicates the boundary of nanocrystallites. (b) enlarged view of (a); the orientation of all the nanocrystallites is same i.e., (112) direction and lattice spacing (~ 0.269 nm) between two interplanar is almost equal.

2.3 Bulk growth by the sol gel method

In the sol gel method [12], the reactions occur in a solution medium and this decreases the diffusion distances through intimate mixing of the cations. Consequently, reactions can occur at lower temperatures and the products formed are more homogeneous.

A sol is a steady distribution of colloidal particles (amorphous or crystalline) or polymers in a solvent. A gel, on the other hand, can be formed of a three dimensional continuous network

which encloses a liquid phase. The sol gel process is based on the evolution of a system from a liquid solution (sol) into a gelatinous network (gel) phase.

The $\text{La}_{1-x}\text{Sr}_x\text{MnO}_3$ ($x = 0.3$ and 0.5) bulk samples have been synthesized by the sol–gel based polymeric precursor route. In a typical synthesis process, High-purity ($> 99\%$) metal acetates (procured from Sigma Aldrich), lanthanum acetate hydrate $[\text{La}(\text{CH}_3\text{CO}_2)_3 \cdot x\text{H}_2\text{O}]$, strontium acetate $[\text{Sr}(\text{CH}_3\text{CO}_2)_2]$ and manganese acetate tetra hydrate $[\text{Mn}(\text{CH}_3\text{CO}_2)_2 \cdot 4\text{H}_2\text{O}]$ are dissolved in the desired stoichiometric proportions in 1:1 volume ratio of acetic acid and deionised water. Appropriate amount of ethylene glycol (molecular weight = 62.07 gm/mol) was added to this solution and heated until a gel was formed. The ethylene glycol polymer is used to form a closed network of cations from the precursor solution and assists the reaction for formation of phase. Pyrolysis is to be done to remove organic precursor materials around $300\text{--}400^\circ\text{C}$ followed by sintering around $\sim 650^\circ\text{C}$ to obtain the desired chemical phase of $\text{La}_{1-x}\text{Sr}_x\text{MnO}_3$ ($x = 0.3$ and 0.5) nanoparticles. The nanoparticles are taken in required quantity and pellets are made at high pressure (around 100 MPa). The pellets are heated at 1200°C for 10 hr and 1600°C for 12 hr which yields bulk crystallites of size 20-30 microns (Fig. 2.8).

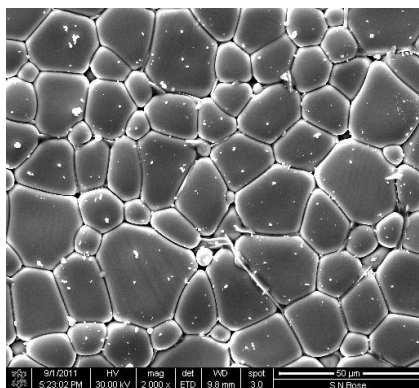


Figure 2.8 SEM micrograph of LSMO-0.5 bulk sample.

2.4 Brief description to characterization techniques

The as synthesized NW samples as discussed above are mainly characterized by X-Ray Diffraction (XRD), Neutron Diffraction (ND) experiment, Scanning Electron Microscope (SEM), Energy dispersive X-ray Analysis (EDX), Transmission Electron Microscope (TEM) for structural characterization. The hydrothermally synthesized $\text{La}_{1-x}\text{A}_x\text{MnO}_3$; (where $\text{A} = \text{Ca}, \text{Sr}$; $x = 0.3$ and 0.5) NWs are characterized in powder form. For TEM based measurements,

NWs are dispersed on carbon coated Cu grid. Here, we will discuss various characterization techniques along with the basic principles and some results obtained from our samples.

2.4.1 Structural Characterization

2.4.1.1 X-Ray Diffraction

X-ray diffraction is the primary and major analytical technique for determining the phase of any synthesized material and to reveal information about the crystallographic structure, chemical composition and physical properties of the samples. If X-rays are incident on samples having the same order of wavelength (λ) as that of the atomic dimensions, then the radiations emitted by the electrons can have a definite phase relations with one another. These radiations may, therefore, go through constructive or destructive interference producing maxima or minima in certain directions. When emitted or scattered waves differ by an integral multiple number of wavelengths ($n\lambda$) for a certain angle it gives constructive interference. Emitted or scattered waves follow the Bragg's relation [40] $2d_{hkl}\sin\theta = n\lambda$ as shown in Fig. 2.9(a), where, n is an integer, θ is the angle of incidence and d_{hkl} is distance between two consecutive lattice planes.

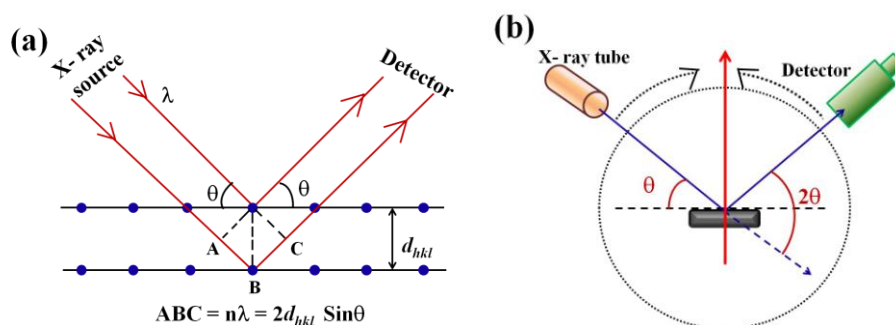


Figure 2.9 Schematic representation of (a) Bragg's law (b) XRD measurement technique.

2.4.1.2 Laboratory based X – ray sources

Powder diffraction using laboratory based X-ray source was used primarily for phase identification of a crystalline material and can provide information on unit cell dimensions using the Bragg's law. The X-Ray diffraction measurements were done with PANalytical X-PERT PRO diffractometer [41]. X-ray diffractometers consist of three basic elements: an X-ray tube, a sample holder and an X-ray detector (shown in Fig. 2.9(b)). This diffractometer works in the Bragg – Brentano geometry with a θ : θ arrangement i.e. the

sample stage is fixed while the tube rotates at a rate of $-\theta^\circ/\text{min}$ and the detector rotates at a rate of $+\theta^\circ/\text{min}$. We have used $\text{Cu}_{K\alpha 1}$ of wavelength 1.5405 \AA at an accelerating voltage of 45 kV and 40 mA current. These X-rays have sufficient energy to penetrate the solids and allow analysing their internal structures. We have used PIXEL detector with low signal to noise ratio.

2.4.1.3 Synchrotron sources for X – ray diffraction

Synchrotron radiation occurs when the charged particles (electrons) are moving with a speed close to the speed of light under the influence of an accelerating field in a curved path or orbit. This radiated energy is proportional to the fourth power of the particle speed and inversely proportional to the square of the radius of the path. The electrons are then injected into a storage ring (an ultrahigh vacuum ring on a closed loop), in which they circulate a vast number of times producing synchrotron radiation, but without gaining further energy. The radiation is projected at a tangent to the electron storage ring and captured by the beamlines which may originate at *bending magnets*. At the end of the beamline, there is the experimental end section, where samples are placed in the line of the radiation and detectors are positioned to measure the resulting diffracted radiation.

We have performed low temperature synchrotron XRD measurement for the structural studies of our samples at Indian beam line BL-18B, Photon Factory, KEK, Japan where the PF ring achieves a final energy around 2.5 GeV. The four circle goniometer is used for powder diffraction measurement in ambient as well as in low and high temperature. For low temperature a cryostat is mounted on the goniometer. Typical scans are in $\theta:2\theta$ arrangement i.e. the source is fixed while the sample stage rotates at a rate of θ°/min and the detector rotates at a rate of $2\theta^\circ/\text{min}$. Low temperature measurements down to 10 K can be performed with the sample in He atmosphere. The usable energy of the synchrotron X-ray radiation is 7 to 20 keV that means available wavelength range is around $0.6 - 1.7 \text{ \AA}$. Point detector or 100 K 2D Pilatus detector can be used for data collection.

Synchrotron sources have a number of advantages over conventional laboratory based X - ray sources:

1. Synchrotron radiation is used because of its high flux and brightness. High intensity photon beam allows fast experiments. The intensity produced by synchrotron radiation is

many orders of magnitude more than that of the X– rays generated in conventional X – ray tubes.

2. Highly collimated photon beam is produced by a small angular divergence of the beam and small size source.
3. The source is highly stable and it is possible to tune the wavelength (or energy) to the value required for a particular experiment.

2.4.1.4 The Rietveld refinement technique

The Rietveld refinement technique has been used in this thesis for the refinement of both X – ray as well as neutron data in order to extract structural information (including the magnetic structure) of the NW samples [42, 43]. This method refines user – selected parameters to minimize the difference between an experimental pattern (observed data) and a model based on the hypothesized crystal structure and instrumental parameters (calculated pattern). Thus, this method can only refine a structure and is not intended for structure solution. The initial structural model must be identified before starting the refinement. We have used the International Centre for Diffraction Data (ICDD) database [44] for obtaining the initial starting model of our samples and the FullProf Suite [45] for Rietveld refinement.

The Rietveld method refines a structure by minimizing the quantity through a Newton – Raphson algorithm.

$$\chi^2 = \sum_{i=1}^n w_i \{y_i - y_{c,i}(\alpha)\}^2$$

Here, y_i is the observed intensity at a certain 2θ , $y_{c,i}$ is the calculated intensity at the same angle, $w_i = 1/y_i$ (weighting factor), $\alpha = (\alpha_1 \alpha_2 \dots \alpha_p)$ are the parameters to be refined. The

minimum necessary condition to be satisfied is $\frac{\partial \chi^2}{\partial \alpha} = 0$. A Taylor expansion of $y_{c,i}(\alpha)$ around

α allows one to convert the problem into determination of the shifts ($\delta\alpha$) that are solutions of a linear system of equations. The calculated shifts of the parameters are then added to the starting parameters. It gives rise to a new set of parameters which can then be used for a new cycle. This process is iterated until a convergence criterion is satisfied and a good agreement with the measured X – ray pattern is achieved.

The goodness of fit can be estimated from the difference pattern and also from the reliability (R) factors. The R – factors are defined as follows:

1. *Profile R-factor* (R_p): $R_p = \frac{\sum_i |y_{io} - y_{ic}|}{\sum_i y_{io}}$
2. *Weighted profile R-factor* (R_{wp}): $R_{wp} = \left[\frac{\sum_i w_i (y_{io} - y_{ic})^2}{\sum_i w_i y_{io}^2} \right]^{\frac{1}{2}}$
3. *Expected R-factor* (R_{exp}): $R_{exp} = \left[\frac{N - P + C}{\sum_i w_i y_{io}^2} \right]^{\frac{1}{2}}$

Here, N is the total number of points used in the refinement, P is the number of refined parameters, C is the number of constraint functions so that $N-P+C$ is the number of degrees of freedom.

4. *Goodness of fit parameter* (χ^2): $\chi^2 = \frac{\sum_i w_i (y_{io} - y_{ic})^2}{N - P + C} = \left(\frac{R_{wp}}{R_{exp}} \right)^2$

The crystallographic structural investigation on hydrothermally grown NWs was done with synchrotron X-ray powder diffraction measurement at wavelength 0.7934 Å using Indian beam line, at photon Factory, Japan. Fig. 2.10 (a)–(d) shows the powder diffraction pattern of NWs of LCMO-0.3, LCMO-0.5, LSMO-0.3 and LSMO-0.5 samples, respectively, with a typical profile fit at room temperature. The profiles are refined in the orthorhombic structure with $Pnma$ space group for LCMO-0.3 and LCMO-0.5 samples using Rietveld refinement method with FullProf Suite software [45-47]. The XRD patterns of LSMO-0.3 and LSMO-0.5 sample are fitted by rhombohedral structure of space group $R\bar{3}c$ and tetragonal structure of $I4/mcm$, respectively. The lattice parameters, cell volumes, atomic positions and reliability factors obtained from Rietveld refinement of the XRD pattern of the NWs at 300 K are given in Table 2.2. For LSMO-0.5 and LSMO-0.3 samples, there are small amount of impurity of $\text{La}(\text{OH})_3$ estimated to be < 5 %. It was noticed that despite heating the samples for prolonged time, the amount of impurity ($\text{La}(\text{OH})_3$) remains constant [27]. Comparison of lattice parameters of NWs with bulk data reported in Inorganic Crystal Structure Database (ICSD) pattern (LCMO-0.3—Ref. code: 01-089-8075, LCMO-0.5—Ref. code: 01-089- 0793, LSMO-0.5—Ref. code: 01-089-0786, LSMO-0.3— Ref. code: 00-051-0409) shows that contraction of lattice parameters occurs on size reduction of the nanostructures to 1D nanostructure. The reduction of cell volume per formula unit is around 6 % compared to its

bulk form. Cell volume contraction on size reduction has already been reported in nanocrystalline particles of manganite [48-51]. More information about the detailed structure and growth directions of the NWs were obtained by structural simulation through Java Electron Microscopy Software (JEMS) software discussed in the section 3.4 of the chapter no. 3.

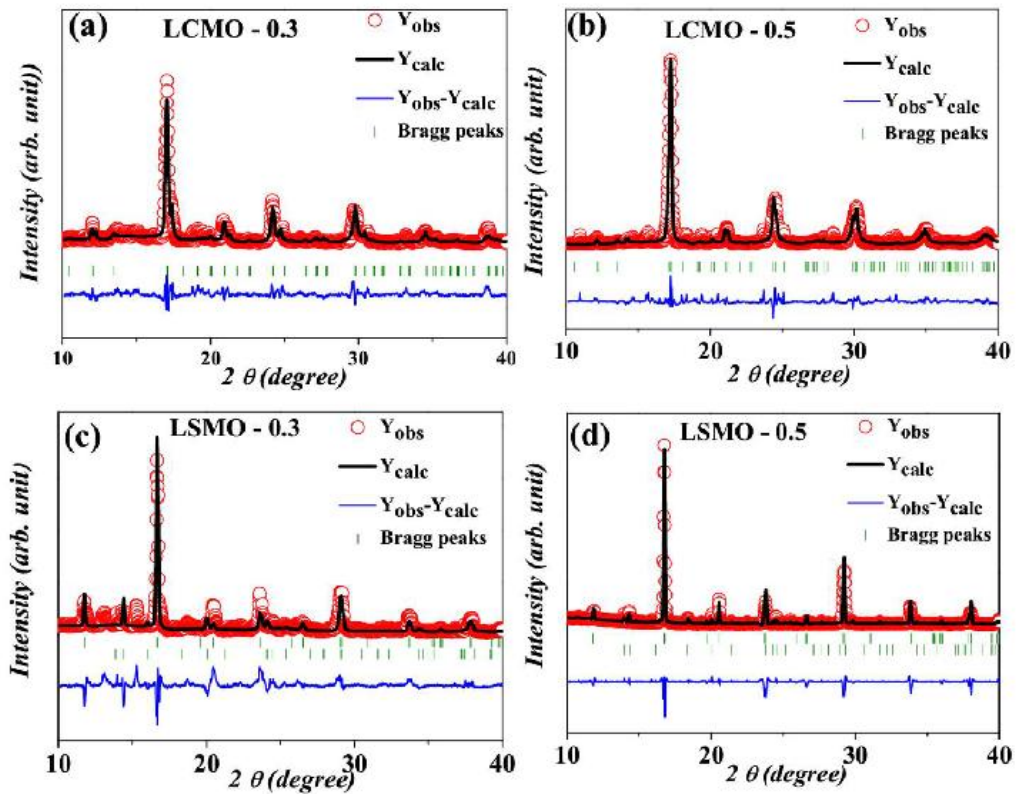


Figure 2.10 The Rietveld refinement of Synchrotron XRD data for (a) LCMO-0.3, (b) LCMO-0.5, (c) LSMO-0.3 and (d) LSMO-0.5 nanowires, respectively. The experimental data points are indicated by open circles, the calculated and difference patterns are shown by solid lines. The Bragg positions of the reflections are indicated by vertical lines below the pattern. For LSMO-0.5 and LSMO-0.3 samples, there are small amount of impurity of $\text{La}(\text{OH})_3$ estimated to be <5 %. $\text{La}(\text{OH})_3$ (impurity) is fitted with the $p63/m$ phase; $a = b = 6.5368 \text{ \AA}$ and $c = 3.8550 \text{ \AA}$ at 300 K for LSMO-0.5 and LSMO-0.3 samples.

Table 2.2 Lattice parameters, cell volumes, atomic positions and reliability factors from the Rietveld refinements of $\text{La}_{1-x}\text{A}_x\text{MnO}_3$; (where A = Ca, Sr; $x = 0.3$ and 0.5) at 300 K.

Compound	$\text{La}_{0.7}\text{Ca}_{0.3}\text{MnO}_3$	$\text{La}_{0.5}\text{Ca}_{0.5}\text{MnO}_3$	$\text{La}_{0.7}\text{Sr}_{0.3}\text{MnO}_3$	$\text{La}_{0.5}\text{Sr}_{0.5}\text{MnO}_3$
Space group	<i>Pnma</i>	<i>Pnma</i>	<i>R-3c</i>	<i>I4/mcm</i>
a (Å)	5.2943(4)	5.3509(4)	5.4867(9)	5.4489(4)
b (Å)	7.5936(6)	7.4685(1)	5.4867(9)	5.4489(4)
c (Å)	5.3671(3)	5.2850(1)	13.3747(7)	7.7415(7)
V (Å ³)	215.77(2)	211.21(1)	348.68(5)	229.85(3)
La/Sr or La/Ca				
x	0.0195(3)	0.0122(1)	0	0
y	0.25	0.25	0	0.5
z	0.9943(1)	0.5087(1)	0.25	0.25
B_{iso}	0.6537(8)	0.9729(1)	0.5332(3)	0.7488(1)
Mn				
x	0	0	0	0
y	0	0	0	0
z	0.5	0	0	0
B_{iso}	0.3187(2)	0.6196(1)	0.85478(1)	0.7033(7)
O/O1				
x	0.3884(6)	0.4522(1)	0.8688(2)	0
y	0.25	0.25	0	0
z	0.0424(8)	0.5391(1)	0.25	0.25
B_{iso}	0.3074(8)	0.8161(2)	0.4704(2)	0.3701(4)
O2				
x	0.2593(2)	0.2908(9)	--	0.7797(4)
y	0.0288(4)	0.0076(5)	--	0.3741(4)
z	0.6699(2)	0.1806(2)	--	0
B_{iso}	0.8865(7)	0.5288(2)	--	0.9627(2)
χ^2	5.41	5.62	6.12	7.57
R_p (%)	13.0	9.2	11.3	12.7
R_{wp} (%)	16.4	13.46	17.59	18.0
R_{exp} (%)	7.07	5.68	7.11	6.54

2.4.1.5 Neutron diffraction

Neutron diffraction is often used to determine the magnetic structure of the samples. Neutron has zero charge, spin $\frac{1}{2}$ and a magnetic moment of $-1.913 \mu_N$ where μ_N is nuclear magneton. The zero electric charge helps the neutrons in penetrating to a greater distance. The zero electric charge of neutrons along with a magnetic moment makes them a useful technique to detect atomic magnetic moments without any interference from Coulomb interaction. The neutron – sample interactions have two major parts, such as nuclear scattering and magnetic scattering. In the isotropic nuclear scattering, the neutrons interact with the nuclei of the

target via short range ($\sim 10^{-12}$ cm) nuclear forces. The magnetic scattering arises from the electromagnetic interaction of the magnetic moment of neutrons with the electrons.

The same Bragg's law ($2d_{hkl}\sin\theta = n\lambda$) which is the main principle of X – ray diffraction (written in Section 2.4.1.1) also governs neutron diffraction. In XRD, λ is always fixed and θ is variable. Neutron diffractometer gives us two options: (i) to keep λ constant and vary θ or (ii) to keep θ constant and vary λ .

1. *Constant wavelength diffractometer*: This is basically an extension of the X – ray powder diffractometer. However, in this method, magnetic refinements are performed and structural parameters can also be determined with more precision than that from XRD data (Fig.2.11 (a)).
2. *Time – of – flight diffractometer*: This method takes benefit of the full “white” spectrum. Adding the two equations $\lambda = h/mv$ and $v = L/t$ (where, m and v are the mass and the velocity of the neutron respectively, L is the length of flight path and t is the time of flight of neutron), we get, $\lambda = ht/mL = 2d\sin\theta$, so that, $t = (2mL d\sin\theta / h)$. L is a constant for the detector and h and m are also fixed so that $t \propto d$. Thus, the d – spacings are obtained by measuring the time of arrival of the diffracted neutrons at the detector. Neutrons are separated in energy after travelling over a constant path length (L). This allows neutrons of many different energies and wavelengths to be used for the experiment. Typically, many separate detectors are used to record the counts and in each of them are added to provide the total intensity.

Schematic representations of the two kinds of neutron diffractometers are depicted in Fig. 2.11.

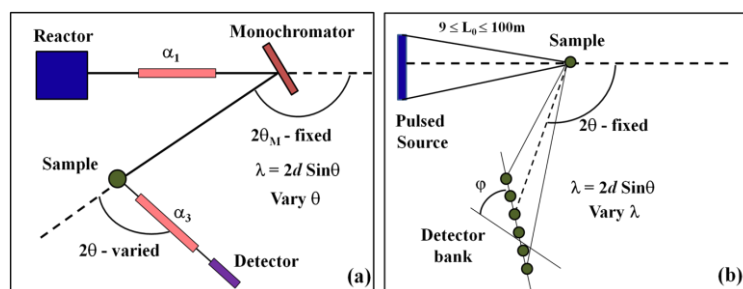


Figure 2.11 Schematic representation of (a) Constant wavelength and (b) Time of flight neutron diffractometer.

The comparative advantages and disadvantages of XRD data and neutron data are listed below.

1. Neutron beams are highly penetrating (penetration depth \sim cm) so larger samples are required (sample volume $\sim 1 \text{ cm}^3$) whereas X- rays are highly attenuated by matter (penetration depth \sim microns to mm) so smaller amount of sample is needed.
2. For neutrons, the nuclear scattering cross – section is governed by a short range nuclear interaction which is independent of atomic number of electrons (Z). This permits one to locate lighter atoms even in the presence of heavier atoms. However, in case of X – ray scattering, the scattering amplitude is proportional to Z in an atom/ion and the diffracted intensities are dominated by heavier atoms.
3. As neutrons are scattered from the nuclei, the neutron scattering factors are independent of $\sin\theta/\lambda$ and do not decrease with 2θ as shown in Fig. 2.12. Thus, the intensities of the high angle peaks are more reliable and thus more reliable structure is determined. On the other hand, X – rays are scattered by electrons and the form factor decreases with $\sin\theta/\lambda$ (Fig. 2.12) and the diffracted intensity falls off at higher scattering angles.

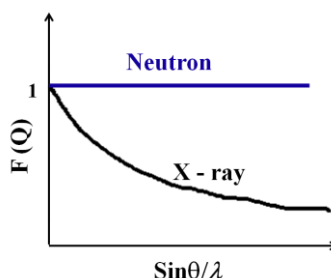


Figure 2.12 Structure factor vs. $\sin\theta/\lambda$ of neutron and X – ray.

4. Neutrons have an intrinsic magnetic moment and hence it can be used to determine ordered magnetic structures. But, X – rays have no magnetic moment.

Temperature dependent (3-300 K) neutron diffraction (ND) experiments on $\text{La}_{0.5}\text{Sr}_{0.5}\text{MnO}_3$ NWs (in powder form) reported in chapter 6 were carried out using the multi-position-sensitive detector-based focusing crystal diffractometer set up by UGC-DAE Consortium for Scientific Research Mumbai Centre at the National Facility for Neutron Beam Research (NFNBR), Dhruva reactor (beam port TT-1015), Mumbai (India) at a wavelength of 1.48 \AA . ND measurements on $\text{La}_{0.5}\text{Sr}_{0.5}\text{MnO}_3$ bulk sample were performed at the Dhruva reactor (beam port T-1013) in Bhabha Atomic Research Centre, Mumbai, India at a wavelength of 1.244 \AA and in the temperature range 6–300 K [52-53]. Temperature variation of neutron powder diffraction measurement was done in a Cryogenics made of cryogen-free magnet system by loading the samples in vanadium can of height 35 mm and diameter 6 mm. The

scattering angular range covered was $2\theta = 3^\circ$ to 140° with a step size of 0.05° . This spectrometer has a flux of 7×10^7 neutrons/cm²/sec and a beam size of 1.5 cm X 2.5 cm. There are total of 5 detectors which allow the Q range to vary from 0.4 \AA^{-1} to 7.4 \AA^{-1} . The typical resolution is around $\Delta d/d \approx 0.3\%$. The ND data were processed with help of the Rietveld refinement program of FullProf Suite software [45].

As an example, we have shown the ND pattern of $\text{La}_{0.5}\text{Sr}_{0.5}\text{MnO}_3$ NWs taken at 300 K in Fig.2.13. The red curve shows the experimental data, the black curve gives the calculated pattern and the blue curve gives the difference pattern. The positions of the Bragg peaks are also denoted by green lines. The structural as well as magnetic Bragg peaks are shown, but since the material is ferromagnetic, there is no appearance of any super-lattice peaks.

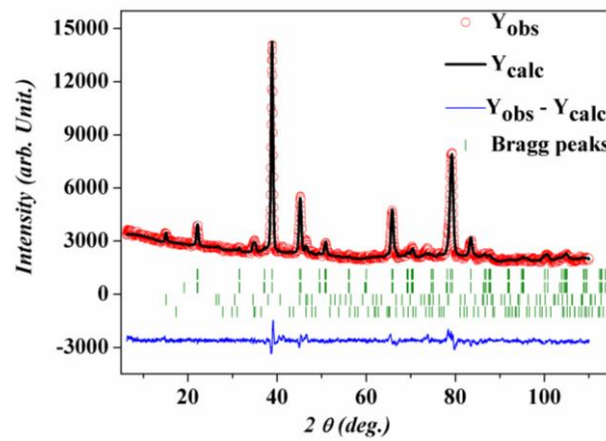


Figure 2.13 Neutron diffraction pattern (along with the fits) for $\text{La}_{0.5}\text{Sr}_{0.5}\text{MnO}_3$ nanowires taken at $T = 300 \text{ K}$. The difference pattern and the position of the structural and magnetic Bragg peaks are also shown. The R – factors obtained were $R_p = 2.80\%$, $R_{wp} = 3.86\%$, $R_{exp} = 1.98\%$.

2.4.1.6 Scanning Electron Microscope

SEM [54] extensively used form of electron microscope usually provides important information regarding the morphology, topography, composition of the samples, size distribution of NWs, spatial distributions, density, NW alignment, etc.

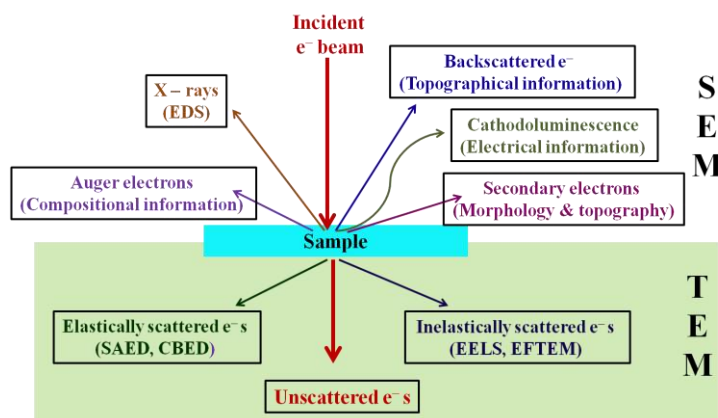


Figure 2.14 Schematic representation of the interaction of incident electron beam with sample.

In SEM, monochromatic electron beams emitted from an electron gun are accelerated and focused by combination of different electromagnetic lens to form a sharply defined electron beam. This electron beam falls on the sample and penetrates the sample to a depth of a few microns, depending on the accelerating voltage and the density of the sample. Then they eject electrons from the sample due to electron-sample interaction which bring out different information producing from different part of sample as shown schematically in Fig. 2.14. Ejected signals consist of secondary electrons; back scattered electrons; characteristic X-rays; Auger electrons and transmitted electrons. Low energy secondary electrons are produced due to inelastic scattering of electron beam with sample atom and back scattered electrons are due to elastic collision. Secondary electrons are used for observing the morphology and topography of samples and backscattered electrons are used to see the contrasts in composition in multiphase samples. X-ray is created by inelastic collisions of the incident electrons with electrons in separate orbital's (shells) of atoms in the sample. These electrons are collected by different detectors and amplified by various types amplifier. The most popular detector in SEM is the Everhart-Thornley detector. It is made of a Faraday cage which accelerates the electrons towards a scintillator. This sequentially produces a current, which is directed towards a photomultiplier and the amplified signal is read on the monitor.

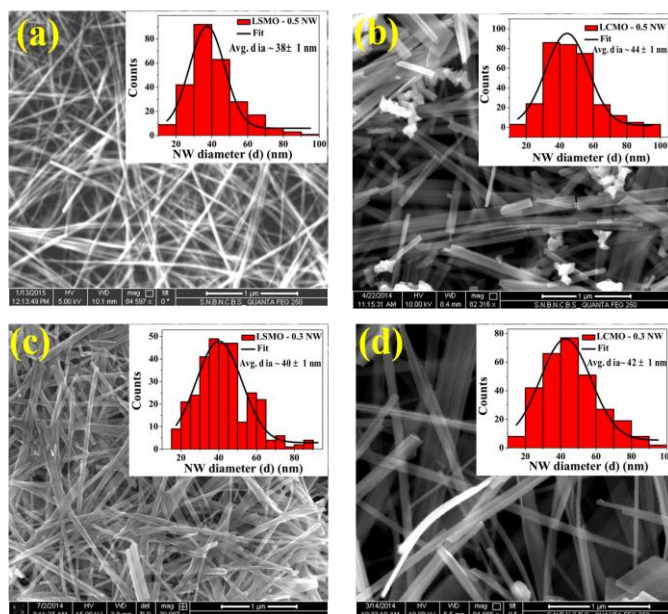


Figure 2.15 FESEM image of ensemble of nanowires (NWs) (a) LSMO-0.5 (inset showing histogram of average diameter ~ 38 nm) (b) LCMO-0.5 (inset showing histogram of average diameter ~ 44 nm) (c) LSMO-0.3 (inset showing histogram of average diameter ~ 40 nm) (d) LCMO-0.3 (inset showing histogram of average diameter ~ 42 nm).

The surface morphology of the ensemble of NWs is provided by Field emission gun scanning electron microscopy (FESEM) (FEI, Quanta FEG 250, 30 kV operating voltage). Fig. 2.15 shows the microstructures of four different compositions (LSMO-0.5, LCMO-0.5, LSMO-0.3 and LCMO-0.3) of ensembles of NWs. The inset shows the histogram of uniform size distribution of the NWs. Images are taken with an operating voltage of 5 - 15 kV. The average length is around 1-10 μm and diameter ~ 40 nm.

2.4.1.7 Energy dispersive X-ray Analysis

Energy-dispersive X-ray analysis (EDAX) is an analytical technique used for the elemental analysis or chemical characterization of a specimen. EDAX utilizes the characteristic spectrum of X-rays that is emitted by a specimen following initial excitation of an inner shell electron to a vacant higher energy level by the high energy electron beam. The emitted X-rays are represented as K, L and M lines depending on the transition to the definite shell of K, L or M. Greek letter α and β subscribed to an X-ray line (K or L or M) to differentiate the transition from different high energy levels to particular low energy levels like K, L and M.

In EDAX, highly localized information about the elemental composition of the sample can be obtained, with the spatial resolution determined primarily by the probe size. Here, we have used FESEM from FEI, Quanta FEG 250, with a maximum operating voltage of 30 kV.

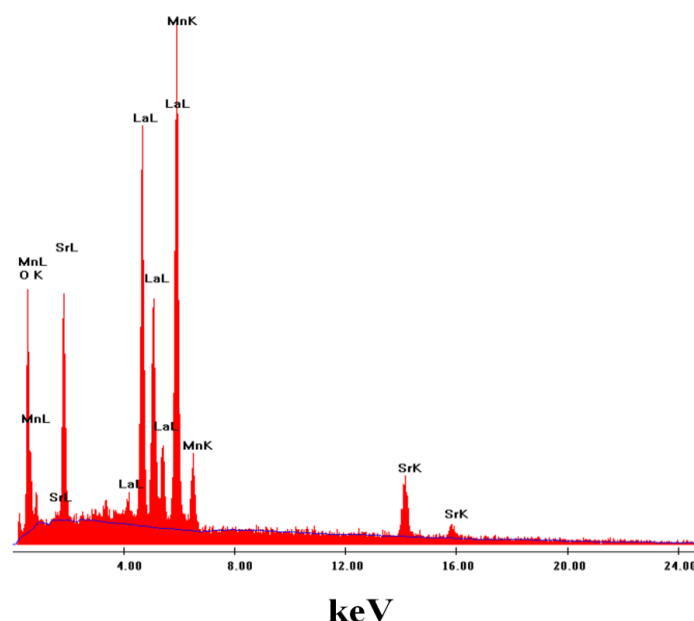


Figure 2.16 EDAX data of La_{0.5}Sr_{0.5}MnO₃ nanowires.

In this thesis, EDAX is used to check the presence of compositional elements and stoichiometry of all the grown NWs. Here, in Fig. 2.16, we have shown EDAX data of only one composition i.e. La_{0.5}Sr_{0.5}MnO₃ NWs. From the EDAX data, it is confirmed that all the compositional element of La_{0.5}Sr_{0.5}MnO₃ NWs are present without having any impurity elements. We also found that the atomic percentage ratio (La: Sr): Mn: O is approximately 1: 1: 3 which is the desired composition. However, as the difference in binding energy (≈ 4 eV) of electrons in Mn³⁺ and Mn⁴⁺ is less than the resolution (≈ 100 eV) of the EDAX, it is difficult to quantify this nominal mix valency (Mn³⁺: Mn⁴⁺) from EDAX. We have tried to found out the mixed valency at Mn site from the EELS measurements which will be discussed in the section 3.2 of the chapter no 3.

2.4.1.8 Transmission Electron Microscope

Transmission Electron Microscope (TEM) is a multipurpose instrument which uses diffraction of electrons to image specimen and where transmitted electrons through the sample are used to collect information about internal structure of the samples with a wide

range of imaging and analytical methods [54]. In TEM, high energetic electron beam (wavelength $< 1 \text{ \AA}$) is collimated from the source and condensed by the condenser lens and passed through a thin ($< 100 \text{ nm}$) slice of specimen. A fraction of the electrons in the beam get either elastically or inelastically scattered. The transmitted beam through the thin specimen is focused on a back focal plane of the objective lens (which is the first lens below the specimen), resulting in an electron diffraction pattern. The diffraction pattern at the back focal plane undergoes inverse Fourier Transform and magnified image is created. The transmitted electrons are used to visualize with sub-nanometer resolution and signal is detected by the detectors. Reflected signals are generally used to take information in SEM and that of transmitted signals are in TEM as shown in Fig. 2.14.

There are some standard methods to prepare the TEM samples depending on the nature of samples. Thin film sample is prepared by cutting, mechanical grinding and polishing, dimple grinding and finally ion milling. To image powder samples, a very dilute solution of the powder in ethanol or acetone is dispersed after sonication on to carbon coated Cu grid or lacey grid. The sample on Cu grid is then mounted on TEM sample holder for imaging. Different signal source from the sample brings different information as listed below:

HRTEM: *Phase contrast imaging or high resolution TEM (HRTEM) imaging* mode can show structures at the atomic scale, lattice fringes and hence can be used to look at the arrangement of atoms in a crystal. Here, the aperture in the back focal plane is larger and multiple beams are allowed to contribute to the final image. One or more diffracted beams impinge with the directly transmitted beam to form the image and the image contrast depends on the relative phases of the various beams. HRTEM, thus, requires interference of the unscattered and the scattered beams.

SAED: As a diffraction technique, *Selected Area Electron Diffraction (SAED)* can be used to identify crystal structures, crystal orientation and examine crystal defects. It is analogous to X-ray diffraction, but unique in that area, as small as several hundred nanometres in size can be observed, whereas in X-ray diffraction typically samples areas are several centimeters in size.

SAED is referred to as "selected" because one can easily select from which part of the specimen to obtain the diffraction pattern. Located below the sample holder on the TEM column, a selected area aperture (a thin strip of metal) can be inserted into the beam path that will block the beam. It is used to block the entire electron beam except for the small fraction passing through one of the holes; by moving the aperture hole to the section of the sample

required to examine. This particular area is “selected” by the aperture and only this part will contribute to the SAED image on the screen.

The TEM image (taken in 200 kV Tecnai G² TF-20) of a single NW of La_{0.5}Sr_{0.5}MnO₃ sample (diameter ~ 45 nm) is shown in Fig. 2.17(a). The magnification is taken around 300 – 400kX for HRTEM imaging and up to 100kX for SAED pattern. The single crystalline nature of the NWs was confirmed from the SAED pattern and HRTEM images shown in Fig. 2.17(b) and 2.17 (c). The lattice spacing is around 3.11 Å and (hkl) values are estimated from HRTEM data which corroborates with the SAED data. From that we can infer that NWs fabricated are of pure phase and single crystalline in nature.

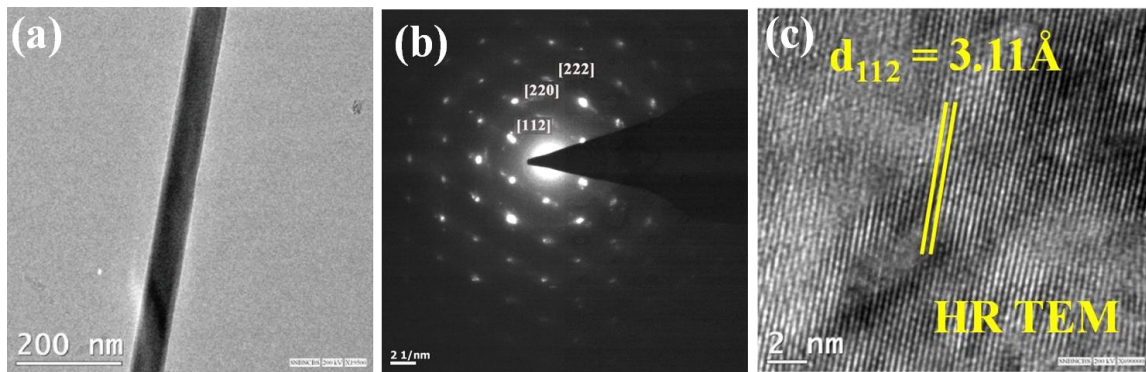


Figure 2.17 (a) Single nanowire La_{0.5}Sr_{0.5}MnO₃ sample of diameter around ~ 45 nm, (b) the selected area diffraction pattern taken with a Transmission Electron Microscope and (c) HRTEM image shows the single crystalline nature of La_{0.5}Sr_{0.5}MnO₃ nanowires.

Indexing of electron diffraction pattern: Ratio-technique

From Bragg’s law, $2d_{hkl}\sin\theta = \lambda$, for small diffraction angle θ , $\sin\theta \approx \theta$ and hence, $2d_{hkl}\theta = \lambda$. Again, if R be the distance of diffracted spot of interest from the central spot and L be the distance between screen and the sample as shown in Fig. 2.18 then, $\tan 2\theta = R/L \approx$ (for small angle of diffraction). Thus, $Rd_{hkl} = L\lambda$, or, $R = L\lambda (1/d_{hkl})$. One can write, $d_1/d_2 = R_2/R_1$. If the camera constant ($L\lambda$) is known, one can easily find out the interplanar spacing. Thus, by measuring R and calculating the corresponding interplanar spacing (d_{hkl}), the diffraction pattern can be indexed.

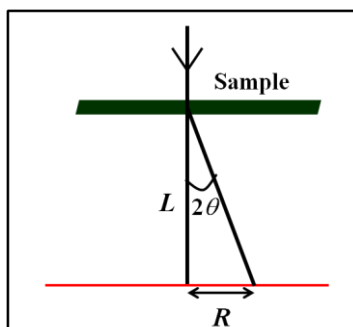


Figure 2.18 Camera lengths (L) in the presence of imaging lenses.

Another way to index different plane is to measure the distance R of diffracted spot from central spot from SAED patterns. This represents reciprocal of the distance of interplanar spacing (d_{hkl}). Match this interplanar spacing d_{hkl} with d_{hkl} value of allowed diffraction planes from XRD analysis and this will give the (hkl) value for that particular spot in SAED pattern as shown in Fig. 2.17(b).

2.5 Conclusion

In this thesis, we have successfully grown the high-quality single crystalline NWs of family of perovskite oxide manganite $\text{La}_{1-x}\text{A}_x\text{MnO}_3$; (where $\text{A} = \text{Ca}, \text{Sr}$; $x = 0.3$ and 0.5). Here we have shown how to tailor shape and size of nanostructures with controlled composition and stoichiometry by tuning the growth parameters in hydrothermal synthesis. Mechanism of shape and size tuning and composition control issues followed by a phase diagram have been proposed in this thesis. It has been shown that amount of the mineralizer (KOH), temperature and growth time are the most important parameters which controls the shape, size of the nanostructures. Analysis of crystallographic structural data, HRTEM and SAED data also shows that the grown NWs are of very pure and single phase. Crystal shape/size tuning of any composition of perovskite oxide family of manganite may provide a new perspective and this knowledge base may help in shape/size tailoring and composition of many other perovskite oxides which are important for technological point of view and could be used for further studying of different important physical and chemical related applications in future.

Bibliography:

- [1] A. K. Raychaudhuri, *Nanolithography and Nanomanipulation, the Chemistry of Nanomaterials Synthesis Properties and Applications*, vol. 2 of edited by C. N. R. Rao, A. Muller, and A. K. Cheetham, Wiley-VCH, Berlin, Germany, 2004.
- [2] T. Sarkar, A. K. Raychaudhuri, A. K. Bera and S. M. Yusuf, *New J. Phys.*, **12**, 123026 (2010).
- [3] S. Chandra, A. I. Figueroa, B. Ghosh, A. K. Raychaudhuri, M. H. Phan, P. Mukherjee and H. Srikanth, *Physica B: Condensed Matter*, **407**, 175–178 (2012).
- [4] Y. Chen, J. Li, Y. Han, X. Yang and J. Dai, *J. Cryst. Growth*, **245**, 163–170 (2002).
- [5] J. R. Heath and F. K. LeGoues, *Chemical Physics Letters*, **208**, 263–268 (1993).
- [6] D. Zhu, H. Zhu and Y. H. Zhang, *J. Phys.: Condens. Matter*, **14**, L519–L524, (2002).
- [7] S. Datta, A. Ghatak and B. Ghosh, *J. Mater. Sci.*, **51**, 9679–9695 (2016).
- [8] S. Datta, S. Chandra, S. Samanta, K. Das, H. Srikanth and B. Ghosh, *Journal of Nanomaterials*, vol. **2013**, Article ID 162315, 6 pages, 2013. doi:10.1155/2013/162315.
- [9] S. Datta and B. Ghosh, *AIP Conference Proceedings* **1665**, 050045 (2015); doi: 10.1063/1.4917686.
- [10] A. Rabenau, *Angew. Chem.*, (English Ed.), **24**, 1026–1040 (1985).
- [11] K. Byrappa and M. Yoshimura, *Handbook of Hydrothermal Technology, A Technology for Crystal Growth and Material Processing*, Noyes, New Jersey, 2001.
- [12] R. Roy, *Science*, **238**, 1664 (1987)
- [13] X. Z. Chen, Z. C. Qiu, J. P. Zhou, G. Zhu, X. B. Bian and P. Liu, *Mater. Chem. Phys.*, **126**, 560–567 (2011).
- [14] T. J. Zhu, X. Chen, Y. Q. Cao and X. B. Zhao, *J. Phys. Chem. C*, **113**, 8085 (2009).
- [15] Q. Zhang, S. J. Liu and S. H. Yu, *J. Mater. Chem.*, **19**, 191–207 (2009).
- [16] J. Zhang, F. Huang and Z. Lin, *Nanoscale*, **2**, 18–34 (2010).
- [17] K. Huang, L. Yuan and S. Feng, *Inorg. Chem. Front.*, **2**, 965–981 (2015).
- [18] K. K. Caswell, C. M. Bender and C. J. Murphy, *Nano Lett.*, **3**, 667–669 (2003).
- [19] Y. Guyodo, A. Mostrom, R. L. Penn and S. K. Banerjee, *Geophys. Res. Lett.*, **30**, 1512–1515 (2003).
- [20] J. Zhang, Z. Lin, Y. Lan, G. Ren, D. Chen, F. Huang and M. Hong, *J. Am. Chem. Soc.*, **128**, 12981–12987 (2006).

- [21] C. Li, T. Bai, F. Li, L. Wang, X. Wu, L. Yuan, Z. Shi and S. Feng, *Cryst. Eng. Comm.*, **15**, 597–603 (2013).
- [22] G. Liu, H. Gui, Y. J. Pan, Y. Q. Yang, G. Q. Lu and H. M. Cheng, *Chem. Rev.*, **114**, 9559–9612 (2014).
- [23] C. Ribeiro, C. M. Barrado, E. M. Camargo, E. Longo and E. R. Leite. *Chem. Eur. J.*, **15**, 2217–2222 (2009).
- [24] Y. Wang, J. Zhang, Y. Yang, F. Huang, J. Zheng, D. Chen, F. Yan, Z. Lin and C. Wang, *J. Phys. Chem. B*, **111**, 5290–5294 (2007).
- [25] A. Querejeta, A. Varela, M. Parras, F. del Monte, M. Garcia-Hernandez and J. M. Gonzalez-Calbet, *Chem. Mater.*, **21**, 1898–1905 (2009).
- [26] D. J. Miller, S. B. Hawthorne, A. M. Gizir and A. A. Clifford, *J. Chem. Eng. Data*, **43**, 1043–1047 (1998).
- [27] J. J. Urban, L. Ouyang, M. H. Jo, D. S. Wang and H. Park, *Nano Lett.*, **4**, 1547–1550 (2004).
- [28] J. Spooren, R. I. Walton and F. Millange, *J. Mater. Chem.*, **15**, 1542–1551 (2005).
- [29] J. Spooren and R. I. Walton, *J. Solid. State. Chem.*, **178**, 1683–1691 (2005).
- [30] C. Li, T. Li, B. Wang and H. Yan, *J. Cryst. Growth*, **295**, 137–140 (2006).
- [31] S. Liang, F. Teng, G. Bulgan and Y. Zhu, *J. Phys. Chem. C*, **111**, 16742–16749 (2007).
- [32] P. Chai, X. Liu, Z. Wang, M. Lu, X. Cao and J. Meng, *Cryst. Growth Des.*, **7**, 2568–2575 (2007).
- [33] J. Spooren, A. Rumplecker, F. Millange and R. I. Walton, *Chem. Mater.*, **15**, 1401–1403 (2003).
- [34] R. L. Penn and J. F. Banfield, *Science*, **281**, 969–971 (1998).
- [35] W. Lv, W. He, X. Wang, Y. Niu, H. Cao, J. H. Dickerson and Z. Wang, *Nanoscale*, **6**, 2531–2547 (2014).
- [36] G. Cao (2004) Nanostructures & nanomaterials: synthesis, properties, & applications. Imperial College Press, London.
- [37] S. G. Kwon and T. Hyeon, *Acc. Chem. Res.*, **41**, 1696–1709 (2008).
- [38] K. Zhu, Y. Cao, X. Wang, L. Bai, J. Qiu and H. Ji, *Cryst. Eng. Comm.*, **14**, 411–416 (2012).
- [39] B. Liu, B. Hu and Z. Du, *Chem. Commun.*, **47**, 8166–8168 (2011).
- [40] B. D. Cullity, S. R. Stock; *Elements of X-ray Diffraction*, Prentice Hall, 2001.
- [41] PANanalytical B. V., Lelyweg 1, 7602 EA Almelo, The Netherlands.

- [42] H. M. Rietveld, *Acta Crystallogr.*, **22**, 151 (1967)
 - [43] H. M. Rietveld, *J. Appl. Crystallogr.*, **2**, 65 (1969)
 - [44] <http://www.icdd.com>
 - [45] <http://www.ill.eu/sites/fullprof/>
 - [46] S. J. Hibble, S. P. Cooper, A. C. Hannon, I. D. Fawcett and M. Greenblatt, *J. Phys. Condens. Matter*, **11**, 9221–9238 (1999).
 - [47] P. G. Radaelli, D. E. Cox, M. Marezio and S. W. Cheong, *Phys. Rev. B*, **55**, 3015–3023 (1997).
 - [48] J. C. Loudon, N. D. Mathur and P. A. Midgley, *Nature*, **420**, 797–800 (2002).
 - [49] T. Sarkar, B. Ghosh, A. K. Raychaudhuri and T. Chatterji, *Phys. Rev. B*, **77**, 235112–235118 (2008).
 - [50] T. Sarkar, B. Ghosh and A. K. Raychaudhuri, *J. Nanosci. Nanotechnol.*, **7**, 2020–2024 (2007).
 - [51] B. Ghosh, V. Siruguri, A. K. Raychaudhuri and T. Chatterji, *J. Phys. Condens. Matter*, **26**, 025603–025611 (2014).
 - [52] S. K. Paranjpe and S. M. Yusuf, *Neutron News*, **13**, 36–38. (2002).
 - [53] V. Siruguri, S. M. Yusuf and V. C. Rakhecha, page 4–5 *Neutron News*, **11**, 4–5 (2000).
 - [54] R. F. Egerton, *Physical Principles of Electron Microscopy: An Introduction to TEM, SEM and AEM*. (Springer, 2005).
-

Chapter 3

Structural analysis of single nanowire using advanced characterization tools

In this chapter, we have performed advanced characterization techniques i.e. Electron Energy Loss Spectroscopy (EELS) and Energy Filtered Transmission Electron Microscopy (EFTEM) study for rigorous elemental analysis to validate the quality of the nanowires (NWs), we mainly focus on homogeneity, stoichiometry, valency etc. The quantitative determination of Mn valency is done using TEM-based Gatan parallel detection EELS and elemental mapping of constituent elements are studied using EFTEM imaging. Moreover, high resolution image simulation technique is adopted to detect lattice imperfections, like stacking disorder, twinning with atomic resolution in the complex layered compounds using multifunctional simulation software named Java electron microscopy simulation (JEMS) software. The structural simulation of diffraction pattern obtained from HRTEM is opted to find the growth direction of NWs also. Such rigorous elemental characterization is not done before on manganite nanocrystals, especially on NWs.

3.1 Introduction

Transition metal oxides (such as manganite, cobaltite) show a variety of physical and chemical properties that are significantly important for developing new materials with functionality and smartness. The unique properties of these materials are correlated to the presence of elements with *mixed valences* of transition elements in the structure unit, by which we mean that an element has two or more different valences while forming a compound [1]. Perovskite $\text{La}_{1-x}\text{A}_x\text{MnO}_3$; (where A = Ca, Sr, Ba) material is an example of the mixed valence chemistry [2-3] where transition and rare earth metal elements with mixed valences made it compulsory for these materials to stimulate electronic, structural and chemical evolution, leading to specific functionality. Several solid-state spectroscopy techniques can be used to investigate the electronic structure of solids. We have used TEM based Electron Energy Loss Spectroscopy (EELS) which is a powerful technique for measuring the valences of some transition metal elements of practical importance. EELS combined with TEM have advantages compared with other spectroscopy techniques (i) it provides spectra recorded from a typical nanometre scale area with a high spatial resolution for a sample which can be identified with imaging and diffraction modes and (ii) a rather wide energy range (500-1000 eV) can be covered within one spectrum, displaying edges relevant to the different elements locally present in the sample. In this work, we have performed EELS study for quantitative determination of Mn valences in manganite NWs.

Further, to resolve the atomic structure of a complex layered crystal of manganite NWs, ($\text{La}_{1-x}\text{A}_x\text{MnO}_3$; A = Sr, Ca, $x = 0.3$ and 0.5), high resolution image simulation technique has been applied using Java electron microscopy simulation (JEMS) software [4]. This technique allows us to study lattice imperfections, like stacking disorder, twinning and layer undulations, with atomic scale resolution in the grown complex oxide NWs. In particular, we are able to view the oxygen atoms which, due to their low scattering power, are not previously accessible. This allows us to detect locally the degree of oxygen-vacancy ordering. In particular, this holds for the materials in which the local oxygen content, twinning as well as atomic column structure sensitively controls the electronic properties.

3.2 Electron energy loss spectroscopy (EELS)

Electron energy loss spectroscopy (EELS) is a powerful analytical technique for elemental characterisation of a sample and to estimate the valence state of an element in a compound [5, 6]. In EELS, we measure the energy distribution of electrons that have interacted with a sample and lost energy due to inelastic scattering. EELS are usually carried out in high vacuum TEM in which higher energy (100-300 keV) electrons pass through the thin sample (provided that the sample thickness is ≤ 100 nm). The electromagnetic lenses of the TEM can be used to focus the high energetic electron beam into a 'probe' of very small diameter (1 nm or even 0.1 nm) to produce a transmitted-electron image of the specimen, with a spatial resolution down to atomic scale. Consequently, EELS has very high spatial resolution. When a high energetic electron passes through a solid, it collides with the atomic nuclei of the constituent elements and with the electrons in the sample due to electrostatic Coulomb force. These interactions can be elastic or inelastic. In elastic collisions, between the atomic nuclei and the electrons with higher kinetic energy, there is no net transfer of energy or very small energy transfer and it is hard to detect by the spectrometer. TEM-EELS instrumentation is based on the magnetic prism, in which a uniform magnetic field (of the order of 0.01 Tesla) is produced by an electromagnet and within this field the electrons follow in a circular path. The transmitted electron beam is focussed into a high-resolution electron spectrometer that divides the electrons according to their kinetic energy and creates an electron energy-loss spectrum exhibiting the number of electrons (scattered intensity) as a function of their decrease in kinetic energy. Fig. 3.1 shows the schematic diagram representation for the working principle of EELS.

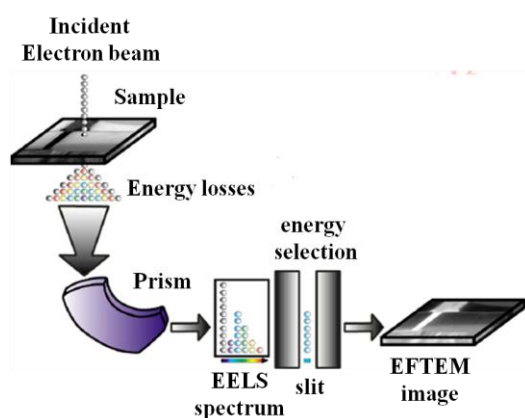


Figure 3.1 Schematic representation of EELS and EFTEM imaging. Image adapted from [7].

A typical EELS spectrum, recorded up to a few tens of electron volts, called the low-loss region [6, 8]. The zero-loss peak (ZLP) (that occurs at 0 eV) represents electrons that did not suffer inelastic scattering (interaction with the electrons of the sample) but might have been scattered elastically (through interaction with atomic nuclei) with an energy loss too small to quantify. The width of the ZLP falls usually between 0.2–2 eV which is essentially the energy distribution of the electron source.

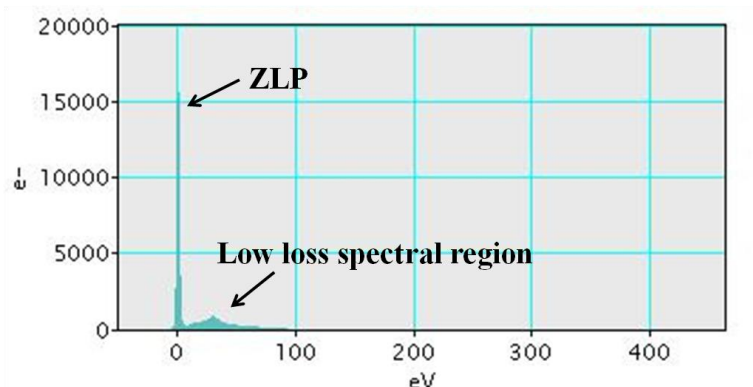


Figure 3.2 EELS spectrum of $\text{La}_{0.5}\text{Sr}_{0.5}\text{MnO}_3$ nanowire in the zero loss peak (ZLP) and low loss region.

The low-loss features that occur other than ZLP in the EELS spectrum is from inelastic scattering caused by conduction or valence electrons. The low loss region corresponds to the excitation of electrons in the outermost atomic orbital and this region is dominated by collective resonant oscillations of valence electrons known as Plasmon. The core loss or high loss region i.e. beyond the low loss region 50 eV to several thousand eV corresponds to excitation of inner shell electrons to the unoccupied electron energy levels just above the Fermi level of material. The energy loss is more for the electrons when it interacts with the inner shell electrons of the elements. For inner shell excitations, electron intensity in EELS takes the type of edges instead of peaks. The inner-shell intensity rises quickly and then falls more slowly with increasing energy loss. The sharp rise takes place at the ionization threshold whose energy-loss is more or less equal to the binding energy of the corresponding atomic shell. Since inner-shell binding energies depend on the atomic number of the scattering atom the ionization edges present in an EELS spectrum reveal which elements are present within the sample. Both the low-loss peaks and the ionization edges possess a fine structure that reflects the crystallographic or energy band structure of the sample [5-8]. It is possible to distinguish between different forms of an element even with an energy resolution of around 0.3-2 eV. That is why; EELS is a powerful technique to measure the valence state

of an element. In Fig. 3.2, we have shown the ZLP and the low loss region in the EELS measurement of $\text{La}_{0.5}\text{Sr}_{0.5}\text{MnO}_3$ NW.

EELS spectrum is acquired at 200 kV using Tecnai G^2 TF-20 TEM equipped with a Gatan parallel-detection electron energy-loss spectrometer. The EELS spectra are taken in the image mode at a magnification of 40–100 K depending on the required spatial resolution and signal intensity. A low-loss valence spectrum and the corresponding EELS core loss spectrum are taken consecutively in the same specimen region. The low energy-loss spectrum is used to remove the multiple-inelastic-scattering effect in the core-loss region using the Fourier ratio technique. The background has been subtracted using standard procedure Fourier ratio method by Gatan's Digital Micrograph software in EELS.

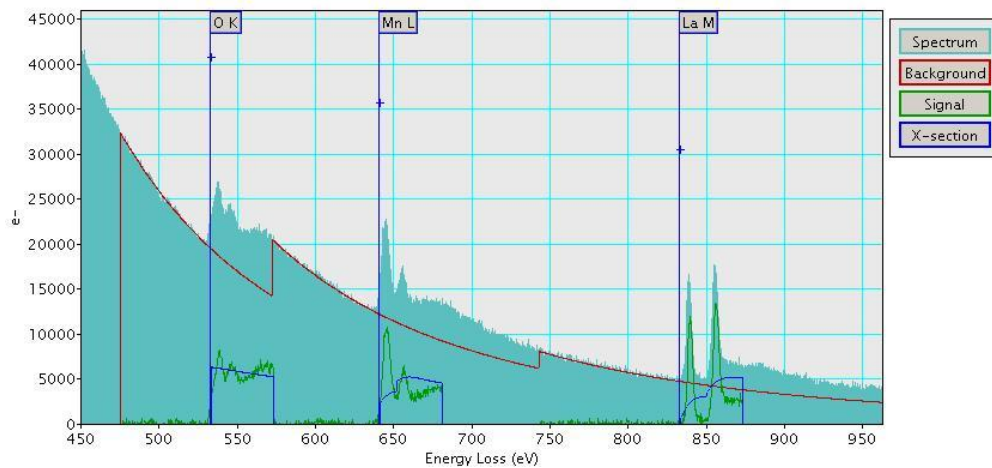


Figure 3.3 EELS core loss spectrum of $\text{La}_{0.5}\text{Sr}_{0.5}\text{MnO}_3$ nanowires which shows the K (inner shell excitations from 1s), L (inner shell excitations from 2p) and M (inner shell excitations from 3d) of O, Mn and La respectively.

To prepare the sample for the EELS measurement we have taken some powder samples and dispersed in ethanol or acetone solution. Then, a colloidal solution of $\text{La}_{1-x}\text{A}_x\text{MnO}_3$; ($\text{A} = \text{Sr}, \text{Ca}$, $x = 0.3$ and 0.5) is drop casted on a TEM carbon coated Cu grid. This Cu grid is dried overnight and loaded to the TEM chamber. In Fig. 3.3, we have shown the EELS spectrum of $\text{La}_{0.5}\text{Sr}_{0.5}\text{MnO}_3$ NWs which exhibits the K (inner shell excitations from 1s), L (inner shell excitations from 2p) and M (inner shell excitations from 3d) of O, Mn and La respectively.

3.2.1 EELS study to estimate the valency of Mn

The elemental analysis of $\text{La}_{1-x}\text{A}_x\text{MnO}_3$ ($\text{A} = \text{Sr}, \text{Ca}$, $x = 0.3$ and 0.5) compound is performed using EELS on different single NWs repeatedly and estimated the valency of Mn. Transition from Mn 2p shell is actually split into two components separated by spin orbit splitting of the ionized 2p core level. Transitions from $2p_{3/2}$ to $3d_{3/2}$, $3d_{5/2}$ and from $2p_{1/2}$ to $3d_{1/2}$ are L_3 and L_2 lines, respectively. The intensities of L_3 and L_2 lines are related to the unoccupied states in the 3d bands. The intensity ratio of L_3/L_2 is sensitive to the valence state of the corresponding element. If a series of EELS spectra are taken from standard specimens with known Mn valence states, an empirical plot of L_3/L_2 ratio vs. valency of Mn serves as the reference to determine the valence state of the element present in our NW sample. Thus, EELS analysis of valence state is performed in reference to the spectra acquired from standard specimens (MnO , Mn_2O_3 and MnO_2) with known Mn valence states.

We have determined Mn valency of $\text{La}_{1-x}\text{A}_x\text{MnO}_3$; ($\text{A} = \text{Sr}, \text{Ca}$, $x = 0.3$ and 0.5) NWs using the white lines (L_2 , L_3 ionization edges of Mn) and the intensity ratio of L_3 and L_2 lines [8-10]. We have fitted each EELS spectra by multiple Gaussian peaks and found the L_3 (blue line), L_2 (Green line) peaks and sum peaks (red line) for all the NWs as shown in Fig. 3.4. We have taken the EELS spectra of some Mn based with known Mn valency (Fig. 3.5 (a)-(c)) and made a calibration curve and plotted in Fig. 3.5 (d) [9-11]. The L_3/L_2 ratio is estimated from the loss spectra of our NW samples of $\text{La}_{0.5}\text{Sr}_{0.5}\text{MnO}_3$, $\text{La}_{0.7}\text{Sr}_{0.3}\text{MnO}_3$, $\text{La}_{0.5}\text{Ca}_{0.5}\text{MnO}_3$ and $\text{La}_{0.7}\text{Ca}_{0.3}\text{MnO}_3$ (Fig. 3.4 (a)-(d)) respectively. Finally the unknown Mn valency of our samples is estimated using this calibration curve (Fig. 3.5 (d)) and we have found that mixed valence state of Mn of all the samples (Fig. 3.5 (d)), which is expected for manganite compounds.

Generally for greater values of x ($x > 5/8$) in $\text{La}_{1-x}\text{A}_x\text{MnO}_3$, ordered structures are produced with distinct Mn^{3+} and Mn^{4+} sites. However, for smaller values of x ($x < 0.5$), the compounds are structurally disordered. This phenomenon is of great interest, because at low temperature in the metallic phase, electrons are delocalized in a conduction band and the manganese atoms become equivalent, leading to a much reduced or even completely removed JT distortion of the MnO_6 octahedra which in turn controls the magnetic behaviour of the samples. Using the measured L_3/L_2 ratio from the calibration curve, the Mn valency of all the NWs has been shown in Table 3.1.

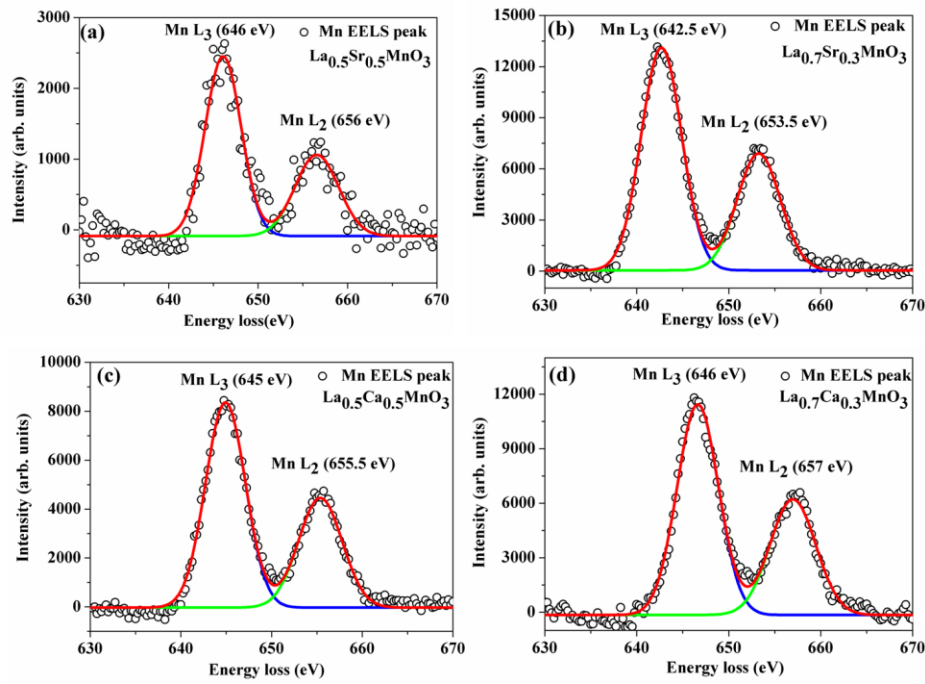


Figure 3.4 The EELS spectra of (a) $\text{La}_{0.5}\text{Sr}_{0.5}\text{MnO}_3$, (b) $\text{La}_{0.7}\text{Sr}_{0.3}\text{MnO}_3$, (c) $\text{La}_{0.5}\text{Ca}_{0.5}\text{MnO}_3$ and (d) $\text{La}_{0.7}\text{Ca}_{0.3}\text{MnO}_3$ nanowires, respectively, showing manganese L_3 and L_2 lines.

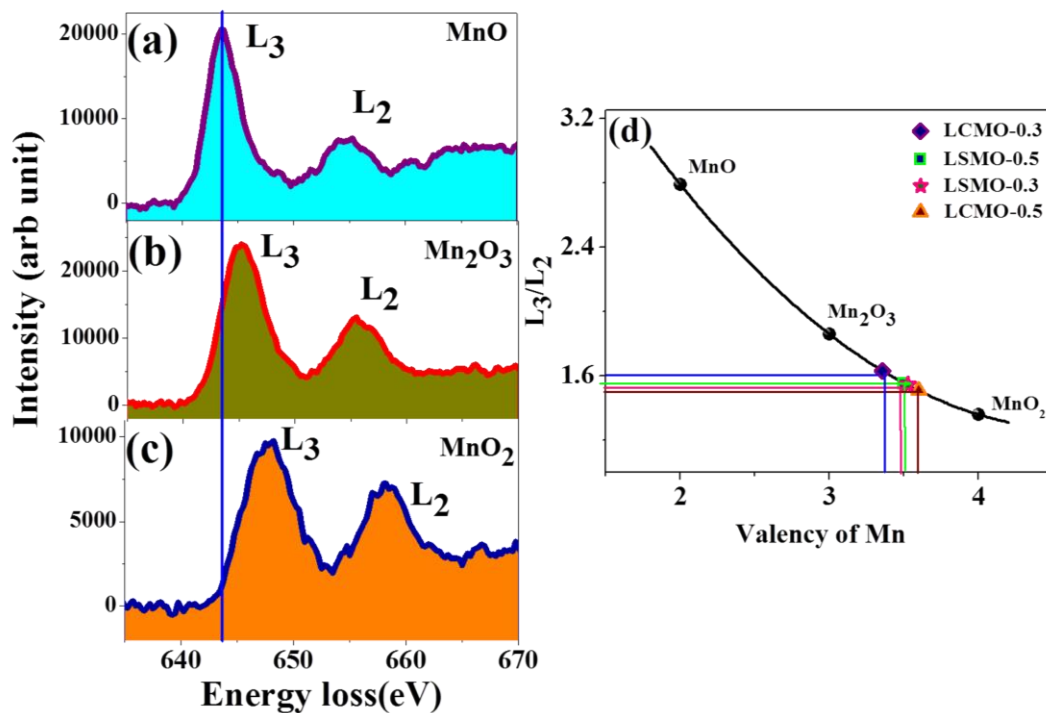


Figure 3.5 The EELS spectra of (a) MnO , (b) Mn_2O_3 and (c) MnO_2 respectively, showing manganese L_3 , L_2 lines. (d) Intensity ratio of L_3 and L_2 lines of different Mn oxide compounds as a function of their known valence. Mn valence of grown nanowires can be estimated from the curve.

Table: 3.1 Mn valence of $\text{La}_{1-x}\text{A}_x\text{MnO}_3$; (A = Sr, Ca, $x = 0.3$ and 0.5) nanowires estimated from calibration curve and compared with the calculated data.

Sample ID	Estimated Mn Valence	Calculated Mn Valence
$\text{La}_{0.5}\text{Sr}_{0.5}\text{MnO}_3$	3.50 ± 0.01	3.50
$\text{La}_{0.7}\text{Sr}_{0.3}\text{MnO}_3$	3.52 ± 0.01	3.30
$\text{La}_{0.5}\text{Ca}_{0.5}\text{MnO}_3$	3.60 ± 0.01	3.50
$\text{La}_{0.7}\text{Ca}_{0.3}\text{MnO}_3$	3.35 ± 0.01	3.30

3.3 Energy Filtered TEM to check the homogeneity

In EFTEM, the parallel beam imaging mode is attached with principles of EELS to produce a filtered image or an elemental map. An energy-loss spectrum is created just below the filter and subsequent TEM lenses project it onto an electronic detector, generally employing a CCD camera. On the other hand, these lenses may focus a plane (within the spectrometer) that contains an image of the specimen, utilizing the imaging properties of a magnetic prism as shown in Fig. 3.1. A narrow slit is inserted at the spectrum plane which can remove all electrons except those within a small energy window, resulting in an energy-filtered (EFTEM) image on the TEM screen or the CCD camera. The image aberrations are corrected by quadrupole and sextupole lenses and the post-column magnetic prism can also produce EFTEM images (Fig. 3.1), as in the GIF spectrometer marketed by the Gatan Company [7].

EFTEM provides higher spatial resolution during analysis because of reduced interaction volume in a thinned electron-transparent TEM section (~ 20 to 200 nm). EFTEM offers better signal collection efficiency to detect elements from small amount of sample because high percentage of electrons carrying elemental information can be directed using the spectrometer. EELS provide 2 orders higher energy resolution than EDX and work best at comparatively low atomic numbers, where the excitation edges tend to be sharp. Though EDX is quite easy to use, identifies the atomic composition of a material and sensitive to heavier elements, the reasons mentioned above justifies our use of EFTEM mapping over EDX mapping as we have Ca, O in our material which can be detected with higher accuracy with EFTEM.

Energy Filtered TEM image is taken to check the homogeneity of the elemental distribution in each NW (diameter ~ 50 nm) of $\text{La}_{1-x}\text{A}_x\text{MnO}_3$; (A = Sr, Ca, $x = 0.3$ and 0.5) samples. Here as a representative, we have shown only two compounds $\text{La}_{0.5}\text{Sr}_{0.5}\text{MnO}_3$ and $\text{La}_{0.5}\text{Ca}_{0.5}\text{MnO}_3$.

Fig. 3.6 shows the EFTEM image of $\text{La}_{0.5}\text{Sr}_{0.5}\text{MnO}_3$ NW, where red, green, blue and yellow colours are used for elements O, Mn, La and Sr, respectively. The EFTEM analysis shows that all the constituent elements La, Sr, Mn and O are homogeneously distributed within the NW.

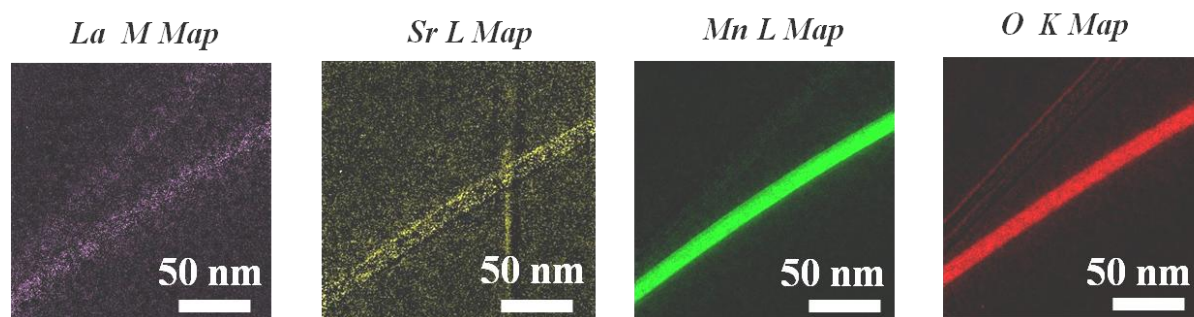


Figure 3.6 Energy Filtered Transmission Electron Microscope (EFTEM) image of each constituent element: M map of La, L map of Sr and Mn and K map of O in $\text{La}_{0.5}\text{Sr}_{0.5}\text{MnO}_3$ nanowire. The red, green, blue and yellow colours represent the distribution of elements O, Mn, La and Sr respectively in the nanowire.

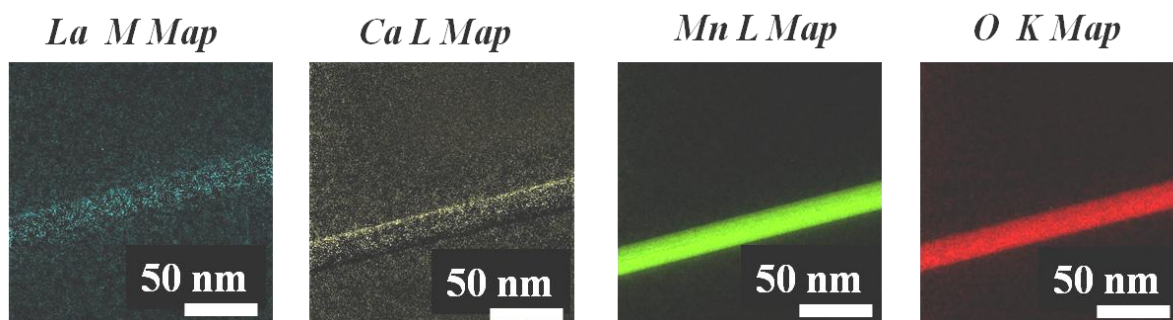


Figure 3.7 Energy Filtered Transmission Electron Microscope (EFTEM) image of each constituent element: M map of La, L map of Ca and Mn and K map of O in $\text{La}_{0.5}\text{Ca}_{0.5}\text{MnO}_3$ nanowire. The red, green, blue and yellow colours represent the distribution of elements O, Mn, La and Ca respectively in the nanowire.

In Fig. 3.7 we have shown EFTEM image of $\text{La}_{0.5}\text{Ca}_{0.5}\text{MnO}_3$ NW, where red, green, blue and yellow colours are used for elements O, Mn, La and Ca respectively. The EFTEM analysis shows that all the constituent elements La, Ca, Mn and O are uniformly spread within the NW.

3.4 Structural simulation of single nanowire (NW) of manganite using Java Electron Microscopy Simulation (JEMS) software

Electron Microscopy Simulation (EMS) is a set of computer programs which has been developed not only for the simulation and analysis of High-Resolution Electron Microscopy (HREM) images, but also for the analysis of diffraction patterns [4]. EMS can be separated into two parts. The first part is the calculations of crystallography encountered in electron microscopy such as automatic indexing of diffraction and Kikuchi patterns, simulation of spot and powder patterns, drawing of stereographic projections, calculation of the Bravais lattice of an unknown structure from two diffraction patterns, etc. The second part is the simulation of structures of both perfect and defect structures using either a Fast Fourier Transform (FFT) based multislice method or the Bloch wave approach. HREM allows us to study sample structures (localised) on the nanometer scale using FFT of images. The respective diffractograms (FFT) have the information of the crystal lattice and sample orientation. Simulation of high-resolution transmission electron microscopy (HRTEM) images for the crystal structure and the zone axis allows us to find out the atomic column structure of the sample in the sub-nanometre scale which, in turn, permits us to understand the mechanism of crystal growth and defects of manganite NWs [9, 12].

3.4.1 Basics of JEMS software

JEMS [4] is quantum-mechanical and wave-optical image computer simulation software for simulating HRTEM images using the multislice and Bloch-wave methods. It can create crystallographic models of various materials in both direct and reciprocal spaces, stereographic projections and three-dimensional images. In TEM, electrons interact strongly with the "thick" specimen which is more than a few Angstroms for most of the samples and the electrons will undergo multiple scattering as they pass through the specimen. There are two principle ways of calculating a TEM image (scanning or conventional), the Bloch wave method and the multislice method.

Bloch wave: A Bloch wave is a type of wave function for a sample in a periodically-repeating environment, most commonly an electron in a crystal. A wave function ψ is a Bloch wave if it has the form: $\psi(\mathbf{r}) = e^{i\mathbf{k} \cdot \mathbf{r}} u(\mathbf{r})$ (3.1)

Where r is the position, u is periodic with the same periodicity as the crystal lattice. The actual quantum state of the electron is entirely determined by ψ , not k or u directly. This is important because k and u are not unique. The electron wave function is expanded in Bloch waves inside a crystalline specimen, which have the periodicity of the specimen and satisfy the Schrödinger equation [13].

Multislice method: In this method, the specimen is divided into many thin slices. It can alternately transmit and propagate the slowly varying portion of the wave function through the specimen [13]. This method is valid for crystalline or nearly amorphous specimens.

The full electron wave function ψ_f travelling in the positive z direction is:

$$\psi_f = \psi \exp\left(\frac{2\pi iz}{\lambda}\right) \quad (3.2)$$

Where, λ is the electron wavelength and ψ is the slowly varying portion of the wave function. Include this expression for ψ_f into the Schrödinger equation and solve for the slowly varying portion of the wave function ψ . The approximation in the multislice method is that the specimen is divided into many slices and each of which is thin enough to be approximated as a simple phase shift of the electron beam as shown in Fig 3.8. The incident wave enters the thin sample at the top, propagates through the sample and exits at the bottom. In conventional TEM the incident wave is a uniform plane wave and the electron beam propagates between slices as a small angle outgoing wave (Fresnel diffraction). The wave is transmitted through a slice of thickness Δz and then propagates a distance Δz to the next layer.

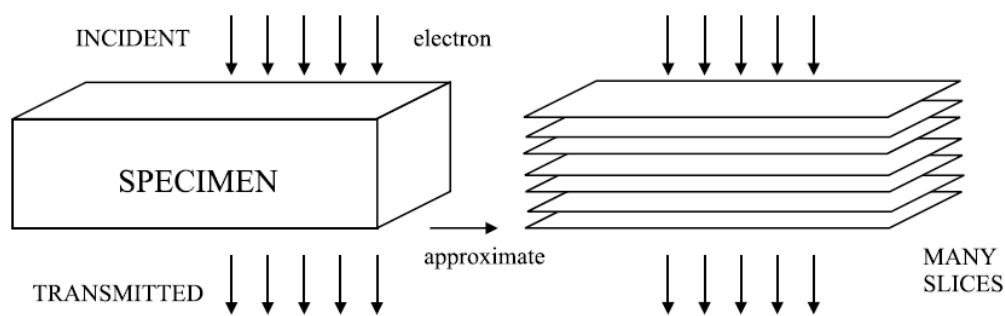


Figure 3.8 The multislice approximation converts a specimen (left) into many thin slices (right). The electron wave is incident on the top of the specimen and transmitted through the specimen and exits on the bottom. Each slice of the specimen is thin enough to be approximated as a phase shift of the electron wave which is propagated between slices as a free space wave.

With some mathematical manipulation of the slowly varying portion of the electron wave function in the Schrödinger equation and neglecting small terms yields the following for the multislice equation:

$$\psi(x, y, z + \Delta z) = p(x, y, \Delta z) \otimes [t(x, y, z)\psi(x, y, z)] + O(\Delta z^2) \quad (3.3)$$

Where \otimes represents convolution and Δz is a small slice of the specimen along the beam direction. For the portion between z and $z + \Delta z$ of the specimen, the transmission function is:

$$t(x, y, z) = \exp[i\sigma \int_z^{z+\Delta z} V(x, y, z_1) dz_1] \quad (3.4)$$

Where $\sigma = 2\pi me\lambda/h^2$ is the interaction parameter and $V(x, y, z)$ is the potential due to the atoms inside the specimen which is calculated from relativistic Hartree-Fock for isolated atoms. The propagator function $p(x, y, z)$ and its Fourier transform $P(k)$ are:

$$P(k, \Delta z) = \exp(-i\pi\lambda k^2 \Delta z) \quad (3.5)$$

$$p(x, y, \Delta z) = FT^{-1}[P(k, \Delta z)] = \frac{1}{i\lambda\Delta z} \exp\left[\frac{i\pi(x^2 + y^2)}{\lambda\Delta z}\right]$$

which is equivalent to Fresnel diffraction for a distance Δz . If each slice of the specimen is regarded as with subscript n ($z = n\Delta z$) then the multislice equation becomes:

$$\psi_{n+1}(x, y) = p_n(x, y, \Delta z_n) \otimes [t_n(x, y)\psi_n(x, y)] + O(\Delta z^2) \quad (3.6)$$

Convolution scales as N^2 where N is the number of points. However, this form of the equation is very suitable for FFT, which is a highly efficient and well developed numerical algorithm. The CPU time for the FFT scales as $N \log(N)$. Using the FFT, labelled as FT :

$$\psi_{n+1}(x, y) = FT^{-1}[P_n(k_x, k_y, \Delta z_n) FT\{t_n(x, y)\psi_n(x, y)\}] + O(\Delta z^2) \quad (3.7)$$

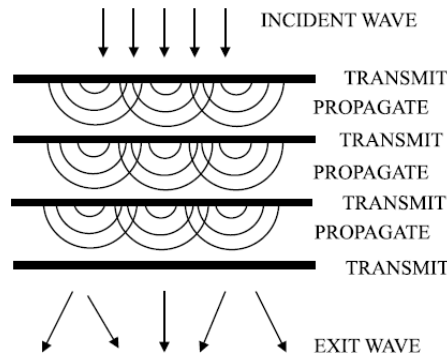


Figure 3.9 The multislice method successively transmits the electron wave through each slice and then propagates it to the next slice. The incident wave is a plane wave for conventional TEM.

The multislice method [13] reduces to a succession of transmit and propagate operations with a FFT in between each slice which is concise in Fig. 3.9.

3.4.2 Importance of image simulation using JEMS software

The resolution of conventional TEM (CTEM) is mainly limited by the aberrations of the lenses in the microscope and multiple scattering in the specimen. That is why; image simulation helps us to understand the detailed structure in the image form to separate what information is due to the specimen and what is due to the instrument. It also helps to resolve the effects of multiple scattering caused by the specimen. Image simulation may help to understand how the image is produced and to improve the image and instrumentation. In CTEM, due to the presence of spherical aberration, HRTEM image produces phase contrast imaging for very thin objects [9]. But due to presence of several defects in case of manganite NWs, the phase contrast imaging is always not achievable in a CTEM [14]. However, HRTEM images obtained for manganite NWs in a CTEM suffer from complicated contrast transfer and strong delocalization of higher spatial frequencies transferred by electrons scattered at larger angles. Tuning of the defocus to particular values may reduce the effects for some frequencies but for the frequencies transferred typically by the optical system cannot be removed. Hence the image artefacts due to spherical aberration are most pronounced in HRTEM images of objects involving a complex crystalline structure or atomic scale defects. With the help of the computer simulation using JEMS, the situation can be changed dramatically [4]. This simulation program allows us using coefficient of the spherical aberration C_s as an additional experimental parameter that can be tuned over a wide range from positive to even negative values [9, 15, 16]. For HRTEM image simulation of very thin samples, it is necessary to tune C_s value and balance its effect by a suitable defocus with the optimal values depending on the information limit of the microscope. Under optimized conditions the delocalization of object information is reduced providing a simple transfer characteristic along with a good phase contrast. Hence the atomic columns in thin crystalline samples appear as bright dots on a dark background generating an image, which closely resembles the projected crystal structure. In comparison with the cations having a higher nuclear charge, it is difficult to image the oxygen sublattice. It is due the fact that oxygen has low scattering power. The conditions under which oxygen gives rise to detectable contrast in the perovskite manganite were studied by quantum-mechanical and wave-optical

image computer simulation [9, 16]. Information on individual oxygen atom columns can be obtained by the focus-variation technique, in which the electron wave function at the exit plane of the specimen is calculated by computer processing [17, 18]. An important advantage of JEMS is the high speed of computations and new possibilities for interpreting results associated with sample drift, vibrations, tilt, astigmatism and image shift. In studies of the compositions of multiphase systems, JEMS allows one to analyze electron diffraction patterns and recognize the constituent phases in a large number of compounds simultaneously. Imaging under certain conditions, structural simulation on a single NW level in complex oxides using JEMS software [4] is able to provide the atomic scale resolution necessary to investigate the atomic column structure of imperfections in such complex layer compounds.

3.4.3 Input parameters of JEMS software

The structural simulation of single NW of $\text{La}_{1-x}\text{A}_x\text{MnO}_3$ ($\text{A} = \text{Sr, Ca}$; $x = 0.3, 0.5$) complex oxides was done using JEMS software [4, 9]. To study the change in the coordination of the atoms, the growth direction of a particular NW and the investigation of the atomic column structure of imperfections, this JEMS software is employed. For our samples, we varied the defocus value keeping the other microscopic parameters (200 kV field, coherent illumination) unchanged for all the cases (Table 3.2) [9]. Here we have used spherical aberration correction coefficient in the order of 0.5 mm (third order). The crystallographic parameters used are lattice parameters, Wyckoff-position of the atoms, Debye Waller factor, occupancy and the bond lengths. In our analysis we have taken into consideration the crystallographic parameters obtained by Rietveld analysis of synchrotron X-ray diffraction data of the ensemble of NWs (Table 2.2 in Chapter 2). In our analysis we have assumed that single NW forms the basis of the ensemble of NWs as the size distribution is homogeneous (shown in Fig. 2.15 in chapter 2).

Table 3.2 Parameters for HREM image simulation

Sample Name	Coefficient of spherical aberration(C_s)	Defocus value	Illumination	Iteration	Average Diameter (nm)
$\text{La}_{0.5}\text{Ca}_{0.5}\text{MnO}_3$	0.5mm	+30 ~ -300	Coherent	20	44
$\text{La}_{0.7}\text{Ca}_{0.3}\text{MnO}_3$	0.5mm	+40 ~ -300	Coherent	20	42
$\text{La}_{0.5}\text{Sr}_{0.5}\text{MnO}_3$	0.5mm	-100~ -600	Coherent	20	38
$\text{La}_{0.7}\text{Sr}_{0.3}\text{MnO}_3$	0.5mm	- 30 ~ -600	Coherent	20	40

3.4.4 Structural simulation of the nanowires

Growth direction of nanowires of four compositions ($\text{La}_{1-x}\text{A}_x\text{MnO}_3$, $\text{A} = \text{Sr}, \text{Ca}$; $x = 0.3, 0.5$)

We have compared our experimental HRTEM data with simulated structure using JEMS software. In case of LCMO-0.5 the indexation is based on an orthorhombic unit cell with cell parameters $a = 5.339 \text{ \AA}$, $b = 7.470 \text{ \AA}$ and $c = 5.294 \text{ \AA}$ [19]. In this case the extinction conditions imposed by the $Pnma$ 62 space group are completely fulfilled in case of a single NW in the diffraction pattern shown in Fig. 3.10 (a). Here the growth is in the [121] direction with a tilt in the axis of 28.2° from the normal w.r.t the zone axis which carries signature of distortion in the coordination of the atomic column structure. Similar change in the coordination of the atomic column structure has been noticed in case of binary oxides [16]. This change in coordination is later verified by generating HREM atomic column maps in JEMS in Fig. 3.16.

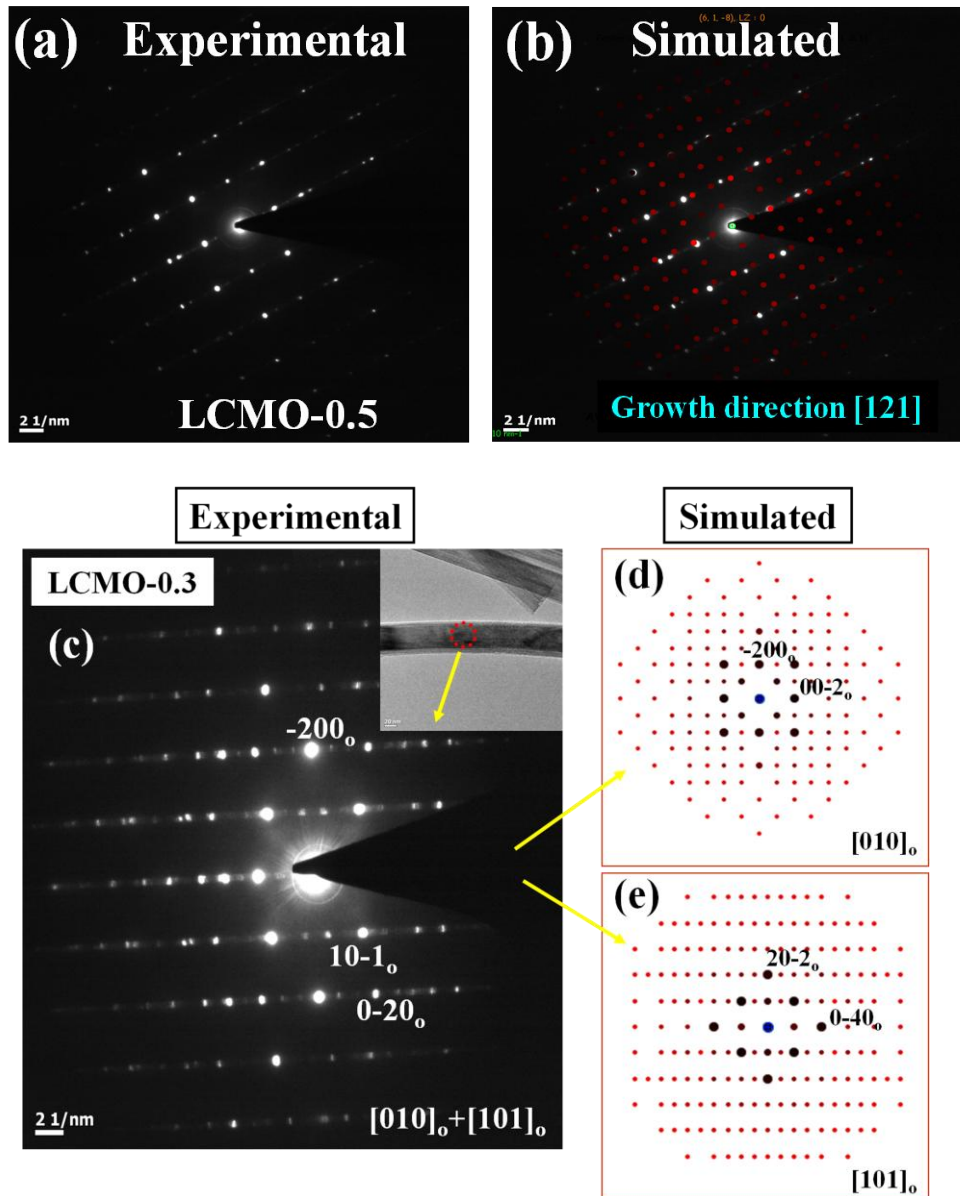


Figure 3.10 (a) Experimental selected area electron diffraction (SAED) pattern of single nanowire (NW) of LCMO-0.5 (b) Simulated diffraction pattern (red spots) showing the growth direction along [121] of LCMO-0.5 NW (c) SAED pattern (taken from red dotted portion) of LCMO-0.3 single nanowire (inset) showing orthorhombic symmetry with a overlapping of two zone axis [010]₀ and [101]₀. (d) and (e) Theoretical simulation of [010]₀ and [101]₀ SAED patterns by JEMS software.

In case of epitaxial LCMO films/NWs, single SAED patterns were occasionally found. However, in case of LCMO-0.3 single NW electron diffraction patterns with twins are observed, where two or more zone axis are overlapped (Fig. 3.10 (c)–(e)). The indexation is based on an orthorhombic unit cell with cell parameters $a = 5.2943 \text{ \AA}$, $b = 7.5936 \text{ \AA}$ and $c = 5.3671 \text{ \AA}$ with $Pnma$, 62 space group [9, 20] (see Table 2.2 in Chapter 2). The extinction

conditions imposed by the $Pnma$, 62 space group are not completely fulfilled in case of a single NW in the diffraction pattern shown in Fig. 3.10 (c), since the reflections $h00$ and $00l$ with $h, l=2n+1$ appear in the $[010]_0$ zone axis, $h00$ with $h=2n+1$ appear in the $[011]_0$ zone axis and $0k0$ with $k=2n+1$ also appears in the $[101]_0$ zone axis. The possibility of double diffraction could be ruled out by performing tilting experiments along the $\langle 100 \rangle$, $\langle 010 \rangle$ and $\langle 001 \rangle$ axis. To explore the possibility that matches with the diffraction pattern, the structural model in $Pnma$ 62 space group is simulated by JEMS software [4]. The simulated result in the case of LCMO-0.3 single NW, the SAED pattern in Fig. 3.10 (c) is well matched with the two zone axis $[010]_0$ (Fig. 3.10 (d)) and $[101]_0$ (Fig. 3.10 (e)) [9, 21, 22].

The picture is somewhat different in case of LSMO NWs. Here no twinning is observed. In case of LSMO-0.5 NW, from the simulated diffraction pattern, it was found out that the growth direction of the NW is along $[112]$ direction in plane (Fig. 3.11 (a) and (b) [4, 9, 12,]. The XRD analysis (Fig. 2.10 (d) in chapter 2) on the ensemble of LSMO-0.5 NWs also shows that the preferential growth direction of the NWs is along $[112]$ direction. As we have mentioned earlier, our assumption was that the single NW forms a basis of the ensemble of NWs because of their homogeneous size distribution (Fig. 2.15 (a) in chapter 2) thus it was observed that the analysis of micro-structural data of single NW of high-resolution TEM pattern are quite comparable with the synchrotron X-ray crystallographic data taken on the ensemble of NWs (Fig. 2.10 (d) in chapter 2). Both the structural data obtained from the grown NWs are corroborating with their bulk form.

LSMO-0.3 NWs structure is Rhombohedral with the extinction condition being $R-3c$. Here the growth direction of the NWs is along $[110]$. From the Fig. 3.11 (c) and (d) it is clearly noticed that the superimposed simulated image (red spots) matches well with the actual image. However, due to defects in NWs, some lattice points are missing in the experimental SAED pattern as compared to simulated SAED pattern.

From the above structural analysis it can be concluded that the doping concentration can control the growth directions as well as the defect states in the NWs in both the cases [19].

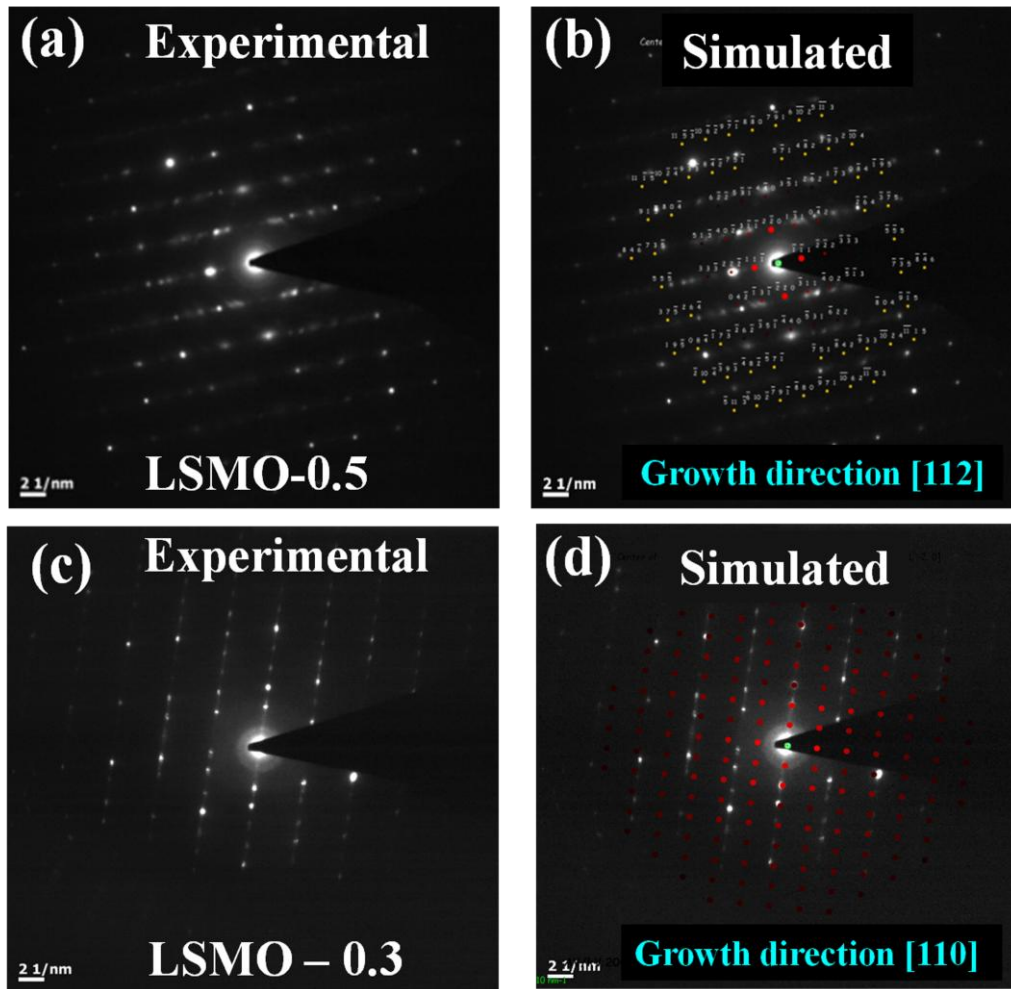


Figure 3.11 (a) Experimental selected area electron diffraction (SAED) pattern of single nanowire (NW) of LSMO-0.5 (b) Simulated diffraction pattern (red spots) showing the growth direction along [112] of LSMO-0.5 NW, (c) Experimental SAED pattern of single NW of LSMO-0.3 (d) Simulated diffraction pattern (red spots) showing the growth direction along [110] of LSMO-0.3 NW.

Thus a detailed structural analysis of the samples may provide some insight into the defects mechanism as seen in LCMO-0.3 NW (mainly twinning) and magnetic phase coexistence in ensemble as well as in single NW level as in LSMO-0.5 (discussed in chapter 5 and 7). Hence we have analyzed LCMO-0.3 and LSMO-0.5 NW further in details to get information regarding growth mechanism which further influences the ultimate physical properties of the materials. TEM analysis of the single NW of LCMO-0.3 (Fig. 3.12 (a)) prepared presents twinning of the NWs. Fig. 3.12 (b) represents the experimental HREM image which seems to indicate a breakdown of the orthorhombic symmetry, at least on the nano-domain scale. Fig. 3.12 (d) shows the FFT corresponding to the HREM image of Fig. 3.12 (b), where two zone

axes coincides. This is due to the twinning of the crystal, which is very often observed in perovskite materials [9, 21]. To emphasize the appearance of structural modification, a Fourier filter of the HREM (Fig. 3.12 (c)) image by Digital Micrograph was generated.

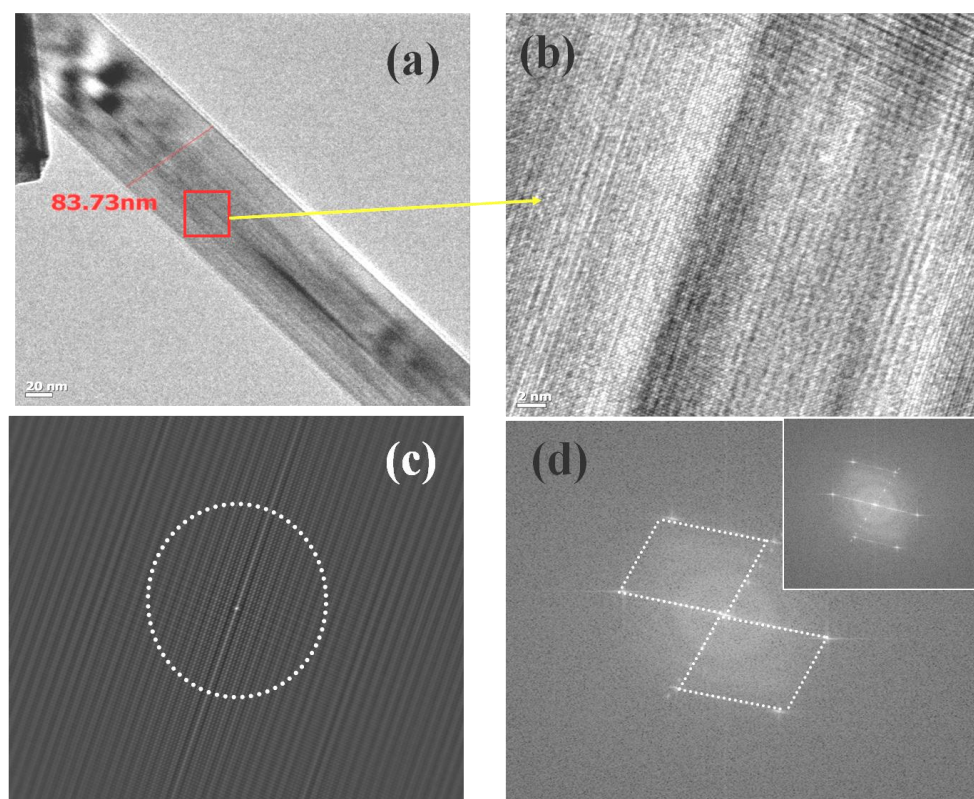


Figure 3.12 (a) HREM image showing single nanowire (NW) of LCMO-0.3 (b) HREM micrograph showing fringes and structural defects on single NW (c) Fourier filtered image of the (b) showing a structural modulation. (d) FFT from (b) with the two projected unit cells (white dotted markings).

In Fig. 3.13, it was observed that in LCMO-0.3 NWs, twins are formed and structural distortions are noticed using JEMS simulation. In order to confirm the distortion in the MnO_6 octahedra, the HRTEM maps corresponding to the different zone axis $[010]_0$ and $[101]_0$ were generated (Fig. 3.13 (a), (c)) in JEMS software at a defocus value of -245 nm [9]. The distortion in the MnO_6 octahedra (Fig. 3.13 (b), (d)) also confirms the presence of twins along with the possibility of explanation of the distortion in the octahedral due to the possible attachment of K^+ ions during the chemical reaction as discussed in growth mechanism part in chapter 2. Fig. 3.13 (b) shows the MnO_6 octahedra and Fig. 3.13 (d) indicates the distorted octahedra. In perovskite oxides, the BO_6 octahedra may show some degree of distortion along some direction due to the size effect of A-site cations [9].

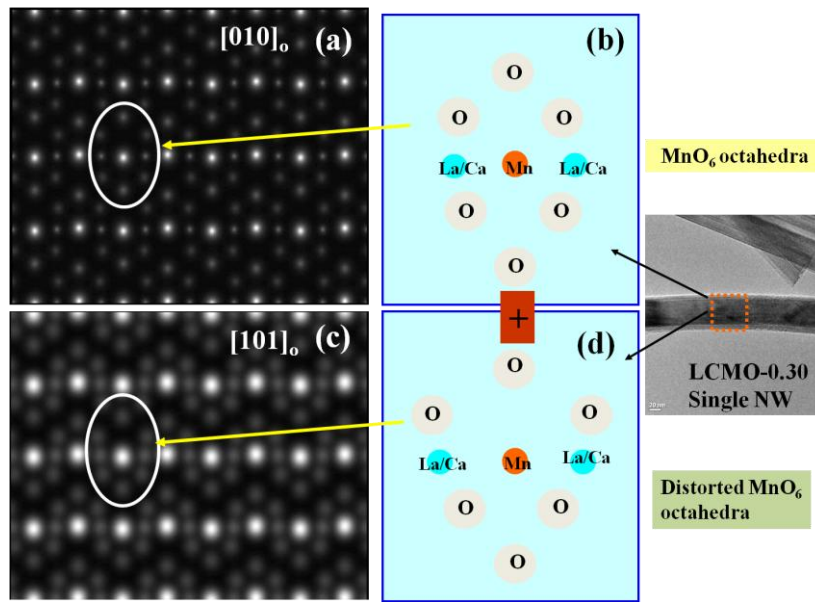


Figure 3.13 (a) and (c) Generated HREM maps along the zone axis $[010]_0$ and $[101]_0$; respectively, showing the atomic coordinations. (b) and (d) showing distortions in the MnO_6 octahedra confirming the presence of twins of LCMO-0.3 nanowires.

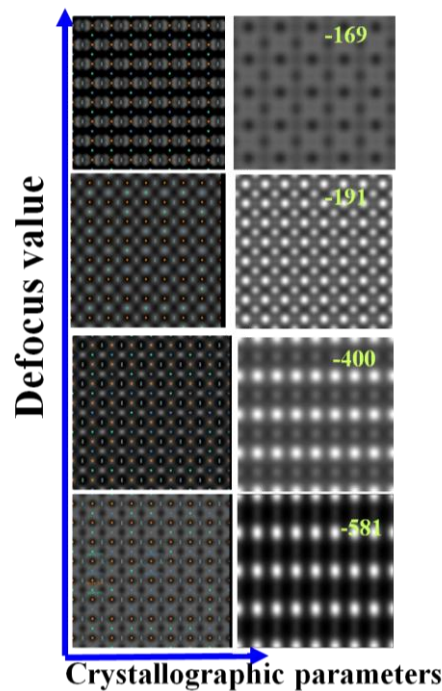


Figure 3.14 Showing the generated HREM maps of LSMO-0.5 with atomic resolution and the phase object function generated at different negative defocus value.

As we have already discussed that in case of LCMO-0.3 NWs, how the MnO_6 octahedra gets distorted due to the termination at AO sites [9]. In case of LSMO-0.5 NWs also our focus is on the distortion of the atomic column structure which ultimately reveals the growth

mechanism in nano-domain. The HRTEM micrograph in Fig. 3.14 is taken at a negative defocus value of -191 nm in our microscope. Now keeping the crystallographic parameters unchanged we have varied the defocus value (-ve) along with a series of iteration which varies ultimately the focus stacking and reconstruct to create a single image entirely in focus (Fig. 3.14) [9]. The defocus value is chosen negative because of the factor that in JEMS negative defocus value relates focused image and positive defocus value corresponds to under focus. It was found that the phase object function generated each time for different defocus value (Fig. 3.14) doesn't match well with the simulated structure along [112] except the structure generated at -191 nm defocus value which shows fourfold symmetry. In order to elucidate the change in the structure of a single NW than the bulk LSMO-0.5, the bulk structure is simulated using the Rietveld data in the crystallographic input and -191 nm defocus value in the microscopic input in Fig. 3.15 (a) and (b). The bulk structure is simulated along [112] direction and the illumination is kept coherent. From the Fig. 3.15 (a) and (b) it is clear that there is a change in the atomic co-ordination (mainly in La and Sr) in the NW than that in the bulk. This change may be due to the strain in the structure due to size reduction.

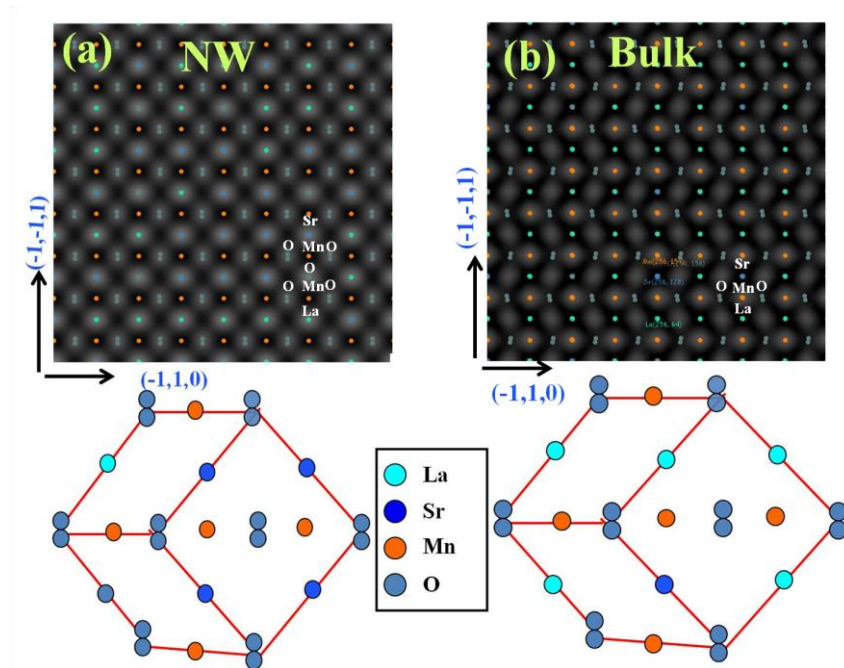


Figure 3.15 (a) and (b) Generated HREM maps of LSMO-0.5 showing the atomic positions in the (-1,-1,1) and (-1,1,0) directions in both i.e., single NW and Bulk. The comparison is made keeping the microscopic parameters similar, only varying the crystallographic parameters. Schematic of the simulated structures show distortion in the co-ordination of La/Sr and also shrinkage in volume in the unit cell due to size reduction.

3.4.5 Atomic column structures of the nanowires

The atomic column structure generation is an important task as for manganite. The crystal structures are much more divergent from cubic perovskite structure and the shape of the crystal depends on the size of the A-site cations. So the generation of a complete atomic column structural map may completely resolve our growth mechanism problem which has been already discussed in chapter 2. In chapter 2 we have found that by changing the KOH concentration the change in phase and crystal shape in manganite can be achieved [9]. So far reports are available on the effect of K^+ and OH^- attachment on B and A sites that leads to various facet growths [9]. In our case of single NWs of LSMO the growth direction is along a particular direction (LSMO-0.3 along [110] and LSMO-0.5 along [112]) and a contraction in the c-axis of the crystal is noticed in comparison to the bulk (see Fig. 3.15). This may be due to the attachment of OH^- ions with the A-site (positively charged ions) along the long axis direction of the NWs that reduces the overall surface energy contribution and leads to a growth along a particular direction (LSMO-0.3 along [110] and LSMO-0.5 along [112]) [9]. On the other hand, in case of another manganite NW, i.e, LCMO-0.3 it was seen that twins are formed with the possibility of the distortion in the octahedral due to the possible attachment of K^+ ions. But the change in the doping concentration changes the scenario and leads to the growth along [121] in case of LCMO-0.5 leading to the reduction of the overall surface energy along the long axis direction of the NWs. The changes in the atomic column structure are much clearly seen in case of the four compositions in Fig. 3.16. We investigated the C_s imaging mode by quantum-mechanical and wave-optical image simulation. Here the linear imaging theory of weak objects can be applied to understand the contrast inversion. Phase-shifting of the diffracted beams by $\pi/2$ means that their amplitude is added to that of the transmitted beam, resulting in bright atom images (Fig. 3.16 (a)-(d)). Fig. 3.16 (a)-(d) demonstrates the high quality of the images and that the oxygen-atom columns can be seen and studied individually. Along with the oxygen columns the termination at the AO sites are also clearly seen. From the Fig. 3.16, the breaking of the layered oxide structure is clearly visible as the symmetry breaks. It has been reported by many authors that during synthesis of perovskite oxides in solution in the presence of some additive, growth of crystal planes may be terminated either A–O or B–O at the surface [23, 24]. In a very high concentration of alkaline hydroxide (KOH) in reaction medium, the crystals are terminated with an A–O layer, leading to a positively charged surface as the bonds of A-site cations are unsaturated. Some of OH^- anions of KOH, in the reaction mixture may attach with the crystal surface to balance

the charge and reduce the surface energy [9, 25, 26]. The crystal surface with the bonded atoms is most stable. The study of such atomic detail, including both the cation and the oxygen sub lattices, provides access to stoichiometry and structural defects in manganite NWs.

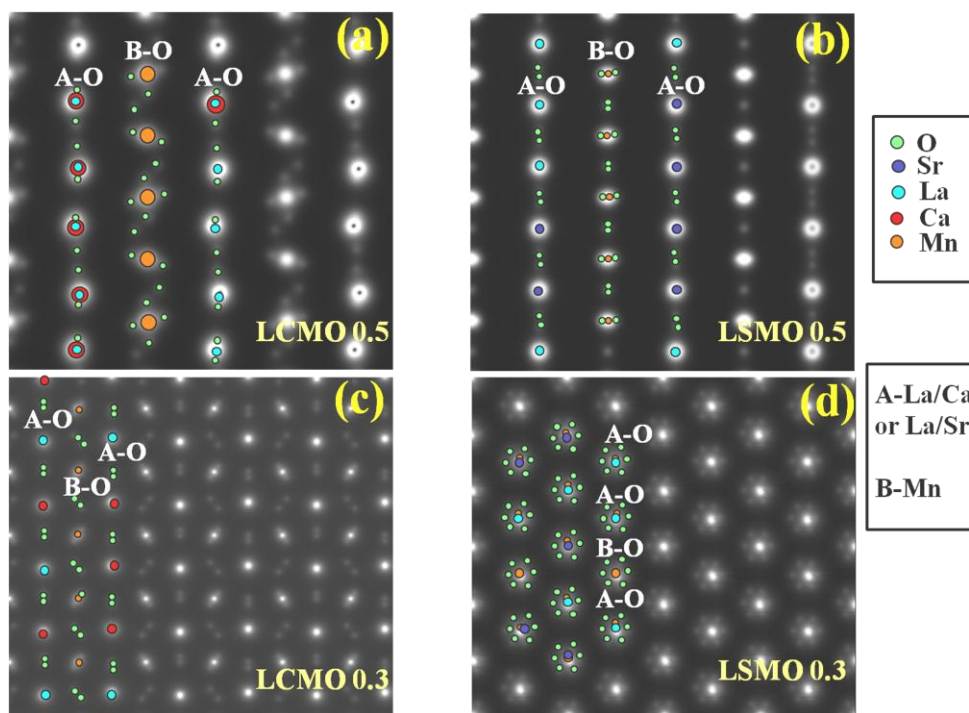


Figure 3.16 (a,c) Showing atomic column structure and arrangements of the layered atoms in LCMO-0.5 and LCMO-0.3 (b,d) Showing atomic column structure and arrangements of the layered atoms in LSMO-0.5 and LSMO-0.3. The colour code of each element is shown at the side of the picture. To understand the termination site (A-O or B-O) La/Ca or La/Sr is marked A and Mn is marked B.

3.5 Conclusion

In this thesis, elemental analysis using EELS measurement and structural simulation using JEMS have been combined as a whole to define the growth mechanism which has been already discussed in chapter 2. Our results strongly suggest that image simulations and analysis must be coupled in order to get a precise knowledge of the structure. Knowledge of the crystal structures involves a corresponding understanding of the effects that the large reciprocal space function of the NW contains on the analysis. For advanced characterization of functional materials that usually contain cations with mixed valences, EELS is a very powerful technique which allows detailed compositional analysis in nano-domain with a

spatial resolution higher than other spectroscopy techniques available. The details of elemental characterization using EELS data reveal the valence of transition metal, Mn ion which is an important issue in mixed valent compound like manganite. Since EFTEM is based on EELS, it also offers superior energy resolution (when compared to EDAX) for elemental mapping. The mixed valence of Mn as estimated from EELS study showed us a way for the need of the study of structural distortions in MnO_6 octahedra (change in Mn-O-Mn bonds) which can justify the physical measurements. Hence a requirement for structural analysis comes into play in our work and JEMS provides us this opportunity.

Analysis of HRTEM diffraction data of JEMS software provides us an idea about the growth mechanism, how the OH^- ion of mineralizer KOH helps in bonding and initiates the growth and also the growth direction. In our case of single NWs of LSMO the growth direction is different for both compositions (LSMO-0.3 along [110] and LSMO-0.5 along [112]) and a contraction in the c -axis of the crystal is noticed in comparison to the bulk (which is also confirmed from synchrotron data in chapter 6). This may be due to the attachment of OH^- ions with the A-site (positively charged ions) along the long axis direction of the NWs that reduces the overall surface energy contribution and leads to a growth along a particular direction (LSMO-0.3 along [110] and LSMO-0.5 along [112]). On the other hand, in case of another manganite NW, i.e., LCMO-0.3 it was seen that twins are formed with the possibility of the distortion in the MnO_6 octahedra due to the possible attachment of K^+ ions. But the change in the doping concentration changes the scenario and leads to the growth along [121] in case of LCMO-0.5 leading to the reduction of the overall surface energy along the long axis direction of the NWs. Hence along with the effect of mineralizer it has been shown that other factors like doping concentration are also involved in the growth of a NW along a particular direction. In cases of manganite nanostructures, a layered oxide material termination at certain site (AO or BO) controls the physical properties as well as their growth mechanism [9]. Hence the micro-structural study along with the image simulation or analysis in the atomic scale is an important tool to correlate the structure-property in manganite system which has been clearly explained in this chapter. Lastly, our work also provides a complete knowledge about a technique which provides opportunities to study lattice imperfections, like stacking disorder, twinning and layer undulations, with atomic scale resolution in comparison to a conventional HRTEM which completely fails in obtaining directly interpretable images due to its aberration limitations.

Bibliography:

- [1] Z. L. Wang and Z. C. Kang, 1998. *Functional and Smart Materials—Structural Evolution and Structure Analysis*, Plenum Press, New York.
- [2] R. von Helmolt, J. Wecker, B. Holzapfel, L. Schultz and K. Samwer, *Phys. Rev. Lett.*, **71**, 2331–2334 (1994).
- [3] S. Jin, T. H. Tiefel, M. McCormack, R. A. Fastnacht, R. Ramech and L. H. Chen, *Science*, **264**, 413–415 (1994).
- [4] P. A. Stadelmann, *Ultramicroscopy*, **21**, 131–146 (1987).
- [5] R. F. Egerton, *Electron Energy-Loss Spectroscopy in the Electron Microscope, Third Edition*, Springer (1996).
- [6] R. F. Egerton, *Rep. Prog. Phys.*, **72**, 016502 (2009).
- [7] www.gatan.com.
- [8] Z. L. Wang, J. S. Yin and Y. D. Jiang, *Micron* **31**, 571–580 (2000).
- [9] S. Datta, A. Ghatak and B. Ghosh, *J. Mater. Sci.*, **51**, 9679–9695 (2016).
- [10] S. Datta, S. Chandra, S. Samanta, K. Das, H. Srikanth and B. Ghosh, *Journal of Nanomaterials*, vol. **2013**, Article ID 162315, 6 pages, 2013. doi:10.1155/2013/162315.
- [11] B. Ghosh, V. Siruguri, A. K. Raychaudhuri and T. Chatterji, *J. Phys. Condens. Matter.*, **26**, 025603–025611 (2014).
- [12] E. I. Suvorova, P. A. Stadelmann and P. A. Buffat, *Crystallogr. Rep.*, **49**, 343–352 (2004).
- [13] E. J. Kirkland. *Advanced Computing in Electron Microscopy*. Plenum, New York, 1998.
- [14] V. Moshnyaga, B. Damaschke, O. Shapoval, A. Belenchuk, J. Faupel, O. I. Lebedev, J. Verbeeck, G. V. Tendeloo, M. Mucksch, V. Tsurkan, R. Tidecks and K. Samwer, *Nat. Mater.*, **2**, 247–252 (2003).
- [15] C. L. Jia, M. Lentzen and K. Urban, *Science*, **299**, 870–872 (2003).
- [16] A. Ghatak, S. Roy Moulik and B. Ghosh, *RSC Adv.*, **6**, 31705–31716 (2016).
- [17] W. Coene, G. Janssen, M. Op de Beeck and D. Van Dyck, *Phys. Rev. Lett.*, **69**, 3743–3746 (1992).
- [18] C. L. Jia and A. Thust, *Phys. Rev. Lett.*, **82**, 5052–5055 (1999).
- [19] Z. H. Wang, O. I. Lebedev, G. Van Tendeloo, G. Cristiani and H.-U. Habermeier, *Phys. Rev. B*, **77**, 115330 (2008).

- [20] J. Blasco, J. Garcia, J. M de Teresa, M. R Ibarra, P. A. Algarabel and C. Marquina, *J. Phys. Condens. Matter*, **8**, 7427–7442 (1996).
- [21] M. H. Aguirre, S. Canulescu, R. Robert, N. Homazava, D. Logvinovich, L. Bocher, T. Lippert, M. D€obeli and A. Weidenkaff, *J. Appl. Phys.*, **103**, 013703–013708 (2008).
- [22] A. Weidenkaff, M. H. Aguirre, T. Lippert, U. Falke and U. Bangert, *Chimia*, **60**, 742–748 (2006).
- [23] Q. Zhang, S.-J. Liu and S.-H. Yu, *J. Mater. Chem.*, **19**, 191–207 (2009).
- [24] J. Zhang, F. Huang and Z. Lin, *Nanoscale*, **2**, 18–34 (2010).
- [25] J. Zhang, Z. Lin, Y. Lan, G. Ren, D. Chen, F. Huang and M. Hong, *J. Am. Chem. Soc.*, **128**, 12981–12987 (2006).
- [26] C. Ribeiro, C. M. Barrado, E. M. Camargo, E. Longo and E. R. Leite, *Chem. Eur. J.*, **15**, 2217–2222 (2009).
-

Chapter 4

Device fabrication and measurement techniques

In this chapter, we have discussed different nanolithography techniques used to combine nano-devices for single nanowire (NW) measurements. By the word 'device' we entail NWs connected to 4 electrodes that are required for electrical transport as well as $1/f$ noise measurements. We have fabricated nano device from the synthesized and well characterized NWs which is an important aspect of this thesis. We have used photolithography, electron and ion beam lithography process for single NW device fabrication. We have also discussed the experimental techniques such as temperature dependent electrical, magneto transport study including noise spectroscopy measurement. The measurement setups are automated by General Purpose Interface Bus (GPIB) interfacing with C++ programming for data acquisition. For magnetization (D.C and A.C) measurement, we have used Vibrating Sample Magnetometer (VSM) technique.

4.1 Introduction

In the modern field of nanoscience and nanotechnology, fabrication of high quality nanostructure is most important for nanodevices. To understand and make use of the unique physical, chemical, electrical and optical properties of materials at nanoscale, we are working at the nanoscale region. The combination of nano structures and nano materials with macroscopic systems can be very challenging in nanotechnology. To comprehend the physical behaviour in nanoscale, nanodevices have to be interfaced with macro electronic systems which are possible through various nanofabrication techniques. The most used fabrication processes are photo, electron and ion beam lithography. Utilization of lithography for device fabrication reveals the field not only for new fabrication schemes, but the incorporation of different material systems into the field of nanodevices. In this thesis, our aim is to investigate the temperature dependent electrical, magneto transport study as well as noise spectroscopy measurement of $\text{La}_{0.5}\text{Sr}_{0.5}\text{MnO}_3$; at nanoscale, particularly at the level of single NW. So, according to the experimental requirement, various nanodevices have been fabricated. In this chapter, we will discuss important specific sub-area i.e. different methods of nano fabrication along with experimental techniques used for measurement.

4.2 Lithography processes

Lithography is a process of patterning fine scale structures onto a substrate. Printer is a well-known example of lithography. Generally this system uses radiation to expose the recording medium, known as resist. Over the last few decades, different kinds of lithography techniques have been developed based on the type of exposure radiation such as optical, X-ray, electron beam and ion beam lithography. Fabrication of device structures which have dimensions approaching to micron or even nanometre size requires doing lithography techniques. In this thesis, *photo lithography*, *electron beam lithography* (EBL) and *ion beam lithography* which are mostly used for device fabrication will be discussed briefly.

4.2.1 Photo lithography

Photo lithography process is used in nano/micro fabrication to pattern part of a film or a substrate which uses light to transfer a geometric pattern from a photo mask to a light sensitive chemical called resist. Photo lithography is consisted of four main elements such as (i) illumination system with energy source, (ii) mask containing the pattern to be fabricated, (iii) exposure system to produce an aerial image of the mask pattern and (iv) a medium known as 'photo resist' or resist for recording the image produced by the exposure system. There is a parallel growth of all the nanostructure using photo-mask reducing the fabrication time considerably. Photo lithography has a disadvantage that it is difficult to fabricate sub-micron nanostructure because of its resolution limitation by the diffraction of light.

4.2.1.1 The steps for photo lithography process and transferring it to a substrate

The general procedure followed in photo lithography process is described below which is also schematically shown in Fig. 4.1.

1. **Substrate cleaning:** The Si/SiO₂ substrates used for photo lithography are at first cleaned by boiling them at 70° C for 15 minutes each in trichloroethylene (TCE), acetone and methanol and followed by standard RCA (RCA stands for Radio Corporation of America, an electronics company) cleaning, where the substrates are boiled in 1:1:5 volume ration of NH₄OH:H₂O₂: DI (de-ionized) water at 75-80° C for 10 minutes to take out the organic materials. The substrates are then rinsed in DI water and again boiled in 1:1:5 (volume ration) of HCl: H₂O₂: DI water at 70-80°C for 15 minutes to remove the ionic contaminations followed by rinsing in DI water. Before using, the substrates are ultrasonicated in acetone and isopropyl alcohol (IPA) and dried in flow of nitrogen gas.

2. **Resist coating:** The substrate is placed on a rotating platform of a spin coater via vacuum suction. Resist is two types i.e. positive and negative. In positive resist, exposure to UV removes resist such as acetone, TCE, Phenol. On the other hand, in negative resist (such as, Methyl ethyl ketone, methyl isobutyl ketone, SU 8) exposure to UV become cross-linked, while the remainder of the film remains soluble and can be washed away during development. We have used SU-8 which is an epoxy-based negative photo resist. SU-8 is spin coated on top of the substrate with 3000 rpm for 40 second. One has to take care to

ensure that the resist spreads uniformly over the whole surface of the substrate without any air bubble. Then the substrate is prebaked in an oven at 90-100° for 15 min to remove solvent in the resist and enhances the adhesion between the resist and the substrate.

3. **Pattern writing:** We have used contact printing method for pattern writing. The photo mask is placed on the substrate and UV is exposed through mask for 90 second. Then the substrate is post baked in an oven at 60-70° for 10 min. The substrate is developed in SU-8 developer solution for 20-30 second followed by a rinsing process in IPA solution.

4. **Metal deposition and lift-off:** After the patterns are developed, the metals for contacts are deposited in a high vacuum chamber. The deposited material thickness has to be at least one-third of the bottom layer resist thickness for successful lift-off. In high vacuum, metal is deposited onto the developed substrate. Metal coated sample is then immersed in SU-8 remover. This removes the remaining resist along with film on top of resist except the film in contact of the substrate after deposition which created the pattern. This process is called 'Lift-off'. For making electrical contacts we use a thin layer of Cr (~10 nm) for adhesion to the SiO₂ based substrate. This is followed by Au evaporation of ~ 50–100 nm.

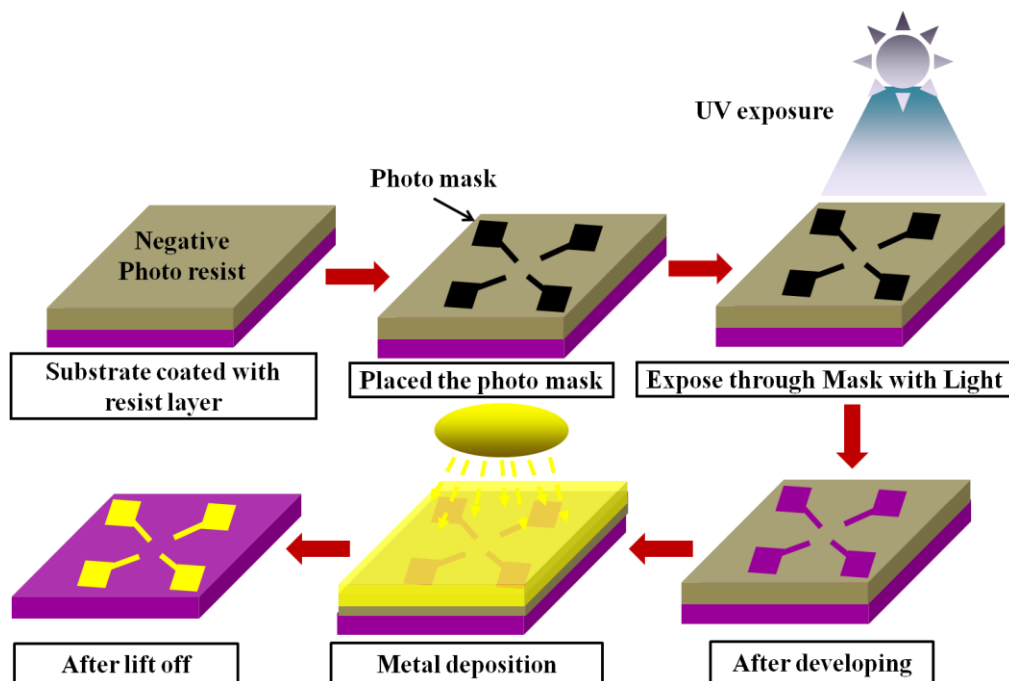


Figure 4.1 Schematic flow chart of photo lithography process.

4.2.2 Electron beam lithography (EBL)

In Electron beam lithography (EBL) technique, a focussed beam of electrons is used to expose an electron sensitive resist to write patterns on the substrate. The electrons are scanned using pattern generator software on a surface of the substrate covered with resist. The resolution of EBL is much higher than that of photo lithography because of the thinner resist thickness (\sim nm) and shorter wavelength (\sim 0.01 nm) of the high energy (keV range) electron beam used in EBL technique. This gives the possibility to form the nano scale patterns.

We have used a Scanning Electron Microscope (SEM) with a Field Emission Gun (FEG) attached with a beam blanker that turns the e-beam ‘on’ and ‘off’ during raster scan. The electron source of the SEM is used for writing patterns as shown in Fig. 4.2 (a) and the photograph of our SEM improved EBL system is shown in Fig. 4.2 (b). Electron column usually consists of an electron gun - a source of generating electron beam, two or more lenses to condense the beam, scan coils for deflecting the beam, a blanker for turning the beam on and off, a stigmator for correcting any astigmatism in the beam and finest focusing of the specimen, apertures to facilitate in defining the beam, alignment systems for centering the beam in the column and finally, an electron detector for focusing and locating marks on the specimen.

4.2.2.1 The steps for generating EBL and transferring it to a substrate

A general process flow for obtaining an EBL patterned sample is schematically shown in Fig. 4.3. Positive e-beam resist PMMA (Polymethyl methacrylate) is coated on the cleaned Si/SiO₂ substrates. In positive resist, the area of the resist exposed by electron-beam is removed when immersed in developer solution and exposure of e-beam changes the chemical structure and breaks the chain of the polymer resist so that it becomes more soluble in the developer solution. In this thesis work, we have used positive e-beam resist as we used lift-off process to create metal electrodes/interconnect.

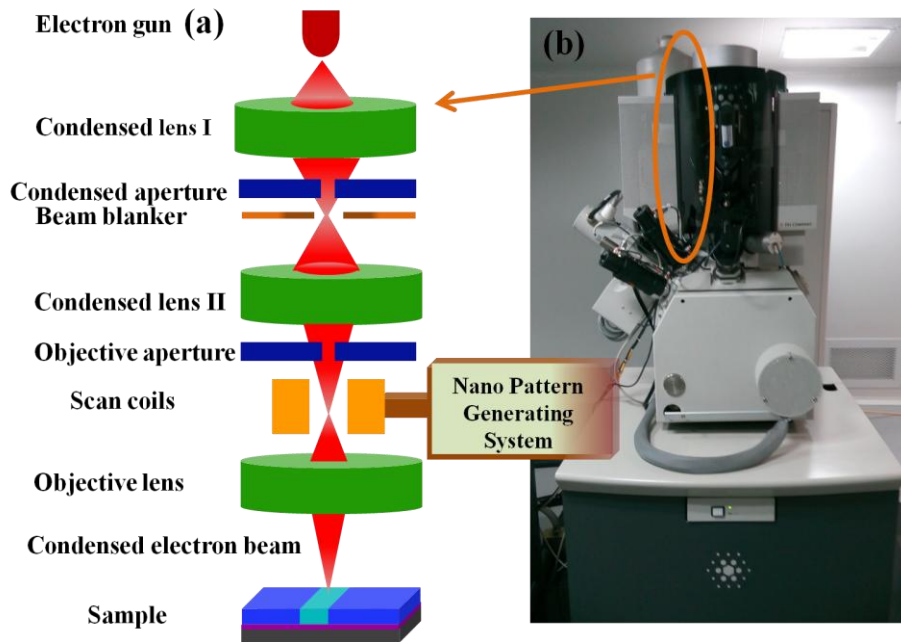


Figure 4.2 (a) Schematic diagram of electron beam column. (b) The photograph of Electron beam lithography system.

Resist is coated on the sample with PMMA 350K at rpm 3000 for 40 second and then baked on a hotplate at 180°C for 2 minutes. A high molecular weight resist (950K PMMA) is coated at rpm 6000 for 40 second on top of a slightly more sensitive bottom layer of low molecular weight resist (350K PMMA) and baked at 120°C for 1 hour. Now, the sample is ready for writing with e-beam and mounted on SEM sample stage. Desired pattern are formed by Nano Pattern Generating System (NPGS) software and written the pattern by e-beam on resist coated substrate by control of scan and beam blanker. NPGS is nano pattern generating system software equipped with FEI HELIOS 600 systems, mainly used by the researchers to create nano size pattern for EBL process. We are using NPGS containing DesignCAD 2008 in FEI HELIOS 600 microscopic system to create pattern to be transferred to the substrate. For writing a pattern user has to control the line spacing between two scanning line, dose, beam current with which pattern has to be exposed and also some degree of magnification. Dose can be given as area dose ($\mu\text{C}/\text{cm}^2$), line dose (nC/cm) or point dose (fC) depending on the created pattern. Beam current and dose are interrelated as $D \times A = I \times t$, where A is dimension (area or length) of the pattern, D is dose, I is beam current and t is exposure time. Large patterns are usually separated into layers so that different patterns can be written with

different beam exposures. Normally larger patterns are written with area dose ($250 - 300 \mu\text{C}/\text{cm}^2$) and higher current ($2700 - 1400 \text{ pA}$), whereas smaller patterns are with line dose ($2 - 3 \text{ nC}/\text{cm}$) and lower current ($11 - 21 \text{ pA}$). According to the user necessity, CAD design is used to illustrate a detailed design and converted to the proper EBL system compatible format (e.g. .DC2 file). Next, correction is done through EBL software and compile to a machine-executive file. Finally, exposure can be applied followed by developing to obtain the required patterns. The substrate is then developed in an e-beam developer (MIBK: IPA=1:3) for ~ 10 seconds then cleaned in IPA and dried with nitrogen gas flow, where, MIBK stands for methyl isobutyl ketone. After the patterns are developed, the Au/Cr metals for contacts are deposited which is done same as in photo lithography process. Metal coated sample is then dipped in acetone for lift off process. In this thesis, EBL system has been used to prepare single NW device for electrical measurement by making four wire electrical contacts on a single NW.

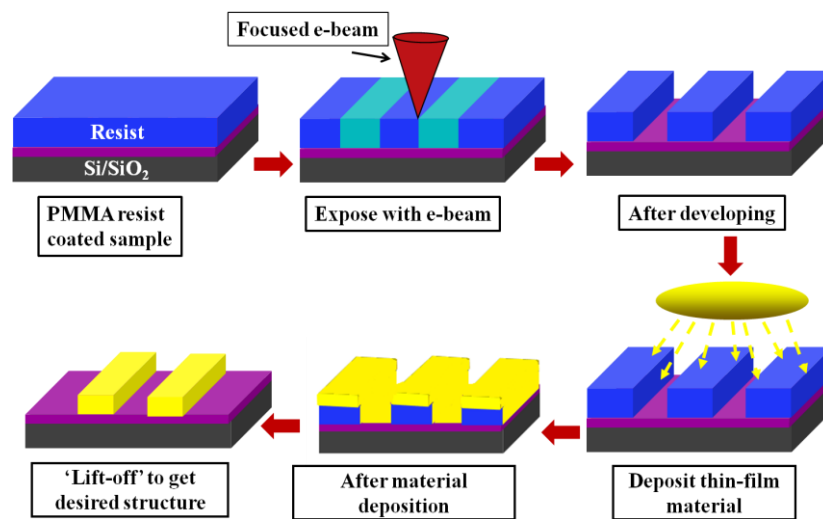


Figure 4.3 Schematic flow chart of EBL process.

4.2.3 Focused ion beam (FIB) lithography

Focused ion beam (FIB) is an efficient and powerful technique for mask less and resistless lithography to construct micro and nano structures and devices. In this process, a metal is directly deposited onto a cleaned substrate from a precursor without any use of resist. The instrument used in this work has dual beam sources: one source is a field emission electron gun (SEM source) which is used for EBL process as described previously and another is a FIB (Gallium ion) source which is used to deposit metal and cutting/milling. In this system Ga⁺ ion is used as liquid metal ion source (LMIS) due to the following advantages including

(i) low melting point, (ii) low vapour pressure, (iii) low volatility (iv) excellent mechanical, electrical and vacuum properties and (v) emission characteristics enabled high angular intensity with a small energy spread. For patterning, we have mounted the sample on the stage and inserted into the chamber which is then evacuated. When the vacuum is reached inside the chamber, the sample stage is tilted to 52° (Fig. 4.4 (a)) in steps to reach the eucentric point which is essentially a particular stage height where the sample image does not move. After all this adjustment, both electron and ion beam are used according to the requirement to deposit Platinum (Pt). The Pt deposition is achieved by the electron/ion beam assisted decomposition of methylcyclopentadienyl platinumtrimethyl $(\text{CH}_3)_3(\text{CH}_3\text{C}_5\text{H}_4)\text{Pt}$, which is a metal-organic gas precursor for Pt metal. Schematic illustration of Ga ion source is shown in Fig. 4.4 (b). During Pt deposition using FIB column sample is tilted at 52° opposite to FIB column to make the sample surface vertical to ion column. However, for focused electron beam (FEB) deposition we don't require to tilt the sample-stage as its surface is usually vertical to electron column. This ion/electron beams are accelerated collimated and focused by a series of apertures and electrostatic lenses on to the sample. Electron/Ion bombardment on the sample produces large amount of secondary electrons which collide and dissociates the precursor gas and take apart Pt from carbon based precursor. Pt produced by decomposition of precursor is then deposited onto the surface of substrate and gaseous residues are pumped out. As ionic mass is larger, ion beam momentum is much higher compared to electron beam which may damage the sample; however the deposition process is faster. Instead, only electron beam assisted Pt deposition takes longer time for the whole process. Thus, to avoid the sample from direct ion bombardment, we always choose electron beam assisted deposition near the sample and ion beam deposition far away from it which save the sample from damage and make the whole process relatively quicker. Fig. 4.4 (c) shows an SEM image of a single NW device connected with Pt using both FEB (near the sample) and FIB (far from the sample) source. For e-beam deposition we have used 86 pA beam current and 30 kV accelerating voltage, whereas ion beam deposition has been performed with accelerating voltage of 15 kV and beam current of 43 pA.

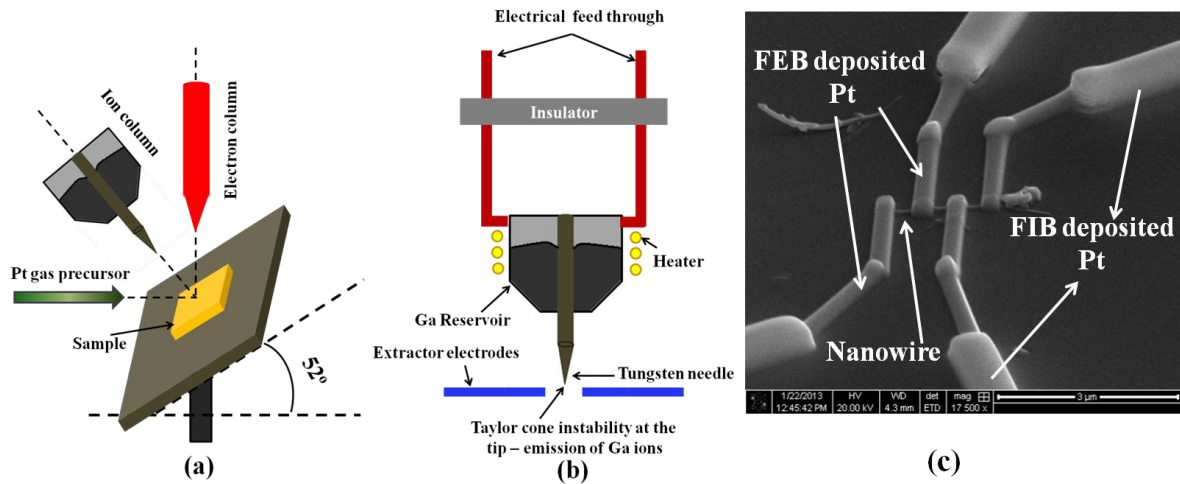


Figure 4.4 Schematic of (a) typical dual-beam column configuration, (b) Gallium ion source, (c) SEM images of single NW device connected with FEB (near the NW) and FIB (far from the NW) deposited Pt.

4.3 Device Fabrication

In this thesis, the single NW device fabrication with top-down approach i.e. attaching contacts to prefabricated NWs mainly is performed using nano lithography techniques. To make the four-wire electrical contacts with single NW, Au/Cr (100 nm/10 nm) contact pads are deposited on SiO₂ (300 nm thick)/Si (insulating) substrate by photo lithography and thermal evaporation methods as shown in schematic of Fig. 4.5 (a) [1-2]. For electrical transport measurements, the NWs dispersed in ethanol solvent are drop casted on a SiO₂/Si substrate (Fig. 4.5 (b)). A single NW (diameter < 50nm) is identified by SEM. It is then connected with pre-fabricated external Au electrodes by a combination of both FIB and FEB deposited Pt (Fig. 4.5 (c)) as described in FIB/FEB lithography section. FEB deposition is done over the NWs to avoid wire damage due to ion exposure. Deposition of Pt is done by focused electron beam (FEB) at a voltage of 30 kV and deposition current of 86 pA. Four wires are connected to NW shown in Fig. 4.5 (d). The enlarged view (Fig. 4.5 (e)) is marked by blue circle region of Fig. 4.5 (d). The separation between two consecutive probes is around ~200 nm. Each contact pad has width of ~ 300 nm.

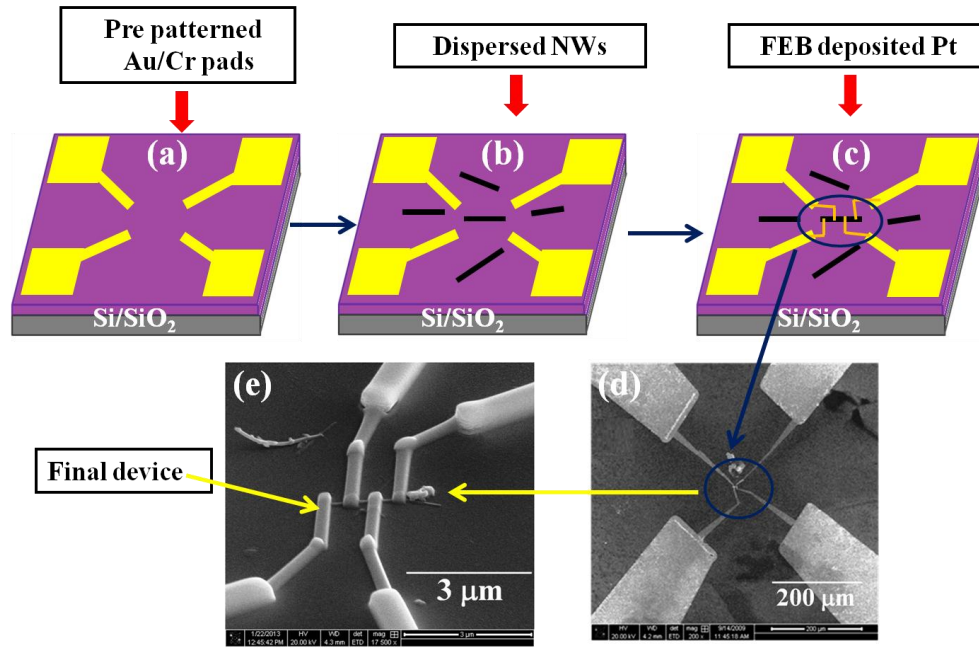


Figure 4.5 Schematic representation of device fabrication by top-down approach with SEM image of four probe configuration.

4.4 Experimental Techniques

4.4.1 Electrical and magneto transport measurement

The temperature (T) dependent electrical, magneto transport including noise spectroscopy measurements are performed using standard four probe electrode configurations. In four probe configurations, outer probes are used to provide current (I) and inner two probes are to determine voltage (V) drop across the sample. We have measured resistance (R) – T and I – V on single NW in cryogen-free variable temperature insert and $1/f$ noise measurement in cryogenic system. In the cryogenic system, temperature range of measurement is from 300 K to 77 K. Here, liquid nitrogen is used for cooling the sample stage. In the cryogen-free system, measurement has been performed from 300 K to 5 K where helium gas is used for sample stage cooling.

The electrical and magneto transport measurement are performed in a commercial cryogen free Variable Temperature Insert (VTI) system from Cryogenic limited [3]. A single two stage Gifford-McMahon cryo-cooler is used to generate temperatures around 4 K and the normal achievable temperature range is 4–325 K. Main components of VTI measurement set

up are (i) a cryostat (vacuum insulated chamber whose primary function is to support and thermally shield the superconducting magnet and VTI), (ii) superconducting solenoid magnet, (iii) cryo-cooling system (vacuum pump, helium gas flow system and compressor) (iv) a variable temperature insert (VTI) and (v) a sample mounting stick containing calibrated cernoxTM [4] temperature sensor, heater, sample mounting stage along with electrical wires for connections. Schematic representation along with an image of the cryogen free VTI system is shown in Fig. 4.6. The magnetic field is applied by a 14 Tesla superconducting magnet system equipped with the VTI. The magnet is prepared in a solenoid form consisted of copper stabilised filamentary superconducting wire of NbTi (outer coil) and Nb₃Sn (inner coil).

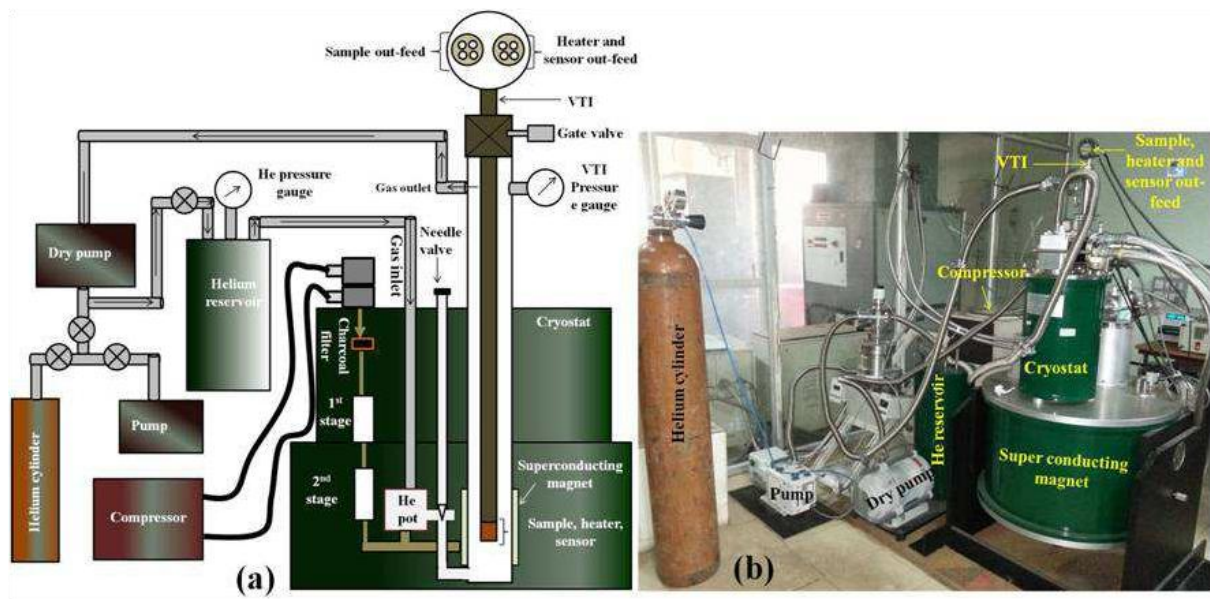


Figure 4.6 (a) Schematic representation of cryogen free VTI measurement system. (b) Image of the entire set up. Courtesy: Ref. [7].

We have measured the temperature (T) variation of resistance (R) of the samples by passing a very low current of $1\mu\text{A}$ through the sample and measuring the voltage drop across the sample to calculate the resistance from the applied current and measured voltage drop in a four probe configuration to avoid unnecessary Joule heating and contact resistance effect in the samples. We have used thermally evaporated Au/Cr pads (thickness of Au, Cr is $\approx 100\text{nm}$ and 10 nm respectively) for electrical contacts and highly conductive silver paint is used to connect Cu wires to a single NW sample under investigation. We have used source meter (Keithley 2410, 2400 source meter (SM)) [5] for applying constant current or voltage across

the sample and to measure corresponding voltage or current respectively across the sample and Lakeshore (Model 340) [6] is used to control temperature in four probes configurations in DC techniques. The control of the magnet and VTI system is totally automated and run with a Cryogenic labview programme. Temperature dependent resistivity with and without field are automated by General Purpose Interface Bus (GPIB) interfacing using C++ programs.

4.4.2 Noise spectroscopy measurement

Study of resistance fluctuations or noise is an important technique to investigate the low frequency dynamics in condensed matter systems [8-11]. Noise in a current carrying conductor shows a power spectrum $S_V(f) \propto 1/f^\alpha$ with $\alpha \sim 0.8-1.2$ and this is denoted as “1/f noise”. In noise measurements, the sample is generally current biased by a low noise source and the fluctuations in the voltage developed across the sample $\delta V(t) = V(t) - \langle V \rangle$ (where $\langle V \rangle$ is the average voltage) is measured. One experimentally measures the fluctuations in voltage $\delta V(t)$ as a function of time about its mean value. The most general method to quantitatively represent the voltage fluctuation through its power spectral density (PSD) $S_V(f)$ is defined as:

$$S_V(f) = \lim_{T \rightarrow \infty} \frac{1}{2T} \left[\int_{-T}^T \delta V(t) \exp(-2\pi i f t) dt \right]^2 \quad (4.1)$$

The power spectral density obtained from the cosine transform of the autocorrelation function $C_V(\tau)$ is defined as:

$$C_V(\tau) = \lim_{T \rightarrow \infty} \frac{1}{2T} \int_{-T}^T \delta V(t+\tau) \delta V(t) dt \quad (4.2)$$

The spectral power is determined on the time scale of the fluctuations over the frequency range. This consecutively depends on the dynamics associated with the underlying physical process that causes the fluctuations. Usually, if the dynamics is taking place at a time scale τ , it will show up in the power spectral density as a Lorentzian $2\tau / (1 + (2\pi f \tau)^2)$ with a corner frequency $f_c = 1/2\pi\tau$. With a distribution of relaxation time $D(\tau)$ the power spectrum is a superposition of Lorentzians and is given by [8]:

$$S_V(f) = \int_0^\infty d\tau D(\tau) 2\tau / (1 + (2\pi f \tau)^2) \quad (4.3)$$

4.4.2.1 The noise measurement setup and data acquisition

Our experimental set-up is competent of temperature dependent a.c resistivity measurement as well as $1/f$ noise measurement at different temperatures. The setup is always reserved isolated from all external noise sources like electromagnetic radiations, mechanical vibrations, power line fluctuations, any kind of electrical sparking and improper grounding of the measuring instruments. The temperature range is from 350 K down to liquid Nitrogen temperature 77 K. The complete design of the cryostat is shown in the Fig. 4.7. The cryostat is composed of two non-magnetic stainless steel hollow cylinders which have high mechanical strength and low thermal conductivity as this will reduce the heat load coming from the top of the cryostat to the sample through the required temperature range. For heater we used a 4 feet length of Manganin wire of resistance ($12.5 \Omega/\text{foot}$) wound on a copper bobbin at the end of the sample holder. Thermometer (Pt-100 film thermometer for 77-350 K) is mounted on the sample holder by GE-varnish at opposite face of the copper plate where sample is mounted as shown in Fig. 4.7. GE-varnish is used as it is good thermally conducting and electrically insulating medium required for any low temperature measurement. The thermometer and its leads are cautiously mounted and thermalized so that they can add very little thermal fluctuations at a particular temperature. For carrying the signal inside the cryostat from the sample to the BNC connectors located at the top of the sample insert we used silver co-axial cables [12].

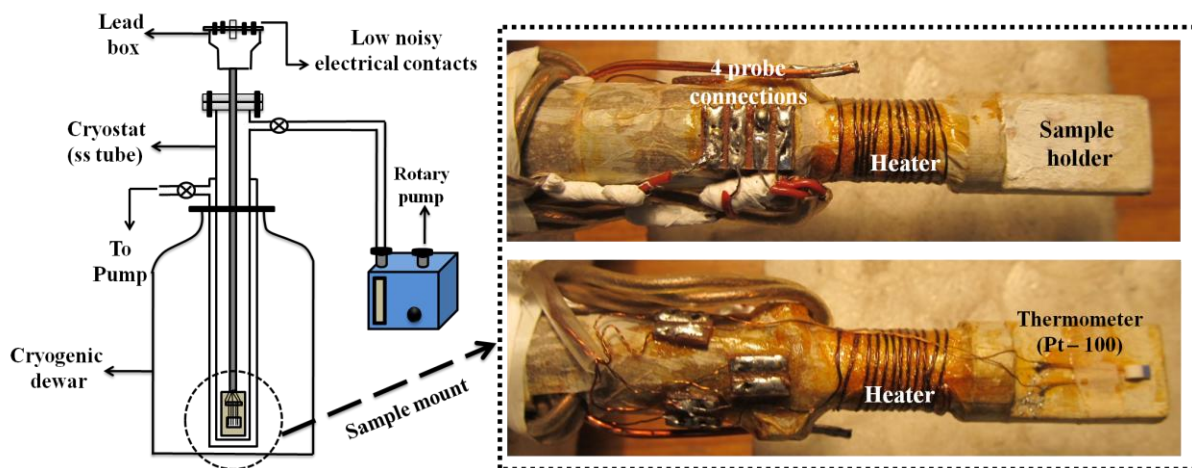


Figure 4.7 Schematic diagram of the cryostat used for noise measurement setup.

Our low frequency noise measurement technique is based on a 4-probe ac-detection system [13] as shown schematically in Fig. 4.8. During the measurement the cryostat is dipped in the

liquid Nitrogen Dewars and the temperature of the sample is measured using a digital temperature controller from Lakeshore (model: 340) using PID control [6]. The temperature stability is always maintained ~ 2 mK. The sample is biased by an ac signal from dual channel lock-in amplifier (LIA) SR830 [14] at a frequency f_0 . The voltage developed across the sample is amplified by preamplifier (SR554) whose output is detected by the same LIA [15]. But it is highly recommended to use a preamplifier to match the impedance of the sample with the input impedance of the LIA. The fundamental steps regarding noise detection are as follows:

- To measure voltage fluctuations across the sample we have made the system as a constant current bias system by using a standard resistor (R_0) in series as shown in Fig. 4.8. The average voltage signal $\langle V \rangle$ coming from the input channel of the LIA is digitally subtracted off by the LIA to provide the fluctuating component $\delta V(t)$ of the signal.
- $\delta V(t)$ is considerably amplified (usually 100 times) by the preamplifier used.
- The amplified signal $\delta V(t)$ is demodulated by the LIA to provide the noise sub bands at frequencies $f \pm \Delta f_0$ where Δf is the frequency at which noise signal required to be measured.
- The time constant τ_{LIA} of LIA's intrinsic low-pass filter at output channel is constant so that $\Delta f_{\max} = 1/(2\pi\tau_{LIA})$ where Δf_{\max} is the maximum frequency at which noise signal can be obtained.
- The signal from the preamplifier output channels are fed to the input channels of LIA and can be amplified more to increase the sensitivity of the measurements depending on the experimental requirements.
- Then the output channels of LIA are connected to the computer motherboard for data collection. The LIA output data is in analog form whereas computer collects the data in digital format. So we have used a dual channel analog-to-digital (ADC) data converter (PCI-DAS6036, 32 bit and 200ksamples/sec) [16] to transfer the data from LIA to computer via a PCI-slot commercially available with the data converter as shown in Fig. 4.8. There is a C++ program which is used for data collection process.

To obtain the “uncorrupted” time series free from background fluctuations, we have used Weiner filter [17] to remove the background signal. We get an in-phase component containing sample information only using Weiner filter. This filter translates the time domain signals into frequency domain and then retains only that fraction of the power that corresponds to the “excess” or $1/f$ noise over the background. It then re-transforms the

“cleaned” spectrum into the time domain to generate an “uncorrupted” time domain signal. The power spectral density of the uncorrupted time domain signal contains only the “excess” noise with the background signal removed.

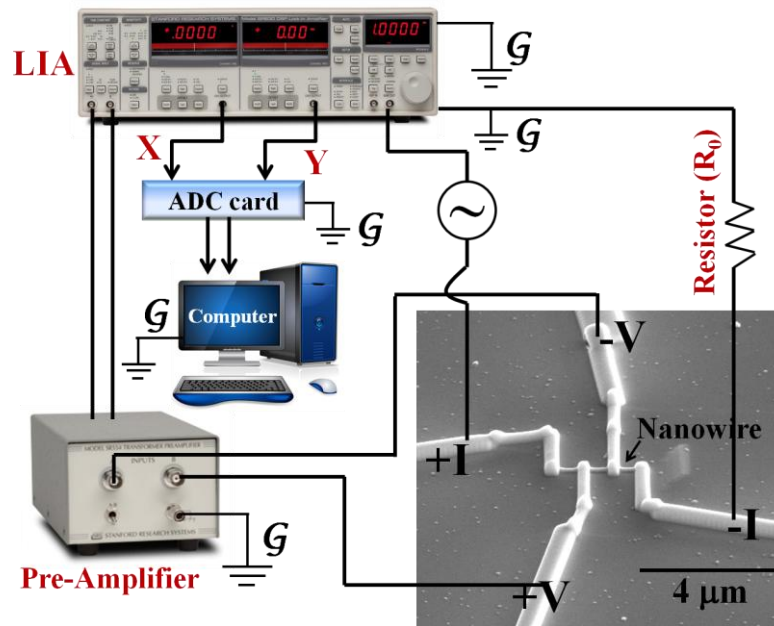


Figure 4.8 Schematic diagram of four-probe noise measurement technique. The ac voltage bias is fed to the sample from LIA and a standard resistor is connected in series with the sample. The voltage drop across the voltage probes on the sample is fed to the low-noise preamplifier input. The amplified signal goes to the input channels of the LIA. The data is collected via ADC card by the computer.

4.4.3 Magnetization measurements

The magnetic measurements were carried out on ensemble of NWs of the sample ($\text{La}_{1-x}\text{A}_x\text{MnO}_3$; $\text{A} = \text{Sr}, \text{Ca}$, $x = 0.3$ and 0.5) using a commercial Vibrating Sample Magnetometer (VSM) [18] from Lakeshore (Model 7400 series) and Quantum Design Physical Property Measurement System (PPMS) equipped with VSM [19]. The schematic of VSM is shown in Fig. 4.9. VSM is used to measure magnetic behaviour with the variation of temperature (T) and field (H) of magnetic materials. VSM operates on Faraday’s Law of Induction according to which a changing magnetic field will produce an electric field. This electric field can be measured and can provide us information about the changing magnetic field. The sample is placed in a fixed magnetic field and oscillated with a fixed frequency near a set of detection

(pick-up) coils. The constant magnetic field induces a magnetic dipole moment in the magnetic sample.

This magnetic dipole moment produces a magnetic field around the sample, known as the magnetic stray field. As the sample is moved vertically up and down (Z direction), this magnetic stray field varies as a function of time and the voltage induced (proportional to the rate of change of flux) can be detected by pick-up coils. The alternating magnetic field (changing magnetic flux ϕ) causes an induced voltage in the pick-up coils according to

Faraday's Law of Induction i.e $V_{induced} = \frac{d\phi}{dt} = \frac{d\phi}{dz} \frac{dz}{dt}$. This induced voltage is proportional to

the magnetization of the sample. If the sample is vibrating sinusoidally, then the induced voltage in the pickup coils will have the form $V_{induced} = cmA\omega \sin \omega t$, where, c is a coupling constant, m is the DC magnetic moment of the sample, A is the amplitude of oscillation and $\omega = 2\pi f$, where, f is the frequency of oscillation of the sample. The detection of the magnetic moment of the sample, thus, measures the coefficient of sinusoidal voltage response induced in the detection coil.

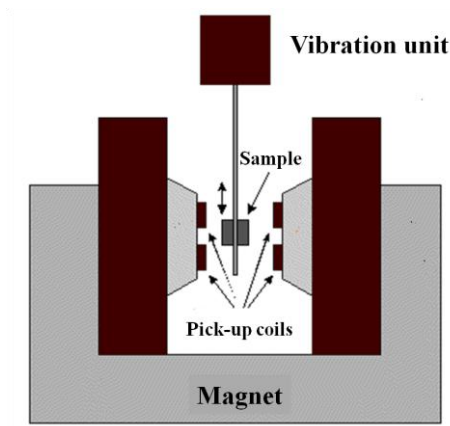


Figure 4.9 Schematic illustration of VSM instrument.

Bibliography:

- [1] S. Datta, S. Chandra, S. Samanta, K. Das, H. Srikanth and B. Ghosh, *Journal of Nanomaterials*, vol. **2013**, Article ID 162315, 6 pages, 2013. doi:10.1155/2013/162315.
- [2] S. Datta, S. Samanta, B. Ghosh and A. K. Raychaudhuri, *Appl. Phys. Lett.*, **105**, 073117 (2014).
- [3] Cryogenic 1.5K VTI system manual.
- [4] Lakeshore Cryotronics Inc. 575, Mc Corkle Blvd, Westerville, Ohio, 43082, USA.
- [5] <http://www.keithley.com>.
- [6] <http://www.lakeshore.com>.
- [7] R. Basori “Investigation of Growth, Electrical and Opto-electronic Transport in Nanowires of Charge Transfer Complexes” Ph.D. Thesis (2015), S N Bose National Centre for Basic Sciences, Kolkata, India.
- [8] P. Dutta and P. M. Horn, *Rev. of Mod. Phys.*, **53**, 497 (1981).
- [9] M. B. Weissman, *Rev. Mod. Phys.*, **65**, 829 (1993).
- [10] B. K. Jones, *Adv. in electronics and electron Physics*, **87**, 201 (1994).
- [11] A. K. Raychaudhuri, *Curr. Opin. Sol. Stat. and Mat. Sci.*, **60**, 67 (2002).
- [12] Cooner Wire, 9265 Owensmouth, Chatsworth, CA 91311, USA, (Stock number CZ1103-1F) www.coonerwire.com.
- [13] J. H. Scoffield, *Rev. Sci. Instr.*, **63**, 4327 (1992).
- [14] User Manual: SR830 Lock-in Amplifier, Stanford Research Systems, Inc. 1290-D Reamwood Ave, Sunnyvale, CA 94089, USA, <http://www.srsys.com>.
- [15] Users Manual: SR554 Preamplifier, Stanford Research Systems, Inc. 1290-D Reamwood Ave, Sunnyvale, CA 94089, USA, <http://www.srsys.com>.
- [16] Use Manual: PCI-DAS6036, Measurement computing, 16 Commerce Boulevard, Middleboro, Massachusetts 02346 USA. <http://www.mccdaq.com>.
- [17] W. H. Press, S. A. Teukolsky, W. T. Vetterling and B. P. Flannery *Numerical Recipes*, (Cambridge University Press 1993).
- [18] <http://www.lakeshore.com/products/Vibrating-Sample-Magnetometer/7400-Series-VSM/Pages/Overview.aspx>.
- [19] <https://www.qdusa.com/sitedocs/productBrochures/1070-002.pdf>.

Chapter 5

Magnetic measurement of $\text{La}_{1-x}\text{A}_x\text{MnO}_3$ ($\text{A} = \text{Ca}, \text{Sr}; x = 0.3, 0.5$) nanowires

In this chapter we investigate magnetic property of ensemble of nanowires (NWs) of $\text{La}_{1-x}\text{A}_x\text{MnO}_3$ ($\text{A} = \text{Ca}, \text{Sr}; x = 0.3$ and 0.5) as well as of bulk samples down to 4 K. Magnetization measurements are performed with the aim to investigate, how the size reduction affects the magnetization behaviour in one dimensional (1D) case and how it differs from its bulk form. It has been found that there is an enhancement of Curie temperature (T_C) in 1D nanostructured form. Moreover in some cases, it shows multiple magnetic phase transitions which are absent in its bulk phase. We tried to explain the magnetic transitions performing magnetocaloric along with transverse susceptibility measurements and found out that NWs show inverse magnetocaloric effect (IMCE). The phase separation of ferromagnetic (FM) and antiferromagnetic (AFM) phases that occurs below 200 K (T_N) can be explained by double exchange (DE) and super exchange (SE) mechanism respectively. The low temperature ~ 42 K transition is explained by exchange bias effect. The magnetic phase transitions are also correlated with crystallographic and magnetic structural data obtained from synchrotron and neutron powder diffraction measurements respectively (See chapter 6). To the best of our knowledge, this kind of detailed understanding of the magnetic properties is not discussed before in case of manganite 1D system.

5.1 Introduction and Motivation

In this thesis the main subject of study is the physics of size reduction from bulk to 1D NWs of hole – doped manganite system. Magnetic properties of nanostructures are significantly modified by their dimensionality [1, 2]. In the past two decades, several works have been performed to understand the physical properties of nanoparticles (0D) and thin films (2D); however, the 1D counterpart of such materials, i.e. nanotubes and NWs, has been less studied [2] as it is difficult in synthesizing high aspect ratio nanostructures with pure phase. The mixed valence perovskite manganite $\text{La}_{1-x}\text{A}_x\text{MnO}_3$ ($\text{A} = \text{Ca}, \text{Sr}; x = 0.3 \text{ and } 0.5$) possess very rich physical properties as there exists an interesting correlation between the electronic, magnetic and structural properties of these systems [3]. In addition to that, manganite exhibits many interesting phenomena such as colossal magneto resistance (CMR), giant magnetocaloric effect, charge ordering etc, which have significance in different practical applications [1-5]. In this area a current trend of research is to understand the change in the properties of these systems when they are synthesized in nano-structured forms [6-9]. Incidentally, the systems were mostly studied in the forms of nanoparticles (0D) and thin films (2D) ($\sim \text{nm}$ thickness) [6-9]. Recently there have been some reports regarding synthesis of manganite NWs and the investigation of their properties in comparison to their bulk counterpart [10-14]. However, extensive study is yet not done in 1D manganite NWs.

Size-induced destabilization of charge and magnetic ordering in nanoparticles of half-doped manganite-based system ($\text{La}_{0.5}\text{Ca}_{0.5}\text{MnO}_3$) have been reported earlier [7, 15] and were further confirmed by recent theoretical calculations [16, 17]. Perovskite manganite nano-crystal shows drastic change in crystallographic symmetry and magnetic ordering when the size is reduced to 50 nm regime [18]. It has been emphasized that the surface plays an important role in determining magnetic and electronic properties of manganite nanostructures [19-21]. The size reduction can affect the manganite nanostructures in a non-trivial way, as seen in optimally doped manganite, where the surface effects usually arise from a disorder layer of thickness $\sim 2.5 \text{ nm}$ [8]. In this regard, there is a main difference between nanoparticles and NWs. Usually, in the case of NWs, the diameters are typically in nano-regime (below 100 nm) and the length of the NWs can extend up to a few microns. Due to their high aspect ratios, the surface effects may play a role in determining their magnetic properties and they may still retain bulk-like properties, which are otherwise suppressed or diminished in nanoparticles.

The work reported here is carried out on single crystalline NWs of $\text{La}_{1-x}\text{A}_x\text{MnO}_3$ ($\text{A} = \text{Ca}, \text{Sr}$; $x = 0.3$ and 0.5) of complex oxide manganite with average diameter ~ 50 nm and length 1-10 μm , where magnetization measurement was done over a wide range of temperature (400 – 4 K). Our motivation is to obtain a comprehensive understanding of the modification in terms of magnetic properties of manganite single crystalline NWs of $\text{La}_{1-x}\text{A}_x\text{MnO}_3$ ($\text{A} = \text{Ca}, \text{Sr}$; $x = 0.3$ and 0.5) [22-23] on size reduction. We have observed that NWs show enhanced T_C near room temperature. Size reduction leads to contraction of bond lengths thereby enhancement of the bandwidth occurs which endorses ferromagnetism. The nature of magnetic phase transition is also changed under size reduction because of bandwidth effect. Other than T_C , NWs exhibit several other magnetic transitions, which are absent in its bulk form. The magnetic transitions and the existence of mixed magnetic phases in nanostructured 1D manganite are confirmed by magnetocaloric study. The NWs show coexistence of FM and AFM phases and inverse magnetocaloric effect (IMCE) below Neel temperature ($T_N < 200$ K). The phase separation of FM and AFM phases is explained by DE and SE mechanism respectively. The magnetic phase transition ~ 42 K is explained by exchange bias effect [24]. Both phenomena are rarely observed in such 1D structure.

In manganite, the existence of competing interactions that occur from orbital, charge and spin degrees of freedom makes them an interesting system. The manganite exhibit a wide range of physical properties leading to rich phase diagrams arising from these competing interactions [25]. Thus, the study of size reduction effect on such a system with multitude of competing interactions is very interesting. In particular, it is essential to understand how the finite size affects the ferromagnetic state as well as the nature of the paramagnetic to ferromagnetic transition. T_C is enhanced in Ca doped samples with respect to its bulk and nanoparticles form and exhibits second order phase transition, whereas its bulk form shows first order phase transition. On the other hand, Sr doped 1D nanostructures having wider band width shows reduction of T_C and second order phase transition. All these issues of magnetic phase transitions in different compounds of 1D NWs of manganite have been discussed in details. We have found T_C using Arrott plot and evaluated a set of critical exponents, β (associated with the spontaneous magnetization), γ (associated with the initial susceptibility) and δ (related to the critical magnetization isotherm). These aspects have not been reported before in such manganite NWs.

5.2 Experimental results and discussions

Before going into details of the experimental results, we make a list of the samples which have been studied here such as $\text{La}_{0.7}\text{Ca}_{0.3}\text{MnO}_3$ (LCMO-0.3), $\text{La}_{0.5}\text{Ca}_{0.5}\text{MnO}_3$ (LCMO-0.5), $\text{La}_{0.7}\text{Sr}_{0.3}\text{MnO}_3$ (LSMO-0.3) and $\text{La}_{0.5}\text{Sr}_{0.5}\text{MnO}_3$ (LSMO-0.5) system. These NWs were prepared using hydrothermal technique and were characterized using X – ray diffraction and imaging tools like transmission electron microscopy (TEM) and field emission gun scanning electron microscopy (FEG-SEM) as discussed in Chapter 2.

5.2.1 $\text{La}_{0.7}\text{Ca}_{0.3}\text{MnO}_3$ (LCMO-0.3) and $\text{La}_{0.5}\text{Ca}_{0.5}\text{MnO}_3$ (LCMO-0.5) nanowires

The magnetization measurement of the ensemble of NWs was done for initial confirmation of the magnetic transitions whether it retains its magnetic property. This concern arises from the fact that magnetic properties at the nanoscale (after size reduction to three orders of magnitude) may be quite different from those observed in the bulk material. Finite size effects and enhanced surface to volume ratio can often change material properties significantly. Thus, a preliminary check of T_C was made by measuring the zero field cooled (ZFC) and field cooled (FC) M versus T curves for the samples at a low field of $H = 100$ Oe. Magnetic measurements were performed on ensemble of NWs. Fig. 5.1 (a) and (b) show the plot of temperature (T) variation of magnetization (M) and M vs. magnetic field strength (H) of LCMO-0.3 NWs respectively. The samples were measured under the applied field of 100 Oe with a vibrating sample magnetometer (VSM) from 400 K down to 80 K. The curves were obtained by cooling the samples to $T = 80$ K and magnetization measurement was done during heating cycle. The occurrence of ferromagnetic-to-paramagnetic phase transitions with the increase in temperature above T_C is observed in Fig 5.1 (a). The inset in the Fig. 5.1 (a) shows plots of dM/dT vs. T . We take the inflection points in the dM/dT vs. T curves to be an estimate of T_C . The value of T_C has been obtained using Arrott plot described later (see Fig. 5.3). From dM/dT vs. T curve, we have estimated the approximate $T_C \sim 300$ K. We have observed that T_C is enhanced ~ 35 K with respect to its bulk ($T_C \sim 265$ K) [26] and slightly increased with respect to its nanoparticles form ($T_C \sim 294$ K) [8]. The possible reason for T_C enhancement is described later in discussion part. From Fig. 5.1 (b), we have found the saturation magnetic moment (M_S) to be ~ 28.5 emu/g at 80 K and ~ 1.2 emu/g at 300 K and coercive field (H_C) of ~ 300 Oe at 80 K and ~ 90 Oe at 300 K.

Magnetization measurement of the half doped (Ca doped) manganite NW system, ($La_{0.5}Ca_{0.5}MnO_3$ (LCMO-0.5)) was done to investigate T_C along with nature of phase transition due to size reduction. Fig. 5.2 (a) and (b) demonstrate the plot of M vs. T at 100 Oe and M vs. H at 80 K and 300 K of LCMO-0.5 NWs respectively. In LCMO-0.5 NWs, M_S is ~ 14 emu/g and H_C is around 280 Oe at 80 K as shown in Fig. 5.2 (b). The T_C was identified from the inflection points in the dM/dT vs. T plot. We have estimated the approximate T_C is ~ 292 K. T_C is enhanced significantly with respect to its bulk ($T_C \sim 230$ K) and nanoparticles ($T_C \sim 250$ K) [7, 27].

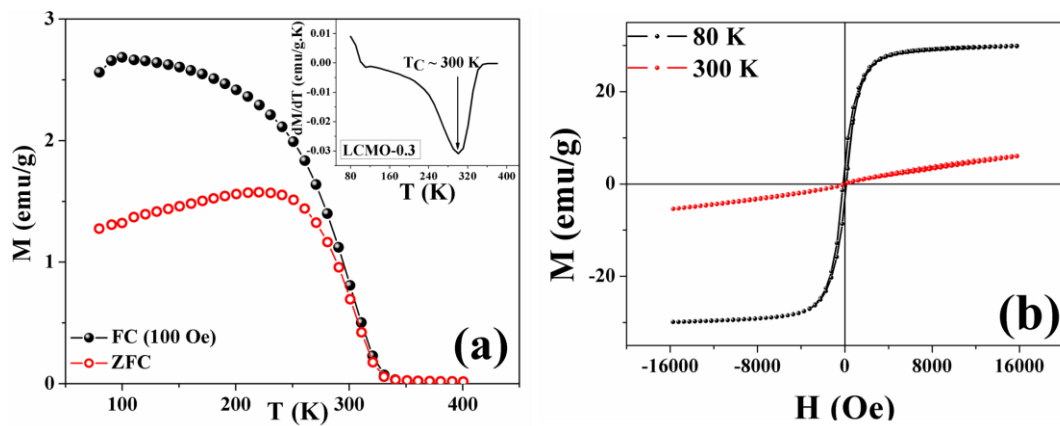


Figure 5.1 (a) Plot of temperature variation of magnetization at 100 Oe of LCMO-0.3 nanowires. The inset in the Fig. 5.1 (a) shows plots of dM/dT vs. T . We take the inflection points in the $M - T$ curves to be an estimate of the Curie temperature (T_C). (b) Plot of field variation magnetization of LCMO-0.3 nanowires at 80 K and 300 K.

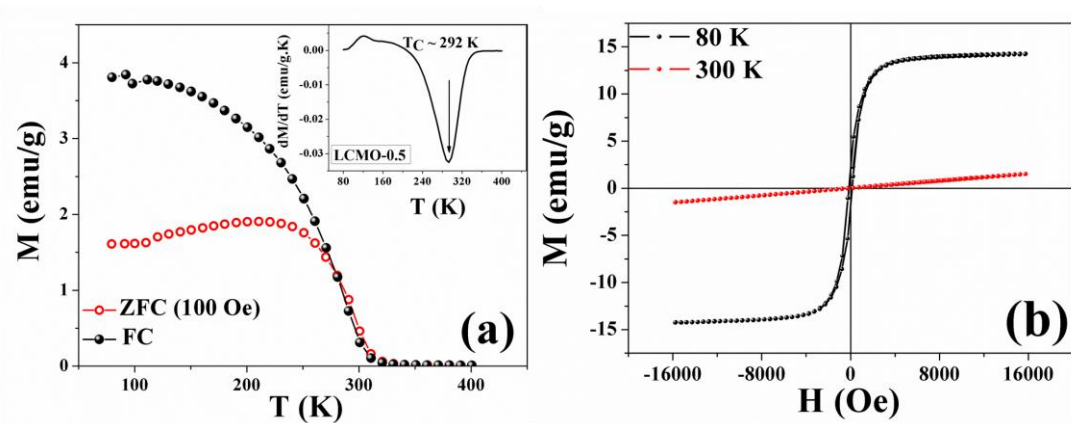


Figure 5.2 (a) Plot of temperature variation of magnetization at 100 Oe of LCMO-0.5 nanowires. The inset in the Fig. 5.2 (a) shows plots of dM/dT vs. T . (b) Plot of field variation magnetization of LCMO-0.5 nanowires at 80 K and 300 K.

Nature of the magnetic phase transition:

To study the phase transition in LCMO-0.3 NWs, we have measured magnetization (M) versus applied magnetic field (H) between 285 K and 306 K with 1 K interval for LCMO-0.3 NWs as shown in Fig. 5.3 (a). Before each run, sample is heated above T_C and cooled to the measuring temperature under zero field in order to ensure a perfect demagnetization of the sample. The nature of the magnetic transition can be obtained experimentally from the slopes of the isotherm plots of M^2 versus H/M . This criterion decides the nature of the transition and it is generally referred to the Banerjee criterion [28]. If the system is in line with the Landau mean-field theory, [29] the relationship of M^2 versus H/M should be shown as a set of parallel straight lines around T_C . Meanwhile, the order of magnetic transition can be determined from the slope of straight line [28]. A positive or a negative slope of M^2 versus H/M curve indicates a second order or first order phase transition, respectively. Arrott plot derived from magnetization isotherm is used to determine T_C and the critical exponent parameters in the vicinity of phase transition temperature [30, 31]. In Fig. 5.3 (b), M^2 versus H/M isotherms (Arrott plot) between 285 K and 300 K is plotted. The critical behaviour of a magnetic system is characterized by a set of interrelated critical exponents β , γ and δ [29]. β describes the temperature dependence of the spontaneous magnetization which is defined as,

$$M_s(T, 0) = M_0(-\varepsilon)^\beta, \varepsilon < 0, T < T_C \quad (5.1) \quad \text{where, } \varepsilon = (T - T_C)/T_C.$$

γ denotes the temperature dependence of the zero-field susceptibility and is defined by,

$$\chi_0^{-1}(T) = (h_0 / M_0) \varepsilon^\gamma, \varepsilon > 0, T > T_C \quad (5.2)$$

δ describes the field dependence of the magnetization at T_C .

$$M = A_0(H)^{1/\delta}, \varepsilon = 0, T = T_C \quad (5.3)$$

The critical exponent, as well as the critical amplitudes M_0 , h_0 and A_0 exhibit universal behavior near the phase transition point. Positive slope of Arrott plot of LCMO-0.3 NWs indicates a second order magnetic phase transition at T_C whereas in its bulk form it shows first order phase transition [26]. Size reduction may lead to change in the nature of phase transition in 1D and 0D (nanoparticles) cases [8].

The values of the critical exponents β , γ and the T_C are determined from a modified Arrott plot by taking β , γ and T_C as parameters to be obtained from fit (from equation 5.1 and 5.2). The mean field value of the exponent δ can be derived using this formula: $\delta = 1 + \gamma/\beta$. One can also obtain δ directly from the plot of $\ln M$ vs. $\ln H$ at T_C (from equation 5.3). The $T_C = 295$ K

which is enhanced than its usual value in the bulk form, matches well with the case of template based grown $\text{La}_{0.67}\text{Ca}_{0.33}\text{MnO}_3$ NW reported earlier [13].

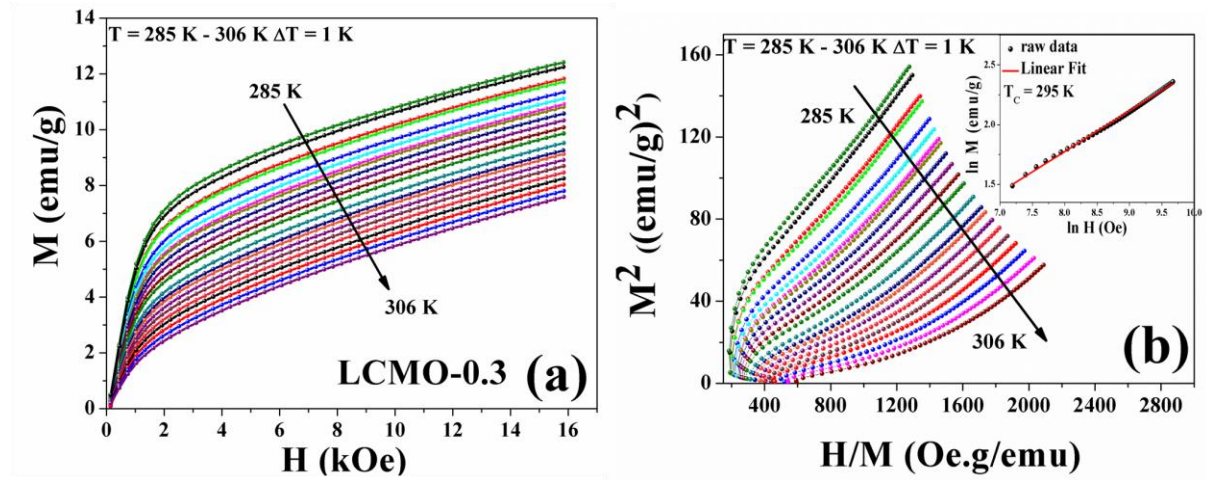


Figure 5.3 (a) Magnetization isotherms around Curie temperature (T_C) (b) Arrott plots (M^2 vs. H/M) for LCMO-0.3 nanowires.

In order to apply the Banerjee criterion for finding out the exact T_C and nature of the phase transition, we have measured initial magnetization isotherms in the vicinity of the critical temperature in LCMO-0.5 NWs as shown in Fig. 5.4 (a). In Fig. 5.4 (b), we plot M^2 vs. H/M isotherms (Arrott plots) between 276 K and 295 K. It is clear that the isotherms present positive slopes and according to the criterion used here, it is second order phase transition. It is already reported that the bulk sample shows first order transition around T_C [7, 26, 27]. In LCMO-0.5 NWs, we have found a positive slope throughout the temperature range. The critical exponents show that the magnetic transition is not only second order similar to LCMO-0.3 NWs and also the exponents are close to the mean field values: $\beta = 0.5$, $\gamma = 1$ and $\delta = 3$. The critical exponents of LCMO-0.3 and LCMO-0.5 NWs obtained experimentally and compared with mean field theory values are summarized in Table 5.1.

Table 5.1 Critical exponents of LCMO-0.3 and LCMO-0.5 nanowires obtained experimentally and compared with theoretical mean field ($\beta = 0.5$, $\gamma = 1$ and $\delta = 3$) values.

Composition	Critical exponents (experimental values)			$\delta = 1 + \gamma / \beta$	T_C (K)
	β	γ	δ		
LCMO-0.3	0.52 ± 0.06	1.01 ± 0.03	2.94 ± 0.03	2.94 ± 0.02	295 K
LCMO-0.5	0.54 ± 0.07	1.04 ± 0.09	3.04 ± 0.01	2.93 ± 0.16	286 K

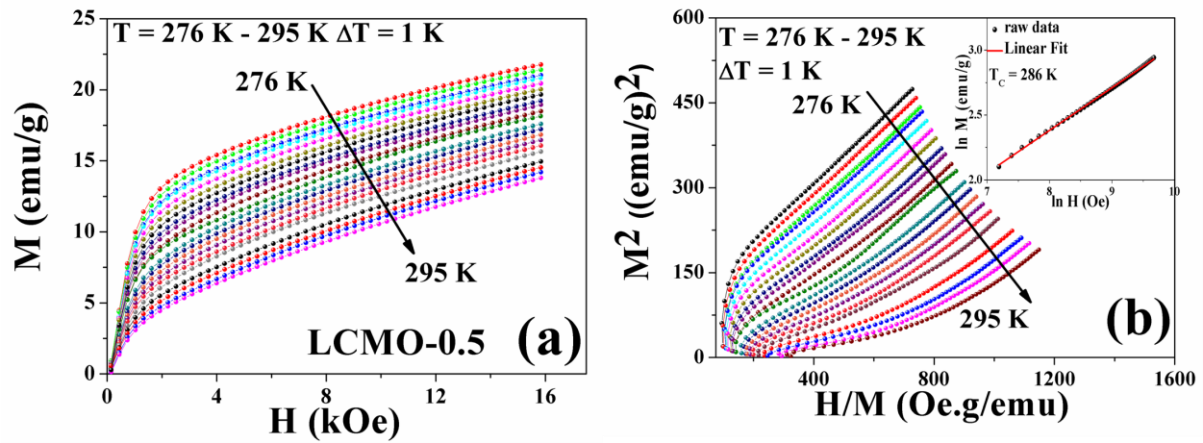


Figure 5.4 (a) Magnetization isotherms around Curie temperature (T_C) (b) Arrott plots (M^2 vs. H/M) for LCMO-0.5 nanowires.

Discussions:

While in most doped manganite bulk system ($A = \text{Sr}, \text{Ba}$ etc.) with wider band width the phase transition is second order, in narrow band width $La_{0.7}Ca_{0.3}MnO_3$ bulk system, the transition has been found to be first order [7,32,33]. It has been reported earlier that in manganite when the bandwidth is increased without changing the carrier concentration (e.g. by substitution of ions with larger ionic radius in A site [32]), the nature of the transition can change from first order to second order. In the Ca substituted manganite which have a smaller band width, the effect of the electron-lattice coupling is stronger. Apparently it can play a very dominant role in deciding the nature of the transition in addition to the contribution arising from the DE interaction which is the cause of ferromagnetism in these materials. Here we have observed the first order phase transition in LCMO-0.3 bulk changes to a second order transition when the size is brought down to the range of few tens of a nanometre. In this change-over the hole concentration (i.e., x) is kept constant and the change over occurs solely due to factors that arise due to size reduction. The other issue is that the critical exponents measured from the magnetization data show values that are close to the mean field values. This would be expected in a system of finite size when the Ginzburg coherence length cannot grow beyond the system size so that order parameter fluctuations cannot grow and the system stays close to the mean field region [34]. Since the NW diameter is much smaller ($\sim \text{nm}$), the system will stay close to the mean field region. To the best of our knowledge, we consider that this detailed investigation has not been performed before in ensemble NWs of manganite system.

We have found that T_C is enhanced ~ 35 K in NWs with respect to its bulk system [26]. This T_C enhancement is occurred due to the size induced lattice contraction and therefore the volume of unit cell reduction in the NWs with respect to bulk. The initial enhancement in T_C was associated to an increase in the bandwidth that occurred due to a compaction of the Mn–O bond length and a straightening of the Mn–O–Mn bond angle, as observed from the refinement of synchrotron XRD data (obtained from Table 6.1 as discussed in chapter 6). The analysis of the synchrotron XRD data shows that a clear change occurs in the MnO_6 octahedron on size reduction as shown through the Mn–O–Mn bond angles and Mn–O bond lengths. These two parameters have a direct role in the determination of the overlap integral and thus of the bandwidth W . The size reduction thus leads to a contraction of the Mn–O bond lengths and Mn–O–Mn bond angles move closer to 180° which leads to an enhancement of the bandwidth and endorses the ferromagnetism of manganite, which ultimately enhances T_C . Moreover the increased bandwidth leads to the nature of the phase transition change from first order to second order. Hence size reduction in Ca doped 1D cases leads to enhance bandwidth along with the changes in the nature of phase transition in NWs and nanoparticles [8]. The unit cell of the manganite is often distorted from the cubic structure and the Jahn–Teller distortion around the Mn^{3+} ions leads to orthorhombic distortions. The reduction of the orthorhombic distortion strengthens the DE interaction, enhances the bandwidth and strengthens the ferromagnetic state.

We define the orthorhombic strains as $OS_{\square} = \frac{2(c-a)}{(c+a)}$ (giving the strain in the ac plane) and $OS_{\perp} = \frac{2(a+c-b\sqrt{2})}{a+c+b\sqrt{2}}$ (giving the strain along the b -axis with respect to the ac plane). The

detailed explanation is written in chapter 6. The analysis of structural data as obtained from the synchrotron XRD data clearly shows the small yet clear change occurs in the MnO_6 octahedra. Mn–O–Mn angle, both for the apical and equatorial oxygen moves closer to 180° that leads to an enhancement of the bandwidth (W). An estimate of the bandwidth (W) (in the double exchange model) can be made from the relation [35, 36].

$$W \propto \cos \omega / d_{Mn-O}^{3.5} \quad (5.4)$$

Where $\omega = \frac{1}{2} (\pi - \theta_{Mn-O-Mn})$. Thus, an increase in the bond angle $\theta_{Mn-O-Mn}$ and a decrease in the bond length d_{Mn-O} would mean an overall increase in the bandwidth W , thereby leading to an enhancement of T_C . However, if the average size is reduced to certain limit (< 30 nm) T_C may

be decreased due to finite size effect. In case of LCMO-0.3 nanoparticles having wider bandwidth, it is already reported that below certain limit (~ 30 nm), T_C is decreased due to finite size effect [8].

As discussed earlier in the case of LCMO-0.3 NWs, same reasons are also applicable in LCMO-0.5 NWs for second order phase transition and T_C enhancement i.e. bandwidth enhancement due to lattice contractions and therefore unit cell volume contraction under size reduction. Detailed structural study of lattice contraction as well as cell volume issues have been discussed in section 6.3.1 of chapter 6.

5.2.2 $La_{0.7}Sr_{0.3}MnO_3$ (LSMO-0.3) nanowires

In this subsection, the magnetization study has been performed on optimum doped Sr ($x = 0.3$), LSMO NWs having wider bandwidth. It has been observed that these compositions show some different behaviours compared to Ca doped compounds on size reduction. The curve of M vs. T at 100 Oe and M vs. H at 80 K and 300 K of LSMO-0.3 NWs are depicted in Fig. 5.5. In LSMO-0.3 NWs, M_S is ~ 14 emu/g and H_C is around 750 Oe at 80 K and 480 Oe at 300 K which is large value compared to Ca doped LCMO NWs (Fig. 5.2 (b)). The T_C was identified from the inflection points in the dM/dT vs. T plot. We have estimated the approximate $T_C \sim 301$ K. However, in Sr doped sample T_C is decreased with respect to that of bulk sample ($T_C \sim 360$ K) [32, 37].

In this situation, to find out the exact T_C and nature of magnetic phase transition around T_C , a set of isothermal magnetization curves for magnetic fields up to 1.6 Tesla has been performed as shown in Fig. 5.6. From M^2 vs. H/M plot, we have clearly observed there is a positive slope which describes second order phase transition. It is already reported that the bulk sample shows also second order transition around T_C [32, 37-39]. The values of the critical exponents β and γ were determined from a modified Arrott plot by taking β , γ and T_C as parameters to be obtained from fit (from equations 5.1 and 5.2). The values of $\beta = 0.53 \pm 0.01$ and $\gamma = 1.02 \pm 0.02$ come out to be close to the mean field values ($\beta = 0.5$, $\gamma = 1$) and $T_C = 311$ K. The mean field value of the exponent δ can be derived using $\delta = 1 + \gamma/\beta$. We find $\delta = 2.924 \pm 0.021$. One can also obtain δ directly from the plot of $\ln M$ vs. $\ln H$ at T_C (from equation 5.3). From such a plot we have obtained $\delta = 3.035 \pm 0.001$. The critical exponents show that the magnetic transition is not only second order and also the exponents are close to the mean field values: $\beta = 0.5$, $\gamma = 1$ and $\delta = 3$.

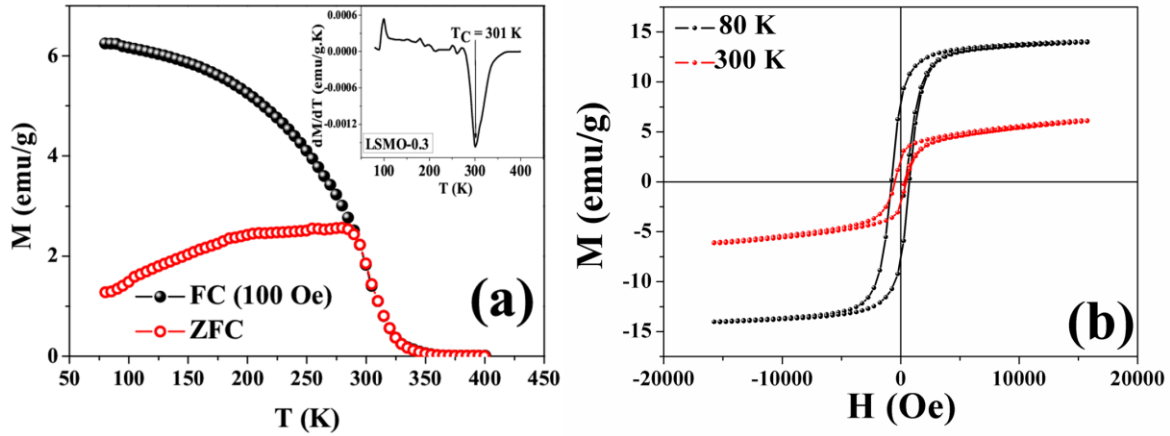


Figure 5.5 (a) Plot of temperature variation of magnetization at 100 Oe of LSMO-0.3 nanowires. The inset in the Fig. 5.5 (a) shows plots of dM/dT vs. T . (b) Plot of field variation magnetization of LSMO-0.5 nanowires at 80 K and 300 K.

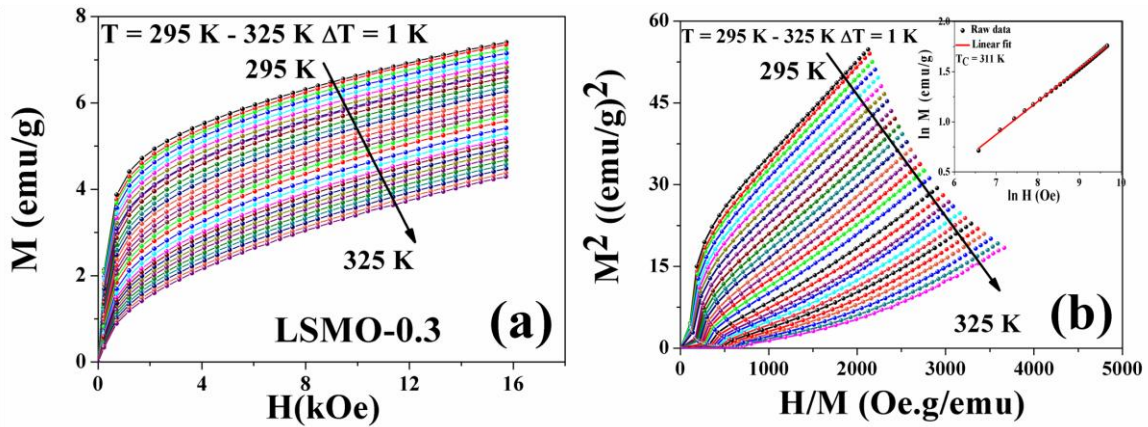


Figure 5.6 (a) Magnetization isotherms around Curie temperature (T_C) (b) Arrott plots (M^2 vs. H/M) for LSMO-0.3 nanowires.

LSMO-0.3 NWs having wider bandwidth, T_C is decreased may be due to finite size effect which is well known reason for T_C value decrement because of size reduction. Magnetic properties at the nanoscale regime strongly depend on the surface atoms and the energetic of spin reversal. As the particle size is decreased from a few microns to a few nano-meters, size – dependent magnetic properties can be changed. In a ferromagnetic substance, the T_C usually decreases with a decrease in size. In the region close to the ordering temperature (T_{order}), the correlation length $\zeta(t)$ of the fluctuation in the order parameter (M) diverges logarithmically with the reduced temperature ($t = \frac{T - T_{order}}{T_{order}}$) where, the ordering temperature (T_{order}) is T_C for a ferromagnetic material. With the geometric confinement effect on $\zeta(t)$, the magnetic

transition temperature (T_C) is reduced from the bulk value. In bulk magnetic systems, the correlation length (ξ) increases with temperature and diverges at the bulk transition temperature $T_C(\infty)$. When one or more dimensions in the system are small such as in our 1D NW sample, the growth of ξ will eventually be limited by the smallest dimension d and the system displays a reduced transition temperature $T_C(d)$ due to finite-size effects. The reduction of T_C for NWs with decreasing diameter is due to finite-size effects. This decrease in T_C is given by the finite size scaling formula [40]:

$$\frac{T_C(\infty) - T_C(d)}{T_C(\infty)} = \pm \left(\frac{d}{\xi_0}\right)^{-\lambda} \quad (5.5)$$

Where, $T_C(\infty)$ corresponds to the bulk T_C and ξ_0 gives the spin-spin correlation length and should be of the order of a characteristic microscopic dimension. According to the standard finite size scaling theory, λ is the critical shift exponent which is the reciprocal of the correlation length exponent ν [41]. The finite particle size limits the divergence of the spin-spin correlation length ξ_0 which in turn results in a decrease of T_C with respect to the bulk value where $d < \xi_0$. The shift exponent λ reflects the appropriate universality class which is mostly characterized by the dimensionality of the system. The shift in the transition temperature from that of the bulk should depend on a dimension of the system. Experimentally, this finite size effect has been reported mostly in two dimensional magnetic films [42, 43]. However, there is much less reports regarding the finite size effect on lower dimensional magnetic samples such as NWs [44] or nanoparticles [45].

5.2.3 $La_{0.5}Sr_{0.5}MnO_3$ (LSMO-0.5) nanowires

This subsection explains the magnetic behaviour of half doped Sr sample ($x = 0.5$) LSMO-0.5 NWs, which show some interesting behaviour in magnetic properties. This compound in 1D form exhibits multiple magnetic transitions with mixed magnetic phases.

To understand the magnetic behaviour, magnetization measurement was performed in ensemble of NWs as well as in bulk sample of same composition. The temperature (T) variation of the dc magnetization of LSMO-0.5 NWs and bulk respectively is shown in Fig. 5.7 (a) and (b). The magnetization measurement was done following the ZFC and FC protocols at the applied magnetic fields 200 Oe in bulk and 100 Oe and 2.5 kOe in NWs respectively. The LSMO-0.5 bulk sample exhibits FM phase throughout the temperature range (2 – 320 K) with $T_C \sim 315$ K. Whereas LSMO-0.5 NW shows several magnetic transitions. It undergoes a paramagnetic (PM) to FM transition at $T_C \sim 310$ K followed by an

AFM transition at $T_N \sim 210$ K. On further lowering the temperature, a small increase in magnetization has been observed at 42 K.

In Fig. 5.7 (a), the ZFC and FC curves measured in an applied field of 100 Oe show a bifurcation or irreversibility below T_C . As the applied magnetic field is increased to 2.5 kOe, the irreversible temperature shifts is removed as shown in Fig. 5.7 (a). The presence of such a bifurcation is common in the case of nanoparticles and can be associated with the blocking temperature [46]. However, in the case of the NWs, due to the high aspect ratio and with the length of the NWs extending to tens of microns, it is not possible to define a blocking temperature. It has also been reported that a bifurcation in the M vs. T curves can be observed due to the presence of a canted magnetic state [47] or due to phase coexistence (FM and AFM), which is common in manganite [48].

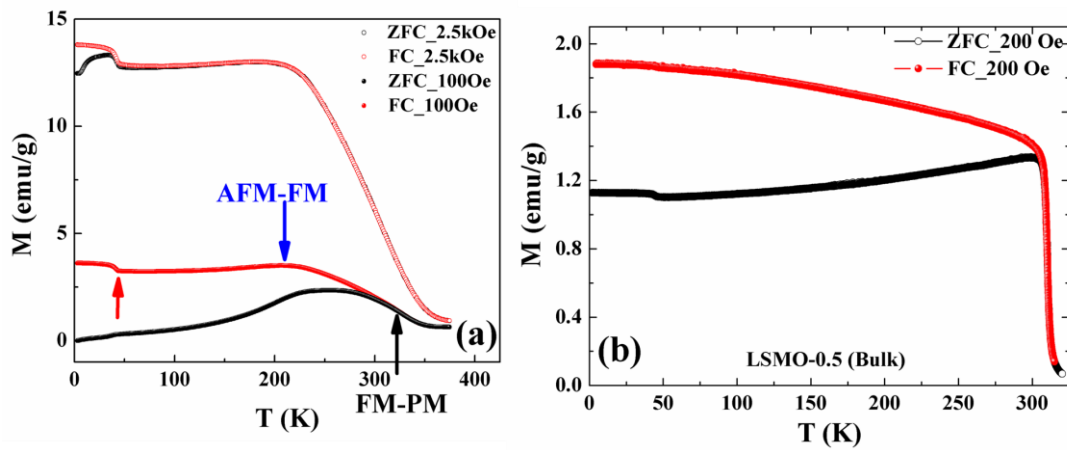


Figure 5.7 Temperature variation of magnetization data measured under applied fields of (a) 100 Oe and 2.5 kOe for LSMO-0.5 nanowires (b) 200 Oe for LSMO-0.5 bulk sample. In bulk there is one FM-PM transition where as in nanowire form it exhibits multiple phase transitions.

Moreover, a common feature in all the M vs. T curves is the rise in magnetization at ~ 42 K (Fig. 5.7 (a)). Such a feature can be associated with a low temperature magnetic transition, or due to the alignment of disordered surface spins usually accompanied by a glass-like behaviour [49]. Interestingly, the location of this rise in magnetization (FC curve) on the temperature scale is independent of the measurement field. However, it can be seen that the shape of the ZFC curve is greatly modified by the applied field and the irreversibility temperature shifts to lower values with increase in field. To understand the multiple magnetic transitions we have carried out ac susceptibility, magnetocaloric measurement, transverse susceptibility and exchange bias experiment on ensemble of LSMO-0.5 NWs in collaboration with Dr. H Srikanth, University of South Florida [24].

AC Susceptibility measurement:

In order to probe the nature of this magnetic transition, ac susceptibility measurements were performed. These magnetic studies were carried out using a Quantum Design Physical Property Measurement System (PPMS) equipped with a VSM over a temperature range of 10–340 K.

At higher frequencies, the ac moment of the sample does not follow along the dc magnetization curve due to dynamic effects in the sample. For this reason, the ac susceptibility is often known as the dynamic susceptibility. In this higher frequency case, the magnetization of the sample may lag behind the drive field. Therefore, the ac magnetic susceptibility measurement yields two quantities: the magnitude of the susceptibility (χ) and the phase shift (ϕ) (relative to the drive signal). Alternately, one can think of the susceptibility as having an in-phase or real component χ' and an out-of-phase or imaginary component χ'' . The two representations are correlated by:

$$\begin{aligned} \chi' &= \chi \cos \phi \\ \chi'' &= \chi \sin \phi \end{aligned} \quad \Leftrightarrow \quad \begin{aligned} \chi &= \sqrt{\chi'^2 + \chi''^2} \\ \phi &= \arctan(\chi''/\chi') \end{aligned} \quad (5.6)$$

In low frequency range, where ac measurement is most similar to dc measurement, the real component χ' is just the slope of the $M(H)$ curve. The imaginary component χ'' , denotes dissipative processes in the sample. In conductive samples, the dissipation is due to eddy currents. Relaxation and irreversibility in spin-glasses give rise to a nonzero χ'' . In ferromagnets, a nonzero imaginary susceptibility can signify irreversible domain wall movement or absorption due to a permanent moment. Also, both χ' and χ'' are especially sensitive to thermodynamic phase changes and are often used to measure transition temperatures.

The ac susceptibility measurements were done by applying an ac magnetic field of 10 Oe within the frequency range of 10 Hz–10 kHz. Fig. 5.8 (a) and (b) show the temperature dependences of the real (χ') and imaginary (χ'') parts of ac susceptibility in the temperature range of 10–340 K respectively. The $\chi'(T)$ curve shows a maximum at $T_N \sim 210$ K with no frequency dependence and a kink at 42 K. In addition, the $\chi''(T)$ curves which give us insight into magnetic lossy behaviour, show a peak at $T_C \sim 310$ K, a broad shoulder at $T_N \sim 210$ K and a kink at ~ 42 K. All these results complement the data obtained from dc magnetization. In the inset of Fig. 5.8 (a), we present a magnified view of the $\chi'(T)$ curves (with more frequencies) and observe weak frequency dependence. The $\chi'(T)$ peak shifts to a higher

temperature as the frequency is increased, which is consistent with other reports [20, 50]. An attempt to fit the peak shift in $\chi'(T)$ to the Néel–Arrhenius law or the Vogel–Fulcher law yielded unphysical results, thereby suggesting that the magnetization dynamics cannot be explained with a non-interacting or a weakly interacting particle model. However, the nature of the peak shift can be empirically understood by the relation, $\Gamma = \Delta T_p / T_p \Delta(\log \omega)$ where Γ ranges from 0.005 to 0.01 for a metallic spin glass (SG) system [51]. The value estimated for Γ was ~ 0.008 , which hints that the NWs are undergoing an SG-type transition at 42 K, which may originate from the surface spins, which are disordered.

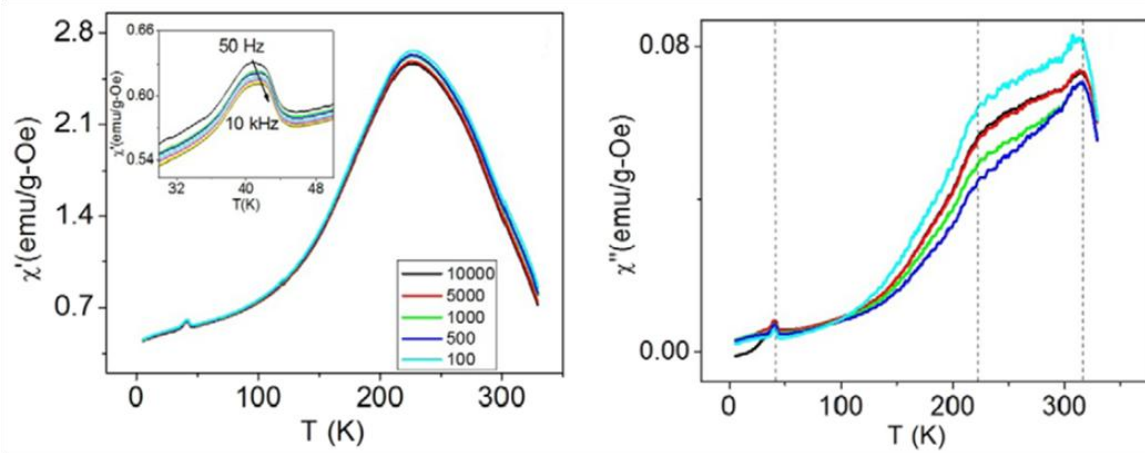


Figure 5.8 (a) Real and (b) imaginary parts of linear ac susceptibility versus temperature plot for different frequencies. The inset of (a) shows a magnified view of $\chi'(T)$ for more frequencies [24].

To understand the magnetic transitions in these NWs more clearly, we have performed magnetocaloric study. In past, it has been shown that the change in magnetic entropy ($-\Delta S_M$) with temperature (T) and field (H) is very sensitive to the magnetic state of the system [47, 52, 53].

Magneto caloric effect (MCE) and Inverse magneto caloric (IMCE) effect:

The magnetocaloric effect (MCE) is defined as the heating or cooling (i.e., the temperature change) of a magnetic material due to the application of a magnetic field. In order to elucidate the origin of the magnetocaloric effect, we use thermodynamics which correlates the magnetic variables (magnetisation and magnetic field) to entropy and temperature. All magnetic materials intrinsically illustrate MCE, although the intensity of the effect depends on the properties of each material. The physical origin of the MCE is the coupling of the

magnetic sub-lattice with the applied magnetic field (H), which changes the magnetic contribution to the entropy of the solid. The MCE can be obtained indirectly from a set of magnetic measurements as a function of temperature and magnetic field. The temperature and field dependent magnetic entropy change is related to the change in magnetization via Maxwell's relation:

$$\left[\frac{\partial S(H, T)}{\partial H}\right]_T = \left[\frac{\partial M(H, T)}{\partial T}\right]_H \quad (5.7)$$

The change in magnetic entropy can be calculated from equation (5.7) by calculating the numerical integral,

$$\Delta S_M = \int_0^{H_{Max}} \left(\frac{\partial M}{\partial T}\right)_H dH \quad (5.8)$$

The sign of $-\Delta S_M(H, T)$ can be either positive or negative depending on the type of magnetic interaction dominating within a field and temperature range [54]. A positive peak in the $-\Delta S_M(H, T)$ curve is indicative of a ferromagnetic transition, which is seen in conventional MCE materials. On the other hand, negative values of $-\Delta S_M(H, T)$ suggest dominating AFM correlations within FM matrix. The consistent increase in magnetic entropy with the application of magnetic field is known as an inverse magnetocaloric effect (IMCE). Such IMCE materials have been proposed for “magnetic cooling” which can be achieved by the adiabatic magnetization of magnetic systems. The materials exhibiting IMCE would be very useful as refrigeration capacity which can be improved by using these materials along with conventional ferromagnetic refrigerants [2, 55].

MCE of a material can be parameterized by the change in magnetic entropy (ΔS_M) associated with the change in applied magnetic field. We have measured a family of isothermal magnetization curves for magnetic fields up to 5 Tesla (inset of Fig. 5.9 (a)). ΔS_M in NWs has been estimated from the isothermal magnetization [$M(H)$] curve plotted in Fig. 5.9 (a). There exist signatures of three distinct magnetic transitions in $-\Delta S_M(T)$: two maxima at ~ 290 K and 42 K; a minimum at ~ 175 K, as shown in Fig. 5.9 (a). As the temperature is lowered from 340 K, first a positive peak is observed at ~ 290 K which can be attributed to the PM–FM transition. This is followed by the crossover of the $-\Delta S_M$ values from positive to negative at ~ 210 K (T_N). Below T_N , a negative peak develops at ~ 175 K, which corresponds to the temperature with strongest AFM interactions within FM matrix and manifests as IMCE. The region, below T_N , indicates the coexistence of both FM and AFM phases. We have also

observed a maximum in $-\Delta S_M(T)$ at a low temperature of ~ 42 K, which is an indication of FM-like magnetic transition.

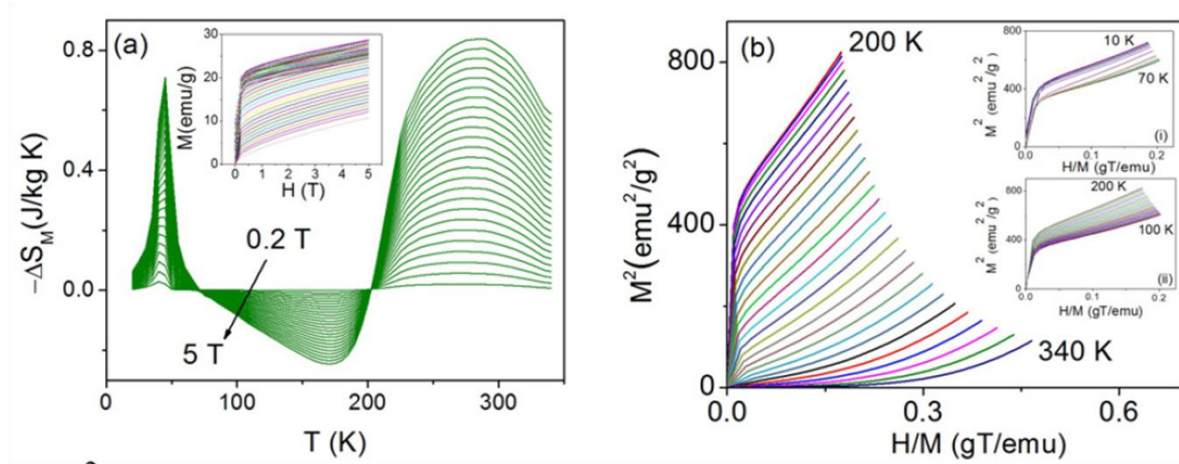


Figure 5.9 (a) Temperature dependence of magnetic entropy change; The inset of (a) shows the $M(H)$ curves for all temperatures. (b) M^2 vs. H/M (Arrott plot) curves for different temperatures. The insets of (b) show the Arrott plots in different temperature ranges [24].

Change in magnetic entropy in the manganite system has been observed previously in ~ 36 nm particles with similar composition [53]. However, the $-\Delta S_M$ values in NWs are significantly less compared to sub-micron particles with composition $\text{La}_{0.45}\text{Sr}_{0.55}\text{MnO}_3$ [53].

It is worth mentioning that there are several previous studies of half-doped manganite nanostructures, highlighting the complete suppression of the AFM state, which was otherwise evident in their bulk form [7, 10, 56]. In this context, the development of AFM correlation in the present NWs is intriguing. Generally, the development of AFM in bulk half-doped manganite is associated with charge ordering (CO), which evolves as a martensitic transition. In the case of nanostructures, it becomes difficult to accommodate the lattice strain associated with typical martensitic transitions [10, 56, 57], which eventually results in the observed suppression of the AFM state. However, for the $\text{La}_{0.5}\text{Sr}_{0.5}\text{MnO}_3$ compound, the AFM state is A-type (observed in neutron diffraction study discussed in chapter 6) and it is not related to the CO transition (discussed in chapter 7 in details). This explains why the AFM phase is stabilized in the NWs and strengthens with applied magnetic field in the IMCE region.

We also observed a positive peak at 42 K in Fig. 5.9 (a) which is associated with the kink observed in the $M(T)$ curves (Fig. 5.7 (a)). This implies that, on further lowering the temperature, the FM contributions overcome the competing AFM interactions at ~ 75 K, below which $-\Delta S_M$ becomes positive. One can argue that the low temperature peak ~ 42 K

can originate from a first order structural transition. In order to check this, we constructed Arrott plots as shown in Fig. 5.9 (b). The M^2 vs. H/M curves are grouped into three temperature ranges corresponding to the three magnetic transitions. Insets (i) and (ii) in Fig. 5.9 (b) correspond to the low temperature FM phase (below 70 K) and the intermediate IMCE region (70–200 K) respectively. According to Banerjee criterion [28], a negative or a positive slope in the M^2 vs. H/M curves can be associated with first order or second order transition respectively. The absence of any negative slope in the entire temperature range rules out the possibility of first order transition. So, both the bulk and NWs of LSMO-0.5 sample exhibit second order phase transitions. Usually for an AFM system exhibiting IMCE, no spontaneous magnetization is observed [54]. The spontaneous magnetization in a system can be estimated by extrapolating M^2 vs. H/M curves from high H/M values and finding the intercept on the M^2 axis. Typically, for AFM system, this intercept passes through the origin. In contrast to this, in the case of the LSMO-0.5 NWs, we observe spontaneous magnetization (see inset (ii) in Fig. 5.9 (b)). This can be attributed to the presence of finite FM regions within the predominantly AFM NWs, which spontaneously align to a small magnetic field. Thus, Arrott plot and magnetocaloric study provide enough evidence of phase coexistence of AFM and FM phases in LSMO-0.5 NWs. Now, for further understanding we have done transverse susceptibility and magnetic anisotropy measurements.

Transverse susceptibility and magnetic anisotropy:

To comprehend the influence of such magnetic phase coexistence on the effective magnetic anisotropy and how it evolves with temperature, we have performed these measurements. The magnetic anisotropy of a system can be directly probed by performing temperature and field dependent transverse susceptibility (TS) study using a sensitive self-resonant tunnel diode oscillator technique [58]. In principle, we want to exploit the fact that the effective anisotropy field would be significantly affected by the volume fraction of the FM phase in the NWs. In the past, we have demonstrated this technique as a probe to detect subtle changes in the magnetization dynamics of nanoparticles [59, 48], polycrystalline materials [60], NWs [61] and thin films [62]. Briefly, the measurement technique is as follows. The sample is placed within an inductor which is part of an ultra stable LC tank circuit resonating at a frequency of $f \sim 12$ MHz. The inductor is placed inside the PPMS such that the rf magnetic field (~ 10 Oe) generated inside the coil is perpendicular to the external dc magnetic field. As the dc magnetic field or the temperature is varied, the inductance of the coil changes, which in turn

shifts the resonant frequency by Δf . The change in the resonance frequency is proportional to the change in the transverse susceptibility ($\Delta\chi_T$) as shown in equation (5.9).

$$\frac{\Delta f}{f} \propto \left(\frac{\Delta\chi_T}{\chi_T} \right) \% = \frac{[\chi_T(H) - \chi_T^{sat}] \times 100}{\chi_T^{sat}} \quad (5.9)$$

Here, $\chi_T(H)$ and χ_T^{sat} are the TS values at magnetic field H and at saturation respectively. Further details about the tunnel diode oscillator technique and the experimental set-up can be found elsewhere [58]. Typical bipolar TS measurements are made by cooling the sample to a desired temperature and then sweeping the dc magnetic field from positive saturation to negative saturation and back.

It was theoretically calculated by Aharoni *et. al* that three singularities would be observed in the TS curve when the dc magnetic field is swept from positive to negative saturation [63]. Two of these peaks occur at the positive and negative anisotropy fields (H_K), while the third peak corresponds to the switching field (H_S). Fig. 5.10 (a) shows a typical TS curve obtained from a bipolar scan at 60 K, where the red and the black curves were generated while sweeping the magnetic field from positive to negative saturation (± 2 Tesla) and vice versa. In the inset, a magnified view of the TS curves is shown to better illustrate the peaks for the descending curve ($+H_K$) and the return curve ($-H_K$). For both the ascending and the return curves, we observe that, while the first anisotropy peak is distinct, the second anisotropy peak appears as a broad shoulder and is not well defined. Generally, under experimental conditions, various factors like particle size distribution or inter-particle interaction cause the negative anisotropy peak to merge with the switching peak [64]. Hence, we will use the first anisotropy peak ($\pm H_K$) to define the anisotropy field. However, the evolution of the second anisotropy peak provides qualitative information about the switching behaviour of the magnetic domains.

The evolution of the anisotropy field ($\pm H_K$) for bipolar scans is shown in Fig. 5.10 (b). At this point, we would like to mention that the maximum applied field of 2 Tesla is not sufficient to align the highly disordered surface spins (also evident from the $M(H)$ curves in the inset of Fig. 5.9 (a)). Hence, only the magnetic moments at the core of the NWs contribute to the anisotropy peaks. In the FM region (above 210 K), the NWs have almost constant anisotropy; however, at $T_N \sim 210$ K, a decrease in the $\pm H_K$ values is noticed, which is consistent with the fact that, as the NWs undergo an FM–AFM transition, the effective anisotropy drops due to the dominant AFM phase. Below T_N , as the temperature is lowered, we observe an increase in $\pm H_K$, indicating magnetic phase separation with an increase in the FM volume fraction.

However, below 80 K, the increase of anisotropy field ceases and remains close to ~ 300 Oe. This suggests that at ~ 80 K the growth of FM in the core of the NWs stabilizes and remains nearly constant. This is also consistent with the magnetocaloric data (Fig. 5.9 (a)), where, below 75 K, the $-\Delta S_M(H, T)$ curves become positive, indicating dominating FM interactions. So, the question that arises is why we do not see any change in the anisotropy field ~ 42 K which is associated with a rise in the magnetization (Fig. 5.7 (a)) and also a peak in the $-\Delta S_M(H, T)$ curves (Fig. 5.9 (a)). As discussed above, since the contribution to H_K is solely from the core spins, any change to the magnetization of the surface spins of the NWs would not be reflected in H_K . Consequently, we can conclude that the anomaly at ~ 42 K originates from the surface spins, probably undergoing magnetic freezing. To understand if there is any exchange coupling between the core and the surface spins below 50 K, we have performed exchange bias experiment at low temperature region.

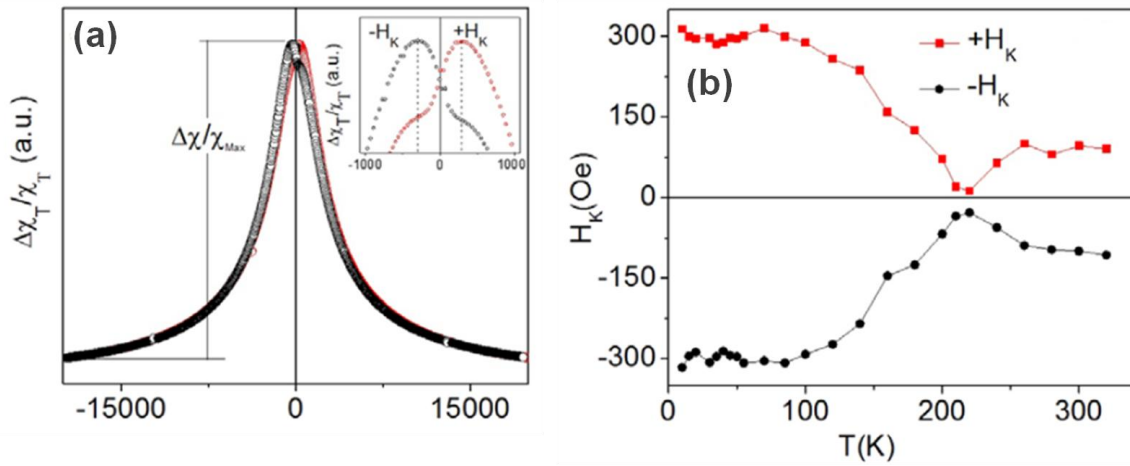


Figure 5.10 (a) Representative bipolar transverse susceptibility (TS) curve at 60 K, The inset of (a) shows a magnified view to illustrate the peaks at the anisotropy fields. (b) temperature dependence of effective anisotropy fields [24].

Exchange bias effect:

Exchange bias (EB) is referred to a shift of the magnetization hysteresis loop along magnetic field axis. The main identifications of the presence of EB effect are (i) a shift of the FC magnetic hysteresis loop along the magnetic-field (H) axis, (ii) enhancement of H_C as compared to the ZFC case. The EB effect is believed to originate from the magnetic coupling across the interface shared by FM and AFM when cooled in magnetic field through T_N of the AFM. Recently, EB effect has been observed in different spontaneously phase separated manganite, [65] and cobaltite,[66] where intrinsic interface exchange coupling between FM

nanodroplets and AFM matrix or SG regions have been proposed. In LSMO-0.5 NWs, EB effect was verified by field cooling (2 Tesla) the NWs to 5 K before measuring hysteresis loops. A clear shift of the FC loop (Fig. 5.11 (a)) along the negative field axis confirms EB in the system. The EB field is calculated as, $H_{EB} = \left[\frac{H^+ + H^-}{2} \right]$, where H^+ and H^- are the coercive fields for the ascending and descending curves respectively. Also, we have noticed an increase in H_C of the FC loop accompanied by vertical shift (Fig. 5.11 (a)), which suggests enhanced unidirectional anisotropy. The temperature dependence of EB is shown in Fig. 5.11 (b). It is widely accepted for phase separated materials that the coexistence of FM clusters in an AFM matrix leads to the natural FM/AFM interfaces. As a result of which EB may develop [67, 68]. However, the NWs are found to exhibit no EB above 45 K, even though phase coexistence persists up to T_N . As expected, above 45 K, due to lack of sufficient exchange coupling between the disordered surface spins and the core, EB vanishes. EB manifests only below the freezing temperature of the surface spins. Above 45 K, due to the unfreezing of the surface spins, they begin to rotate with the core spins on sweeping the magnetic field, which results in disappearance of the EB effect.

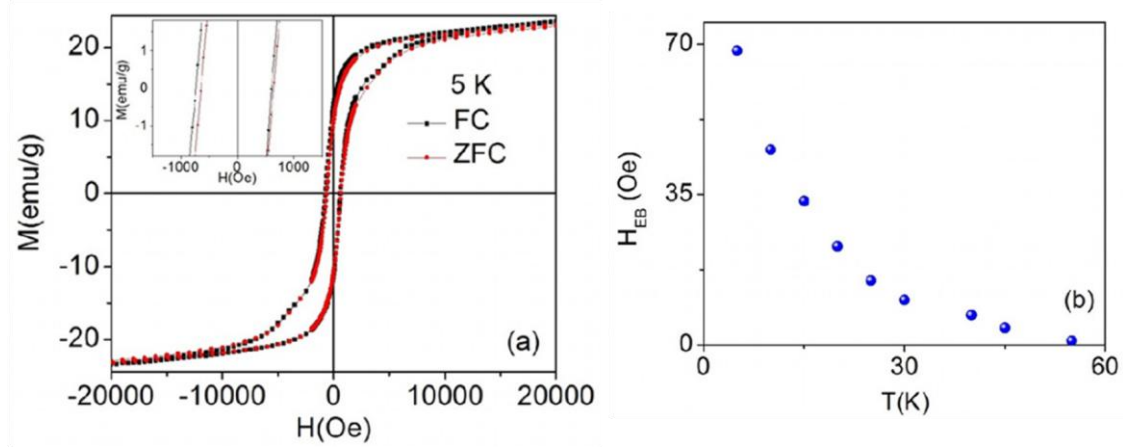


Figure 5.11 (a) $M(H)$ hysteresis loops at 5 K under FC (2 Tesla) and ZFC conditions; the inset of (a) shows a magnified view at low fields. (b) Temperature dependence of exchange bias field [24].

5.3 Conclusion

In summary, single crystalline $\text{La}_{1-x}\text{A}_x\text{MnO}_3$ ($A = \text{Ca, Sr}$; $x = 0.3$ and 0.5) NWs were synthesized by the hydrothermal technique. We performed dc and ac magnetic, Arrott plot, magnetocaloric, transverse susceptibility and exchange bias studies to understand the

temperature and field dependent magnetization dynamics of the NWs. In case of LCMO-0.3 and LCMO-0.5 NWs, the size reduction induced magnetic phase transition is an important observation because the system has the same chemical composition (no change in hole concentration) and the only difference is the size of the system. Although bulk LCMO-0.3 and LCMO-0.5 exhibit first order transition at T_C , the nature of the transition can be changed to second order by bringing down the size to the nanometre level without any change in the stoichiometry of the samples. The critical exponents' β , γ and δ come out close to the mean field values for an isotropic system. The analysis of the structural data exhibits a small but distinct compaction of the MnO_6 octahedron with smaller $d_{\text{Mn-O}}$ and with $\theta_{\text{Mn-O-Mn}} \rightarrow 180^\circ$. This leads to an enhancement of the bandwidth and therefore T_C is enhanced for both cases. FM in the manganite system arises from the DE mechanism between the Mn^{3+} and Mn^{4+} ions. The crystal structure as obtained from the synchrotron XRD data shows that there are small yet definite changes in lattice parameters upon size reduction. The basic perovskite structure of the bulk manganite is preserved although there is a clear compaction of the MnO_6 octahedra and the orthorhombic distortion OS_\perp is somewhat reduced in bulk. We have discussed here how these small but definite changes upon size reduction have effects on the magnetic properties.

On the other hand, Sr doped LSMO-0.3 and LSMO-0.5 NWs both the bulk and NW system show second order phase transitions around T_C . In LSMO-0.3 NWs, T_C value is decreased with respect to bulk due to finite size effects. LSMO-0.5 NWs undergo a PM–FM transition at $T_C \sim 310$ K followed by an FM–AFM transition at $T_N \sim 210$ K, exhibiting conventional MCE and IMCE respectively. Our results point to the presence of magnetic phase coexistence with competing DE and SE interactions arising from the FM and AFM domains. As the temperature is lowered, the FM volume fraction increases and overcomes the AFM interactions (~ 75 K), which is marked by re-entrance of conventional MCE. On further lowering the temperature (~ 45 K), the surface spins undergo a freezing phenomenon with weak frequency dependence. It is to be stressed that, precisely at the surface spin freezing temperature (~ 45 K), we observe the onset of EB. To our knowledge, these particular issues in NWs have not been addressed before and no experiments have been reported in NWs that specially observe this change-over of the nature of the magnetic phase transition on size reduction.

Bibliography:

- [1] S. A. Majetich and M. Sachan, *J. Phys. D: Appl. Phys.*, **39**, R407 (2006).
- [2] K. Bennemann, *J. Phys.: Condens. Matter*, **22**, 243201 (2010).
- [3] *Colossal Magnetoresistive Oxides*, edited by Y. Tokura (Gordon and Breach Science Publishers, The Netherlands, 2000).
- [4] J. M. D. Coey, M. Viret and S. von Molnar, *Adv. Phys.*, **48**, 167 (1999).
- [5] M. H. Phan and S. C. Yu, *J. Magn. Magn. Mat.*, **308**, 325 (2007).
- [6] A. Biswas, T. Samanta, S. Banerjee and I. Das, *Appl. Phys. Lett.*, **92**, 212502 (2008).
- [7] T. Sarkar, B. Ghosh and A. K. Raychaudhuri, *Phys. Rev. B*, **77**, 235112 (2008).
- [8] T. Sarkar, A. K. Raychaudhuri, A. K. Bera and S. M. Yusuf, *New J. Phys.*, **12**, 123026 (2010).
- [9] T. Sarkar, M. V. Kamalakar and A. K. Raychaudhuri, *New J. Phys.*, **14**, 033026 (2012).
- [10] S. S. Rao, K. Anuradha, S. Sarangi and S. V. Bhat, *Appl. Phys. Lett.*, **87**, 182503 (2005).
- [11] D. Zhu, H. Zhu and Y. H. Zhang, *J. Phys.: Cond. Mat.*, **14**, L519 (2002).
- [12] T. Zhang, C. G. Jin, T. Qian, X. L. Lu, J. M. Bai and X. G. Li, *J. Mater. Chem.*, **14**, 2787 (2004).
- [13] K. S. Shankar, S. Kar, A. K. Raychaudhuri and G. N. Subbanna, *Appl. Phys. Lett.*, **84**, 993 (2004).
- [14] K. S. Shankar, S. Kar and A. K. Raychaudhuri, *Nanotech.*, **15**, 1312 (2004).
- [15] T. Sarkar, B. Ghosh and A. K. Raychaudhuri, *J. Nanosci. Nanotechnol.*, **7**, 2020–2024 (2007).
- [16] H. Das, G. Sangiovanni, A. Valli, K. Held and T. Saha-Dasgupta, *Phys. Rev. Lett.*, **107**, 197202–197205 (2011).
- [17] A. Valli, H. Das, G. Sangiovanni, T. Saha-Dasgupta and K. Held, *Phys. Rev. B*, **92**, 115143–115149 (2015).
- [18] B. Ghosh, V. Siruguri, A. K. Raychaudhuri and T. Chatterji, *J. Phys. Condens. Matter.*, **26**, 025603–025611 (2014).
- [19] V. Markovich, R. Puzniak, D. Mogilyansky, X. Wu, K. Suzuki, I. Fita, A. Wisniewski, S. Chen and G. Gorodetsky, *J. Phys. Chem. C*, **115**, 1582 (2011).
- [20] V. Markovich, I. Fita, A. Wisniewski, D. Mogilyansky, R. Puzniak, L. Titelman, C. Martin and G. Gorodetsky, *Phys. Rev. B*, **81**, 094428 (2010).
- [21] T. Zhang, X. P. Wang and Q. F. Fang, *J. Phys. Chem. C*, **114**, 11796 (2010).

- [22] S. Datta, A. Ghatak and B. Ghosh, *J. Mater. Sci.*, **51**, 9679 (2016).
- [23] S. Datta, S. Chandra, S. Samanta, K. Das, H. Srikanth and B. Ghosh, *Journal of Nanomaterials*, vol. **2013**, Article ID 162315, 6 pages, 2013. doi:10.1155/2013/162315.
- [24] S. Chandra, A. Biswas, S. Datta, B. Ghosh, A. K. Raychaudhuri and H. Srikanth, *Nanotechnology*, **24**, 505712 (2013).
- [25] C. N. R. Rao and B. Raveau 1998 (ed) *Colossal Magnetoresistance, Charge Ordering and Related Properties of Manganese Oxides* (Singapore: World Scientific).
- [26] The-Long Phan, T. A. Ho, T. V. Manh, N. T. Dang, C. U. Jung, B. W. Lee and T. D. Thanh, *J. Appl. Phys.*, **118**, 143902 (2015).
- [27] J. C. Loudon, N. D. Mathur and P. A. Midgley, *Nature*, **420**, 797 (2002).
- [28] S. K. Banerjee, *Phys. Lett.*, **12**, 16 (1964).
- [29] H. E. Stanley, *Introduction to Phase Transitions and Critical Phenomena*. Oxford University Press, London (1971).
- [30] A. Arrott, *Phys. Rev.*, **108**, 1394-1396, (1957).
- [31] A. Arrott and J. E. Noakes, *Phys. Rev. Lett.*, **19**, 786-789 (1967).
- [32] J. Mira, J. Rivas, F. Rivadulla, C. Vazquez-Vazquez and M. A. Lopez-Quintela, *Phys. Rev. B*, **60**, 2998 (1999).
- [33] N. Moutis, I. Panagiotopoulos, M. Pissas and D. Niarchos, *Phys. Rev. B*, **59**, 1129 (1999).
- [34] P. M. Chaikin and T. C. Lubensky 1995 *Principles of Condensed Matter Physics* (Cambridge: Cambridge University Press).
- [35] M. Medarde, J. Mesot, P. Lacorre, S. Rosenkranz, P. Fischer and K. Gobrecht, *Phys. Rev. B*, **52**, 9248 (1995).
- [36] A. Arulraj, P. N. Santosh, R. G. Srinivasa, A. Guha, A. K. Raychaudhuri, N. Kumar and C. N. R. Rao, *J. Phys.: Condens. Matter*, **10**, 8497 (1998).
- [37] A. Urushibara, Y. Moritomo, T. Arima, A. Asamitsu, G. Kido and Y. Tokura, *Phys. Rev. B*, **51**, 14103 (1995).
- [38] M. C. Martin, G. Shirane, Y. Endoh, K. Hirota, Y. Moritomo and Y. Tokura, *Phys. Rev. B*, **53**, 285 (1996).
- [39] S. E. Lofland, V. Ray, P. H. Kim, S. M. Bhagat, M. A. Mannheimer and S. D. Tyagi, *Phys. Rev. B*, **55**, 2749 (1997).
- [40] M. N. Barber in *Phase Transitions and Critical Phenomena*, edited by C. Domb and J. L. Lebowitz (Academic, New York, 1983),
- [41] M. E. Fisher and M. N. Barber, *Phys. Rev. Lett.*, **28**, 1516 (1972),

- [42] L. Sun, P. C. Searson and C. L. Chien, *Phys. Rev. B*, **61**, R6463 (2000).
- [43] D. Fuchs, T. Schwarz, O. Moran, P. Schweiss and R. Schneider, *Phys. Rev. B*, **71**, 092406 (2005).
- [44] D. Fuchs, O. Moran, P. Adelman and R. Schneider, *Physica B*, **349**, 337 (2004)
- [45] L. Sun, P. C. Searson and C. L. Chien, *Phys. Rev. B*, **61**, R6463 (2000)
- [46] T. D. Thanh, D. H. Manh, T. L. Phan, P. T. Phong, L. T. Hung, N. X. Phuc and S. C. Yu, *J. Appl. Phys.*, **115**, 17B504 (2014)
- [47] S. Chandra, A. Biswas, S. Datta, B. Ghosh, V. Siruguri, A. K. Raychaudhuri, M. H. Phan and H. Srikanth, *J. Phys.: Condens. Matter*, **24**, 366004 (2012).
- [48] S. Chandra, A. I. Figueroa, B. Ghosh, M. H. Phan, H. Srikanth and A. K. Raychaudhuri, *J. Appl. Phys.*, **109**, 07D720 (2011).
- [49] E. L. Salabas, A. Rumplecker, F. Kleitz, F. Radu and F. Schuth, *Nano Lett.*, **6**, 2977 (2006).
- [50] S. Kundu and T. K. Nath, *J. Appl. Phys.*, **111**, 113903 (2012).
- [51] J. A. Mydosh, 1993 Spin Glasses: An Experimental Introduction (London: Taylor and Francis).
- [52] A. Biswas, T. Samanta, S. Banerjee and I. Das, *J. Phys.: Cond. Mat.*, **21**, 506005 (2009).
- [53] A. Rostamnejadi, M. Venkatesan, J. Alaria, M. Boese, P. Kameli, H. Salamati and J. M. D Coey, *J. Appl. Phys.*, **110**, 043905 (2011).
- [54] A. Biswas, T. Samanta, S. Banerjee and I. Das, *Appl. Phys. Lett.*, **94**, 233109 (2009).
- [55] M. H. Phan, S. Chandra, N. S. Bingham, H. Srikanth, C. L. Zhang, S. W. Cheong, T. D. Hoang and H. D. Chinh, *Appl. Phys. Lett.*, **97**, 242506 (2010).
- [56] A. Biswas and I. Das, *J. Appl. Phys.*, **102**, 064303 (2007).
- [57] V. Podzorov, B. G. Kim, V. Kiryukhin, M. E. Gershenson and S. W. Cheong, *Phys. Rev. B*, **64**, 140406 (2001).
- [58] H. Srikanth, J. Wiggins and H. Rees, *Rev. Sci. Instrum.*, **70**, 3097 (1999).
- [59] S. Chandra, H. Khurshid, M. H. Phan and H. Srikanth, *Appl. Phys. Lett.*, **101**, 232405 (2012).
- [60] N. A. F. Huls, N. S. Bingham, M. H. Phan, H. Srikanth, D. D. Stauffer and C. Leighton, *Phys. Rev. B*, **83**, 024406 (2011).
- [61] S. Chandra, A. I. Figueroa, B. Ghosh, A. K. Raychaudhuri, M. H. Phan, P. Mukherjee and H. Srikanth, *Physica B*, **407**, 175 (2012).
- [62] T. Dhakal, D. Mukherjee, R. Hyde, P. Mukherjee, M. H. Phan, H. Srikanth and S. Witanachchi, *J. Appl. Phys.*, **107**, 053914 (2010).

- [63] A. Aharoni, E. H. Frei, S. Shtrikman and D. Treves, *Bull. Res. Counc. Isr., Sect. A: Math., Phys. Chem.*, **6A**, 215 (1957).
- [64] P. Poddar, M. B. Morales, N. A. Frey, S. A. Morrison, E. E. Carpenter and H. Srikanth, *J. Appl. Phys.*, **104**, 063901 (2008).
- [65] S. Karmakar, S. Taran, E. Bose, B. K. Chaudhuri, C. P. Sun, C. L. Huang and H. D. Yang, *Phys. Rev. B*, **77**, 144409 (2008).
- [66] Y.-K. Tang, Y. Sun and Z.-H. Cheng, *J. Appl. Phys.*, **100**, 023914 (2006)
- [67] S. M Zhou, S. Y. Zhao, Y. Q. Guo, J. Y. Zhao and L. Shi, *J. Appl. Phys.*, **107**, 033906 (2010).
- [68] B. G. Kim, A. Kumar, S. Ki, S. Kim and J. Dho, *J. Appl. Phys.*, **110**, 123907 (2011).
-

Chapter 6

Crystal structure analysis using synchrotron XRD measurement and magnetic structure refinement using neutron diffraction method

In this chapter we investigate the crystal structure property of ensemble of nanowires (NWs) of $La_{1-x}A_xMnO_3$ ($A = Ca, Sr$; $x = 0.3$ and 0.5) using synchrotron X-ray diffraction (XRD) study and magnetic structural analysis of $La_{0.5}Sr_{0.5}MnO_3$ NWs using neutron diffraction (ND) method. Our interest is to explore, how crystal structure evolves on size reduction to one dimensional (1D) manganites NWs. In previous chapter 5, we have discussed about how the size reduction induces T_C enhancement, multiple phase transitions, phase separation and exchange bias (EB) effect in the NWs which is absent in its bulk form. In this chapter we would like to explore how the size reduction induced physical properties are correlated with the structural properties of the NWs. The contraction of lattice parameters due to size reduction can lead to change in magnetic properties. These structural studies show the coexistence of crystallographic (tetragonal and orthorhombic) and magnetic phases (FM and AFM) respectively below T_N (< 200 K) in $La_{0.5}Sr_{0.5}MnO_3$ NWs. In contrast, bulk $La_{0.5}Sr_{0.5}MnO_3$, showing FM (tetragonal phase) throughout the measured temperatures (6 - 300 K), does not show any phase separation. Our study will provide in-depth understanding of the underlying physics and basic mechanism of size induced phase separation in the NWs and the role of crystal structure in stabilizing a specific ground state of the manganite NWs.

6.1 Introduction and Motivation

One of the most interesting aspects of the physics of manganites is the strong interaction between charge carriers and lattice degrees of freedom, due to the size difference between Mn^{4+} and Mn^{3+} and to the tendency of the latter to lower the octahedral symmetry of its coordination shell, thereby lowering the energy of its e_g electron (Jahn-Teller effect). This strong ‘‘electron-phonon’’ coupling can be tuned by varying the electronic doping, electronic bandwidth and disorder. This gives rise to a complex phenomenology in which crystallographic structure, magnetic structure and transport properties are closely related. The ground state of manganite system can be tuned by various factors such as, carrier density, magnetic field, pressure and biaxial strain, even size reduction [1-11]. Modification in many physical properties as well as magnetic properties is widely reported phenomenon in nanoparticles of manganites. Study of magneto-structural correlation is not very common in 1D manganite nanostructures. In this chapter, we pursue crystal and magnetic structure study of manganite nanowires (NWs). Recent reports reveal that the properties of manganites get strikingly altered due to nanostructuring [12-15], particularly at half doping in nanocrystals ($\text{La}_{0.5}\text{Ca}_{0.5}\text{MnO}_3$), where size induced destabilization of charge and magnetic ordering was found [2,16] and were further established by recent theoretical calculations [17,18]. So far, few reports on size-dependent exchange bias effect and glassy behaviour in magnetic phases of nanostructures are available [7]. The magnetic and structural properties of nano-sized materials are significantly changed by their dimensionality [19, 20]. When the size of the parent compound of perovskite manganite LaMnO_3 is reduced to 50 nm regimes, it unveils a drastic change in crystallographic symmetry and magnetic ordering [1]. Control of structural and magnetic phases by size reduction is, therefore, an interesting proposition in nanocrystals of complex correlated oxides like manganites. Previously, immense importance has been given to the understanding of the physical properties of nanoparticles (0D) and thin films (2D); however, the 1D counterpart of such materials, i.e. nanotubes and NWs, has been less investigated [20]. Other than the nanocrystals, manganites, even in 1D NW form, show many novel physical properties, both in ensemble and single NW level due to large surface-to-volume ratios and thus, are very promising candidates for realizing nanoscale devices [21, 22].

Phase coexistence with different structural, electrical and magnetic properties is one of the most interesting phenomena observed in manganites [23]. The phase separation changes with

temperature, magnetic field and particle size. The phase coexistence has been studied by different techniques such as magnetization [24], electron spin resonance (ESR) [25], nuclear magnetic resonance (NMR) [26, 27], neutron powder diffraction [28], electron diffraction-dark-field imaging [29, 30] and Raman scattering [31]. EB effect has also been observed in single phase perovskite manganites and cobaltites with intrinsic phase separation [32-35]. In recent years, the phase coexistence of manganites has been investigated by magneto-caloric studies, i.e., using the magnetic entropy change (ΔS_M) [13, 21, 36-38].

The main motivation of the present work is to obtain an extensive understanding of modification of structural and magnetic phases in manganite NWs on size reduction. So far, previous studies have explored the crystal and magnetic structural aspects in bulk and nanocrystals of half doped manganite systems [10, 15, 39, 40]. To the best of our knowledge, till now no report exists on the understanding of crystal structure and its correlation with the magnetic phases of manganite NWs, except for a few reports on the growth [41, 42]. In chapter 5 and 7 we have discussed magnetic measurements and $1/f$ noise spectroscopy study [21, 22], where the presence of phase coexistence in magnetic phases has been confirmed both in ensemble of NWs and in single NW of half doped manganite system. To understand the temperature and magnetic-field dependent magnetization dynamics in NWs, we have carried out ac & dc magnetization study, magnetocaloric study and transverse susceptibility study. Our study has pointed out the coexistence of DE and SE interactions arising from the AFM and FM domains (discussed in chapter 5) [21]. The existence of phase coexistence in the same composition via noise spectroscopy study of a single NW, where it was pointed out that identification of magnetic phases is possible from the time series of resistance fluctuation measurements (discussed in chapter 7) [22]. Though the presence of phase coexistence was confirmed in the half doped manganite NWs both in ensemble and single NW level, the reason for this phase separation, its possible origin and whether there is any correlation with crystal and magnetic structures are some of the fundamental issues in manganite system. Thus, it is necessary to understand the magnetic and electronic properties in the 1D NW systems from crystallographic structural aspect, where atomic bonds and atomic angles, magnetic spins, etc., play a vital role. In this context, our study will provide in-depth understanding of the underlying physics and basic mechanism of phase separation in the NWs and the role of crystal structure in stabilizing a specific ground state of the NWs. This knowledge support will be provided by extensive crystallographic and magnetic structural study using synchrotron and neutron powder diffraction experiments of manganite NWs.

6.2 Experimental details

For crystallographic structural investigation, synchrotron XRD at Indian beam line BL-18B, Photon Factory, KEK, Japan was employed for all ensemble of NWs of $\text{La}_{1-x}\text{A}_x\text{MnO}_3$ (A = Ca, Sr; $x = 0.3$ and 0.5) samples. The sample was illuminated by monochromatic X-ray beam with wavelength $\lambda = 0.7934 \text{ \AA}$. All the XRD measurements were performed in temperature range of $14 - 300 \text{ K}$. The powder diffraction data were collected during heating cycle. Rietveld method (described in chapter 2) was used to refine the structural parameters [43, 44].

Temperature dependent ($3-300 \text{ K}$) neutron diffraction (ND) experiments were carried out on LSMO-0.5 NWs (in powder form) using the multi-position-sensitive detector-based focusing crystal diffractometer set up by UGC-DAE Consortium for Scientific Research Mumbai Centre at the National Facility for Neutron Beam Research (NFNBR), Dhruva reactor, Mumbai, India with a wavelength of 1.48 \AA [45]. Temperature variation of neutron powder diffraction measurement from 3 K to 300 K was done in a Cryogenics make cryogen-free magnet system by loading the samples in vanadium can of height 35 mm and diameter 6 mm . ND measurements on LSMO-0.5 bulk sample were performed at the PD-2 diffractometer, Dhruva reactor, Mumbai, India with a wavelength of 1.244 \AA and in the temperature range of $6-300 \text{ K}$ [46-48]. The ND data were analyzed with the help of the Rietveld refinement program implemented in FullProf Suite software [43, 44].

6.3 Results and discussions

6.3.1 $\text{La}_{0.7}\text{Ca}_{0.3}\text{MnO}_3$ (LCMO-0.3) and $\text{La}_{0.5}\text{Ca}_{0.5}\text{MnO}_3$ (LCMO-0.5) nanowires

The synchrotron XRD patterns of LCMO-0.3 and LCMO-0.5 NWs taken at different temperatures (temperature range $20-300 \text{ K}$) have been plotted in Fig. 6.1 (a)-(b). Analysis of the full patterns reveals that LCMO-0.3 and LCMO-0.5 NWs are orthorhombic in structure at all temperatures having space group $Pnma$, i.e., $a \neq b \neq c$, $\alpha = \beta = \gamma = 90^\circ$. [49]. The fitting of XRD patterns with residue obtained from the Rietveld refinement for LCMO-0.3 and LCMO-0.5 NWs at 20 K and 300 K are shown in Figs. 6.2 (a)-(d). The experimentally observed and Rietveld calculated diffraction profiles are quite matching well confirming the

orthorhombic structure of both manganites system. The refined lattice parameters, Mn-O bond angle and bond lengths of LCMO-0.3 and LCMO-0.5 NWs are tabulated in Table 6.1 and compared with the bulk samples. The detailed atomic positions of LCMO-0.3 and LCMO-0.5 NWs are listed in Table 2.2 in chapter 2. The refined structural parameters for LCMO-0.3 and LCMO-0.5 bulk samples in Table 6.1 are taken from the earlier reports [50-51].

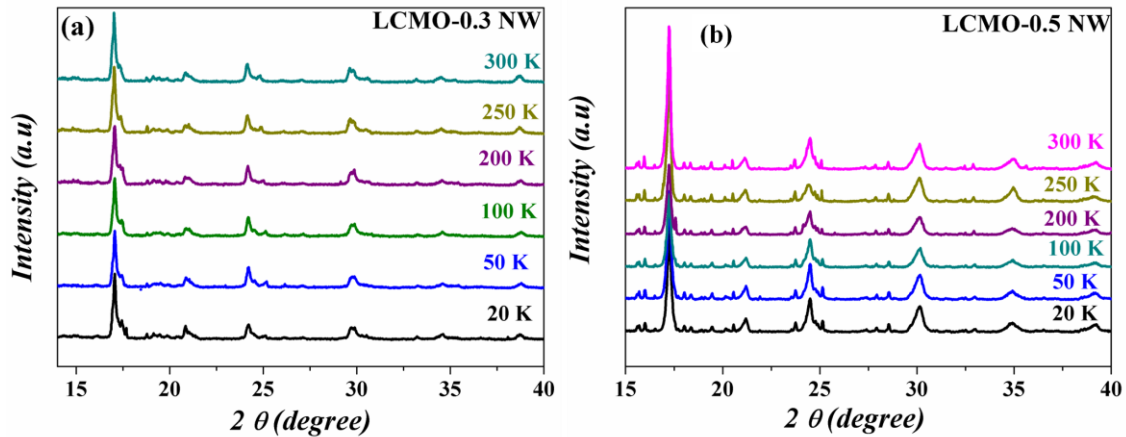


Figure 6.1 Synchrotron XRD patterns for (a) LCMO-0.3 (b) LCMO-0.5 nanowires (NWs) taken at different temperatures.

Even though the crystal structure of both bulk and NW samples are orthorhombic with space group $Pnma$, crystallite size reduction into NW form affects the orthorhombic strain, lattice parameter and unit cell volume. From Table 6.1 it is clearly observed that the size induced lattice contraction is occurred in both LCMO-0.3 and LCMO-0.5 NWs therefore, the volume of unit cell reduces in both the NWs with respect to bulk. The initial enhancement in T_C (as discussed in chapter 5) was associated to an increase in the bandwidth that occurred due to a compaction of the Mn–O bond length and a straightening of the Mn–O–Mn bond angle, as observed from the refinement of synchrotron XRD data (see Table 6.1). The analysis of the synchrotron XRD data shows that a clear change occurs in the MnO_6 octahedron on size reduction as shown by the Mn–O–Mn bond angles and Mn–O bond lengths. These two parameters have a direct role in the determination of the overlap integral and thus on the bandwidth W . The size reduction thus leads to a contraction of the Mn–O bond lengths and Mn–O–Mn bond angles move closer to 180° which leads to an enhancement of the bandwidth and endorses the ferromagnetism of manganite, which ultimately enhances T_C in both the compositions. Moreover, the increased bandwidth leads to the nature of the phase transition change from first order to second order. Hence size reduction in Ca doped 1D cases leads to

enhancement of bandwidth along with the changes in the nature of magnetic phase transition as discussed in chapter 5. There are some papers which report the lowering of unit cell volume with decreasing particle size in LCMO-0.5 [10,17]. Recently using density functional theory and dynamical mean field theory calculations on LCMO, Das *et. al.* [17] has reported that destabilization of low temperature AFM phase in nanocrystalline samples is related to the structural changes in the samples. They have validated the work of Sarkar *et. al* [2] who has reported the reduction of unit cell volume with decreasing particle size. The unit cell of the manganite is often distorted from the cubic structure and the JT distortion around the Mn^{3+} ions leads to orthorhombic distortions. The reduction of the orthorhombic distortion strengthens the double-exchange interaction, enhances the bandwidth and strengthens the FM state.

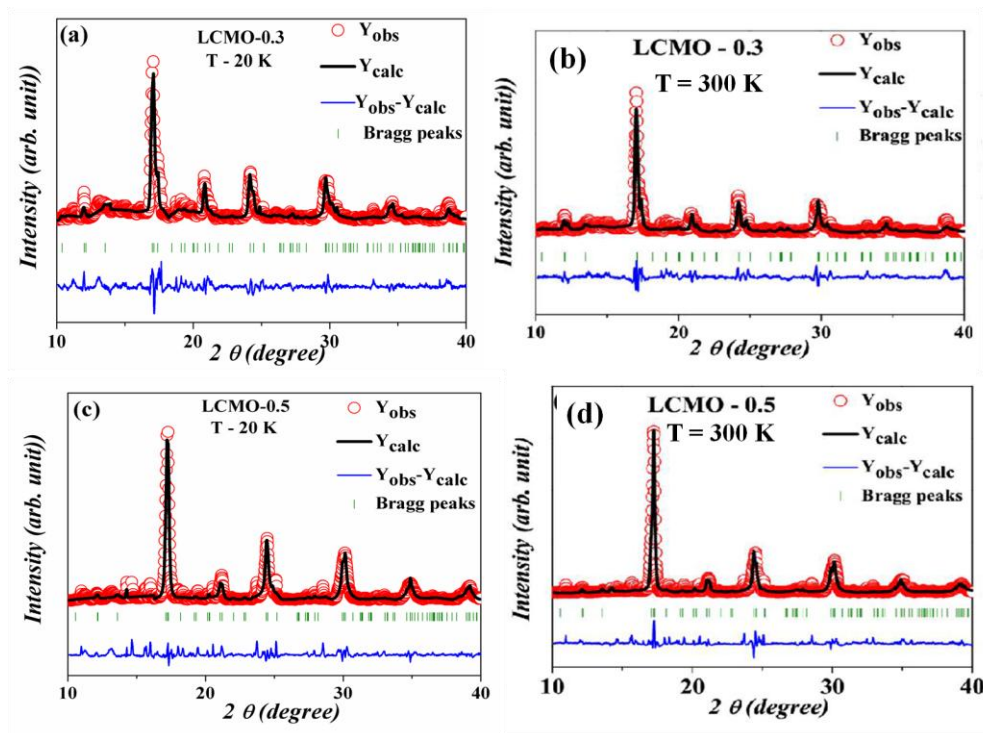


Figure 6.2 The fitting of XRD patterns with residue obtained from the Rietveld refinement of LCMO-0.3 nanowires at (a) 20 K, (b) 300 K and of LCMO-0.5 NW at (c) 20 K and (d) 300 K respectively. Experimentally observed (red circles), Rietveld calculated (black curves) and their difference (continuous bottom line of blue colour) profiles are obtained after Rietveld analysis of the XRD data using orthorhombic space group $Pnma$. The vertical tick marks (green colour) between the observed and difference plot show the Bragg peak positions.

We define the orthorhombic strains as $OS_{\parallel} = \frac{2(c-a)}{(c+a)}$ (giving the strain in the ac plane) and $OS_{\perp} = \frac{2(a+c-b\sqrt{2})}{a+c+b\sqrt{2}}$ (giving the strain along the b -axis with respect to the ac plane).

As reported by earlier authors also, [2, 52] for LCMO, the orthorhombic strains are small in bulk samples with $OS_{\perp} > OS_{\parallel}$ as shown in Table 6.2. In case of both LCMO-0.3 and LCMO-0.5, the orthorhombic strains significantly increase for the NW samples. Significantly larger orthorhombic strains in nanocrystallite samples than the bulk LCMO is also reported by Sarkar *et. al* [53].

The analysis of structural data as obtained from the synchrotron XRD data of LCMO-0.3 and LCMO-0.5 NWs clearly shows that the small but clear change in the MnO_6 octahedra and the Mn–O–Mn angle, both for the apical and equatorial oxygen moves closer to 180° . This leads to an enhancement of the bandwidth (W). W depends on both the Mn–O–Mn bond angles and Mn–O bond lengths, through the overlap integrals between the $3d$ orbitals of the metal ion Mn and the $2p$ orbitals of the O anion. An estimate of the bandwidth (W) (in the double exchange model) can be made from the relation [54],

$$W \propto \cos \omega / d_{Mn-O}^{3.5} \quad (6.1)$$

Where $\omega = \frac{1}{2} (\pi - \theta_{Mn-O-Mn})$. Thus, an increase in the bond angle $\theta_{Mn-O-Mn}$ and a decrease in the bond length d_{Mn-O} would mean an overall increase in the bandwidth W , thereby leading to an enhancement of T_C . Using this relationship we find that the bandwidth for NW LCMO-0.3 is ~ 0.1154 which is higher than the bulk bandwidth ~ 0.0977 and for NW LCMO-0.5 is ~ 0.0977 which is higher than the bulk bandwidth ~ 0.0963 . Thus we have observed a decreased unit cell volume with decreasing particle size, increased bandwidth, increased T_C and stabilization of ferromagnetic state. In fact, Sarkar *et. al* [2] has reported that with decreasing crystallite size, T_C increases. This suggests that the bandwidth for the nano-size samples is increasing with decreasing crystallite size leading to enhancement in the T_C . The crystal structure is orthorhombic for both bulk and NWs LCMO-0.3 and LCMO-0.5 samples but the lattice parameters and Mn–O bond lengths are significantly affected by crystallite size reduction in the NWs.

Table 6.1 Lattice parameters, selected inter-atomic distances and bond angles and reliability factors of LCMO-0.3 and LCMO-0.5 nanowires (NWs) at 300 K and 20 K determined from Rietveld refinement of XRD data using FULLPROF software and compared with the reported bulk data [50,51].

<i>Sample</i>	<i>LCMO-0.3 Bulk [51]</i>	<i>LCMO-0.3 NW</i>	<i>LCMO-0.3 NW</i>	<i>LCMO-0.5 bulk [50]</i>	<i>LCMO-0.5 NW</i>	<i>LCMO-0.5 NW</i>
T (K)	300 K	300 K	20 K	300 K	300 K	20 K
<i>a</i> (Å)	5.3812 (1)	5.2943(4)	5.2531 (2)	5.4248 (1)	5.3509(4)	5.3391(8)
<i>b</i> (Å)	7.5687 (1)	7.5936(6)	7.5895(7)	7.6470 (2)	7.4685(1)	7.4831(5)
<i>c</i> (Å)	5.3864 (1)	5.3671(3)	5.3741 (4)	5.4355 (1)	5.2850(1)	5.2839(8)
<i>V</i> (Å ³)	219.38 (9)	215.77(2)	214.25(3)	225.48 (9)	211.21(1)	211.1 (6)
Mn-O(1) (Å)	1.9196 (3)	1.8817 (4)	1.8715 (3)	1.9406 (3)	1.8659 (2)	1.8593 (5)
Mn-O(2) (Å)	1.936 (2)	1.8526 (4)	1.8393 (7)	1.944 (2)	1.9377 (3)	1.9397 (5)
Mn-O(1)-Mn (°)	160.6 (1)	175.4(5)	174.58(6)	160.23 (9)	161.5(6)	161.65(9)
Mn-O(2)-Mn (°)	161.13 (6)	174.54(5)	173.60(6)	161.65 (6)	163.6(1)	163.56(6)
χ^2	3.95	5.41	6.13	5.803	5.62	6.1
R_p (%)	--	13.0	15.8	--	9.2	15.3
R_{wp} (%)	5.38	16.4	19.7	4.54	13.46	21.8
R_{exp} (%)	--	7.07	7.96	--	5.68	8.9

Table 6.2 Orthorhombic strains of bulk and NWs of LCMO-0.3 and LCMO-0.5 at 300K.

<i>Orthorhombic strains</i>	<i>LCMO-0.3 bulk [51]</i>	<i>LCMO-0.3 NW</i>	<i>LCMO-0.5 bulk [50]</i>	<i>LCMO-0.5 NW</i>
OS	0.0009	0.01365	0.002	0.01234
OS _⊥	0.006	0.0072	0.0044	0.007

6.3.2 $La_{0.7}Sr_{0.3}MnO_3$ (LSMO-0.3) nanowires

The temperature dependent synchrotron XRD data of LSMO-0.3 NWs (temperature range 25-300 K) have been plotted in Fig. 6.3. Analysis of the full patterns reveals that LSMO-0.3 NWs are rhombohedral in structure at all temperatures having space group $R\bar{3}c$ i.e., $a = b \neq c$, $\alpha = \beta = 90^\circ$, $\gamma = 120^\circ$ [55]. The fitting of XRD patterns with residue obtained from the Rietveld refinement for LSMO-0.3 NWs at 25 K and 300 K are shown in Figs. 6.4 (a)-(b). The experimentally observed and Rietveld calculated diffraction profiles are quite matching well confirming the rhombohedral structure of LSMO-0.3 NWs. The refined lattice parameters, reliability factors of LSMO-0.3 NWs are listed in Table 6.3 and compared with the bulk samples. The detailed atomic positions of LCMO-0.3 and LCMO-0.5 NWs are listed in Table 2.2 in chapter 2. The refined structural parameters for LSMO-0.3 bulk samples in Table 6.3 are taken from the earlier reports [55]. For LSMO-0.3 sample, there is small amount of impurity of $La(OH)_3$ estimated to be $< 5\%$. It was noticed that despite heating the samples for prolonged time, the amount of impurity ($La(OH)_3$) remains constant [56].

In previous chapter (chapter 5) we have already discussed that LSMO-0.3 NWs having wider bandwidth T_C is decreased may be due to finite size effect which is well known reason for T_C value decrement due to size reduction.

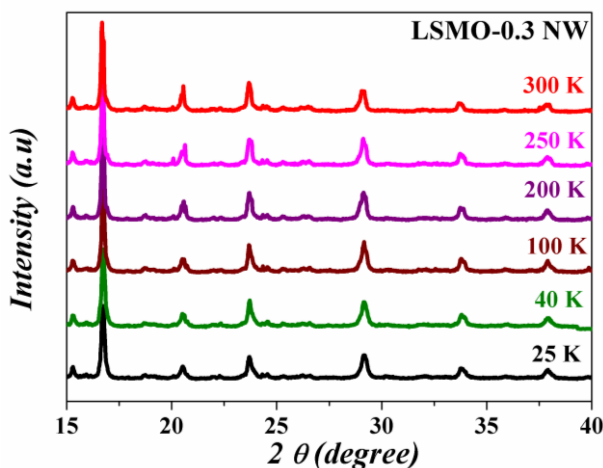


Figure 6.3 Synchrotron XRD patterns for LSMO-0.3 nanowires (NWs) taken at different temperatures.

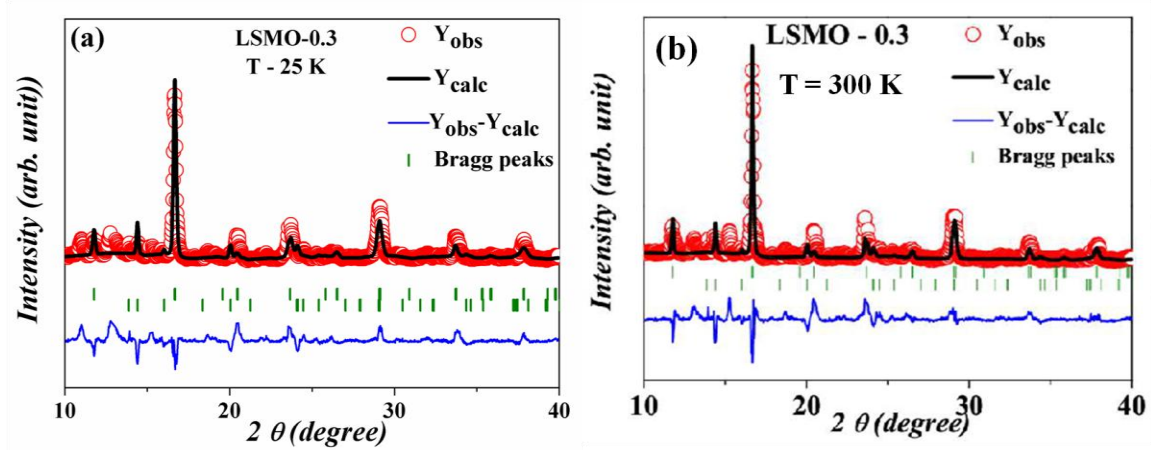


Figure 6.4 The fitting of XRD patterns with residue obtained from the Rietveld refinement of LSMO-0.3 nanowires at (a) 25 K, (b) 300 K respectively. Experimentally observed (red circles), Rietveld calculated (black curves) and their difference (continuous bottom line of blue colour) profiles are obtained after Rietveld analysis of the XRD data using rhombohedral space group $R-3c$. The vertical tick marks (green colour) between the observed and difference plot show the Bragg peak positions.

Table 6.3 Lattice parameters and reliability factors of LSMO-0.3 nanowires (NWs) at 300 K and 25 K determined from Rietveld refinement of XRD data using FULLPROF software and compared with the reported bulk data [55].

Sample	<i>LSMO-0.3</i> <i>Bulk</i> [55]	<i>LSMO-0.3 NW</i>	<i>LSMO-0.3 NW</i>
Temperature	300 K	300 K	25 K
$a = b$ (Å)	5.5060 (1)	5.4867(9)	5.4808 (1)
c (Å)	13.3564 (3)	13.3747(7)	13.3993(6)
V (Å ³)	350.66 (1)	348.68(5)	348.57 (2)
χ^2	2.262	6.12	7.64
R_p (%)	--	11.3	21.9
R_{wp} (%)	5.78	17.59	19.6
R_{exp} (%)	--	7.11	7.09

6.3.3 $\text{La}_{0.5}\text{Sr}_{0.5}\text{MnO}_3$ (LSMO-0.5) nanowires

In LSMO-0.5 NWs, structural correlations with the magnetic transitions were accomplished with synchrotron and neutron diffraction experiments. The synchrotron X-ray powder diffraction data (temperature range 14–300 K) have been plotted in Fig. 6.5. The inset shows an enlarged view of 100% peak intensity with hkl (112) at 16.7° , where the peak broadening occurs near 200 K, which is the AFM transition temperature (T_N) of LSMO-0.5 NWs. At room temperature, the structure is tetragonal with space group of $I4/mcm$. Below 200 K, the peak intensities at 16.7° , 34° and 38° are reduced and a new peak appears around 24° . The results of Rietveld refinement shows that when temperature is lowered below 200 K, evolution of orthorhombic phase (space group $Fmmm$) occurs along with the tetragonal phase. The crystallographic structural change is accompanied by T_N . On further lowering the temperature, orthorhombic volume fraction increases.

In chapter 5, we have described that there are multiple magnetic transitions and phase coexistence (FM and AFM phases) below 200 K. This issue was investigated by refining the structural parameters using the Rietveld method.

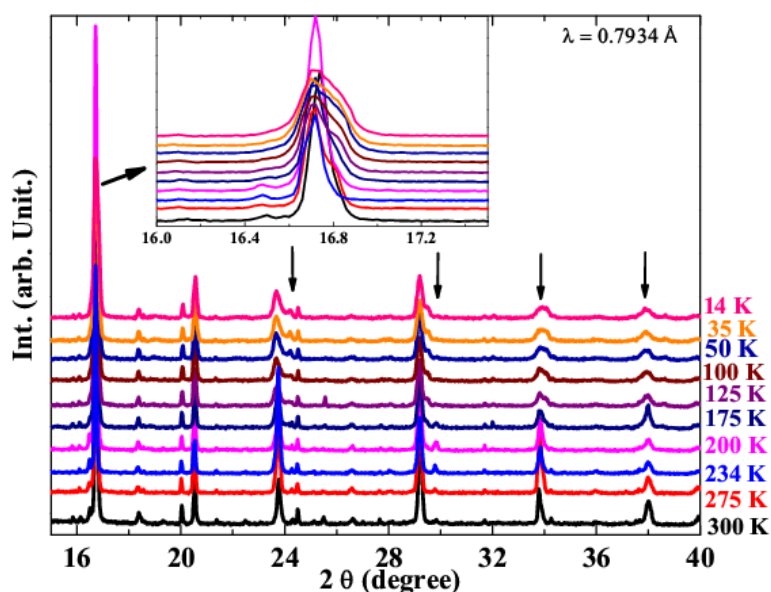


Figure 6.5 Synchrotron XRD data for LSMO-0.5 NWs in the range 14 – 300 K. At 300 K, the crystal structure is tetragonal (space group $I4/mcm$) and when the temperature is lowered below 200 K, orthorhombic phase (space group $Fmmm$) comes into play along with tetragonal phase. The inset of this Fig. shows the enlarged view of 100% peak intensity with hkl (112) at 16.7° .

6.4 Neutron diffraction experiment of LSMO-0.5 bulk and nanowires

Crystal structure refinement of neutron diffraction data (temperature range: 3-300K):

The neutron powder diffraction experiments were performed on ensemble of LSMO-0.5 NWs and bulk sample in low temperature regime. The fitting of neutron diffraction patterns with residue obtained from the Rietveld refinement for LSMO-0.5 bulk and NWs are shown in Figs. 6.6 (a-d). The red circles show the experimental data, the black curve denotes the calculated pattern and the blue curve gives the difference pattern. The data obtained are analyzed with Rietveld refinement using the FULLPROF software [43, 44] and Pseudo-Voigt function for line profile. From this figure, a good agreement between the experimental and calculated profiles can be observed. The analysis of the LSMO-0.5 bulk sample at 300 K (Fig. 6.6 (b)) shows tetragonal structure with $I4/mcm$ symmetry which is similar to as reported in our synchrotron X-ray study and previously by others for $La_{0.5}Sr_{0.5}MnO_3$ and $Pr_{0.5}Sr_{0.5}MnO_3$ samples [57, 58]. The bulk system retains its tetragonal structure till the lowest temperature (~ 6 K) of measurement. Fig. 6.6(a) shows the ND pattern of the bulk LSMO-0.5 at 6 K. The pattern could be indexed with tetragonal structure having $I4/mcm$ symmetry. The refined lattice parameters, atomic coordinates, bond lengths and angles are summarized in Table 6.4 for LSMO-0.5 bulk at different temperatures. The obtained reliability parameters (R_p , R_{wp} and R_{exp}) and the goodness of fit (GoF) or χ^2 reflect high quality structural refinement [Fig. 6.6 (a), (b)]. In bulk LSMO-0.5, presence of a minor impurity peak of Mn_3O_4 has been noticed whose volume fraction is $\sim 1.5\%$.

In case of LSMO-0.5 NW, the 300 K powder diffraction pattern (Fig. 6.6 (d)) has been indexed in tetragonal phase with $I4/mcm$ space group, but with decreasing temperature, the system undergoes a structural transition below 200 K. At this temperature, evolution of orthorhombic structure ($Fmmm$) with volume fraction 15% occurs within the tetragonal phase ($I4/mcm$). The orthorhombic volume fraction increases gradually in a very broad temperature range below 200 K on cooling and at the lowest temperature measured (~ 3 K), it finally reaches 35%. Below 200 K, there is a coexistence of both orthorhombic ($Fmmm$) and tetragonal ($I4/mcm$) structural phases. However, little amounts of impurities of $La(OH)_3$ ($\sim 5\%$) and Mn_3O_4 ($\sim 3\%$) are also estimated. The cell parameters obtained from refinement of ND data of NWs have been tabulated in Table 6.5. We compare the refinement results of the bulk and NWs, the following comparison can be noted from Table 6.4 and 6.5.

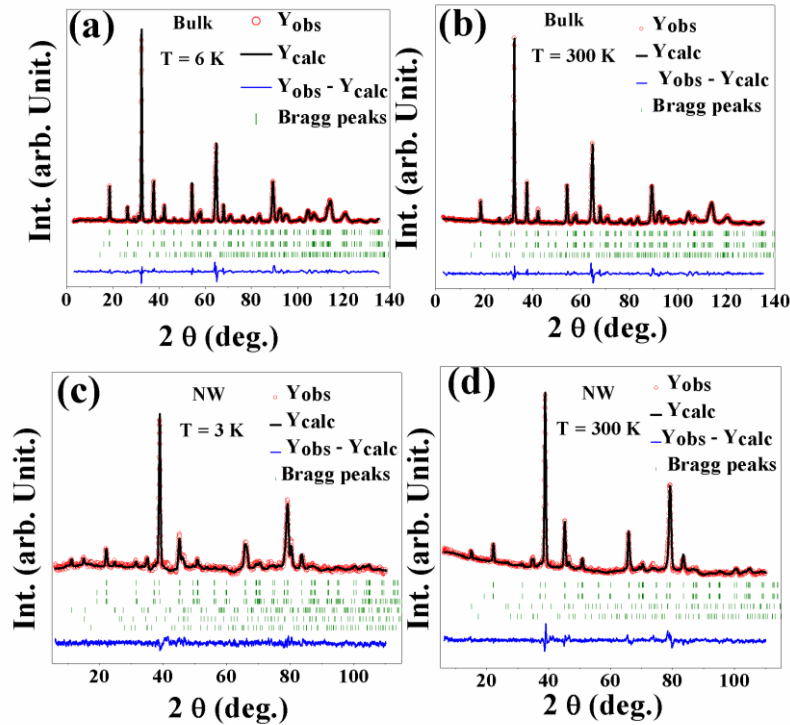


Figure 6.6 The typical profile fits of neutron diffraction patterns with residuals obtained from the Rietveld refinement of LSMO-0.5 bulk at (a) 6 K, (b) 300 K and of LSMO-0.5 NW at (c) 3 K and (d) 300 K respectively. The red circles show the experimental data, the black curve denotes the calculated pattern and the blue curve is the difference pattern. The Bragg positions of the reflections are indicated by vertical lines (green colour) below the pattern.

The volume per formula unit reduces by about 0.75% at 300 K from bulk to NWs. The bulk system maintains tetragonal symmetry all through the temperature range. On the other hand, crystallographic structure changes for NWs. The NWs show tetragonal symmetry at room temperature and maintain the symmetry till T_N , but below T_N , structural evolution of orthorhombic phases occurs within the tetragonal phase and thereafter co-existence of both the phases persists till the lowest temperature. The temperature variation of the weight percentage of the crystallographic phases of the LSMO-0.5 NWs is demonstrated in Fig 6.7. It appears that the volume fraction of the orthorhombic $Fmmm$ phase increases gradually below 200 K and finally reaches a constant value of 35% at 3 K with 60% of tetragonal phase with $I4/mcm$ symmetry. The temperature evolution of lattice parameters obtained from the Rietveld refinement of LSMO-0.5 bulk and NW is shown in Figs. 6.8 (a-b). The temperature variation of lattice constants of NWs is sharply different from that of bulk system. For the bulk system, lattice constants are unchanged throughout the temperature range measured.

Table 6.4 Structural parameters, selected inter-atomic distances and bond angles of $\text{La}_{0.5}\text{Sr}_{0.5}\text{MnO}_3$ bulk sample at 300 K and 6 K determined from Rietveld refinement of neutron powder diffraction data using FULLPROF software.

Temperature	300 K	6 K
Space group	98.5% $I4/mcm^\#$	98.5% $I4/mcm^\#$
a (Å)	5.4455(2)	5.4341 (2)
b (Å)	5.4455(2)	5.4341 (2)
c (Å)	7.7625(7)	7.7515 (4)
V (Å ³)	230.18(2)	228.89(7)
V (Å ³)/f.u	57.54	57.22
La/Sr	Site 4b	Site 4b
x	0	0
y	0.5	0.5
z	0.25	0.25
B_{iso}	0.3169(4)	0
Mn	Site 4c	Site 4c
x	0	0
y	0	0
z	0	0
B_{iso}	0.1010(2)	0
O/O1	Site 4a	Site 4a
x	0	0
y	0	0
z	0.25	0.25
B_{iso}	0.4548(1)	0
O2	Site 8d	Site 8d
x	0.77469(3)	0.7766(1)
y	0.27469(2)	0.2766(1)
z	0	0
B_{iso}	0.6983(1)	0
Mn-O(1) (Å)	1.9406 (1)	1.9381 (1)
Mn-O(2) (Å)	1.9346 (1)	1.9322 (2)
Mn-O(1)-Mn (°)	180.0	180.0
Mn-O(2)-Mn (°)	168.7 (5)	167.8 (2)
χ^2	4.98	8.39
R_p (%)	4.06	5.10
R_{wp} (%)	5.63	6.75
R_{exp} (%)	2.52	2.33

1.5% is coming from Mn_3O_4 sample which is in the Tetragonal ($I4_1/amd$) phase; $a = b = 5.7358$ Å, $c = 9.4701$ Å, $V = 311.56$ Å³ at 300 K and $a = b = 5.73236$ Å, $c = 9.61864$ Å, $V = 316.06$ Å³ at 6 K.

However, the c axis of the lattice parameters of NWs changes substantially near T_N and the change is much more pronounced below T_N . The changes in the lattice constant are associated with the structural change, where the room temperature tetragonal structure ($I4/mcm$) undergoes a transition to orthorhombic ($Fmmm$) as plotted in Fig. 6.8 (b). At room temperature, a significant contraction of c axis (0.45%) has been observed in NWs compared to the bulk. Whereas, the value of ' a ' axis of NW is quite comparable to bulk at 300 K. It also

undergoes a change near T_N , which is associated with structural change. Below T_N , the cell parameters of orthorhombic phase ($Fmmm$) of NWs are almost constant down to lowest temperature (3 K) measured [57]. The crystallographic structure of tetragonal ($I4/mcm$) at 300 K and orthorhombic ($Fmmm$) phases at 200 K (reproduced from Rietveld analysis) is plotted in vesta software and is shown in Fig. 6.9.

Table 6.5 Structural parameters, selected inter-atomic distances and bond angles of $La_{0.5}Sr_{0.5}MnO_3$ nanowires at different temperatures determined from Rietveld refinement of neutron powder diffraction data using FULLPROF software.

Temperature	300 K	3 K	3 K
Space group	92 % $I4/mcm^{\#}$	60% $I4/mcm^{\#}$	35% $Fmmm$
a (Å)	5.4370(2)	5.4390(5)	7.5838(9)
b (Å)	5.4370(2)	5.4390(5)	7.7102(1)
c (Å)	7.7276(7)	7.7313(6)	7.7659(2)
V (Å ³)	228.43(2)	228.71(5)	454.09(1)
V (Å ³)/f.u	57.1	57.17	56.76
La/Sr	Site $4b$	Site $4b$	Site $8h$
x	0	0	0
y	0.5	0.5	0.2413(1)
z	0.25	0.25	0
B_{iso}	0.7382(1)	0	0
Mn	Site $4c$	Site $4c$	Site $8d$
x	0	0	0.25
y	0	0	0
z	0	0	0.25
B_{iso}	0.2285(1)	0	0
O/O1	Site $4a$	Site $4a$	Site $8g$
x	0	0	0.2380(2)
y	0	0	0
z	0.25	0.25	0
B_{iso}	0.6009(1)	0	0
O2	Site $8d$	Site $8d$	Site $8i$
x	0.77469(5)	0.7766(9)	0
y	0.27469(2)	0.2766(1)	0
z	0	0	0.2784(5)
B_{iso}	0.2519(1)	0	0
O3	--	--	Site $8f$
x	--	--	0.25
y	--	--	0.25
z	--	--	0.25
B_{iso}	--	--	0
Mn-O(1) (Å)	1.93 (1)	1.9328(2)	1.9435(1)
Mn-O(2) (Å)	1.932(2)	1.9338(3)	1.9087(4)
Mn-O(3) (Å)	--	--	1.9275(3)
Mn-O(1)-Mn(^o)	180.0	180.0	174.6(6)
Mn-O(2)-Mn(^o)	168.72 (6)	167.8 (1)	166.7(6)
Mn-O(3)-Mn(^o)	--	--	180.0
χ^2	3.81	3.32	3.31
R_p (%)	2.80	3.82	3.81
R_{wp} (%)	3.86	4.83	4.82
R_{exp} (%)	1.98	2.65	2.65

5% is coming from $\text{La}(\text{OH})_3$ sample which is in the hexagonal ($P6_3/m$) phase; $a = b = 6.5033 \text{ \AA}$, $c = 3.8603 \text{ \AA}$, $V = 141.39 \text{ \AA}^3$ at 300 K. 3% is coming from Mn_3O_4 sample which is in the Tetragonal ($I4_1/amd$) phase; $a = b = 5.7358 \text{ \AA}$, $c = 9.4701 \text{ \AA}$, $V = 311.56 \text{ \AA}^3$ at 300 K.

* 3% is coming from $\text{La}(\text{OH})_3$ sample which is in the hexagonal ($P6_3/m$) phase; $a = b = 6.5121 \text{ \AA}$, $c = 3.8713 \text{ \AA}$, $V = 142.17 \text{ \AA}^3$ at 3 K. 2% is coming from Mn_3O_4 sample which is in the Tetragonal ($I4_1/amd$) phase; $a = b = 5.7378 \text{ \AA}$, $c = 9.4575 \text{ \AA}$, $V = 311.36 \text{ \AA}^3$ at 3 K.

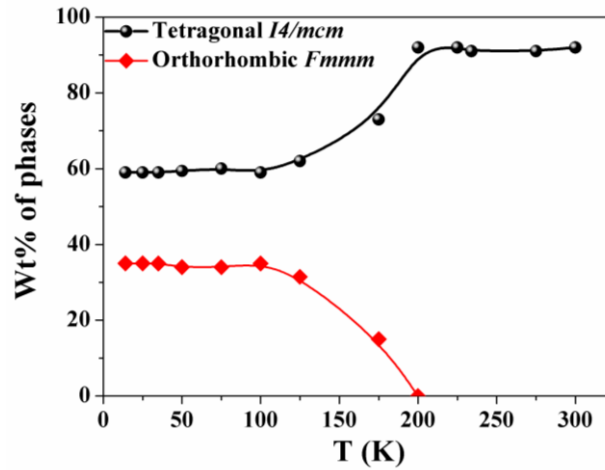


Figure 6.7 Volume fraction of the $Fmmm$ (red curve) and $I4/mcm$ (black curve) phases of LSMO-0.5 NWs.

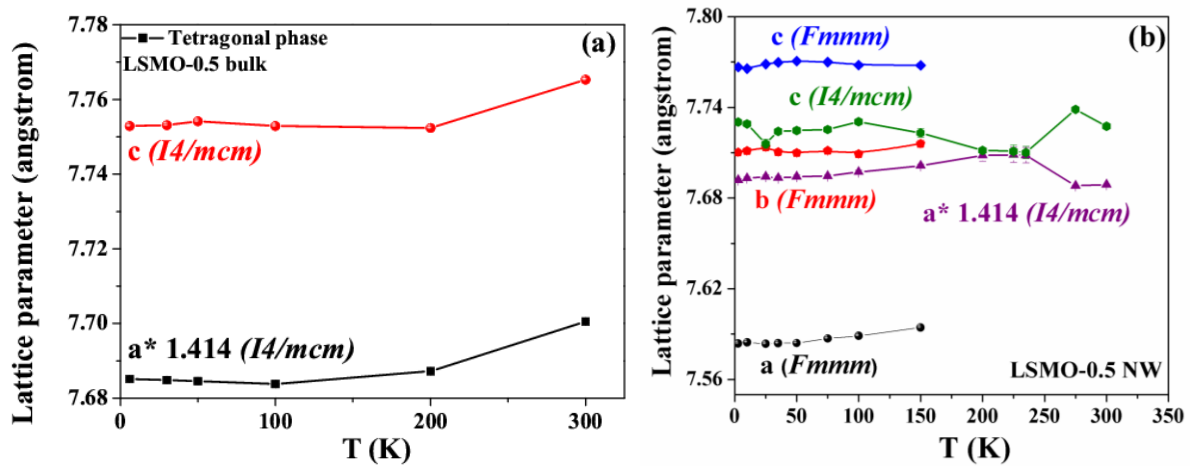


Figure 6.8 The temperature dependence of lattice constants obtained from the Rietveld refinement of (a) LSMO-0.5 bulk and (b) LSMO-0.5 NW. The error bars are smaller than the symbol.

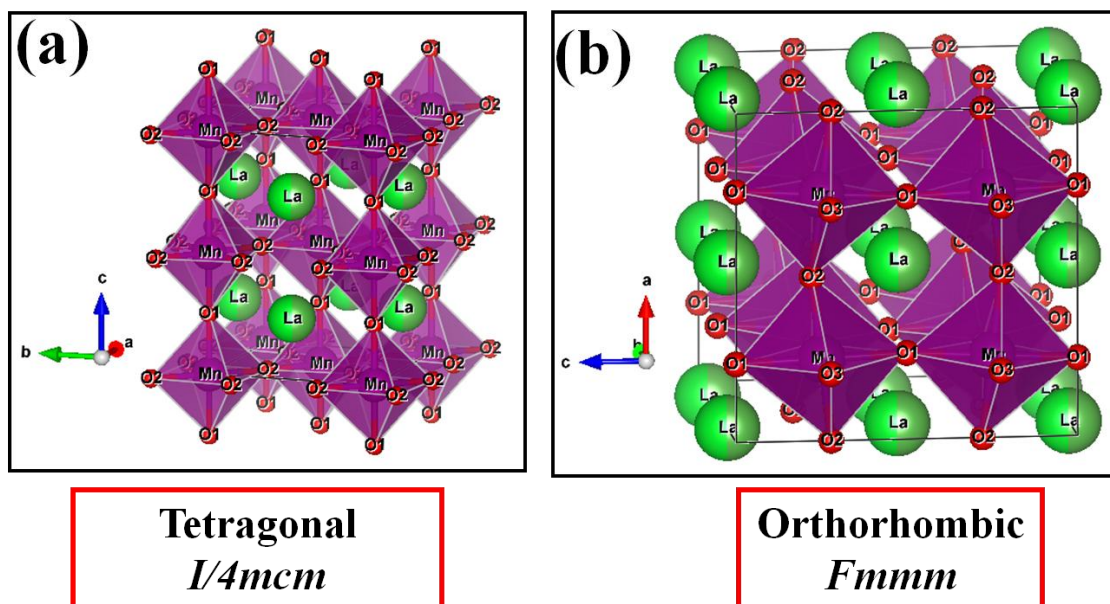


Figure 6.9 The crystallographic structure of (a) tetragonal (*I4/mcm*) at 300 K and (b) orthorhombic (*Fmmm*) phases at 200 K (reproduced from Rietveld analysis) plotted in vesta software.

Magnetic structure refinement of neutron diffraction data (temperature range: 3 – 300 K)

The bulk LSMO-0.5 system shows FM behaviour throughout the temperature measured (6 - 300 K). The temperature variation of spontaneous magnetic moment at Mn site obtained from refinement of ND data has been plotted in Fig. 6.10 (a). The magnetic moment from refinement of ND data is estimated to be $3.1(1) \mu_B$ per Mn ion at 6 K. The Mn spins are aligned ferromagnetically along *c* axis, as shown in Fig. 6.11 (a).

On the other hand, on size reduction, multiple magnetic transitions have been observed from magnetization measurements in LSMO-0.5 NWs. From ND refinement results, spins of Mn align ferromagnetically at temperatures below 315 K, near T_C and then antiferromagnetically below 200 K near T_N . Below T_N A- type AFM orthorhombic *Fmmm* phase arises within the FM tetragonal *I4/mcm* matrix. The two phases coexist till the lowest temperature measured (3 K) (Fig. 6.7). The peak related to AFM structure at 11.2° of the LSMO-0.5 NW has been marked in Fig. 6.6 (c). The temperature variation of magnetic moment at Mn site obtained from refinement of ND data has been plotted in Fig. 6.10 (b) where black circles represent FM moments and red circles represent AFM moment. Co-existence of both the magnetic moments due to FM and AFM phases have been observed in the low temperature region up to

200 K (T_N). Above T_N the magnetic moment due to FM phase has been observed. The magnetic phase transitions in NWs are coupled with the sharp transformation from tetragonal to orthorhombic structure. An upturn in the magnetic moment is seen around 40 K (Fig. 6.10 (b)). This feature has also been observed in magnetization data (Fig. 5.7 (a) in chapter 5). Such feature may be associated with glass like behaviour, disordered surface spin alignment or low temperature magnetic transition [21]. The tetragonal structure arises due to stretching and rotation of MnO_6 octahedra along and around the c axis, as a result of that, there are two apical oxygen atoms (O1) and four in-plane oxygen atoms (O2), with one rotation angle around c axis. In Glazer notation [59, 60], the $I4/mcm$ structure can be characterized for one tilt system $a^0a^0c^-$ type. Tilt about $[001]$ leave a four-fold axis and therefore have tetragonal symmetry. In the simple perovskite subcell $\sqrt{2}a_p \times \sqrt{2}a_p \times 2a_p$, because of rotation of MnO_6 octahedra in LSMO-0.5 NWs along $2a_p$ axis (tilt angle $\sim 5.6^\circ$), basal axis $\sqrt{2}a_p$ are usually contracted. This is seen in the refined lattice parameters of NWs in Table 6.5, where $a = 5.4370 \text{ \AA}$ and $c = 7.7276 \text{ \AA}$ and $c/\sqrt{2}a = 1.005$. On cooling below 200 K, FM phase ($I4/mcm$) transforms partially to A-type AFM phase of the orthorhombic $Fmmm$ symmetry. The c axis remains an axis of rotation of MnO_6 octahedra. In the $Fmmm$ phase, Mn atoms form a bond with two oxygen atoms and rotate around c axis independently and hence make two angles with a very small difference. In Glazer notation, the A type AFM phase of orthorhombic symmetry the crystallographic subcell is $2a_p \times 2a_p \times 2a_p$ and MnO_6 octahedra tilt about $[001]$ and tilt angle is $\sim 3.6^\circ$. The lattice distortion in orthorhombic phase is $\sim 0.182 \text{ \AA}$.

At 300 K, the NW has FM ordering (tetragonal phase) with Mn spins parallel to each other along b axis. No canting of Mn spins has been observed (Fig. 6.11 (b)). The two Mn-O bonds are out of the plane ($2 \times Mn-O(1) \sim 1.93 \text{ \AA}$) and the other four Mn-O bonds are in plane direction ($4 \times Mn-O(2) \sim 1.932 \text{ \AA}$) and $Mn-O(2)-Mn \sim 168.72^\circ$ at 300 K as shown in Fig. 6.9 (a). On cooling below 200 K, AFM ordering of orthorhombic phase arises within FM matrix and spin arrangements of FM order becomes slightly canted in presence of AFM ordering. The canting angle of FM spins increases on cooling down to low temperature (see Fig. 6.11 (c)). While, Mn spins of AFM ordering aligned antiparallel to each other without any canting till the lowest temperature measured as shown in Fig. 6.11 (d) and Mn spins forms A-type configuration. The A-type configuration consists of antiferromagnetically coupled parallel ferromagnetic planes. Mn octahedron is distorted with four long Mn-O bonds, which are $\{2x$

$MnO(1) \sim 1.942 \text{ \AA}$ and $2 \times MnO(3) \sim 1.928 \text{ \AA}$ in the ferromagnetic plane and two short Mn-O bond perpendicular to ferromagnetic plane; $2 \times Mn-(O2) \sim 1.911 \text{ \AA}$ and the bond angles are $Mn-O(1)-Mn \sim 177.66^\circ$, $Mn-O(2)-Mn \sim 168.1^\circ$ at 200 K as shown in Fig. 6.9 (b). The results are quite different from bulk sample, where the system shows FM spin arrangements of Mn atoms with magnetic moment $3.1(1) \mu_B$ per Mn ion till the lowest temperature (6 K) measured without any phase separation. The two Mn-O bonds are out of the plane ($2 \times Mn-O(1) \sim 1.9406 \text{ \AA}$) and the other four Mn-O bonds are in plane direction ($4 \times Mn-O(2) \sim 1.9346 \text{ \AA}$) and $Mn-O(2)-Mn \sim 168.7^\circ$ at 300 K. Few previous reports [61, 62] on bulk half doped LSMO shows existence of magnetic phase separation. In those cases presence of several nano domains of smaller size particles connecting the bigger crystallites is the origin of phase separation. Whereas, in our case, the bulk sample consists of crystallites, which are much bigger in size, comparable to single crystalline like (30-40 μm) structure; without any nano domain, as shown in Fig. 2.8 in chapter 2. Hence it provides sharp FM- PM transition at T_C without any phase separation. Size reduction to NW leads to several magnetic transitions along with the coexistence of magnetic phases. Neutron diffraction results clearly identify the magnetic transitions and infer the presence of magnetic phase coexistence arising due to phase separation.

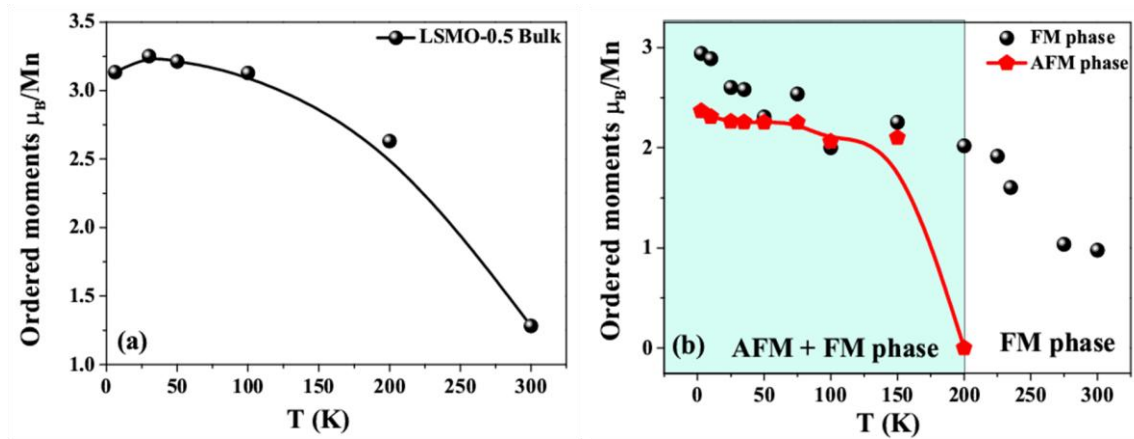


Figure 6.10 The spontaneous magnetic moment for the (a) LSMO-0.5 bulk and (b) LSMO-0.5 NW obtained from the neutron diffraction data. In bulk sample there is only FM phase whereas in NW form below 200 K there is a mixture of FM and AFM phases.

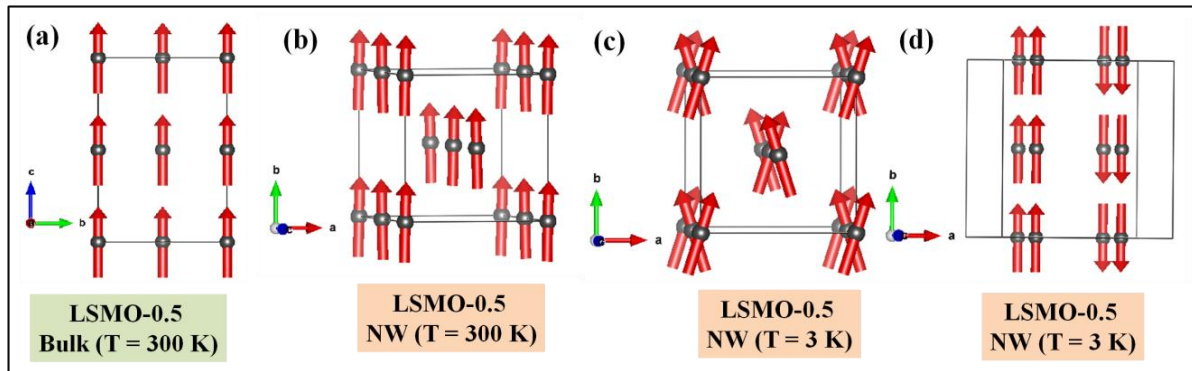


Figure 6.11 (a) Magnetic FM spin alignment of LSMO-0.5 bulk at 300 K along c direction. and throughout the measured temperature range (6-300 K) it shows same spin alignment. (b) Magnetic FM spin alignment of LSMO-0.5 NW at 300 K along b direction. (c) FM spin is canted at 3 K in LSMO-0.5 NW because of FM and AFM phase coexistence. (d) AFM spin alignment at 3 K of LSMO-0.5 NW at 3 K along b direction.

The magnetization curve shows rise in the magnetization at ~ 42 K (Fig. 5.7 (a) in chapter 5). Neutron refinements of Mn magnetic moment also provides enhancement of FM moment (Fig. 6.10 (b)) in the low temperature region. Such feature could be due to alignment of disordered surface spins (spin glass like) [63] or low temperature magnetic transition.

The half doped manganite LSMO-0.5 NWs show ferromagnetic insulating behavior with very low MR even at very high field of ~ 14 Tesla. Absence of MR indicates the absence of any charge order (CO) state in these NWs as discussed in chapter 7 [22]. As it is half doped system, the FM state is quite unstable, thus leading to AFM order below T_N . The magnetization curve shows large bifurcation of $M(T)$ curves (Fig. 5.7 (a) in chapter 5), this could be due to canted spin states [64] or phase coexistence of FM and AFM order as observed in manganites [65]. We have also observed canting of FM spins in LSMO-0.5 NWs from ND measurement as shown in Fig. 6.11 (c).

The FM and AFM phases in mixed-valence manganites could be originated due to DE and SE interactions between Mn atoms respectively. The phase coexistence in LSMO -0.5 NWs arises below T_N due to these interactions. The phase coexistence in ensemble of half doped manganite NWs and also on single strand of NW is previously reported by us from magnetocloric and $1/f$ noise study [21, 22]. The measurements of transverse susceptibility and anisotropy field (H_K) on ensemble of NW demonstrate the coexistence of FM phase within an AFM matrix below T_N as discussed in chapter 5 [26]. In FM region, H_K is almost constant (see Fig. 5.10 in chapter 5). It reaches a very low value at T_N and below T_N , H_K again start

increasing. This indicates increase of FM volume fraction and ultimately provides magnetic phase separation.

In chapter 7 we have discussed that the noise spectroscopy study of a single NW also provides the presence of coexistence of magnetic phases demonstrating the intrinsic nature of the single NW [22]. Investigation of noise spectroscopy of single NW was done by measuring the time series of the fluctuation in resistance (R) at different temperatures. Analysis shows that the total noise ($\langle \Delta R^2 \rangle / R^2$) increases below T_N and finally saturates at lower temperature closely follow the magnetization data. Noise spectroscopy detected phase co-existence of FM and AFM states below T_N . The present report demonstrates that presence of phase coexistence has direct correlation with crystallographic and magnetic structural transitions.

Magnetization in bulk LSMO-0.5 shows clear FM-PM transition at ~ 315 K. FM interactions is governed by DE interaction. Whereas, LSMO-0.5 NW provides FM-PM transition at ~ 310 K and on cooling below 200 K, FM ($I4/mcm$ phase) is partially transformed into AFM (with $Fmmm$ phase). On further cooling below 45 K, (the spin freezing temperature) surface spin of NWs undergoes freezing phenomena. Several experiments of ensemble of NW and of single NW have established that half doped NW of LSMO-0.5 is a phase separated system with coexistence of canted FM and AFM phases along with surface with disordered magnetic spins [21, 22]. Similar observation has been reported in manganite nanoparticles [62, 66]. The origin of magnetic spin alignment in NWs of LSMO-0.5 can be explained by core-shell model as reported previously in nanoparticles of manganites [62, 66]. On size reduction to nanoscopic dimension, surface plays an important role in physical properties of nanostructures. Several reports exist on this aspect [67, 68]. As observed from the experimental results on LSMO-0.5 NWs, the core of the NWs is phase separated with DE mediated spin canted FM along with A-type AFM order with SE interaction without any charge order (CO). The shell consists of disordered magnetic spin arrangements with EB effect as discussed in chapter 5. It is known that any phase separated system with AFM phase within FM matrix leads to formation of natural AFM/FM interface, which may induce EB [69]. The exchange coupling at the interface induces unidirectional exchange anisotropy when the system is cooled through T_N [66, 70, 71]. Presence of EB in LSMO-0.5 NW was confirmed from plot of hysteresis loop [21], though the phase coexistence occurs till T_N but no EB has been observed above 45 K, the spin freezing temperature [21]. Due to lack of exchange coupling between disordered surface spin and core spin, EB vanishes (see Fig. 5.11

in chapter 5). The magnetic state of the system is also related to change in magnetic entropy [21]. Positive and negative entropy change ($-\Delta S_M$) is associated with FM and AFM respectively. Above T_N , systems show conventional magnetocaloric effect (MCE). Whereas, below T_N it exhibits inverse magneto caloric effect (IMCE) [21]. Below 75 K, the positive entropy change ($-\Delta S_M$) is an indicative of dominant FM interaction, rise in magnetization curve and magnetic moment from ND data supports the observation but anisotropy field (H_K) does not increase in this region, is nearly constant [21]. Since the contribution to anisotropy field is entirely from core spins hence any change in the spins of surface would not be contemplated in H_K .

It has been observed that magnetization process in LSMO-0.5 NWs involves the spin arrangement of FM order in collinear form above T_N . However, below T_N the Mn spins of FM order have small canting and canting angle increases on cooling as shown in Fig. 6.11 (c). Coey surveyed the experimental results of solid crystals on non collinear spin structures and found that occurrence of this type of canted structure may be related to the presence of competing interactions like exchange coupling with different shell of neighbours etc [72]. Canted spin arrangements has also been observed in manganite nanoparticles [66]. In our system of NWs the competing DE and SE interaction of FM and AFM phases may be the cause of non linearity /canting in FM spins. We may draw the inference that below T_N , NWs reveal phase coexistence and low temperature rise in magnetic moment arises due to surface spin freezing.

6.5 Conclusion

In summary, we report here size reduction induced modification of magnetic phases of 1D nanostructures of manganite, which was not looked into before. Synchrotron XRD taken at all the samples ($La_{1-x}A_xMnO_3$; $A = Ca, Sr$; $x = 0.3$ and 0.5) and ND studies of ensemble of LSMO-0.5 NWs and bulk samples are performed to understand the magnetic phase coexistence and its correlation to crystallographic and magnetic structure of the NWs. The T_C enhancement of LCMO-0.3 and LCMO-0.5 NWs are explained from crystallographic structures. The analysis of the structural data exhibits that the lattice parameters contract due to size reduction in NWs and MnO_6 octahedra compact with smaller d_{Mn-O} and $\theta_{Mn-O-Mn} \rightarrow 180^\circ$. This leads to an enhancement of the bandwidth and therefore T_C is enhanced for both cases.

LSMO-0.5 NWs undergo PM–FM transition at $T_C \sim 310$ K followed by FM–AFM transition at $T_N \sim 210$ K. The presence of magnetic phase coexistence with competing DE and SE interactions arises from the FM and AFM domains which is absent in its bulk form. Our crystallographic structural analysis exhibits that the coexistence of FM and AFM phases arises due to structural phase coexistence. On cooling below 200 K, AFM ordering of orthorhombic phase arises within FM matrix and spin arrangements of FM order becomes slightly canted in presence of AFM ordering. The canting angle of FM spins increases on cooling down to low temperature (3 K). On the other hand, Mn spins of AFM ordering aligned antiparallel to each other without any canting till the lowest temperature measured and Mn spins forms A-type configuration. As the temperature is lowered, the FM volume fraction increases and overcomes the AFM interactions (~ 50 K), which is marked by dc magnetic measurement and neutron diffraction study.

Bibliography:

- [1] B. Ghosh, V. Siruguri, A. K. Raychaudhuri and T. Chatterji, *J. Phys.: Condens. Matter.*, **26**, 025603 (2014).
- [2] T. Sarkar, B. Ghosh, A. K. Raychaudhuri and T. Chatterji, *Phys. Rev. B*, **77**, 235112 (2008).
- [3] M. Paranjape, A. K. Raychaudhuri, N. D. Mathur and M. G. Blamire, *Phys. Rev. B*, **67**, 214415 (2003).
- [4] M. Paranjape, K. S. Shankar and A. K. Raychaudhuri, *J. Phys. D: Appl. Phys.*, **38**, 3674–3681 (2005).
- [5] J. Mitra, A. K. Raychaudhuri, Ya. M. Mukovskii and D. Shulyatev, *Phys. Rev. B*, **68**, 134428 (2003).
- [6] P. Malla Chowdhury, B. Ghosh, A. K. Raychaudhuri, S. D. Kaushik and V. Siruguri, *J. Nanopart. Res.*, **15**, 1585 (2013).
- [7] V. Markovich, I. Fita, A. Wisniewski, G. Jung, D. Mogilyansky, R. Puzniak, L. Titelman and G. Gorodetsky, *Phys. Rev. B*, **81**, 134440 (2010).
- [8] K. S. Shankar, S. Kar, G. N. Subbanna and A. K. Raychaudhuri, *Appl. Phys. Lett.*, **84**, 993 (2004).
- [9] T. Sarkar, A. K. Raychaudhuri, A. K. Bera and S. M. Yusuf, *New J. Phys.*, **12**, 123026 (21pp) (2010).
- [10] Z. Jiráček, E. Hadová, O. Kaman, K. Knížek, M. Maryško, E. Pollert, M. Dlouhá and S. Vratislav, *Phys. Rev. B*, **81**, 024403 (2010).
- [11] S. Arumugam, B. Ghosh, A. K. Raychaudhuri, N. R. Tamil Selvan, T. Nakanishi, H. Yoshino, K. Murata and Ya. M. Mukovskii, *J. Appl. Phys.*, **106**, 023905 (2009).
- [12] L. Liang, L. Li, H. Wu and X. Zhu, *Nanoscale Res. Lett.*, **9**, 325 (2014).
- [13] N. S. Bingham, P. Lampen, M. H. Phan, T. D. Hoang, H. D. Chinh, C. L. Zhang, S. W. Cheong and H. Srikanth, *Phys. Rev. B*, **86**, 064420 (2012).
- [14] L. Li, L. Liang, H. Wu and X. Zhu, *Nanoscale Res. Lett.*, **11**, 121 (2016).
- [15] A. Biswas, I. Das and C. Majumdar, *J. Appl. Phys.*, **98**, 124310 (2005).
- [16] B. Samantaray, S. K. Srivastava and S. Ravi, *J. Appl. Phys.*, **111**, 013919 (2012).
- [17] H. Das, G. Sangiovanni, A. Valli, K. Held and T. Saha-Dasgupta, *Phys. Rev. Lett.*, **107**, 197202 (2011).

- [18] A. Valli, H. Das, G. Sangiovanni, T. Saha-Dasgupta and K. Held, *Phys. Rev. B*, **92**, 115143 (2015).
- [19] S. A. Majetich and M. Sachan, *J. Phys. D: Appl. Phys.*, **39**, R407 (2006).
- [20] K. Bennemann, *J. Phys.: Condens. Matter.*, **22**, 243201 (2010).
- [21] S. Chandra, A. Biswas, S. Datta, B. Ghosh, A. K. Raychaudhuri and H. Srikanth, *Nanotechnology*, **24**, 505712 (2013).
- [22] S. Datta, S. Samanta, B. Ghosh and A. K. Raychaudhuri, *Appl. Phys. Lett.*, **105**, 073117 (2014).
- [23] E. Dagotto, T. Hotta and A. Moreoa, *Phys. Rep.*, **344**, 1 (2001).
- [24] R. S. Freitas, L. Ghivelder, P. Levy and F. Parisi, *Phys. Rev. B*, **65** 104403 (2002).
- [25] F. Rivadulla, M. Freita-Alvite, M. A. Lopez-Quintela, L. E. Hueso, D. R. Miguens, P. Sande and J. Rivas, *J. Appl. Phys.*, **91**, 785 (2002).
- [26] G. Allodi, R. De. Renzi, F. Licci and M. W. Pieper, *Phys. Rev. Lett.*, **81**, 4736 (1998).
- [27] J. Dho, I. Kim and S. Lee, *Phys. Rev. Lett.*, **60**, 14545 (1999).
- [28] Q. Huang, J. W. Lynn, R. W. Erwin, A. Santoro, D. C. Dender, V. N. Smolyaninova, K. Ghosh and R. L. Greene, *Phys. Rev. B*, **61**, 8895 (2000).
- [29] C. H. Chen and S. W. Cheong, *Phys. Rev. Lett.*, **76**, 4042 (1996).
- [30] S. Mori, C. H. Chen and S. W. Cheong, *Phys. Rev. Lett.*, **81**, 3972 (1998).
- [31] M. Kim, H. Barath, S. L. Cooper, P. Abbamonte, E. Fradkin, M. R  ubhausen, C. L. Zhang and S. W. Cheong, *Phys. Rev. B*, **77**, 134411 (2008).
- [32] W. G. Huang, X. Q. Zhang, H. F. Du, R. F. Yang, Y. K. Tang, Y. Sun and Z. H. Cheng, *J. Phys.: Condens. Matter.*, **20**, 445209 (2008).
- [33] D. Niebieskikwiat and M. B. Salamon, *Phys. Rev. B*, **72**, 174422 (2005).
- [34] Y. K. Tang, Y. Sun and Z. H. Cheng, *Phys. Rev. B*, **73**, 174419 (2006).
- [35] W. J. Luo and F. W. Wang, *Appl. Phys. Lett.*, **90**, 162515 (2007).
- [36] M. H. Phan, M. B. Morales, N. S. Bingham, H. Srikanth, C. L. Zhang and S. W. Cheong, *Phys. Rev. B*, **81**, 094413 (2010).
- [37] M. S. Reis, V. S. Amaral, J. P. Araujo, P. B. Tavares, A. M. Gomes and I. S. Oliveira, *Phys. Rev. B*, **71**, 144413 (2005).
- [38] M. Khondabi, H. Ahmadvand, P. Kameli, P. Amirzadeh, H. Salamati, P. Dasgupta and A. Poddar, *J. Appl. Phys.*, **118**, 233908 (2015).
- [39] S. Zhou, Y. Guo, J. Zhao, L. He and L. Shi, *J. Phys. Chem. C*, **115**, 1535 (2011).

- [40] S. Kundu, A. Das, T. K. Nath and A. K. Nigam, *J. Magn. Magn. Mater.*, **324**, 823 (2012).
- [41] S. Datta, S. Chandra, S. Samanta, K. Das, H. Srikanth and B. Ghosh, *Journal of Nanomaterials*, vol. **2013**, Article ID 162315, 6 pages, 2013. doi:10.1155/2013/162315.
- [42] S. Datta, A. Ghatak and B. Ghosh, *J. Mater. Sci.*, **51**, 9679–9695 (2016).
- [43] J. R. Carvajal, *Physica B*, **192**, 55 (1993).
- [44] www.ill.eu/sites/fullprof/php/downloads.html
- [45] V. Siruguri, P. D. Babu, D. M. Gupta, A. V. Pimpale and P. S. Goyal, *Pramana-J. Phys.*, **71**, 1197 (2008).
- [46] S. K. Paranjpe and S. M. Yusuf, *Neutron News*, **13**, 36 (2002).
- [47] V. Siruguri, S. M. Yusuf and V. C. Rakhecha, *Neutron News*, **11**, 4 (2000).
- [48] S. M. Yusuf, K. R. Chakraborty, A. Kumar, A. Jain, V. Siruguri and P. D. Babu, *Neutron News*, **25**, 22 (2014).
- [49] M. A. Gilleo, *Acta Crystallogr.*, **10**, 161 (1957)
- [50] P. G. Radaelli, D. E. Cox, M. Marezio and S.-W. Cheong, *Phys. Rev. B*, **55**, 3015 (1997).
- [51] P. G. Radaelli, D. E. Cox, L. Capogna, S.-W. Cheong and M. Marezio, *Phys. Rev. B*, **59**, 14440 (1999).
- [52] S. Zhou, Y. Guo, Z. Jiang, J. Zhao, X. Cai and L. Shi, *J. Phys. Chem. C*, **117**, 8989-8996 (2013).
- [53] T. Sarkar, A. K. Raychaudhuri and T. Chatterji, *Appl. Phys. Lett.*, **92**, 123104 (2008).
- [54] M. Medarde, J. Mesot, P. Lacorre, S. Rosenkranz, P. Fischer and K. Gobrecht, *Phys. Rev. B*, **52**, 9248 (1995).
- [55] P. G. Radaelli, G. Iannone, M. Marezio, H. Y. Hwang and S-W. Cheong, J. D. Jorgensen and D. N. Argyriou, *Phys. Rev. B*, **56**, 8265 (1997).
- [56] J. J. Urban, L. Ouyang, M. H. Jo, D. S. Wang and H. Park, *Nano Lett.*, **4**, 1547–1550 (2004).
- [57] O. Chmaissem, B. Dabrowski, S. Kolesnik, J. Mais, J. D. Jorgensen and S. Short, *Phys. Rev. B*, **67**, 094431 (2003).
- [58] F. Damay, C. Martin, M. Hervieu, A. Maignan, B. Raveau, G. Andre and F. Bouree J. *Magn. Magn. Mater.*, **184**, 71 (1998).
- [59] A. M. Glazer, *Acta Cryst.*, **B28**, 3384 (1972).
- [60] A. M. Glazer, *Acta Cryst.*, **A31**, 756 (1975).

- [61] Z. Jirak, J. Hejtmanek, K. Knizek, M. Marysko, V. Sima and R. Sonntag, *J. Magn. Magn. Mater.*, **217**, 113 (2000).
- [62] A. Rostamnejadi, M. Venkatesan, J. Alaria, M. Boese, P. Kameli, H. Salamati and J. M. D. Coey, *J. Appl. Phys.*, **110**, 043905 (2011).
- [63] E. L. Salabas, A. Rumplecker, F. Kleitz, F. Radu and F. Schuth, *Nano Lett.*, **6**, 2977 (2006).
- [64] S. Chandra, A. Biswas, S. Datta, B. Ghosh, V. Siruguri, A. K. Raychaudhuri, M. H. Phan and H. Srikanth, *J. Phys.: Condens. Matter.*, **24**, 366004 (2012).
- [65] S. Chandra, A. I. Figueroa, B. Ghosh, M. H. Phan, H. Srikanth and A. K. Raychaudhuri, *J. Appl. Phys.*, **109**, 07D720 (2011).
- [66] A. Rostamnejadi, M. Venkatesan, P. Kameli, H. Salamati and J. M. D. Coey, *J. Appl. Phys.*, **116**, 043913 (2014).
- [67] V. Markovich, R. Puzniak, D. Mogilyansky, X. Wu, K. Suzuki, I. Fita, A. Wisniewski, S. Chen and G. Gorodetsky, *J. Phys. Chem. C*, **115**, 1582 (2011).
- [68] T. Zhang, X. P. Wang and Q. F. Fang, *J. Phys. Chem. C*, **114**, 11796 (2010).
- [69] S. M. Zhoua, S. Y. Zhao, Y. Q. Guo, J. Y. Zhao and L. Shi, *J. Appl. Phys.*, **107**, 033906 (2010).
- [70] W. H. Meiklejohn and C. P. Bean, *Phys. Rev.*, **105**, 904 (1957).
- [71] J. Nogues, J. Sort, V. Langlais, V. Skumryev, S. Surinach, J. S. Munoz and M. D. Baro, *Phys. Rep.*, **422**, 65 (2005).
- [72] J. M. D. Coey, *Can. J. Phys.*, **65**, 1210 (1987).
-

Chapter 7

Resistivity and 1/f noise measurement of single nanowire

In this chapter, we report electrical transport measurement of single nanowire (NW) (diameter (d) \sim 35-50 nm) of $\text{La}_{1-x}\text{Ca}_x\text{MnO}_3$ ($x = 0.3$ and 0.5) and $\text{La}_{0.5}\text{Sr}_{0.5}\text{MnO}_3$ samples and compare with their bulk counterpart to understand how the electrical behaviour changes under size reduction. So far we have observed enough affirmation of size reduction induced modification of different physical properties, as discussed in previous chapters. We experimentally demonstrate transport measurement as well as temperature and magnetic field dependent low frequency noise spectroscopy in a single NW ($d \sim 45\text{nm}$) of half doped manganite NW of $\text{La}_{0.5}\text{Sr}_{0.5}\text{MnO}_3$ which is a building block of ensemble of NWs. The coexistence of magnetic phases arising from phase separation observed in the system leading to modification of physical property of NWs compare to bulk was explored in previous chapters. This was further successfully probed by low frequency noise spectroscopy study other than bulk magnetic measurement which has not been reported till date except ours. The magnetic phase separation issues what we have observed in these NWs through magnetic and structural measurements may arise due to size distribution, as measurements was done on ensemble of NWs. The phase separation observed may not be the intrinsic to single NW. Due to sensitivity and other issues, magnetic measurement on single NW in not possible, thus we have done electrical transport experiment including noise spectroscopy of a single NW to explore these issues without the size dispersion problem. We demonstrated that noise spectroscopy in a single NW can cleanly detect the magnetic transitions including the phase-coexistence. Noise investigates interaction of charge carriers with magnetically ordered phases and phase separated regions. We propose that the low frequency noise have origin of carrier number density and mobility fluctuations. The calculated normalized Hooge parameter (related to nature and kinetics of disorder, scattering cross section of charge carriers, single crystallinity) is as low as $\gamma_H/n \approx 10^{-32} \text{ m}^3$ which indicates the good single crystalline nature of NW and low defect density. The normalized noise in the single NW is an order less than that reported in ultralow-noise Si Junction Field Effect Transistor.

7.1 Introduction and Motivation

In recent years the physics of magnetism in nanowires (NWs) has attracted considerable attention [1, 2]. In NWs of complex oxides (manganite), which can have competing co-existing phases arising from phase separation; one would expect the size reduction to have an effect on the different phases as well as on the co-existence of the phases. This would lead to physical properties different from that of the bulk. As an example in NWs of $\text{La}_{0.7}\text{Ca}_{0.3}\text{MnO}_3$ with diameters < 100 nm, the FM transition was found to have enhanced considerably over that of the bulk. [3] The size induced changes in magnetic order in nano-crystals of manganite for sizes below 50 nm has been established by past studies [4, 5]. Half-doped manganite NWs are particularly interesting to study because they show behaviour marginal between a FM metallic ground-state (as observed for $x < 0.5$ for $\text{La}_{1-x}\text{Ca}_x\text{MnO}_3$) and a charge-ordered, AFM insulating ground state (observed for $x > 0.5$ for $\text{La}_{1-x}\text{Ca}_x\text{MnO}_3$) [6, 7]. The competition between FM double exchange and AFM super exchange and the ratio of these competing interactions are being determined by intrinsic parameters such as doping level, average cation size, cation disorder, oxygen stoichiometry, Mn-O bond angle and bond lengths, charge transfer integrals and distortions of MnO_6 octahedra [6-10]. In chapter 5 and 6, we have discussed how the size reduction induced modification in Mn-O bond angle and bond lengths enhance the bandwidth. Hence T_C is increased in $\text{La}_{1-x}\text{Ca}_x\text{MnO}_3$ ($x = 0.3$ and 0.5) NWs. In this chapter we would like to investigate how these structural changes affect the transport property in a single NW level of manganite NWs and compare to its bulk counterpart. Investigation of electronic transport in single NWs of $\text{La}_{0.5}\text{Sr}_{0.5}\text{MnO}_3$ (LSMO-0.5) shows that the enhancement of the FM order leads to lowering of resistivity in NW compared to that of the bulk [11]. Magnetic and structural measurement of ensemble of NWs of LSMO-0.5 shows coexistence of magnetic phases [12]. The NWs showed a PM to FM transition at $T_C \sim 310$ K (close to that seen in the bulk) followed by an AFM transition at $T_N \sim 210$ K. Analysis of the anisotropy field (H_K) measured in NWs shows phase coexistence of FM and AFM phases below T_N and cooling leads to growth of the FM phase within the AFM phase which, however, saturates below 100 K. These magnetic and neutron experiments are carried out in an ensemble of NWs with some degrees of size dispersion.

One immediate concern arises whether the phase coexistence observed in the NWs arise from size dispersion. In NWs (as well as nano-crystals) of manganite, T_C and T_N can be size dependent due to a number of factors including conventional finite size effect [13]. As a

result of the size dispersion in an ensemble of NWs one can have an apparent co-existence of phases which may not be intrinsic to a single NW. Resolution of this would need magnetic measurements on a single NW. Due to limits on sensitivity as well as problems in handling a single NW, magnetic measurements are difficult on single NW. Thus, one would like to explore whether electrical transport experiments, including noise experiments, which can be carried out at a single NW level with good degree of resolution, can be used to explore these issues without the associated problem of size dispersion. In the chapter, we have investigated the temperature as well as magnetic field dependent low frequency noise spectroscopy in a single NW of LSMO-0.5 with diameter (d) ~ 45 nm, with the specific aim of corroborating the magnetic phase transitions as well as phase co-existence at a single NW level [14]. The NW shows excellent single crystalline quality even in a nanometer length scale. In such NW systems, noise can be generated from sources like inevitable imperfections (crystalline defects, impurities), magnetic domain or spin fluctuations, electronic traps, different conductivity channels within inhomogeneous magnetic phases. These microscopic fluctuators once get activated and physically coupled to the charge carriers give different contributions to overall conductivity. Hence we observe time dependent fluctuations in resistivity and our results provide evidence for a dynamic phase separation in a single NW system. Use of magnetic field allows separation of the noise contributions arising from magnetic (spin) origin and from other non-magnetic sources, e.g., structural defects. The expectation is that if the phase co-existence is of dynamic type with a slow kinetics, it can be picked up by resistance noise measurements as has been done in films and bulk samples of a variety of manganite, near metal-insulator transition [15, 16] or near charge ordering transition [17]. It is noted that investigation of noise spectroscopy of a single NW of such a complex oxide has not been reported before. There are reports of noise spectroscopy done on single NW of metals and semiconductors [18, 19]. However, no experiment of single NW of manganite has been reported due to the difficulty in obtaining highly single crystalline oxide NWs of sub-100 nm diameter and problems of contact resistance. Our experiment thus opens up a new dimension for noise measurements in complex oxides. It needs to be pointed out that though it is more difficult to carry out noise measurements at a single NW level, it is a viable and plausible measurement compared to magnetic measurements at a single NW level.

7.2 Brief introduction of noise

An important parameter for electrical transport is the fluctuations in resistance (or electrical “noise”), which can arise from basic reasons. The source of fluctuation (“noise”) in current is the random back and forth motion of the charge carriers in any conductor, i.e., by the fluctuations of the directions of the charge carriers velocities. In the same systems many other physical quantities also fluctuate, e.g. the temperature, the number of scattering centres and their orientation in the crystal and the distribution of charge carriers in energy etc. However, these fluctuations due to their symmetry are not measured in the current or voltage fluctuations unless a mean current produced by an external current source, is passed through the conductor. The magnitude of the mean current, which is sufficient to reveal the “hidden” fluctuations and generate a measurable “excess” noise is often so small that the conductor in all other respects can be considered as equilibrium one. In resistors the excess noise becomes prominent at low frequencies. The occurrence of these fluctuations is one of the most fundamental and universal phenomenon in a various class of systems. The dependence of these fluctuations is directly correlated with time or equivalent with the frequency dependence of spectral density in any physical system. Alternatively, the response of the same system to external perturbations is governed by the kinetic processes which are directly correlated to the fluctuation dynamics. Hence, study of fluctuation phenomenon is a sensitive and successful approach to condensed matter for investigation of essential kinetics or dynamics as well as from an applied perspective. The fluctuations in conduction process affect the important physical quantity of electronic transport i.e., resistance R . The fluctuations in resistance (“electrical noise”) occur from very basic reasons namely, various relaxation processes of the charge carriers, defects, group of defects etc. Resistance noise is quantified by the dynamical fluctuations $\delta R(t) = R(t) - \langle R \rangle$ of the resistance about its time averaged mean value R . On the other hand, noise may come from the fluctuations of macroscopic entities and it can therefore act as a probe of what is happening physically in the system at the microscopic scale. In this thesis the resistance fluctuation (noise) has been used as a unique and fundamental measurement tool to investigate the phase separation issue of manganites.

7.2.1 Types of noise and shape of the spectra

“Nyquist noise” or “Johnson noise”

The voltage fluctuations are caused by the thermal motion (noise termed as “thermal noise”) of the charge carriers in any conductor. This equilibrium thermal noise is an expression of the fluctuation-dissipation theorem. The power spectral density of thermal noise of a wire of resistance R at a temperature T is given by $S_{th} = 4k_BTR$ [20] where k_B is the Boltzmann constant. This component of the electrical noise is frequency independent (i.e. its power spectral density is “white”) and depends only on the sample resistance R . However, since the value of Nyquist noise for a conductor of known resistance can be predicted precisely, it is generally used to check the accuracy of a noise measurement system. Obtaining a background noise close to the calculated value of S_{th} is often taken to indicate that other extraneous sources of noise have successfully been eliminated from the measurement.

Shot noise

The shot noise is short form of Schottky noise which arises across a junction due to arrival of individual electron at random times. This gives rise to broadband white noise and increases with increase of average current flow. It is independent of temperature and the spectral density of the shot noise is given by $S_{shot} = 2e\langle I \rangle$ [21]. For $I = 1 \times 10^{-3}$ Amp, $S_{shot} \sim 2 \text{ pA}/\sqrt{\text{Hz}}$ is observed. The shot noise is observed in devices like tunnel junctions, vacuum tubes where electron arrives randomly and independently and their distribution can be described by Poisson distribution only.

Flicker or 1/f noise

Flicker noise is well-known as “1/ f noise” as its spectral power varies as $1/f^\alpha$, where α is very close to unity ($\alpha = 1.0 \pm 0.2$). This is “excess” noise and is made visible by passing a current through the resistor. There are some systems that show “Random Telegraphic Noise” (RTN) that shows a Lorentzian power spectrum which has $1/f^2$ frequency dependence. For metallic films, past studies have shown that an estimate of the value of the 1/f noise can be made from the empirical Hooge’s formula given as:

$$S_v(f) = \frac{\gamma_H V^2}{N_c f} \quad (7.1)$$

Where N_c is the number of charge carriers in the system and V is the applied voltage across the sample and γ_H is an empirical constant which lie in the range $\sim 10^{-3} - 10^{-5}$ for metallic films [22].

An example of noise at 300 K of high quality Ag thin film [23] of thickness 150 nm and resistance 7 Ω is shown in Fig. 7.1. The power spectral density of the resistance fluctuations goes as $1/f^{1.05}$ and the value of the Hooge parameter (γ_H) is 10^{-4} . The white thermal noise is shown as a solid line and the value is $\sim 2 \times 10^{-19}$ V²/Hz which is very close to the theoretically predicted value 1.15×10^{-19} V²/Hz for a resistor of resistance 7 Ω . Flicker noise is found in all active devices including homogenous semiconductors, junction devices, metal films, liquid metals, electrolytic solutions and even superconducting Josephson junctions.

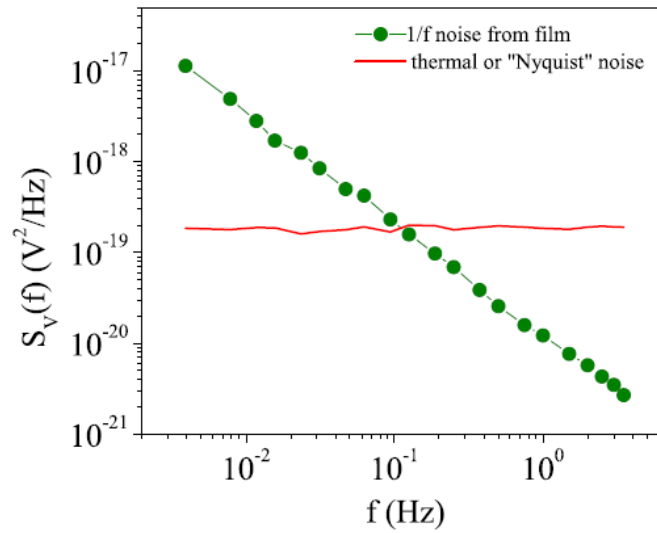


Figure 7.1 Power spectral densities of resistance fluctuations in a good Ag film [23]. The filled circles are the $1/f$ current noise coming from the sample while the solid line is the thermal background noise.

F. K. Du Pré first proposed a simple model to get $1/f$ spectra [24]. Consider a simple double well potential where two accessible energy states are split by energy E_a . The system fluctuates between two states with a characteristic time τ (relaxation time) which depends on E_a . According to random signal theory, one can define an autocorrelation function $C(\tau) \propto \exp(-\tau/\tau)$ of the fluctuation. Hence the spectral density of the fluctuation is of Lorentzian

form:


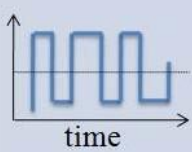
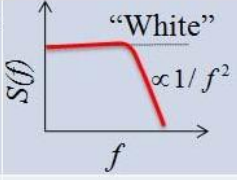
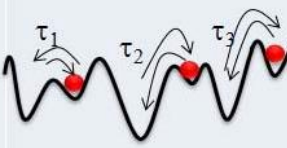
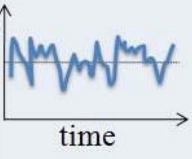
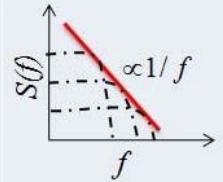
$$S(f) \propto \frac{2\tau}{1 + (2\pi f\tau)^2} \quad (7.2)$$

For $f\tau \ll 1$ the power spectrum is white and for $f\tau \gg 1$, $S_V(f) \propto 1/f^2$. The time series of this fluctuation gives RTN. If $D(\tau)$ is a distribution of relaxation times for fluctuation processes the spectral power will be a superposition of Lorentzians given by

$$S(f) = \int d\tau D(\tau) \frac{2\tau}{1 + (2\pi f\tau)^2} \quad (7.3)$$

If we choose $D(\tau) \propto 1/\tau$ and $\tau_1 \leq \tau \leq \tau_2$, spectral density $S_V(f) \propto 1/f^\alpha$ ($\alpha \sim 1$) will be within the frequency range $2\pi/\tau_2 \leq f \leq 2\pi/\tau_1$. At a glance the characteristics discussed above is given in Table. 7.1.

Table 7.1 A comparative study: the characteristics of Random Telegraphic noise and typical 1/f noise [25].

	Schematic energy diagram	Schematic time series	Relaxation time	Spectral power $S(f)$	Characteristic of spectrum
RTN			Single relaxation time τ	$S_V(f) \propto 1/f^2$ Lorentzian spectrum	
1/f Noise			Distribution of relaxation times τ $D(\tau) \propto 1/\tau$	$S_V(f) \propto 1/f^\alpha$ ($\alpha \sim 1$) Superposition of Lorentzian spectrum	

7.2.2 Using of noise spectroscopy to probe the phase separation issue in manganite

For the basic physics of manganites, the investigation of low frequency fluctuation has the same importance as the dependence of resistance on the external parameters like temperature, magnetic field, current injection. The magnitude of the low frequency noise carries information about the quality of the samples, i.e. films, crystals; single crystalline NWs. Podzorov *et. al.* [26] explained noise in phase separated manganites by a model based on percolation theory. We have discussed that although DE and electron-phonon coupling

effects are most common accepted interactions in manganites, but these are still insufficient to describe correctly the complex transport properties, fluctuations in resistances and obviously the features associated with phase separation. There are theoretical as well as experimental studies to rectify the intrinsic in-homogeneity due to the presence of strong tendencies towards phase separation. Keeping in mind all the dynamic features we have measured time dependent $1/f$ noise spectroscopy (resistance fluctuation process) which will explore the dynamic phase separation.

7.3 Single nanowire device fabrication

For transport measurement of a single NW, the four wire connections of a NW were done in a dual beam system FEI HELIOS 600 as discussed in chapter 4. A single NW with $d \sim 50$ nm was selected and connected to Au/Cr contact pads by inter-connections made of Pt deposited using e-beam-assisted local deposition in a dual beam system FEI-HELIOS 600 as shown in Fig. 7.2 (a). The separation between two consecutive probes is ~ 2 μm . Each contact pad has width of ~ 300 nm.

7.4 Electrical transport measurements

The temperature (T) dependent electrical, magnetoresistance including noise spectroscopy measurements are performed using standard four probe electrode configurations as discussed in chapter 4. We have measured $R-T$ and $I-V$ of single NW in cryogen-free variable temperature insert (VTI) system down to 5 K and $1/f$ noise measurement in cryogenic system down to 77 K. We have used source meter (Keithley 2410, 2400 source meter (SM)) for applying constant current or voltage across the sample and to measure corresponding voltage or current respectively across the sample. Lakeshore (Model 340) is used to control temperature in four probes configurations in DC techniques. The electrical measurements were performed on $\text{La}_{1-x}\text{Ca}_x\text{MnO}_3$ ($x = 0.3$ and 0.5) and $\text{La}_{0.5}\text{Sr}_{0.5}\text{MnO}_3$ NWs. The discussion on the electrical transport measurements on these NWs and the results are represented in the following sections.

7.5 Experimental Results and Discussions

7.5.1 $\text{La}_{0.7}\text{Ca}_{0.3}\text{MnO}_3$ (LCMO-0.3) nanowires

Measurement at single NW level is very challenging. AC measurement techniques were used to measure electrical property of LCMO-0.3 single NW devices with lower diameter ($d \sim 50$ nm) to avoid measurement using high current and the problem of thermo emf. arising due to temperature gradient across the sample. In AC technique one can use very low signal to excite the sample and thermo emf problem can be avoided. In this technique a low frequency AC current is passed through the samples and voltage drop corresponding to the excitation frequency was measured by phase sensitive detection technique. Fig. 7.2 (b) shows the temperature variation of resistivity data taken at $0.1 \mu\text{A}$ from 350 - 220 K. In single NW, ρ shows a distinct peak corresponding to the transition from the high temperature insulating polaronic phase to the low temperature metallic phase at $T_p \sim 332$ K. We obtained $\rho_{peak} \sim 0.9$ m Ω -cm at $T_p \sim 332$ K which is much lower value than that of bulk and film of LCMO-0.3 samples. The single crystalline nature of LCMO-0.3 NWs provides reasonably low value of resistivity compared to its bulk and film.

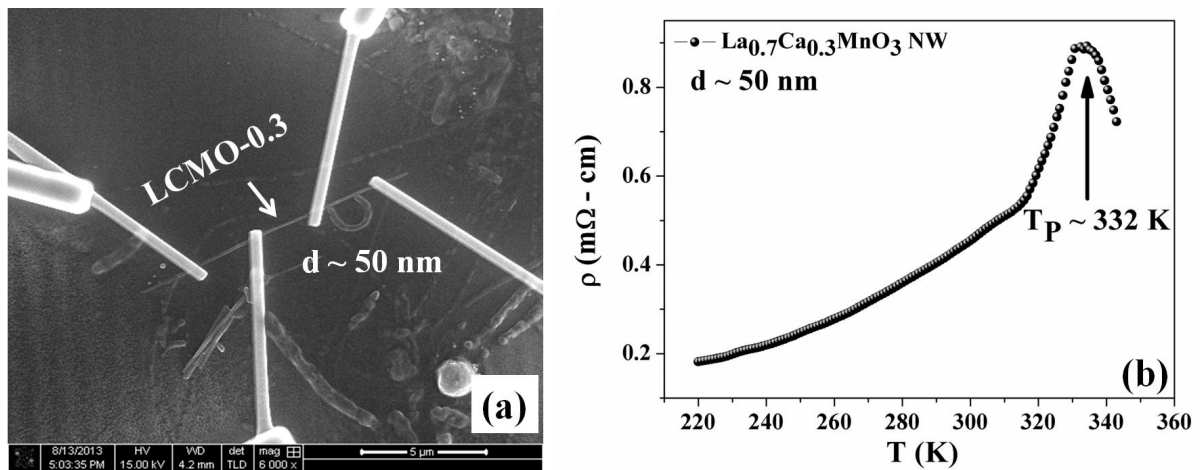


Figure 7.2 (a) SEM image of the four wire connected single NW ($d \sim 50$ nm) of LCMO-0.3. (b) The temperature variation of resistivity data of LCMO-0.3 NW ($d \sim 50$ nm) taken at $0.1 \mu\text{A}$.

The mixed valence manganite systems are interesting because of the interplay between charge, spin, orbital and structural degrees of freedom. It is well established that for optimal doping concentration, i.e., $x \sim 0.33$ in $\text{La}_{1-x}\text{Ca}_x\text{MnO}_3$, the material undergoes PM to FM transition at T_C accompanied by a metal-insulator transition at T_P . We note that in some of the literature shows optimal doping concentration as $\text{La}_{0.7}\text{A}_{0.3}\text{MnO}_3$ instead of $\text{La}_{0.67}\text{A}_{0.33}\text{MnO}_3$ [6, 27, 28]. In any case, in the framework of the phase diagram proposed by Urushibara *et al.* [27] for $\text{La}_{1-x}\text{Sr}_x\text{MnO}_3$, it is clear that variations from $x = 0.3$ to $x = 0.33$ are negligible. So we can say that the phase diagram for $x \sim 0.33$ is also valid for $x \sim 0.30$ composition. The same argument is applicable for $x = 0.30$ and $x = 0.33$ for Ca-doped samples [6]. The bulk single crystal of LCMO-0.33 has $T_P \sim 250$ K [29] as shown in Fig. 7.3 (a) and the plot of resistivity of thin film of LCMO-0.33 grown on single crystalline substrate SrTiO_3 shows $T_P \sim 270$ K (Fig. 7.3 (b)) [25]. The NWs exhibit T_P enhancement to 332 K because of size reduction to 1D. We have observed T_C is also enhanced as well in case of magnetic transitions (discussed in chapter 5). This enhancement may further be explained by enhancement of band width, which happen due to changes in Mn-O bond length, bond angles on size reduction (as seen from structural data refinement in chapter 6).

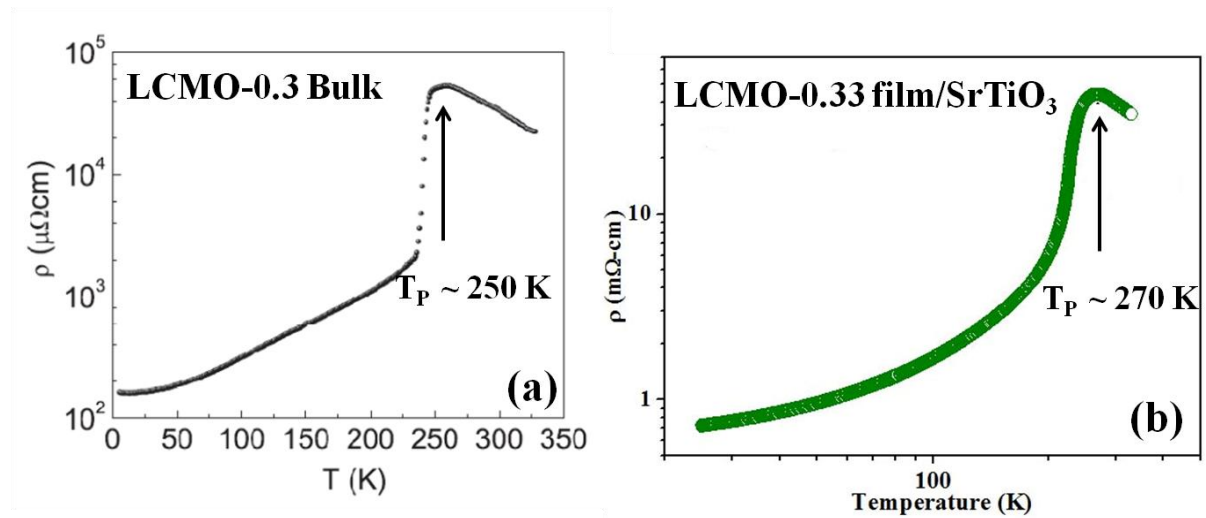


Figure 7.3 (a) The metal-insulator transition in $\text{La}_{0.7}\text{Ca}_{0.3}\text{MnO}_3$ at $T_P \sim 250$ K. The sample is insulating above T_P and metallic below T_P [29]. The temperature dependent resistivity data for LCMO-0.33 film is grown on SrTiO_3 with thickness ~ 500 nm. The resistivity shows high temperature polaronic insulating to low temperature metallic phase transition at $T_P \sim 270$ K [25].

7.5.2 $\text{La}_{0.5}\text{Ca}_{0.5}\text{MnO}_3$ (LCMO-0.5) nanowires

Four wire dc measurement is done on single NW of LCMO-0.5 ($d \sim 35$ nm) from 30-300 K as shown in Fig. 7.4 (a). The resistivity data as a function of temperature of a single NW of LCMO-0.5 ($d \sim 35$ nm) are plotted in Fig. 7.4 (b). The data were taken at a current of $1 \mu\text{A}$. Fig. 7.4 (b) shows insulating behaviour within the measured temperature range (30 – 300 K). The ρ at 30 K is around $1.8 \times 10^{-2} \Omega\text{-m}$ measured at $1 \mu\text{A}$ current and the resistivity at the highest temperature (300 K) is $5.2 \times 10^{-4} \Omega\text{-m}$. The comparison of the resistivity data of our NW sample compared to the bulk sample reported previously is depicted in Fig. 7.4 (c) [4]. The bulk sample was prepared by sol gel polymeric (polyol) precursor method which shows quite higher resistivity than the NW [4]. In NW, the resistivity at room temperature is about one order higher than that of the bulk sample. However, in the bulk sample, the resistivity rises rapidly as the sample is cooled due to the charge ordering (CO) transition temperature at 50 K the resistivity in the bulk (which are polycrystalline) sample becomes 7 orders higher than that in the single NW [4]. It is well established that the contribution from grain boundaries introduces increase in the resistance and thus in bulk samples, the resistance is much higher than that of our single crystalline NWs as shown in Fig. 3.10 (a) in chapter 3 (SAED image) [4, 30]. The conductivity data were fitted with variable range hopping model (VRH) ($\sigma = \sigma_0 \exp(-(T_0/T))^{1/4}$) appropriate for whole temperature range ($\sim 30 - 300$ K) as shown in inset of Fig. 7.4 (b) [31, 32]. This model considers that the hopping occurs only between nearest neighbour sites. Any electron hopping between any two sites are determined by the potential energy difference and the distance between these two sites. This has been termed as “variable range hopping” as the carrier tends to optimize between the distance of the hop and the barrier energy of the hop. The thick solid line is a fit to the VRH model. From the slope of the fitted curve, the estimated characteristic temperature (T_0) is around 21.5×10^5 K which is one order smaller than that of $\text{La}_{0.5}\text{Ca}_{0.5}\text{MnO}_3$ thin film [31]. The density of states (DOS) at Fermi level, $N(E_F)$, is estimated from the fitted value of T_0 by through $N(E_F) = (24/\pi a^3 K_B T_0)$, where a is Localization length (~ 0.4 nm) which is around one unit cell and K_B is the Boltzmann’s constant. From measured T_0 , we obtain $N(E_F) \sim 6.44 \times 10^{20} \text{ eV}^{-1} \text{ cm}^{-3}$. In $\text{La}_{0.5}\text{Ca}_{0.5}\text{MnO}_3$ thin film, the estimated $N(E_F)$ value is $9.89 \times 10^{19} \text{ eV}^{-1} \text{ cm}^{-3}$ [30]. The DOS values for both are quite comparable and this validates the use of VRH model for the electrical conduction in the NW. In NW, VRH type T dependence shows that the insulating state seen is not due to charge ordering/orbital (both of which lead to insulating state) but due

to electron localization as found in a disordered insulating system [33]. It is already reported in case of $\text{Pr}_{0.67}\text{Sr}_{0.33}\text{MnO}_3$ film that the change in the site distortions affects the electron-phonon interactions which ultimately decreases the resistivity [34]. Similar changes occur in case of our NWs. The modification of magnetic and structural properties on size reduction due to the changes in Mn-O bond angle, bond lengths, MnO_6 octahedra [35] issues have been discussed in previous chapters (chapter 5 and 6).

The temperature variation of magnetoresistance (MR) of the said NW has been plotted in Fig. 7.5. MR is the change in resistance of a material in response to a magnetic field. It is a result of the ability of magnetic fields to change the scattering of the conduction electrons. This is commonly defined as $\frac{\Delta\rho}{\rho} = 100 \times (\rho_H - \rho_0) / \rho_0$ where ρ_0 is the resistivity without a magnetic field and ρ_H is the resistivity in presence of magnetic field. Fig. 7.5 shows temperature dependent MR data of LCMO-0.5 single NW ($d \sim 35$ nm) at 14 Tesla. The NW has very low MR even at 14 Tesla. MR increases as the temperature is decreased and negative MR reaches a magnitude of only 3.5% at 30 K. The absence of significant MR shows absence of significant charge ordering because if it exists, it can be destabilized by the magnetic field of 14 Tesla leading to substantial MR and often onset of metallic behaviour [36]. In LCMO-0.5 NW and nanoparticles, there is also a signature of suppression of the CO insulating phase and absence of significant MR which is present in its bulk form [4]. Size reduction leads to suppression of MR in manganite NWs and nanoparticles [4].

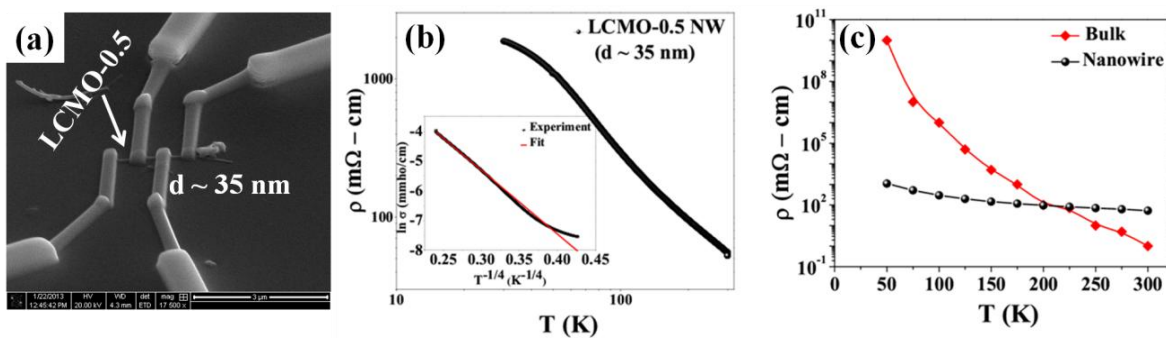


Figure 7.4 (a) SEM image of the four wire connected single NW ($d \sim 35$ nm) of LCMO-0.5. (b) Temperature variation of resistivity of single NW of $\text{La}_{0.5}\text{Ca}_{0.5}\text{MnO}_3$ (LCMO-0.5) ($d \sim 35$ nm) measured in the temperature range from 30 K to 300 K. Inset curve ($\ln \sigma$ versus $T^{-1/4}$) shows that conductivity data fitted with variable range hopping model for the whole temperature ranges and (c) quantitative comparison of resistivity of LCMO-0.5 NWs and bulk [4].

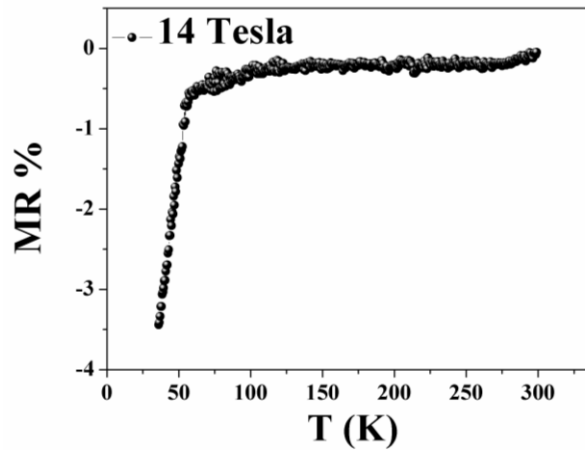


Figure 7.5 Temperature dependent MR data of LCMO-0.5 single NW ($d \sim 35$ nm) at 14 Tesla.

7.5.3 $\text{La}_{0.5}\text{Sr}_{0.5}\text{MnO}_3$ (LSMO-0.5) nanowires

The half doped LSMO-0.5 NWs have competing coexisting phases arising from phase separation. Detailed study has been done using magnetic measurements as well as crystallographic and magnetic structural measurements on ensemble of NWs, where size dispersion issues may arise which have already mentioned. To solve these issues we have performed single NW electrical as well as noise spectroscopy measurements by making proper electrical contacts using lithographic techniques.

The LSMO-0.5 NWs were drop casted on a SiO_2/Si substrate. A single NW with $d \sim 45$ nm selected and connected to Au/Cr contact pads by inter-connections made of Pt deposited using e-beam-assisted local deposition in a dual beam system FEI-HELIOS 600. Inset of Fig. 7.6 (a) shows the SEM image of a typical four-terminal sample used for making the resistivity and noise measurements. The distance (L) between two voltage (V) probes (indicated by V_+ and V_-) is ~ 550 nm. Variation of resistivity as a function of temperature taken at a current of $1 \mu\text{A}$ plotted in Fig. 7.6 (a), shows insulating behaviour within the measured temperature range. The behaviour is similar to that seen in the bulk LSMO ($x = 0.5$) system [37]. The comparison of the resistivity of NW compared to the bulk ceramic sample is depicted quantitatively in Fig. 7.6 (b). The bulk sample was prepared by ceramic method which shows quite higher resistivity than the NW. The ρ at 5 K is around 2.7×10^{-3}

$\Omega\cdot\text{m}$ measured at $1\ \mu\text{A}$ current and the resistivity at the highest temperature (310 K) is $4 \times 10^{-5}\ \Omega\cdot\text{m}$. We have fitted our conductivity data with variable range hopping model ($\sigma = \sigma_0 \exp(-(T_0/T))^{1/4}$) appropriate for whole temperature ranges ($\sim 10\ \text{K}$ – $310\ \text{K}$) as shown in inset of Fig. 7.6 (a) [32]. We have found the characteristic temperature (T_0) and density of states (DOS) at Fermi level ($N(E_F)$) from the fitted equation. From the slope of the fitted curve the estimated T_0 is $\sim 2.4 \times 10^4\ \text{K}$. $N(E_F)$ is related to T_0 by the relation $N(E_F) = (24/\pi a^3 K_B T_0)$, where a is localization length ($\sim 0.39\ \text{nm}$) which is around one unit cell. From measured T_0 , we obtain $N(E_F) \sim 6.22 \times 10^{22}\ \text{eV}^{-1}\ \text{cm}^{-3}$ or $1.55 \times 10^{43}\ \text{J}^{-1}\ \text{mole}^{-1}$. From heat capacity data for a similar compound (LSMO, $x = 0.3$) we obtain $N(E_F) \sim 0.96 \times 10^{43}\ \text{J}^{-1}\ \text{mole}^{-1}$ [38]. The two DOS values are quite comparable and this validates the use of VRH model for the electrical conduction in the NW.

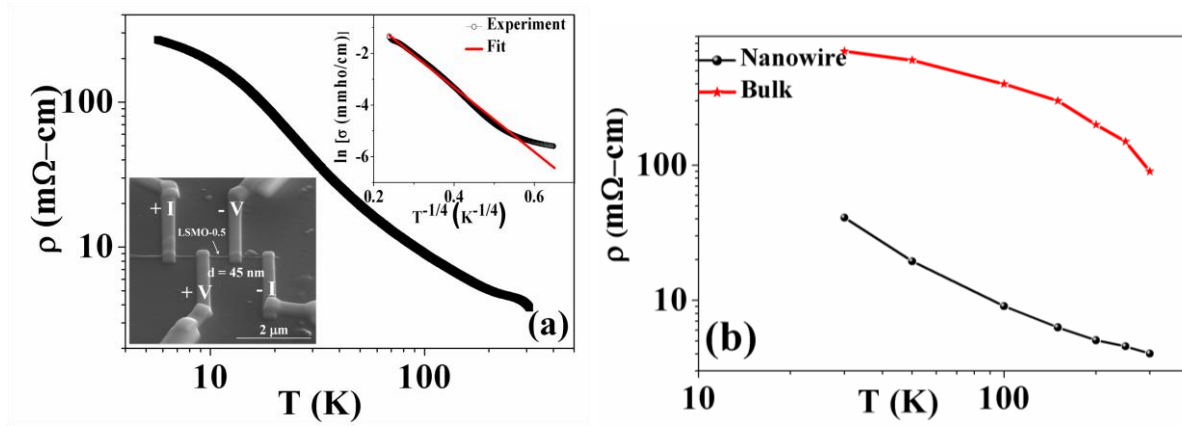


Figure 7.6 (a) Temperature variation of resistivity of single NW of LSMO-0.5 measured in the temperature range from 5 K to 310 K. Inset curve shows SEM image of the single LSMO-0.5 NW with four electrical contact pads used for resistivity measurement. Inset curve of Fig. 7.6 (a) ($\ln \sigma$ versus $T^{-1/4}$) shows that conductivity data fitted with variable range hopping model for the whole temperature ranges. (b) Quantitative comparison of resistivity of LSMO-0.5 NWs and bulk [37].

ρ vs. T curve (ρ at 300 K $\sim 10\ \text{m}\Omega\cdot\text{cm}$) and the magnetoresistance (MR) data taken in a field of 14 Tesla are shown in Fig. 7.7 (a) [14]. The MR data taken on NW does not show significant MR even at 14 Tesla (12% at 80 K) as shown in Fig. 7.7 (a). MR increases as the temperature is decreased and negative MR reaches a magnitude of only 12% at 80 K. The absence of significant MR shows absence of significant CO because if it exists, it can be destabilized by the magnetic field of 14 Tesla leading to substantial MR and often onset of metallic behaviour [36].

We have plotted the current-voltage (I - V) characteristics in four-probe for few representative temperatures as shown in Fig. 7.7 (b). The inset of Fig. 7.7 (b) shows the calculated contact resistance (R_C) by taking difference in the slope of I - V curves between two-probe and four-probe measurements using the relation $2R_C = R_T - R_{NW}$, where R_T is the two-probe resistance. We have assumed the two contacts are equal in nature and the contact resistivity is $\rho_C = A_C R_C$ where A_C is the active area of contact. At $T = 150$ K, with $I = 0.1$ μ A (at low bias) we found $\rho_C = 17 \mu\Omega\text{-cm}^2$ indicating ohmic contacts to LSMO-0.5 NW with FEB deposited Pt contact electrodes. We avoided unnecessary Ga ion implantation which ensures us about very low contribution of contact noise compared to the noise coming from the NW itself [19].

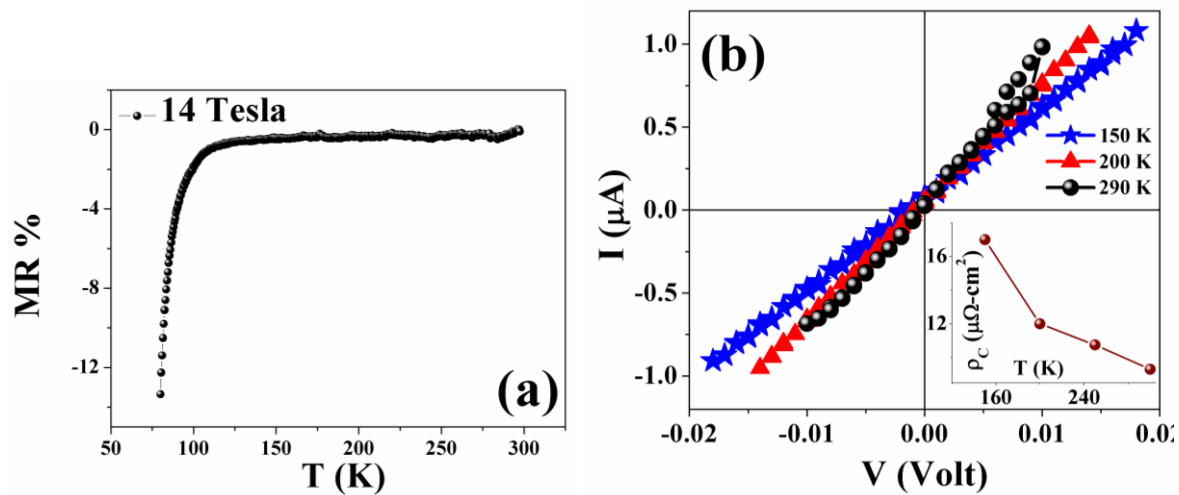


Figure 7.7 (a) Temperature dependent MR data of LSMO-0.5 single NW ($d \sim 45$ nm) at 14 Tesla. (b) I - V characteristics at different temperatures in four probe of the single LSMO-0.5 NW ($d \sim 45$ nm) device. Inset of Fig. 7.7 (b) shows the calculated contact resistance (R_C) by taking difference in the slope of I - V curves between two-probe and four-probe measurements.

The conductivity is similar in magnitude to the Mott minimum conductivity,[32] signifying the insulating behaviours. ρ vs. T is describable by a VRH model within the temperature region where, it is ferromagnetic [11]. VRH type T dependence shows that the insulating state seen is not due to charge ordering/orbital (both of which lead to insulating state) but due to electron localization as found in a disordered insulating system [33]. This insulating state arises from the electron localization effects, as in a disordered electronic system and not from polaronic effects or orbital ordering. The onset of FM order at T_C and the insulating behaviour as well as absence of significant MR indicates that for $T < T_C$ and $T > T_N$, the NW

is in a ferromagnetic insulating state. The FM order, however, is being unstable in half doped composition, leading to the AFM order at lower T_N , while the insulating state is maintained. As the transition occurs as a change in magnetic order in an insulating state, there is no discernible signature on the temperature dependence of ρ . Thus, just measurement of ρ alone does not resolve the issue of magnetic transitions and resulting coexisting phases in a single NW. The noise measurements that have more sensitivity than the resistivity measurements thus become a necessity.

7.5.3.1 Noise measurement of LSMO-0.5 single nanowire

Temperature dependent resistance fluctuations (noise) were measured with a four-probe phase sensitive ac detection technique [39, 40] within a frequency (f) window $0.01\text{Hz} \leq f \leq 10\text{Hz}$ with ac excitation frequency 233 Hz as discussed in chapter 4. Schematic representation of noise measurement set up is shown in Fig. 7.8 (a). Very low biasing current (current density $j_{ac} = 0.6 \times 10^4 \text{A-cm}^{-2}$) was used to avoid unnecessary heating and electro-migration stressing of the wire [41]. Fig. 7.8 (b) shows a non-monotonous dependence of normalized variance of resistance fluctuations $\langle \Delta R^2 \rangle / R^2$ with T . The total noise is the relative variance expressed as $\langle \Delta R^2 \rangle / R^2 = \int S_V(f) / V^2 df$. In Fig. 7.8 (b), the black curve is the total noise at zero field which includes magnetic and non magnetic part. The red curve is taken at magnetic field. A magnetic field is applied to suppress the spin related noise. After subtracting we got the magnetic part of the total noise. The total noise ($\langle \Delta R^2 \rangle / R^2$) is highest near T_C , it decreases rapidly when cooled and has a small value till T_N . It increases by one order again for $T < T_N$. The $\langle \Delta R^2 \rangle / R^2$ thus identifies clearly the two magnetic transitions that were not discernible in resistivity measurements. Let us look much more details in the results of noise data.

In an insulator sample LSMO-0.5 NW, the resistance (or conductance) noise can originate from fluctuations in the carrier density (n) due to charge trapping de-trapping processes and as well as from fluctuations in mobility (μ). The fluctuation in conductivity (σ) thus can be written as

$$\sqrt{\frac{\langle \Delta \sigma^2 \rangle}{\sigma^2}} \approx \sqrt{\frac{\langle \Delta n^2 \rangle}{n^2}} + \sqrt{\frac{\langle \Delta \mu^2 \rangle}{\mu^2}} \quad (7.4)$$

Where the first term is due to number density fluctuation and the second term arises from fluctuations in mobility (μ), which can arise from fluctuations associated with scattering cross

section. In our sample, the probable reason of the mobility fluctuations can be inhomogeneous phase separation with nanoscopic regions of different conductivities. The observed noise contains contributions from both magnetic origin and non-magnetic origin like structural defects that are present in all materials and are regarded as a common source of the $1/f$ noise [22, 40, 42-44]. To separate out these two contributions, we applied a magnetic field larger than anisotropy field (H_K) = 0.03 Tesla [12]. This suppresses the spin-fluctuations leading to suppression of the magnetic part of the noise. Use of magnetic field to separate out the magnetic and nonmagnetic part has been used in manganite and multilayer magnetic samples (NiFe) before [45, 46]. The observed noise is the least at $\mu_0 H \sim 0.04$ Tesla. Fig. 7.8 (b) shows that $\langle \Delta R^2 \rangle / R^2$ with magnetic field is suppressed over the whole temperature range except for $T \rightarrow T_C$. Below 250 K ($\sim 0.8 T_C$), noise is originating from non-magnetic sources [45] ($\langle \Delta R^2 \rangle / R^2_{\text{Nonmag}}$) which is nearly temperature independent. We obtain the magnetic part of the noise $\langle \Delta R^2 \rangle / R^2_{\text{magnetic}}$ by subtracting the non-magnetic part as $\langle \Delta R^2 \rangle / R^2_{\text{magnetic}} = \langle \Delta R^2 \rangle / R^2_{H=0} - \langle \Delta R^2 \rangle / R^2_{\text{Nonmag}}$. This is shown in the inset of Fig. 7.8 (b). $\langle \Delta R^2 \rangle / R^2_{\text{magnetic}}$ makes a dominant contribution to the total noise except the region around 250 K in the FM region. As $T \rightarrow T_C$ from below, the noise rises due to large contribution due to spin fluctuations. For $T \sim 0.8 T_C$, the fluctuations in the FM phase become small because the alignment of spins in the FM ordered phase. Thus, the noise measurement clearly identifies the FM transition in the single NW that is not easily identifiable by conventional resistivity measurement. $\langle \Delta R^2 \rangle / R^2_{\text{magnetic}}$ stays small below $0.8 T_C$, till $T \sim T_N$. However, below T_N it rises appreciably and reaches a temperature independent value for $T < 150$ K. The observed rise in fluctuation below T_N is taken as the signature of phase coexistence and as has been done in case of manganite films and single crystals [15, 16]. In manganite, the FM and AFM interactions are originating from DE and SE interaction, respectively. This makes the region below T_N prone to phase-co-existence. In addition, neutron diffraction results on the ensemble of NWs of the same composition, demonstrate the presence of phase coexistence below T_N . Crystallographic structural transition from room temp tetragonal ($I4/mcm$) to orthorhombic ($Fmmm$) partially below 200 K, accompanied by magnetic phase transition from Ferromagnetic (related to tetragonal $I4/mcm$ phase) to antiferromagnetic (related to orthorhombic $Fmmm$ phase) within FM matrix (discussed in chapter 6). Besides, measurements of transverse susceptibility and H_K done on ensemble of NWs reported the existence of FM phase within an AFM matrix below T_N as discussed in chapter 5 (see Fig.

5.10 (b)) [12]. It was found that while in the region above T_N (FM region), the NWs have almost constant anisotropy H_K , near T_N where the noise shows a low value, H_K reaches a low value at onset AFM transition. However, as the temperature is lowered below T_N , H_K increases indicating magnetic phase separation with an increase in the FM volume fraction. This growth stabilizes for $T < 100$ K when H_K reaches a T independent value. The enhancement of $\langle \Delta R^2 \rangle / R^2_{\text{magnetic}}$ below T_N and its eventual saturation at lower temperature closely follow the magnetic data and neutron data.

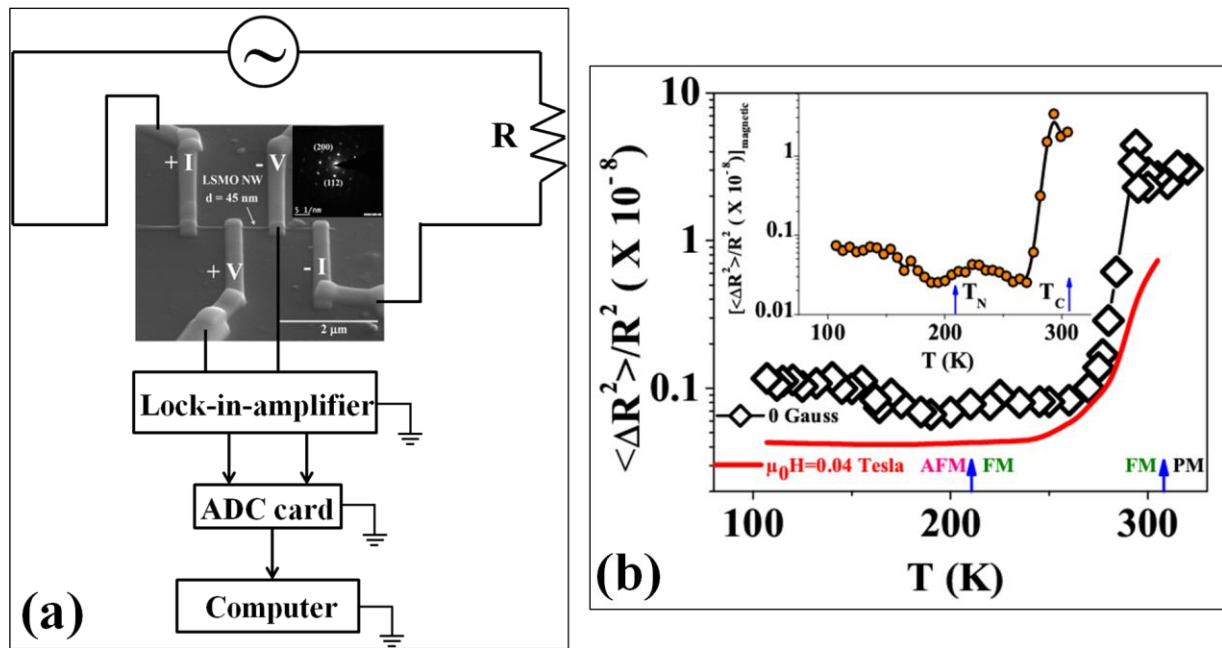


Figure 7.8 (a) Schematic representations of 1/f noise measurement set-up. (b) Normalized variance of resistance fluctuations ($\langle \Delta R^2 \rangle / R^2$) as a function of temperature (T) for field (H) = 0 and 0.04 Tesla and the inset shows the magnetic part of $\langle \Delta R^2 \rangle / R^2$ as a function of T .

A theoretical model was used [47] to calculate noise spectrum in non-metallic phase separated manganite containing small metallic droplets. The noise arises due to electron transfer between FM droplet and the insulating matrix thus changing their relative occupations. In LSMO-0.5 NW, the insulating matrix is the majority AFM phase and as the previous magnetic experiment as well as the neutron diffraction study suggest there is a co-existing FM phase. The concentration of FM droplets, however, is less than the percolation threshold so that the insulating behaviour does not change. While in a general way such a

model can be applicable here also, the details of transport in the two co-existing phases in our case may have differences from that given in Ref. [47].

In Fig. 7.9, we show the recorded time series of resistance fluctuations ($\Delta R/R$) at some representative temperatures close to T_C , T_N and for $T \ll T_N$. The fluctuation ($\Delta R/R$) is small and development of discrete jumps in R with increase of temperature as T_C is approached as shown in the enlarged portion of “**” time range at 300 K in Fig. 7.9. However, the resistance jumps are often superimposed with each other and they are distinct from resistance jumps expected for Random Telegraphic Noise (RTN).

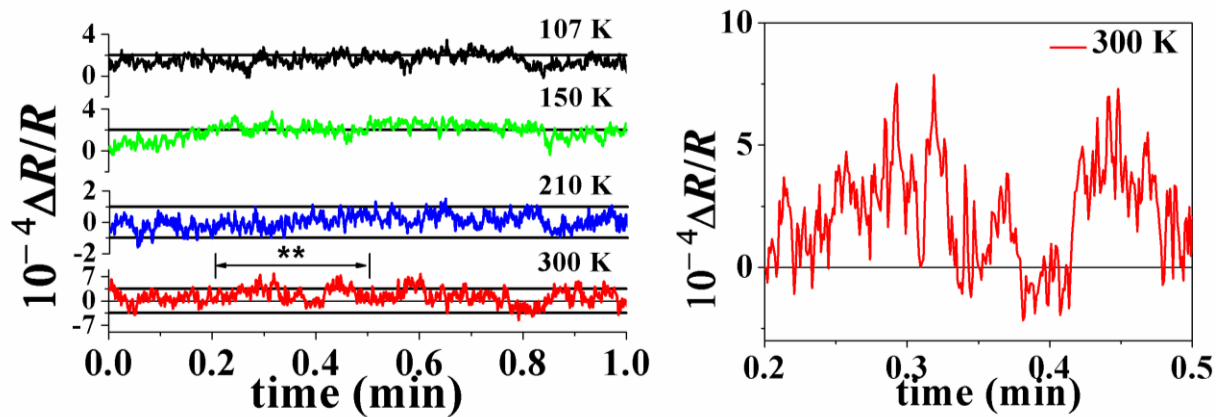


Figure 7.9 Recorded time-series of the fluctuation in resistance (R) at different temperatures. The discrete jump in resistance at 300 K in the “**” time range enlarged in the right side figure.

We measured the power spectral density (PSD) S_V [39] and the background noise (S_{bg}) independently. S_{bg} is distinct from the flicker noise arising from the sample containing the information about the materials only [40, 42]. S_{bg} contains thermal noise (Nyquist Noise = $4k_B T R$, where k_B is Boltzmann constant) as well as extraneous contact noise arising from contact resistivity (ρ_C). As ρ_C is low, S_{bg} is very close to Nyquist noise = $10^{-14} \text{ V}^2/\text{Hz}$ at 80 K indicating significant absence of contact noise contribution. In Fig. 7.10, we have plotted the PSD ($S_V(f)/V^2$) at few representative temperatures for the entire time series of fluctuations in R . For the complete frequency range measured $S_V(f)/V^2$ is proportional to $1/f$. We analyzed the PSD with two components: $S_V(f)/V^2 = A/f^\alpha + B/f^\beta$, where the first term is the conventional $1/f$ contribution [22] with $\alpha \sim 1$ and the other term ($1/f^\beta$) with $\beta \neq 1$ measures the deviation (if any) from $1/f$ behaviour. For the fit we used $\beta = 1.5$ which generally arises

from defect diffusion including oxygen diffusion [48]. The fit to the PSD data with equation above is shown as straight lines. The variation of coefficients A, B as a function of T in zero field and in an applied field are shown in inset of Fig. 7.10. The temperature dependent $A(T)$ and $B(T)$ represent the weightage of two terms, i.e., $1/f$ and Lorentzian term respectively. The coefficient A is much larger than B showing the predominant $1/f$ nature of $S_V(f)$. The application of the field does not change the nature of the spectral dependence; however, the variation of A reflects the behaviour seen in the relative variance (see Fig. 7.8 (b)).

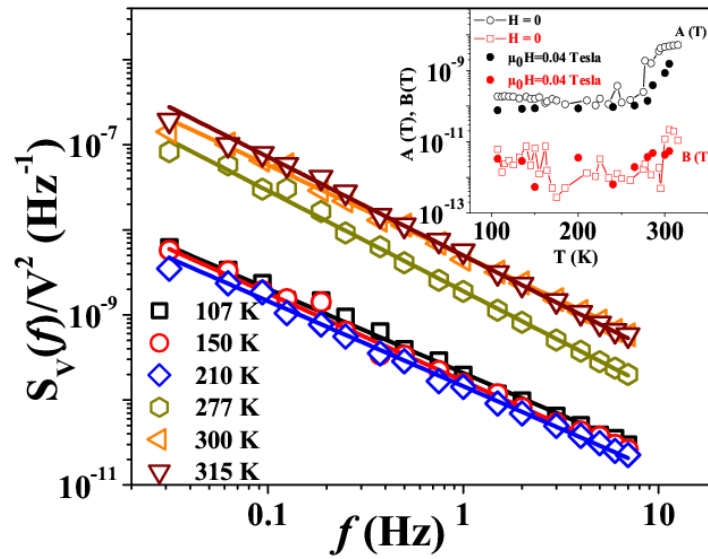


Figure 7.10 The calculated PSD at the few representative temperatures at field (H) = 0. The solid lines show the fitted curves as $S_V(f)/V^2 = A/f^\alpha + B/f^\beta$ and the inset shows temperature dependence of coefficients A and B in zero field and in an applied field.

The temperature dependence of α is shown in the Fig. 7.11. There is a nontrivial temperature dependence of α and $\langle \Delta R^2 \rangle / R^2$ showing signatures of distinct phase separation. We have studied magnetocaloric effect on this system (discussed in chapter 5) indicating AFM - FM transition at ~ 210 K followed by FM to PM transition ~ 310 K. From the ND study (chapter 6) we have also confirmed the phase separation in ensemble of NWs. The resistance of the sample is directly coupled to the magnetic phases by the spin orientations. The measured variance of fluctuation is pronounced due to the different conductive channels associated with different magnetic orders. The FM phase is an ordered phase than a PM phase and hence noise is less compared to a disordered PM phase. $\alpha \sim 1$ below 275 K and had started increasing with increase of temperature.

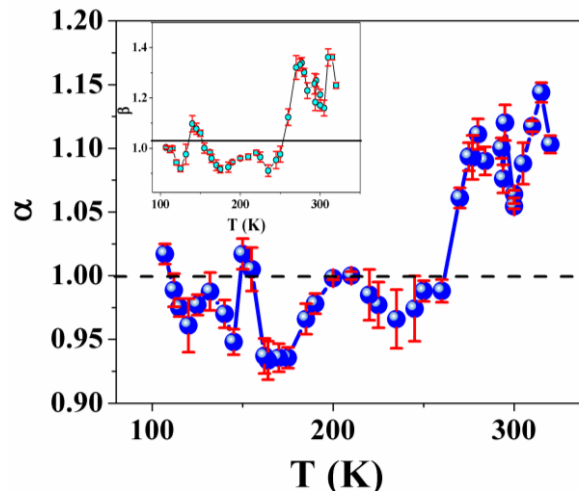


Figure 7.11 The temperature variation of frequency exponent α . Inset shows the temperature dependence of β .

Probability distribution function (PDF)

An important parameter that characterizes the nature of fluctuations in any system is the estimation of its probability density function (PDF) [49]. The essential criteria for estimation of PDF are: one has to estimate the approximate frequency at which excess noise is comparable to background level, the excess noise magnitude should be at least one order higher in magnitude than the background level and the real time series of voltage fluctuations then decimated down so that the band width is restricted below this frequency. The PDF so obtained is an experimental quantity. Next step is to analyse the nature of the PDF to check whether it is Gaussian or some other distribution.

For Gaussian fluctuation, the probability of the voltage fluctuation follows the relation:

$$P(\Delta V) = \frac{1}{\sqrt{2\pi}w} \exp \left(\frac{-(\Delta V)^2}{2w^2} \right) \quad (7.5)$$

In Fig. 7.12 we collected the statistical information about the kinetics of resistance jumps (i.e., voltage jumps ΔV) by checking the Gaussianity of noise at few temperatures encompassing different transition regimes. We calculated PDF by calculating $P(|\Delta V|)$ of occurrence of voltage jumps ΔV due to ΔR . The data have been plotted as (ΔV^2) versus $\ln[P(\Delta V)]$. We have fitted the straight line with equation $\ln[P(\Delta V)] = K + m[(\Delta V^2)]$ (linearized form of Gaussian PDF) where K and m are the fitting parameters. It had been reported earlier that canted AFM [50] and phase coexistence [51] are possible near FM-AFM phase transition in NWs ensemble. We found that for $107 \text{ K} \leq T \leq 275 \text{ K}$, noise statistics is essentially

Gaussian. It may happen that though there is AFM phase is growing in the wire, still a fair amount of FM volume fraction retains in the system which is contributing to Gaussian PDF. Due to defined low diameter NW structure, it can also happen the FM state is more favourable other than the growth of competing AFM phase. Non-Gaussian tails become significantly strong for $T > 275\text{K}$. Such non-Gaussian component (NGC) indicates correlated motion of the charge carriers in disordered PM- FM phase mixtures. At low temperatures, $T < 175\text{ K}$, the resistance increases sharply due to the availability of the less number of carriers with slow dynamics. Hence, the growth of correlations among the fluctuators becomes prominent with signatures of non- Gaussian tails even at low temperatures.

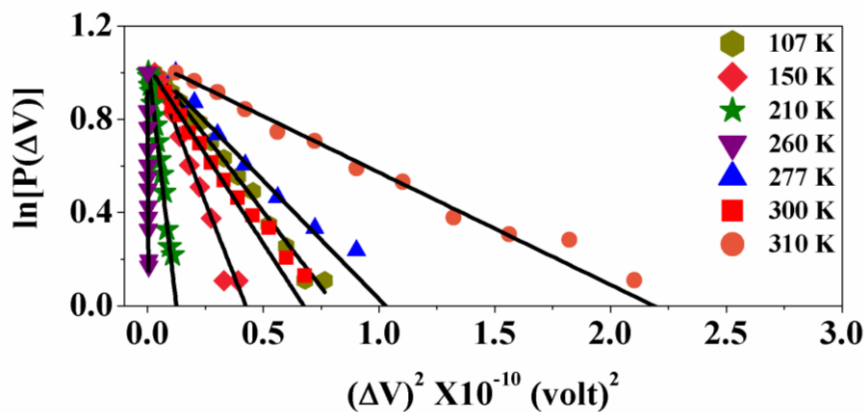


Figure 7.12 Variation of probability distribution function (PDF) of resistance jumps in single NW at different temperatures, which shows how the statistics becomes non-Gaussian with temperatures.

Hooge Parameter:

It is an important parameter related to nature and kinetics of disorder, scattering cross section of charge carriers, crystallinity and so on. F. N. Hooge [52, 53] an empirical relation for 1/f noise in terms of voltage fluctuations, where the spectral density is related

as $\frac{\gamma_H}{n} = \frac{S_V(f)f^\alpha \Omega}{V^2}$. We estimated normalized Hooge parameter ($\frac{\gamma_H}{n}$) (at $f = 1\text{Hz}$) taking

carrier density (n) $1.2 \times 10^{22}/\text{cm}^3$ and the volume (Ω) between two voltage leads $\sim 1.7 \times 10^{-15}\text{cm}^3$. We assume the contribution of B/f^β is much smaller than A/f^α at higher frequencies. In

Fig. 7.13 we show the estimated value of $\frac{\gamma_H}{n}$ is low as $\sim 10^{-32}\text{ m}^3$ and nearly temperature

independent ≤ 275 K. Such low value of $\frac{\gamma_H}{n}$ has not been reported earlier. The low value of $\frac{\gamma_H}{n}$ indicates good quality of the wire and less number of defect density. For $T > 275$ K, $\frac{\gamma_H}{n}$ starts increasing rapidly and changes drastically over two orders of magnitude as it goes over from FM to PM phase. We did not find any report on temperature dependence of $\frac{\gamma_H}{n}$ in such single NW system till date.

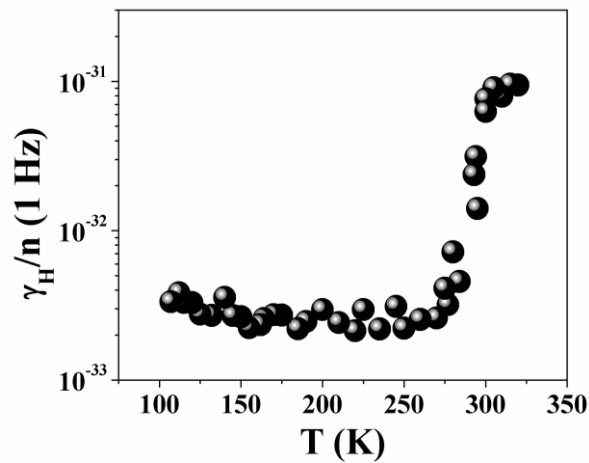


Figure 7.13 Variation of $\frac{\gamma_H}{n}$ with temperature.

Using the empirical 1/f noise relation [43, 44, 54], the relative noise (at $f = 1$ Hz), $C_{1/f} = fS_V(f)/V^2$ is used to calculate the noise parameter γ (γ_H Hooge parameter) if the total number of free carriers, N (between the voltage contacts) is known. Here, the concentration of free carriers, n and hence N is not known. There is still a possibility to compare noise between different materials or in the same material under different conditions with the parameter $K_{\text{sample}} = C_{1/f} V_{\text{vol}}/\rho$ [54, 55] cm^2/Ω . Here, ρ is the resistivity and V_{vol} the sample volume between the voltage sensing contacts $V_{\text{vol}} (\text{cm}^3) = 10^{-15} \text{ cm}^3$ [54]. Evaluating $C_{1/f}$ at $f = 1$ Hz, the estimated values of K_{sample} of LSMO-0.5 NW is around $4 \times 10^{-22} \text{ cm}^2/\Omega$ and $6.6 \times 10^{-24} \text{ cm}^2/\Omega$ at 300 K and 107 K, respectively. We have compared the values of K_{sample} of different materials with that of LSMO-0.5 single NW in Table 7.2. The possible reasons of such low K_{sample} value are related to good single crystalline nature of the NW.

Table. 7.2 Comparison of the value of K_{sample} of different materials.

K_{sample} (cm^2/Ω)	Materials	References
$K_{\text{sample}} < 10^{-23}$	Ultra low noise: e.g., Si JFETs	[55]
$10^{-23} < K_{\text{sample}} < 10^{-21}$	Mature semiconductor technology, e.g., bulk Si, Si NW (2×10^{-21}), GaN on AlN buffer / sapphire substrate	[56]
$10^{-21} < K_{\text{sample}} < 10^{-19}$ (largest group)	Poly crystalline metals and semiconductors and single crystals, e.g., GaN on SiC, carbon, Ge, InAs-NWs ,	[57]
$K_{\text{sample}} \sim 4 \times 10^{-22}$ at 300 K $K_{\text{sample}} \sim 6.6 \times 10^{-24}$ at 107 K	LSMO-0.5 single NW	Our result ref [14]

7.6 Conclusion

Electrical transport measurement of single NW itself is a very challenging work, which was not done before on complex oxide manganite system. Moreover, we have reported first time, the 1/f noise spectroscopy study of a single manganite NW.

The electrical transport measurement performed of single NW of different compositions shows size reduction induced modification of the transport property. Size reduction to 1D, optimally doped LCMO-0.3 single NW exhibits enhancement of metal insulator transition temperature (T_P) to 332 K compared to its bulk (250 K). Enhancement is also observed in case of magnetic transitions (T_C). The modification of Mn-O bond angle and bond length on size reduction leads to enhancement of band width which ultimately enhances T_C and T_P as well. In case of the composition LCMO-0.5 NW, VRH type T dependence shows that the insulating state seen is not due to charge ordering/orbital (both of which lead to insulating state) but due to electron localization as found in a disordered insulating system.

We experimentally demonstrated the temperature and magnetic field dependent flicker noise (1/f noise) spectroscopy in a single NW ($d \sim 45$ nm) device of complex oxide system like LSMO-0.5, which is a building block of NW ensemble. The multiple magnetic phase transitions and the magnetic phase coexistence which was observed in ensemble of NWs of half doped (Sr doped) LSMO-0.5, manganite system from magnetic as well as neutron diffraction experiments, 1/f noise spectroscopy study of single NW also detected the magnetic transition (T_C , T_N) and as well as phase coexistence of FM and AFM phases and

thus corroborates the results of ensemble based magnetic and structural results (discussed in chapter 5 and 6) [12]. We have also successfully demonstrated that the magnetically ordered phases and their phase coexistence tune the resistance fluctuation by several orders of magnitude. We identified the intrinsic and extrinsic physical processes taking place in the NW and their role in the low frequency noise spectra. The study of non Gaussian component (NGC) by calculating probability distribution function (PDF) also supports the magnetic order which directly influences the power spectral density (PSD). It established that the noise spectroscopy can be a viable tool to detect magnetic transitions at the level of single NW, which may not be done using magnetic or structural measurement. This overcomes the difficulty in doing magnetic measurements of single NW and suggests an alternate route to identify magnetic transitions. We have clearly demonstrate that the observed magnetic transitions and phase coexistence of FM and AFM states observed in an ensemble based magnetic and neutron measurement on LSMO-0.5 sample, is not an artefact due to size dispersion but is an intrinsic phenomena occurring at single NW level. We calculated Hooge parameter (γ_H) which can have structural origin of the NW and not been stated earlier. K_{sample} obtained in the 45 nm diameter single NW was found to be lower than that seen in low-noise Si-JFET's. The low value of the noise could arise from single crystalline nature of the NW used in the work.

Bibliography:

- [1] A. Fert and L. Piraux, *J. Magn. Magn. Mater.*, **200**, 338 (1999).
- [2] D. J. Sellmyer, M. Zheng and R. Skomski, *J. Phys.: Condens. Matter.*, **13**, R433 (2001).
- [3] K. S. Shankar, S. Kar, A. K. Raychaudhuri and G. N. Subbanna, *Appl. Phys. Lett.*, **84**, 993 (2004).
- [4] T. Sarkar, B. Ghosh, A. K. Raychaudhuri and T. Chatterji, *Phys. Rev. B*, **77**, 235112 (2008).
- [5] T. Sarkar, A. K. Raychaudhuri, A. K. Bera and S. M. Yusuf, *New J. Phys.*, **12**, 123026 (2010).
- [6] P. Schiffer, A. P. Ramirez, W. Bao and S.-W. Cheong, *Phys. Rev. Lett.*, **75**, 3336 (1995).
- [7] A. P. Ramirez, *J. Phys.: Condens. Matter.*, **9**, 8171–8199 (1997).
- [8] P. G. Radaelli, D. E. Cox, M. Marezio and S-W. Cheong, *Phys. Rev. B*, **55**, 3015 (1997).
- [9] Z. Jirák, E. Hadová, O. Kaman, K. Knížek, M. Maryško, E. Pollert M. Dlouhá and S. Vratislav, *Phys. Rev. B*, **81**, 024403 (2010).
- [10] A. Asamitsu, Y. Tomioka, H. Kuwahara and Y. Tokura, *Nature*, **388**, 50-52 (1997).
- [11] S. Datta, S. Chandra, S. Samanta, K. Das, H. Srikanth and B. Ghosh, *Journal of Nanomaterials*, vol. **2013**, Article ID 162315, 6 pages, 2013. doi:10.1155/2013/162315.
- [12] S. Chandra, A. Biswas, S. Datta, B. Ghosh, A. K. Raychaudhuri and H. Srikanth, *Nanotechnology*, **24**, 505712 (2013).
- [13] M. N. Barber, Phase Transitions and Critical Phenomena, edited by C. Domb and J. L. Lebowitz (Academic, New York, 1983).
- [14] S. Datta, S. Samanta, B. Ghosh and A. K. Raychaudhuri, *Appl. Phys. Lett.*, **105**, 073117-073120 (2014).
- [15] V. Podzorov, M. E. Gershenson, M. Uehara and S. W. Cheong, *Phys. Rev. B*, **64**, 115113 (2001).
- [16] B. Raquet, A. Anane, S. Wirth, P. Xiong and S. von Molnar, *Phys. Rev. Lett.*, **84**, 4485 (2000).
- [17] A. Bid, A. Guha and A. K. Raychaudhuri, *Phys. Rev. B*, **67**, 174415 (2003).
- [18] A. Singh, S. Mukhopadhyay and A. Ghosh, *Phys. Rev. Lett.*, **105**, 067206 (2010).
- [19] S. Samanta, K. Das and A. K. Raychaudhuri, *Nanoscale Res. Lett.*, **8**, 165 (2013).
- [20] H. Nyquist, *Phys. Rev.*, **32**, 110, (1928).
- [21] W. Schottky, *Ann. Phys. (Leipzig)*, **57**, 541 (1918).

- [22] P. Dutta and P. M. Horn, *Rev. of Mod. Phys.*, **53**, 497 (1981).
- [23] A. Bora, Ph. D Thesis, Indian Institute of Science, Bangalore, India.
- [24] F. K. Du Pré, *Phys. Rev.*, **78**, 615 (1950).
- [25] S. Samanta, Ph. D Thesis (2009) Jadavpur University, India.
- [26] V. Podzorov, M. Uehara, M. E. Gershenson, T. Y. Koo and S.-W. Cheong, *Phys. Rev. B*, **61**, R3784 (2000).
- [27] A. Urushibara, Y. Moritomo, T. Arima, A. Asamitsu, G. Kido and Y. Tokura, *Phys. Rev. B*, **51**, 14103 (1995).
- [28] J. Mira, J. Rivas, F. Rivadulla, C. Vazquez-Vazquez and M. A. Lopez-Quintela, *Phys. Rev. B*, **60**, 2998 (1999)
- [29] J. Mitra, Ph. D Thesis, Indian Institute of Science, Bangalore, India.
- [30] G. Q. Gong, C. L. Canedy, G. Xiao, J. Z. Sun, A. Gupta and W. J. Gallagher, *J. Appl. Phys.*, **79**, 4538-4540 (1996).
- [31] S. G. Zhao, K. X. Jin and C. L. Chen, *J. Appl. Phys.*, **101**, 083701 (2007).
- [32] N. F. Mott and E. A. Davis, Eds., *Electronic Processes in Non-Crystalline Materials*, Clarendon Press: Oxford University Press, Oxford, UK, 2nd edition.
- [33] P. A. Lee and T. V. Ramakrishnan, *Rev. Mod. Phys.*, **57**, 287-337 (1985).
- [34] B. Zhang, L. Wu, W. G. Yin, C. J. Sun, P. Yang, T. Venkatesan, J. Chen, Y. Zhu and G. M. Chow, *Nano Lett.*, **16**, 4174–4180 (2016).
- [35] S. Datta, A. Ghatak and B. Ghosh, *J. Mater. Sci.*, **51**, 9679–9695 (2016).
- [36] H. Kuwahara, Y. Tomioka, A. Asamitsu, Y. Moritomo and Y. Tokura, *Science*, **270**, 961-963 (1995).
- [37] Z. Jirak, J. Hejtmanek, K. Knmzek, M. Marysk, V. Smma and R. Sonntag, *J. Magn. Magn. Mater.*, **217**, 113–119 (2000).
- [38] J. M. D. Coey, M. Viret, L. Ranno and K. Ounadjela, *Phys. Rev. Lett.*, **75**, 3910–3913 (1995).
- [39] J. H. Scofield, *Rev. Sci. Instrum.*, **58**, 985 (1987).
- [40] A. K. Raychaudhuri, *Curr. Opin. Solid State Mater. Sci.*, **6**, 67 (2002).
- [41] A. Bora and A. K. Raychaudhuri, *J. Appl. Phys.*, **99**, 113701 (2006).
- [42] M. B. Weissman, *Rev. Mod. Phys.*, **60**, 537 (1988).
- [43] F. N. Hooge, T. G. M. Kleinpenning and L. K. J. Vandamme, *Rep. Prog. Phys.*, **44**, 479 (1981).
- [44] L. K. J. Vandamme and F. N. Hooge, *IEEE Trans. Electron Devices*, **55**, 3070 (2008).

- [45] S. Samanta and A. K. Raychaudhuri, *Phys. Rev. B*, **78**, 014427 (2008).
 - [46] M. A. M. Gijs, J. B. Giesbers, J. W. van Est, J. Briare, L. K. J. Vandamme and P. J. L. Belien, *J. Appl. Phys.*, **80**, 2539 (1996).
 - [47] A. L. Rakhmanov, K. I. Kugel, Ya. M. Blanter and M. Yu. Kagan, *Phys. Rev. B*, **63**, 174424 (2001).
 - [48] A. Ghosh and A. K. Raychaudhuri, *Phys. Rev. B*, **64**, 104304 (2001).
 - [49] A. Ghosh, Ph.D thesis (1999), Indian Institute of Science, Bangalore, India.
 - [50] S. Chandra, A. Biswas, S. Datta, B. Ghosh, V. Siruguri, A. K. Raychaudhuri, M. H. Phan and H. Srikanth, *J. Phys.:Condens. Matter.*, **24**, 366004 (2012).
 - [51] S. Chandra, A. I. Figueroa, B. Ghosh, M. H. Phan, H. Srikanth and A. K. Raychaudhuri, *J. Appl. Phys.*, **109**, 07D720 (2011).
 - [52] F. N. Hooge, *Physics Letters*, **29**, 139-140 (1969).
 - [53] F. N. Hooge, *Physica*, **60**, 130-144 (1976).
 - [54] L. K. J. Vandamme, *Fluctuation Noise Lett.*, **10**, 467 (2011).
 - [55] F. A. Levinzon and L. K. J. Vandamme, *Fluctuation Noise Lett.*, **10**, 447 (2011).
 - [56] L. K. J. Vandamme, X. Li and D. Rigaud *IEEE Trans. Electron Devices*, **41**, 1936-1945 (1994).
 - [57] R. P. Mertens and C. L. Claeys, Eds. IEEE, New York USA, 365-368 (2004).
-

Chapter 8

Summary and concluding remarks

In this final chapter, we have summarized important observations of this thesis work and discuss the scope for future works. The focus of this dissertation is the ground state property of manganites nanowires (NWs) and how it modifies due to size reduction. During this work we have emphasized on NW synthesis, experimental techniques such as EELS, nanolithography techniques (optical and e-beam lithography), single NW measurement which were extensively used during this work. Important observations during this thesis work are pointed out below.

8.1 Conclusions

This thesis leads to definite results because we are able to grow high quality single crystalline manganite NWs. In this thesis, we mainly focus on the rational synthesis, growth mechanism, and detailed characterization of ensemble of NWs as well as single NW level of manganite ($\text{La}_{1-x}\text{A}_x\text{MnO}_3$; $\text{A} = \text{Ca}, \text{Sr}$; $x = 0.3$ and 0.5). We have investigated how the crystallographic and magnetic structures (obtained from ND measurement) evolve on size reduction to 1D (with large aspect ratio structure) and how it affects the electrical, magnetic and other physical properties. We have tried to find out the correlation between them and compared with their bulk and nanoparticles. We have performed micro-structural simulation using crystallographic structural parameters obtained from Rietveld analysis. Along with the study of ensemble of NWs where size dispersion issues may arise, we have explored single NW based transport measurement to resolve the size dispersion issues and also performed $1/f$ noise spectroscopy study of single NW with the aim to understand magnetic phase separation in manganite system. The main outcomes of this thesis are given below:

- (a) In chapter 2, we have discussed the complete growth process and growth mechanism of manganite $\text{La}_{1-x}\text{A}_x\text{MnO}_3$; (where $\text{A} = \text{Ca}, \text{Sr}$; $x = 0.3$ and 0.5) nanostructures. Here we have shown how to tailor shape and size of nanostructures with controlled composition and stoichiometry by tuning the growth parameters in hydrothermal synthesis. Mechanism of shape and size tuning and composition control issues followed by a phase diagram have been proposed in this chapter. It has been shown that amount of the mineralizer (KOH), temperature and growth time are the most important parameters which control the shape, size of the nanostructures. Analysis of crystallographic structural data, HRTEM and SAED data also show that the grown NWs are of pure phase and single crystalline. We have further characterized the NWs using advanced characterization techniques in chapter 3.
- (b) In chapter 3, elemental analysis using Electron Energy Loss Spectroscopy (EELS) measurement and structural simulation using JEMS have been combined as a whole to define the growth mechanism which has been already discussed in chapter 2. The details of elemental characterization using EELS data reveal the valence of transition metal, Mn ion which is an important issue in mixed valent compound like manganite. The mixed valence of Mn as estimated from EELS study showed us a way for the need of the study

of structural distortions in MnO_6 octahedra (change in Mn-O-Mn bonds) which can justify the physical measurements. Hence a requirement for structural analysis comes into play in our work and JEMS provides us this opportunity.

Analysis of HRTEM diffraction data of JEMS software provides us an idea about the growth mechanism, how the OH^- ion of mineralizer KOH helps in bonding and initiates the growth and also the growth direction. In our case of single NWs of LSMO the growth direction is different for both the composition (LSMO-0.3 along [110] and LSMO-0.5 along [112]) and a contraction in the c -axis of the crystal is noticed in comparison to the bulk and nanoparticles (which is also confirmed from synchrotron XRD data in chapter 6). This may be due to the attachment of OH^- ions with the A-site (positively charged ions) along the long axis direction of the NWs that reduces the overall surface energy contribution and leads to a growth along a particular direction (LSMO-0.3 along [110] and LSMO-0.5 along [112]). On the other hand, in case of another manganite NW, i.e., LCMO-0.3 it was seen that twins are formed with the possibility of the distortion in the MnO_6 octahedra due to the possible attachment of K^+ ions and this also changes the orthorhombic distortion. But the change in the doping concentration changes the scenario and leads to the growth along [121] in case of LCMO-0.5 leading to the reduction of the overall surface energy along the long axis direction of the NWs. Hence along with the effect of mineralizer it has been shown that other factors like doping concentration are also involved in the growth of NW along a particular direction. Hence the microstructural study along with the image simulation in the atomic scale is an important tool to correlate the structure-property in manganite system.

- (c) In chapter 5, we have discussed dc and ac magnetic, Arrott plot, magnetocaloric and transverse susceptibility, exchange bias studies to understand the temperature and field dependent magnetization dynamics of the single crystalline $\text{La}_{1-x}\text{A}_x\text{MnO}_3$ ($\text{A} = \text{Ca}, \text{Sr}; x = 0.3 \text{ and } 0.5$) NWs. In case of LCMO-0.3 and LCMO-0.5 NWs, the size reduction induced magnetic transition is observed where the system has the same chemical composition (no change in hole concentration) and the only difference is the size of the system. We have observed T_C is enhanced more in NWs with respect to its bulk form and slightly increased with respect to its nanoparticles form. We have shown that the nature of phase transition can be changed by tuning the size. Although bulk LCMO-0.3 and LCMO-0.5 exhibit first order transition at T_C , the nature of the transition can be changed to second order by

bringing down the size to the nanometre level in nanoparticles and NWs, without any change in the stoichiometry of the samples.

On the other hand, Sr doped LSMO-0.3 and LSMO-0.5 NWs, the bulk, nanoparticles and NW system show second order phase transitions around T_C . In LSMO-0.3 NWs, T_C value is decreased with respect to bulk due to finite size effects. In bulk LSMO-0.5, there is one magnetic transition PM to FM ($T_C \sim 315$ K) whereas in LSMO-0.5 nanoparticles due to size reduction there are two magnetic phase transitions (PM-FM and FM-AFM; $T_C \sim 315$ K and $T_N \sim 200$ K). We have observed multiple magnetic phase transitions on size reduction to 1D (LSMO-0.5 NWs) with large aspect ratio structure. LSMO-0.5 NWs undergo PM–FM transition at $T_C \sim 310$ K followed by an FM–AFM transition at $T_N \sim 210$ K, exhibiting conventional MCE and IMCE respectively. Our results point to the presence of magnetic phase coexistence with competing DE and SE interactions arising from the FM and AFM domains. As the temperature is lowered, the FM volume fraction increases and overcomes the AFM interactions (~ 75 K), which is marked by re-entrance of conventional MCE. On further lowering the temperature (~ 45 K), the surface spins undergo a freezing phenomenon with weak frequency dependence. It is to be stressed that, precisely at the surface spin freezing temperature (~ 45 K), we observe the onset of exchange bias (EB). To the best of our knowledge, these particular issues in NWs have not been addressed before and no experiments have been reported in NWs that specially observe this change-over of the nature of the magnetic phase transition on size reduction.

- (d) In chapter 6, we have discussed the size reduction induced modification of crystallographic and magnetic structures of 1D nanostructures of manganite ($\text{La}_{1-x}\text{A}_x\text{MnO}_3$; $\text{A} = \text{Ca}, \text{Sr}$; $x = 0.3$ and 0.5), which was not looked into before. From the analysis of structural data, the T_C enhancement of LCMO-0.3 and LCMO-0.5 NWs are explained. The lattice parameters contract due to size reduction in NWs and the MnO_6 octahedra compact with smaller $d_{\text{Mn-O}}$ and $\theta_{\text{Mn-O-Mn}} \rightarrow 180^\circ$. This leads to an enhancement of the bandwidth and therefore T_C is enhanced for both cases.

LSMO-0.5 NWs undergo PM–FM transition at $T_C \sim 310$ K followed by an FM–AFM transition at $T_N \sim 210$ K. The presence of magnetic phase coexistence with competing DE and SE interactions arises from the FM and AFM domains which is absent in its bulk form. Our crystallographic structural analysis exhibits that the coexistence of FM and AFM phases arises due to structural phase coexistence of tetragonal and orthorhombic phases. Contraction in the c -axis of LSMO-0.5 NWs is noticed in comparison to the bulk

and nanoparticles. As the temperature is lowered, the FM volume fraction increases and overcomes the AFM interactions (~ 50 K), which is manifested by dc magnetic measurement and neutron diffraction study.

- (e) In chapter 7, we have observed that size reduction to 1D, optimally doped LCMO-0.3 single NW exhibits enhancement of metal insulator transition temperature (T_P) to 332 K compared to its bulk ($T_P \sim 250$ K) and nanoparticles ($T_P \sim 265$ K), enhancement is also observed in case of magnetic transitions (T_C). Though this enhancement was observed in ensemble of NWs grown in anodized alumina template, this is the first report of such an investigation in a single NW. The modification of Mn-O bond angle and bond length on size reduction leads to enhancement of band width which ultimately enhances T_C and T_P as well. In case of LCMO-0.5 NW, VRH type T dependence shows that the insulating state seen is not due to charge ordering/orbital (both of which lead to insulating state) but due to electron localization as found in a disordered insulating system. In LCMO-0.5 NW and nanoparticles, there is also a signature of suppression of the CO insulating phase and absence of significant MR which are present in its bulk form. Size reduction leads to suppression of MR in manganite NWs and nanoparticles.

From magnetic as well as ND experiments, the multiple magnetic phase transitions and the magnetic phase coexistence were observed in ensemble of LSMO-0.5 NWs. Noise spectroscopy study of single NW also detected the magnetic transition (T_C , T_N) and as well as phase coexistence of FM and AFM phases and thus corroborates the results of ensemble based magnetic and structural results (discussed in chapter 5 and 6). It established that the noise spectroscopy can be a viable tool to detect magnetic transitions at the level of single NW, which may not be done using magnetic or structural measurement. This overcomes the difficulty in doing magnetic measurements of single NW and suggests an alternate route to identify magnetic transitions.

8.2 Scope for future work

1. In the NW fabrication front, it will be a great prospect to grow NWs of parent compound (RMnO_3 , R = rare earth element) and all the other doping concentrations ($\text{R}_{1-x}\text{A}_x\text{MnO}_3$; R = La, Nd, Sm etc, A = Ca, Sr, Ba; $x = 0$ to 1) using hydrothermal method and compare their physical properties.

2. We have taken HRTEM data using conventional TEM instrument. Our next target to take HRTEM data of single NW using aberration corrected TEM and compared with simulated structure obtained from crystallographic structural refinement.
 3. We have measured temperature dependent AC susceptibility of LSMO-0.5 NWs. The temperature dependent second and third harmonic of AC susceptibility at various frequencies and size dependent detailed magnetic measurement will be studied on manganite NWs.
 4. Size dependent magnetic memory, relaxation and interaction can be performed on manganite NWs and compared with their bulk counterpart.
 5. Transport measurement of single NW of $\text{La}_{0.7}\text{Sr}_{0.3}\text{MnO}_3$ system will be a very challenging work.
 6. We have found metal insulator transition temperature (T_P) of single NW of $\text{La}_{0.7}\text{Ca}_{0.3}\text{MnO}_3$ system. Size dependent transport measurements, $1/f$ noise spectroscopy study and magnetoresistance measurements will be done on single NW of $\text{La}_{0.7}\text{Ca}_{0.3}\text{MnO}_3$ with different diameter ranges from 30-200 nm.
 7. We will also try to find out the metal insulator transition of single NW of $\text{La}_{0.7}\text{Ca}_{0.3}\text{MnO}_3$ from scanning transmission microscope and calculate density of states of single NW level and compare with its theoretical values.
-

Appendix A

Size dependence in magnetic memory, relaxation and interaction of $\text{La}_{0.7}\text{Sr}_{0.3}\text{MnO}_3$ system

We have demonstrated here the study of memory effect, relaxation and interaction of hydrothermally grown $\text{La}_{0.7}\text{Sr}_{0.3}\text{MnO}_3$ (LSMO-0.3) nanowires (NWs) and its bulk form synthesized by using polymeric precursor route. Magnetic relaxation measurement has been carried out and the analysis shows the existence of two relaxation times in both the cases. It has been observed that both the samples show signature of magnetic memory effect and prefer magnetized state.

A.1 Introduction

Observation of magnetic memory in magnetic samples is an interesting phenomenon, since the reason can be either attributed to inter-particle interaction or particle size distribution. Most of such works have been focused on ferromagnetic and ferrimagnetic nanoparticles due to their high magnetic moments which make them industrially valuable. Hole doped perovskite manganites are well known magnetic materials for their fascinating physical properties and technological viability. However, the effect of size reduction on their physical properties is a topic of very recent interest [1–5]. Generally, properties of magnetic materials can arise from intrinsic properties arising from interactions of nanocrystals [6, 7]. Depending on the composition and hole-doping level, many manganites exhibit unusual non-equilibrium dynamics and time-dependent phenomena such as ageing, rejuvenation, memory, etc. [8–9]. $\text{La}_{0.7}\text{Sr}_{0.3}\text{MnO}_3$ (LSMO-0.3) belongs to hole doped manganite family and is known to be potential candidate for technological application, since it has ferromagnetic transition temperature (T_C) around 380 K and a large magnetic moment at room temperature [10–11]. This present work is concentrated on the study of memory effect and relaxation phenomena of LSMO-0.3 bulk and NWs. We report the detailed investigation in the non-equilibrium magnetic behaviour of LSMO-0.3 NW and bulk. The main objective is to understand the type of interaction and to investigate the effect of size reduction on magnetic interactions, since interaction plays important role to influence the magnetic properties.

A.2 Experimental details

LSMO-0.3 NWs and bulk samples are grown by hydrothermal method and sol gel method respectively which is discussed in details in chapter 2. These particles are characterized by Scanning Electron Microscopy (SEM). For ZFC measurements at $H = 40$ Oe with 2 hrs stop at 90 K when compared with the uninterrupted ZFC measurements, we found the signature of magnetic memory effect. In order to do magnetic relaxation measurement, the sample is cooled down to 95 K in the absence of any field. Then a field $H = 1$ Tesla is applied in 20 sec and it took again around 20 sec to remove the field. After removing the field, the magnetization is recorded as a function of time ($t = 7$ hrs). In order to probe the inter-particle interaction for the LSMO-0.3 NW and bulk samples, the measurement of isothermal remnant

magnetization (m_{IRM}) and dc demagnetization (m_{DCD}) as a function of magnetic fields have been carried out [12] at 120 K. Isothermal remnant magnetization (m_{IRM}) is the magnetization measured at a particular temperature after reducing an applied field (H_{app}) to zero isothermally. For measuring m_{DCD} , one has to apply a positive saturation field at particular temperature. Then, a field in the opposite direction ($-H_{\text{app}}$) has to be applied. The measured magnetization after reducing $-H_{\text{app}}$ to zero is the m_{DCD} . We have investigated the validity of Wohlfarth relation in the LSMO-0.3 particles; which is applicable for a non-interacting system with uniaxial anisotropy [13].

A.3 Experimental results

The morphology of LSMO-0.3 bulk and NWs has been studied by SEM and the results are shown in Fig. A.1 (a) and (b) respectively. It is observed that there are bulk particles with the size range of 60–170 μm and the average diameter of the NWs is around 40 nm as discussed in chapter 2.

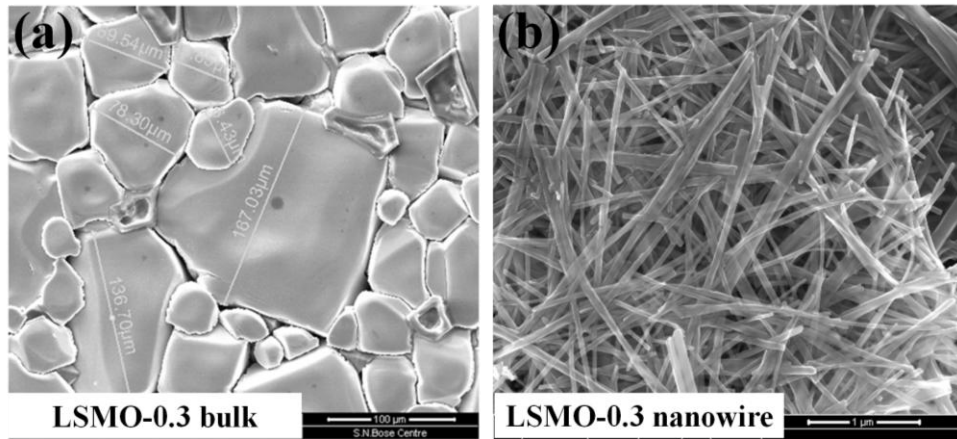


Figure A.1 Results of SEM study of (a) bulk LSMO-0.3 showing particles with the size range of 60–170 mm. (b) LSMO-0.3 nanowires having average diameter of 40 nm.

We have cooled both the samples down to 90 K at zero field and waited for 2 hrs at 90 K in zero field. Then we have further cooled the samples down to 80 K. At 80 K, we have applied the field of 40 Oe and taken the ZFC data at heating cycle. We have again cooled the sample down to 80 K at zero field. Then at 80 K we have applied the field of 40 Oe and taken the ZFC data at heating cycle for reference. We have compared the ZFC magnetization data with stops of 2 hrs at 90 K with the uninterrupted reference ZFC magnetization for studying the

non-equilibrium magnetic behaviour of LSMO-0.3 bulk and NWs as shown in Fig. A.2. It has been observed that there is a dip presents around 90 K in NWs because of freezing of moments in the ZFC curve with stops (see Fig. A.2). When the LSMO-0.3 NWs has been cooled again without any field and warmed at $H = 40$ Oe up to 400 K, the recorded ZFC magnetization shows similar but very smaller dip around that same temperature region around 90 K. Therefore, it is evident that the LSMO-0.3 NWs can “remember” the history of incidents which confirms the observation of memory effect. The similar magnetic measurements are performed on LSMO-0.3 bulk (see inset of Fig. A. 2) and nanoparticles which support the fact that both the samples also exhibit magnetic memory effect [14].

The magnetic relaxation of both LSMO-0.3 samples has been measured for 7 hrs waiting time at 95 K after sudden application and removal of $H = 1$ Tesla magnetic field. The data are plotted in Figure A.3 (a) for LSMO-0.3 NWs. The relaxation of magnetization is about 75% for LSMO-0.3 NWs. The modelling of magnetic relaxation data suggests the existence of two relaxation times. We have found similar behaviour for magnetic relaxation from the analysis for LSMO-0.3 bulk at 95 K which is described in Fig. A.3 (b). The relaxation of magnetization is about 90% for LSMO-0.3 bulk. The values of fit parameters with errors are given in Table A.1.

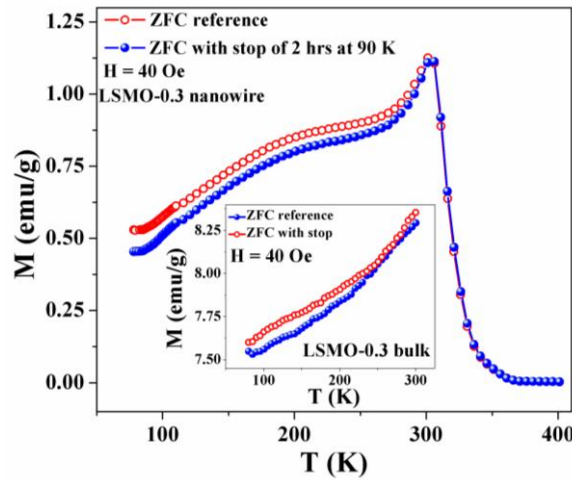


Figure A.2. Results of ZFC magnetization measurements with stops of 2 hrs at 90 K at applied field $H = 40$ Oe and the uninterrupted reference ZFC magnetization for studying memory effect of LSMO-0.3 nanowires. Inset shows the results of same measurements for LSMO-0.3 bulk.

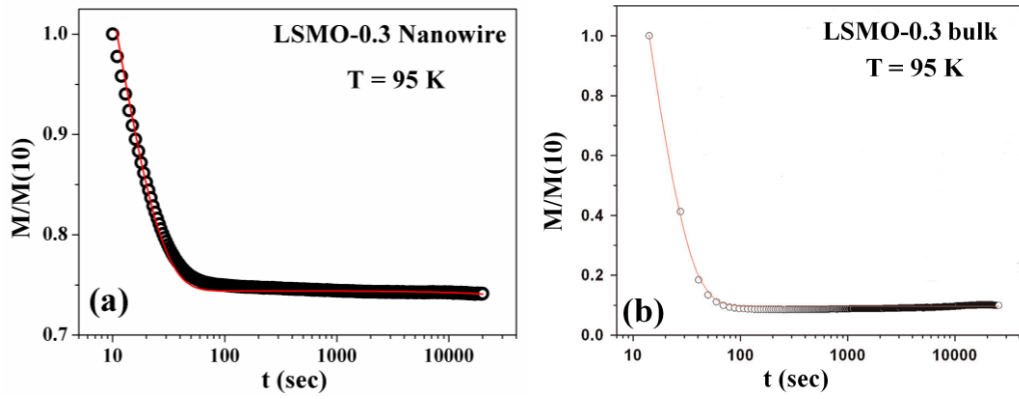


Figure A.3 Results of relaxation experiment for LSMO-0.3 (a) nanowires (b) bulk where normalized magnetization is plotted with respect to time at 95 K. Symbols are experimental points and solid line is the result of fitting with two relaxation times.

Table A.1 The fitting parameters and standard deviations for fitting of normalized magnetization data according to Eq. (A.3) for LSMO-0.3 nanowires and bulk samples.

Sample	τ_1 (sec)	τ_2 (sec)	χ^2
LSMO-0.3 NW	10.25 ± 0.008	$4.76 \times 10^6 \pm 30562.6$	1.89×10^{-6}
LSMO-0.3 bulk	12.19 ± 0.14	$3.24 \times 10^6 \pm 14009.8$	2.0×10^{-5}

Magnetic memory and relaxation phenomena are strongly influenced by the inter-particle magnetic interaction which is studied by measuring m_{IRM} and m_{DCD} as a function of magnetic fields. Fig. A.4 (a) shows the variation of m_{IRM} and m_{DCD} (normalized) taken at 120 K as a function of H_{app} (without sign) ranging from 0 to 500 Oe for LSMO-0.3 NWs. It is noticed that m_{IRM} increases but m_{DCD} decreases with applied fields. The quantity, $\delta m (= m_{\text{DCD}} - (1 - 2m_{\text{IRM}}))$ which is generally used to probe interaction between NWs, has been observed to be positive for LSMO-0.3 NWs in the range of $H_{\text{app}} = 50 - 500$ Oe favouring magnetized state (Fig. A.4 (b)) [12]. The variation of m_{IRM} and m_{DCD} (normalized) with applied fields for LSMO-0.3 bulk is plotted in Fig. A.5 (a). δm remains positive in the range of $H_{\text{app}} = 100 - 500$ Oe (except at $H_{\text{app}} = 50$ Oe) in LSMO-0.3 bulk as seen in Fig. A.5 (b). As reported earlier, this kind of interaction favours magnetized state in LSMO-0.3 bulk [12, 15].

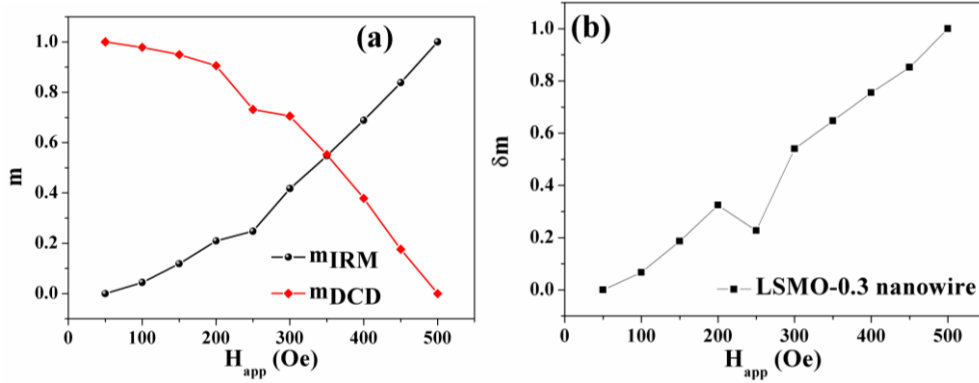


Figure A.4 (a) The plot of normalized m_{IRM} and m_{DCD} of LSMO-0.3 nanowires as a function of applied field H_{app} (The sign of H_{app} has been ignored). M vs. H data taken at 120 K. (b) Variation of δm with H_{app} for LSMO-0.3 nanowires.

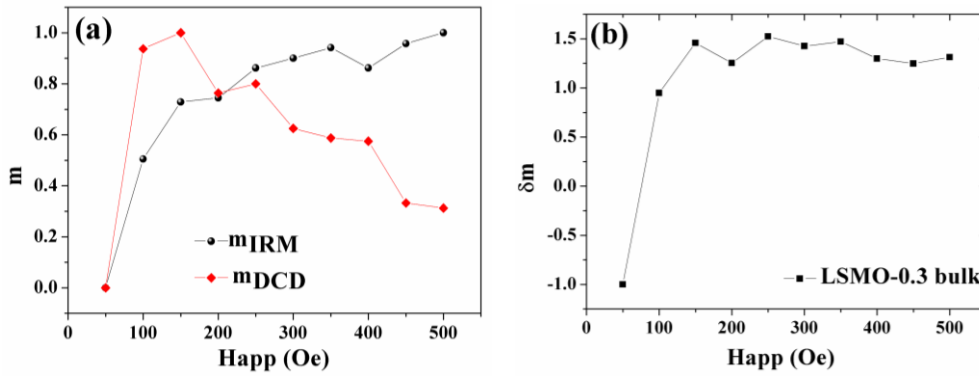


Figure A.5 (a) The plot of normalized m_{IRM} and m_{DCD} of LSMO-0.3 bulk as a function of applied field H_{app} (The sign of H_{app} has been ignored). M vs. H data taken at 120 K. (b) Variation of δm with H_{app} for LSMO-0.3 bulk samples.

A.4 Discussions

Fig. A.2 and inset show the results of memory effect for LSMO-0.3 NWs and bulk measured by ZFC protocol at 90 K supporting the fact that the system “remembers” the time when the intermittent stop is made [16]. Observation of memory effect generally suggests spin-glass like behaviour where finite interaction should be present among the particles [16]. Our measurements have already suggested (see Fig. A.4) that LSMO-0.3 NWs have finite inter-particle interactions which justifies the observation of their magnetic memory. In case of LSMO-0.3 bulk, the similar observation is supported by existence of different kind of interactions as described in the results of Fig. A.5. In this respect, our magnetic relaxation measurements for 7 hrs have provided some important results. It is known that for an

ensemble of identical particles each with the same energy barrier to magnetization reversal, the time decay of the magnetization is an exponential function as given below,

$$M(t) = M(0) \exp(-t/\tau) \quad (\text{A.1})$$

Here $M(0)$ is the magnetization at time (t) zero and τ is the relaxation time [17]. In real systems of magnetic nanoparticles there is always a distribution of energy barriers due to a distribution of the magnetic anisotropy constants K (caused by crystalline and predominantly shape anisotropy) as well as of the core volumes V of the particles [18]. Hence, if there is a distribution of energy barriers, the magnetization decays logarithmically in time as

$$M(t) = M(0) - S \ln(t) \quad (\text{A.2})$$

where S is the magnetic viscosity [19]. We have plotted the normalized magnetization $M(t)/M(10)$ against time (t) for LSMO-0.3 NWs in logarithmic scale where $M(10)$ is the magnetization recorded at 10^{th} second (Fig. A.3(a)). As it is seen $M(t)/M(10)$ is not following a straight line with t (<100 sec), it is clearly understood that the system is not suitable to be described by the function in Eq. (A.2). We have tried to fit the data to a stretched relaxation function ($M(t)/M(10) = (1 - \exp[-(t/\tau)^\beta])$), but the results are not satisfactory for the whole range of temperature. Finally, we have used superposition of two exponential functions involving two relaxation times as given below,

$$M(t) = M(0) [\exp(-t/\tau_1) + \exp(-t/\tau_2)] \quad (\text{A.3})$$

The results of the fit for $M(t)/M(10)$ vs. t of LSMO-0.3 NWs and bulk samples are plotted in Fig. A.3. Symbols are experimental points and solid line is the result of fitting. The fitting results appear to be satisfactory for the whole range of time scale. Presence of two relaxation times may indicate the existence of two independent and negligibly interacting systems. The superposition of two relaxation times can arise from particle size distribution considering a theoretical model (based on poly dispersity and interaction effects) involving just two kind of particles ‘large’ and ‘small’ [20]. Since the present LSMO-0.3 NWs and bulk particles do have certain size distribution (as discussed in chapter 2) this model can be applied to explain two relaxation times. In order to explore the inter-particle interactions; we have measured

normalized m_{IRM} and m_{DCD} as a function of magnetic fields for LSMO-0.3 NWs and bulk. For any non-interacting system of particles with uniaxial anisotropy, Wohlfarth relation $m_{DCD} = (1 - 2m_{IRM})$ is valid which is not applicable for present LSMO-0.3 system. The results of our measurements yield non zero and positive value of δm (see Fig. A.4(b)) for LSMO-0.3 NWs indicating that the particles of same size are interacting and positive δm corresponds to the fact that this interaction actually favours magnetized state for LSMO-0.3 NWs [12, 15]. Fig. A.5 (b) also shows finite and positive δm for LSMO-0.3 bulk. From the above results we can infer that both the samples are interacting and this interaction actually favours magnetized state.

A.5 Summary

We have investigated the memory effect, relaxation and interaction of LSMO-0.3 NWs and bulk particles. The LSMO-0.3 NWs have been grown by hydrothermal method and LSMO-0.3 bulk is synthesized by the sol-gel based polymeric precursor route and heated at higher temperatures. Magnetic memory effect measurements in ZFC protocol at $H = 40$ Oe displays that both the LSMO-0.3 samples can “remember” the history of incidents. Our magnetic relaxation measurement at 95 K and analysis show the existence of two relaxation times for LSMO-0.3 NWs and bulk. This is attributed to the fact that particles of different sizes can relax separately. Both LSMO-0.3 samples are found to be interacting and the nature of interaction favours magnetized state.

Bibliography

- [1] P. Dey and T. K. Nath, *Phys. Rev. B*, **73**, 214425 (2006).
 - [2] M. M. Savosta, V. N. Krivoruchko, I. A. Danilenko, V. Yu, T. E. Tarenkov, A. V. Konstantinova, Borodin and V. N. Varyukhin, *Phys. Rev. B*, **69**, 024413 (2004).
 - [3] S. S. Rao, S. Tripathi, D. Pandey and S. V. Bhat, *Phys. Rev. B*, **74**, 144416 (2006).
 - [4] A. Biswas and I. Das, *Phys. Rev. B*, **74**, 172405 (2006).
 - [5] J. Curiale, M. Granada, H. E. Troiani, R. D. Sanchez, A. G. Levy, P. Levy and K. Samwer, *Appl. Phys. Lett.*, **95**, 043106 (2009).
 - [6] X. Batlle and A. Labarta, *J. Phys. D: Appl. Phys.*, **35**, R15 (2002).
 - [7] R. H. Kodama, *J. Magn. Magn. Mater.*, **200**, 359 (1999).
 - [8] R. S. Freitas, L. Ghivelder, F. Damay, F. Dias and L. F. Cohen, *Phys. Rev. B*, **64**, 144404 (2001).
 - [9] P. Levy, F. Parisi, L. Granja, E. Indelicato and G. Polla, *Phys. Rev. Lett.*, **89**, 137001 (2002).
 - [10] H. Y. Hwang, S. W. Cheong, N. P. Ong and B. Batlogg, *Phys. Rev. Lett.*, **77**, 2041 (1996).
 - [11] A. Chainani, M. Mathew and D. D. Sarma, *Phys. Rev. B*, **47**, 15397 (1993).
 - [12] J. Geshev, M. Mikhov and J. E. Schmidt, *J. Appl. Phys.*, **85**, 7321 (1999).
 - [13] E. P. Wohlfarth, *J. Appl. Phys.*, **29**, 595 (1958).
 - [14] N. Ghosh, S. Datta and B. Ghosh, *J. Magn. Magn. Mater.*, **382**, 277–282 (2015).
 - [15] X. Che and H. N. Bertram, *J. Magn. Magn. Mater.*, **116**, 121 (1992).
 - [16] O. Petracica, X. Chena, S. Bedantaa, W. Kleemanna, S. Sahoob, S. Cardosoc and P. P. Freitasc, *J. Magn. Magn. Mater.*, **300**, 192 (2006).
 - [17] E. C. Stoner, F. R. S. Wohlfarth and E. P. Wohlfarth, *Phil. Trans. R. Soc.*, **A240**, 599 (1948).
 - [18] R. Koetitz, W. Weitschies, L. Trahms, W. Brewer and W. Semmler, *J. Magn. Magn. Mater.*, **194**, 52 (1999).
 - [19] R. Street and J. C. Woolley, *Proc. Phys. Soc.*, **62**, 562 (1949).
 - [20] S. Chakraverty, M. Bandyopadhyay, S. Chatterjee, S. Dattagupta, A. Frydman, S. Sengupta and P. A. Sreeram, *Phys. Rev. B*, **71**, 054401 (2005).
-